ABSTRACT

Title of dissertation: SPECTRAL LADAR: ACTIVE RANGE-RESOLVED IMAGING SPECTROSCOPY

Michael Annona Powers, Doctor of Philosophy, 2011

Dissertation directed by: Professor Christopher C. Davis
Department of Electrical and Computer Engineering

Imaging spectroscopy using ambient or thermally generated optical sources is a well developed technique for capturing two dimensional images with high per-pixel spectral resolution. The per-pixel spectral data is often a sufficient sampling of a material's backscatter spectrum to infer chemical properties of the constituent material to aid in substance identification. Separately, conventional LADAR sensors use quasi-monochromatic laser radiation to create three dimensional images of objects at high angular resolution, compared to RADAR. Advances in dispersion engineered photonic crystal fibers in recent years have made high spectral radiance optical supercontinuum sources practical, enabling this study of Spectral LADAR, a continuous polychromatic spectrum augmentation of conventional LADAR. This imaging concept, which combines multi-spectral and 3D sensing at a physical level, is demonstrated with 25 independent and parallel LADAR channels and generates point cloud images with three spatial dimensions and one spectral dimension.

The independence of spectral bands is a key characteristic of Spectral LADAR. Each spectral band maintains a separate time waveform record, from which target parameters are estimated. Accordingly, the spectrum computed for each backscatter reflection is independently and unambiguously range unmixed from multiple target reflections that may arise from transmission of a single panchromatic pulse.

This dissertation presents the theoretical background of Spectral LADAR, a shortwave infrared laboratory demonstrator system constructed as a proof-of-concept prototype, and the experimental results obtained by the prototype when imaging scenes at stand off ranges of 45 meters. The resultant point cloud voxels are spectrally classified into a number of material categories which enhances object and feature recognition. Experimental results demonstrate the physical level combination of active backscatter spectroscopy and range resolved sensing to produce images with a level of complexity, detail, and accuracy that is not obtainable with data-level registration and fusion of conventional imaging spectroscopy and LADAR.

The capabilities of Spectral LADAR are expected to be useful in a range of applications, such as biomedical imaging and agriculture, but particularly when applied as a sensor in unmanned ground vehicle navigation. Applications to autonomous mobile robotics are the principal motivators of this study, and are specifically addressed.

SPECTRAL LADAR: ACTIVE RANGE-RESOLVED IMAGING SPECTROSCOPY

by

Michael Annona Powers

Dissertation submitted to the Faculty of the Graduate School of the
University of Maryland, College Park in partial fulfillment
of the requirements of the degree of
Doctor of Philosophy
2011

Advisory Committee:

Professor Christopher C. Davis, Chair
Professor Rama Chellappa
Professor Mario Dagenais
Professor Wendell Hill III
Professor Thomas Murphy

DEDICATION

To my parents

ACKNOWLEDGEMENTS

I am grateful to have many people to thank for their support of my research work, this dissertation, and my graduate studies in general. First, I thank my parents, to whom I have dedicated this work. From the very beginning their guidance, support, and encouragement has made me who I am today. They instilled in me the value of performing to the best of one's ability. I thank my advisor, Professor Christopher C. Davis, for his helpful advice over the course of this work. My initial supervisors at General Dynamics, Pete Peterman and Jay Kurtz, allowed me the time and flexibility to complete this research. Bill Borgia, consortium manager for the Robotics Collaborative Technology Alliance, provided key support and assistance in organizing the programmatic aspects of this work in addition to the critical review and improvement of numerous manuscripts. For the last few months of this project, I have Dr. Bob Mitchell to thank for this role. Special thanks go to Chuck Shoemaker, a recognized pioneer in U.S. Army robotics, for consistently supporting the Spectral LADAR project from its earliest stages. Thanks to colleagues Parth Patel, Mike Wild, and Tod Oblak for assistance with board layout, mechanical design, and review of the manuscript, respectively. I appreciate the consistent and continued sponsorship of the U.S. Army Research Lab in conducting this research, and General Dynamics Robotic Systems for material and infrastructure support. Finally, I would like to express gratitude to my wife for her support of my graduate school and research activities that often diverted my time and attention.

-Michael A. Powers
April 2011

TABLE OF CONTENTS

TABLE OF FIGURES

LIST OF ABBREVIATIONS

2D	Two-dimensional
3D	Three-dimensional
a.u.	Arbitrary units
ABS	Acrylonitrile butadiene styrene
AC	Alternating current
ACU	Army combat uniform
ADC	Analog-to-digital converter
ADU	Analog-to-digital unit
AFB	Air Force base
AGC	Automatic gain correction
AM	Amplitude modulation
ANSI	American national standards institute
AOM	Acousto-optic modulator
AOTF	Acousto-optic tunable filter
APD	Avalanche photodiode
API	Application programming interface
AR	Anti-reflective, often describing a coating
ASIC	Application specific integrated circuit
ATR	Automatic target recognition
AVIRIS	Airborne visible/infrared imaging spectrometer (NASA instrument)
BRDF	Bi-directional reflectance distribution function

BS	Beamsplitter
CAD	Computer aided design
CCD	Charge-coupled device (type of image sensor)
CDMA	Code division multiple access
CMOS	Complementary metal oxide semiconductor (type of image sensor)
CW	Continuous wave
CWL	Center wavelength (of a tunable instrument)
DARPA	Defense Advanced Research Projects Agency
DC	Direct current
deg	Degrees (angular unit)
DIAL	Differential absorption LIDAR
DOP	Degree of polarization
DSO	Digital storage oscilloscope
DSP	Digital signal processing
EFL	Effective focal length
EMI	Electromagnetic interference
F/#	F-number
FLIM	Fluorescence lifetime imaging microscopy
FM	Frequency modulation
FOPEN	Foliage penetration, often referring to RADAR
FOV	Field-of-view
FP	Fabry-Pérot type resonator
FPS	Frames per second

FSR	Free spectral range
FTIR	Fourier transform infrared spectroscopy, a type of instrument
FWM	Four-wave mixing
GTRI	Georgia Tech Research Institute
GVD	Group velocity dispersion
HMMWV	Humvee, or high mobility multipurpose wheeled vehicle
HNLF	Highly nonlinear fiber
HV	High voltage
HVAC	Heating, ventilating, and air conditioning
IF	Intermediate frequency
IFF	Identification friend or foe
iFOV	Instantaneous field-of-view (of a scanned imaging system)
InAlAs	Indium aluminum arsenide, a compound semiconductor alloy
InGaAs	Indium gallium arsenide, a compound semiconductor alloy
InP	Indium phosphide, a compound semiconductor alloy
IR	Infrared
I-V	Current-voltage
KNN	K nearest neighbors
LADAR	Laser detection and ranging (syn. LIDAR, Laser Radar)
LCS	LADAR cross-section
LCTF	Liquid crystal tunable filter
LEP	Lateral-effect photodiode
LHS	Left hand side, of an equation

LIBS	Laser-induced breakdown spectroscopy
LIDAR	Light detection and ranging (syn. LADAR, Laser Radar)
LO	Local oscillator
LP	Linear polarizer or linearly polarized
LPF	Low-pass filter
LWIR	Long-wavelength infrared
MC	Multi-component
MFD	Mode field diameter ($1 / e^2$ intensity definition)
MI	Modulation instability
MLC	Maximum likelihood classifier
MMF	Multi-mode fiber
MMW	Millimeter wave
MOPA	Master oscillator power amplifier
MPE	Maximum permissible exposure
MTF	Modulation transfer function
MWIR	Mid-wavelength infrared
NA	Numerical aperture
ND	Neutral density
NEDR	Noise equivalent delta reflectivity
NEP	Noise equivalent power
NETD	Noise equivalent temperature difference
NIR	Near-infrared
OPO	Optical parametric oscillator

OSA	Optical spectrum analyzer
PC	Personal computer
PCA	Principal component analysis
PCF	Photonic crystal fiber
PD	Photodiode
PDF	Probability density function
PID	Proportional-integral-derivative, a type of control system
PIN	A type of photodiode
PM	Polarization maintaining, a type of optical fiber
PMMA	Poly(methyl methacrylate)
PRF	Pulse repetition frequency
PSF	Point spread function, the spatial impulse response of an imaging system
PTFE	Polytetrafluoroethylene
PVC	Polyvinyl chloride
RADAR	Radio detection and ranging
RC	Resistor capacitor circuit, referring to a decay time constant
RF	Radio frequency
RGB	Red-green-blue, a color system based on human perception
RHS	Right hand side, of an equation
RMS	Root-mean-square
ROC	Receiver operating characteristic
ROIC	Read-out integrated circuit
Rx	Receiver

SAGM	Separate absorption, grading, and multiplication
SAM	Spectral angle map
SAR	Synthetic aperture RADAR
SC	Supercontinuum
SCG	Supercontinuum generation
SCPI	Standard commands for programmable instruments
SM	Single mode
SMA	An RF connector or fiber optic ferrule connector specification
SMF	Single mode fiber
SNR	Signal-to-noise ratio
SONAR	Sound navigation and ranging
SOP	State-of-polarization
SPM	Self-phase modulation
SWaP-C	Size, weight, power, and cost
SWIR	Short-wavelength infrared
TCP/IP	Transmission control protocol / internet protocol
TE	Transverse electric
TEC	Thermo-electric cooler
TIA	Transimpedance amplifier
TL	Transmitter lens
TM	Transverse magnetic
TO	Transistor-outline, a type of electronics package
ToF	Time-of-flight

TTL	Transistor-transistor logic
Tx	Transmitter
UAV	Unmanned air vehicle
UGV	Unmanned ground vehicle
UHMW	Ultra-high molecular weight
USB	Universal serial bus
USD	United States Dollar
UV	Ultraviolet spectrum
VIS	Visible spectrum
YAG	Yttrium aluminum garnet
ZDW	Zero-dispersion wavelength

1. Introduction

This dissertation[*] presents the analysis, design, and experimental evaluation of an augmented form of conventional LADAR[†] as a new approach to multispectral 3D imaging using a pulsed optical supercontinuum source. The real-time ability to create digital images of scenes in three spatial dimensions with specific chemical signature information at each image element is an enabling technology in several areas of engineering and scientific inquiry, including agriculture and biomedical imaging [1]. In this study, the sensor is specifically applied to problems in robotic perception.

Conventional LADAR sensors, which use the technique of transmitting a quasi-monochromatic laser line and using direct or coherent detection of the backscatter signal, are popular as primary perception system sensors onboard large and small unmanned ground vehicles (UGVs). Such sensors are also integral parts of reconnaissance and Automatic Target Recognition (ATR) sensor payloads. LADAR is an optical frequency variant of RADAR that first appeared around the time of the invention of the laser / maser and is frequently used for atmospheric studies [2, 3, 4]. The key benefit of a conventional LADAR system is its ability to produce highly accurate and unambiguous 3D images of a scene at a very high angular resolution. The subject of this dissertation,

[*] Various figures in this document require full-color printing / display for proper interpretation

[†] Laser (Light) Detection and Ranging, alternatively: Laser Radar, LIDAR

Spectral LADAR, uses backscatter absorption spectroscopy to enhance 3D images. This spectral information enables the recognition of objects that are difficult or impossible to identify using conventional LADAR or passive sensors with an acceptable probability of detection and false alarm rate trade-off. There are relatively common situations where contemporary robotic perception systems using shape recognition alone are critically inadequate.

Significant innovations beyond the current state-of-the art in 3D spectral sensing are developed. Active, single-pulse time resolved reflectance spectroscopy is the technique used in this investigation of Spectral LADAR. This mode of spectral imaging maintains the characteristics that are necessary for three dimensional perception of dynamic environments, which is a fundamental necessity to autonomous vehicle applications. To date, literature reports of similar active spectral imaging techniques, expounded upon in Section 2, have lacked the combination of long range, high range resolution, and high pixel rate attributes. Recent advances in areas of optical component technology including photonic crystal fibers have encouraged the pursuit of this work which would have otherwise been impossible or impractical several years ago. To the knowledge of the author, this is the first reported system to implement many (25) continuous spectral bands, as independent high bandwidth[*] range resolved channels, in the shortwave infrared with sufficient transmitter power and receiver sensitivity for quasi-single-pulse[†] sensing at long standoff range. Most other systems reported in the literature have not

[*] Electronic bandwidth, relating to the pulse envelope

[†] The fundamental technique described is single-pulse spectroscopy, but available hardware limits experimental demonstrations to quasi-single-pulse operation.

considered the problem of eye safety, which is a requirement for unattended systems. The conclusions presented here establish the feasibility of the Spectral LADAR concept and are supported by a combination of analysis and experimental demonstration. The results show that, with further development, a Spectral LADAR sensor can be deployed on UGVs and offer increased perception ability to increase safety and operating capability.

The introduction section discusses the motivation of the autonomous navigation application, and the benefits of Spectral LADAR to a perception system. Next, the requirements of a practical Spectral LADAR sensor are discussed. The introduction concludes with an overview of the technical approach taken in this research. Section 2 describes similar published work in active spectral imaging, and work done to specifically address the UGV problems considered here. Section 3 discusses the background analysis and fundamental physical processes used in Spectral LADAR. The initial work of developing the technique and characterizing the spectrometer and supercontinuum source is presented in Section 4. In Section 5, the design and testing of a Spectral LADAR laboratory demonstrator is discussed. This laboratory demonstrator was constructed as an experimental proof-of-concept to assess the capability of the system with real objects in arranged, static scenes. The experimental analysis and performance results of this system are presented in Sections 7, 8, and 9. Investigations into polarimetric sensing and detection are discussed separately in Section 6. This dissertation concludes with a summary, conclusion, and suggestions for future work in Section 10.

1.1. Robotic Perception Systems

Unmanned ground vehicles (UGVs) are a specific subset of robotics concerning vehicles capable of autonomous operation. A robotic vehicle is said to operate autonomously when human control is limited to issuing sparse waypoints and objectives while specific, timely action concerning heading, speed, and other parameters are automatically determined by the vehicle computer system. In this case, the navigation, guidance, and control systems must respond to events that require dynamic planning and re-planning of routes. These activities are supported by essential sensor data supplied to the UGV computer system. Perception data is developed into a "world model," which is a digital representation of the three dimensional environment augmented with semantic understanding and identification of objects in the scene.

Although the application focus of this work is on UGVs, low-altitude unmanned air vehicles (UAVs) that closely support or concern objects on the ground is a related application.

1.1.1. Motivation

Self-guided, driverless vehicles for general transportation have long been pursued to alleviate many problems inherent to modern transportation, including traffic, driver/pilot error, and overall inefficiency. Although the concept of driverless vehicles may be as old as the automobile itself, the means to implement such devices has remained elusive due to technological limitations, economic limitations, or both. Historically, the approach taken to the problem could be broadly categorized in one of two groups: infrastructure systems or autonomous systems. The infrastructure approach relies on a networked system in which communication supporting centralized coordination is established on all vehicles, whereas an autonomous system can operate independently from any established network or protocol and operates based on local perception data. Certainly a practical system may borrow aspects from each approach. While an infrastructure type solution may be suitable for highways where communications and protocol/procedural compliance can be made dependable, off-road and military vehicles must perform in unstructured environments where all communications may be denied and the surroundings may be dynamic and hostile. This difficult situation has significant implications for the system design, requiring that each vehicle have the capability to perceive the environment with adequate fidelity to navigate and complete its mission independently of other assets in completely unstructured and random environments. It should be no surprise that the interest in autonomous-type systems is perhaps most vibrant in the defense community. The force protection and logistical advantages of using UGVs in lieu of manned vehicles for many applications are obvious. Clearly there

are also situations where autonomous vehicles, ground, air, or marine based, have significant tactical advantages over their manned counterparts such as in reconnaissance operations where long hours on station are required. This robotic technology is especially well suited to military tasks involving one or more of the 3 Ds: tasks that are dirty, dull, or dangerous.

Research and development of such vehicles and their complement of sensors and computing systems has been the subject of much research for some time. Since the early 1990s, the technology has evolved from initial "semi-autonomous" systems, which follow predetermined paths and avoid minor obstacles, toward "fully-autonomous" vehicles, which are given an overarching mission objective or destination to complete without human intervention or foreknowledge of the terrain. One central challenge of autonomous navigation is perception-based object detection and classification. Early systems implemented a rudimentary obstacle avoidance technique, but increasingly, later systems are moving toward ATR-like characteristics where objects are uniquely identified. Unique identification of objects is crucial for understanding the surroundings, anticipating events to support tactical decision-making, and integrating social understanding and constructs.

Current state-of-the-art systems utilize a variety of sensors to perceive the environment and make tactical decisions in real-time. These sensors include stereo cameras, millimeter wave RADAR, thermal infrared cameras, and LADAR. The data from each of these sensors is "fused" in software in an effort to represent the most accurate depiction

of the vehicle's surroundings as the world model. Perhaps the most well known contemporary development efforts are the 2004 and 2005 DARPA Grand Challenge competitions. Although the participants demonstrated highly advanced technology, it should be noted that the systems operated in a semi-contrived, closed environment free from dynamic hazards (such as pedestrians or armed aggressors) with foreknowledge of the overall terrain environment. Ultimately, practical autonomous vehicles will have to operate in a full range of difficult terrain environments where major concerns include collision with humans, camouflage, ambush, and intentional terrain obstacles. The current sensor technology is not adequate in these situations, and also suffers from impractical economics (SWaP-C: size, weight, power and cost) [5]. Figure 1 shows several vehicles from the DARPA Grand Challenge competition with impractical arrays of LADAR and other sensors. The development of sensors that produce specific, high fidelity representations of the environment is a priority in the technical evolution of these vehicles.

Figure 1: DARPA Grand Challenge vehicles, clockwise from left: University of Louisiana (CajunBot) [6], Team ENSCO [7], IndyRobotics LLC [8]

1.1.2. Terminology

It is necessary to clarify some terminology used in the remainder of this work. A LADAR pixel is one ray defined by azimuth and elevation angles which is imaged by the sensor. This is equivalent to a pixel in the conventional passive imager sense. LADAR voxels are spatial "bins" along the path of the pixel which may or may not contain a

backscattered return pulse. The voxels have three dimensions, determined by the cross range resolution and range resolution.

The range accuracy of LADAR refers to the statistical variance around a mean value when multiple observations of a fixed target are made. This is often defined as precision in most other measurement contexts. It is assumed that the systematic error, the difference of the mean range to the true or actual range, can be reduced to zero by proper calibration. The range resolution in LADAR is defined by the minimum separation of two targets, imaged by partial occlusion of the same pixel, which is discernable as two actual targets by the signal processing technique.*

1.1.3. Benefits of Spectral LADAR

The economics of UGVs dictate that a sensor must benefit the perception system to a degree that justifies its cost in size, weight, power and cost (SWaP-C). Consequently, the capabilities of Spectral LADAR must provide appreciable advantages with respect to the established alternatives of conventional LADAR, MMW RADAR, and passive sensing in VIS/NIR/SWIR/MWIR/LWIR bands, including passive hyperspectral imaging.

Figure 2 shows a scene typical of a UGV concept of operations. Specific areas where Spectral LADAR will demonstrate significantly improved object classification are

* Resolution is not to be confused with the digital resolution of the circuitry which determines time-of-flight, or the amplitude resolution of ADC equipment, unless specified in context.

highlighted with green ellipses. These situations include: recognition of partially obscured pedestrians (1), recognition of partially obscured objects (2), recognition of humans in a variety of postures (3), identification of disfigured objects (4), identification of friendly forces using spectral taggants (5), and identification of tagged vehicles that have been cleared at a security checkpoint (6). The additional information provided by Spectral LADAR is helpful in establishing contextual understanding of the environment. With contextual understanding, UGVs will be more able to anticipate future actions, formulate better plans, and act as a better substitute for human skill.

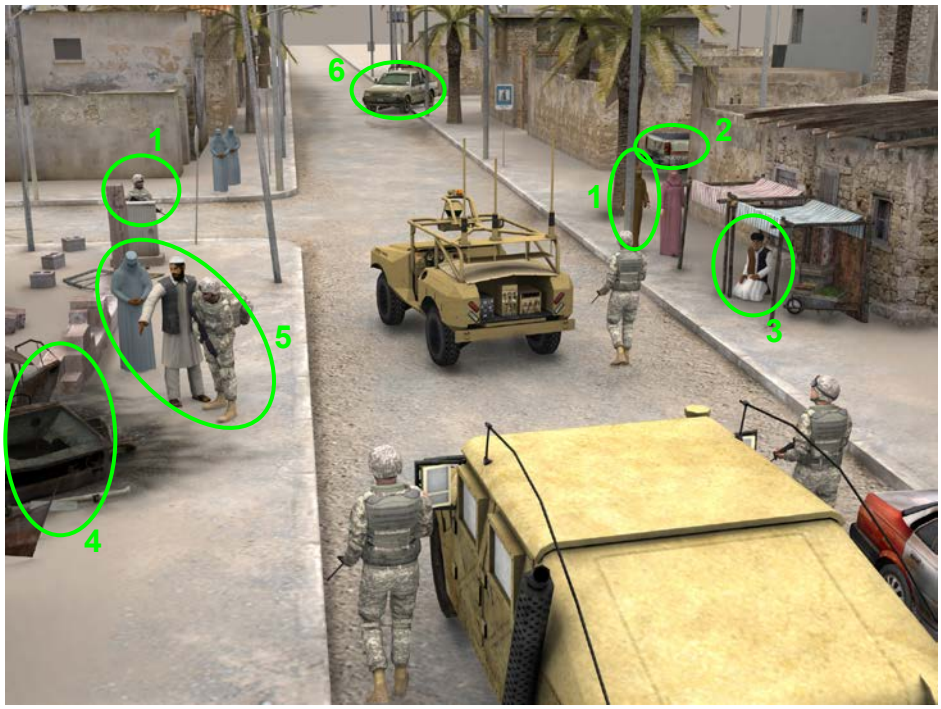

Figure 2: A concept of operations scene (Credit: Lou Bonbrest, GDRS)

Figure 3 shows a scene in which the classification of terrain (dirt vs. mud) may not be possible using spatial information alone. Passive sensor studies have demonstrated alternative detection techniques in daylight and clear weather conditions based on the

scattering properties of mud versus dry ground [9]. The water content of mud has very strong signatures in the SWIR. Spectral classification of terrain types is needed to either avoid risky or impassable areas by seeking favorable surfaces (indicated by the green polygon), or to adjust vehicle handling parameters to avoid getting stuck in the mud (indicated by the red polygon).

Figure 3: Terrain classification scenario (Credit: L. Matthies group, NASA JPL)

1.1.3.1. Benefits Relative to Passive Sensing

Passive sensing, using ambient radiation (sunlight, moonlight, airglow) or thermal self-emission is an attractive option for several reasons [10]. First, it requires no energy to be transmitted from the sensor which may substantially reduce the sensor's power

requirements. Second, it is inherently covert since it emits no intentional radiation that may be detected by a third party. Since human operation of vehicles is easily accomplished with passive human vision, it may be tempting to assume that passive sensing is the ultimate solution for UGVs to the exclusion of all other sensors. At the time of this writing, passive sensor processing algorithms do not come close to human vision processing speed or acuity. Even if one temporarily assumes that computer and algorithm technology advance to a point paralleling human visual processing, active sensors such as LADAR are still desirable since, as will be described in the following paragraphs, they produce sensory information that is not obtainable with passive sensing. Enhanced perception information may partially compensate for the inferior situational understanding abilities of robotic vehicles compared to humans.

Most 3D passive sensors utilize stereo vision with a baseline* of no more than the width of a vehicle. The geometry of two images is compared by identifying corresponding features in each image and geometrically computing the range based on the known perspective of two cameras. Range values are only computed for pixels which have identified correspondence in both channels, which in many cases results in a sparse point-cloud. The accuracy and ranging ability of this technique decreases with longer ranges. At sufficiently long ranges compared to the baseline, (e.g. 100x baseline distance) stereo vision is no longer effective [11]. In contrast, the range accuracy of LADAR decreases mildly with increasing range. This allows high fidelity 3D images at ranges which are impractical using the stereo technique (e.g., 1 km). LADAR produces a high density

* Linear separation distance between cameras

point cloud with regularly spaced pixels, which eases the processing of the three dimensional image.

As an active sensor, LADAR is not susceptible to readily deployable spoofing techniques that may affect the operation of passive sensors. Since passive sensors are entirely dependent upon the ambient or self-emitted radiation, a third party may manipulate these sources of radiation to confuse or blind the sensor. Examples of such spoofing or decoy techniques include using light projection equipment to create false images or patterns that interfere with computing the correspondence of two perspectives. Effective jamming equipment for LADAR sensors is considerably more expensive and difficult to deploy since it must involve high power, fast modulation lasers.

The stereo vision techniques employed by passive sensors are not as effective at ranging in dense clutter compared to LADAR systems. A vehicle or other object covered in foliage or camouflage is one example of such a situation [12]. The time of flight ranging technique used in LADAR systems allows for more than one range value to be computed for a given look angle. This allows for LADAR to have penetrating vision in dense clutter situations, not by transmission through foliage or camouflage as in FOPEN RADAR, but around the partial pixel occlusions in this situation. This capability is highly valuable in a military UGV sensing application. For the most part, this is not possible with passive ranging. Passive or active sensors may use spectral unmixing algorithms to determine if a pixel contains a combination of two or more signatures. The multiple return capability of LADAR intrinsically unmixes signatures in the raw data if

separated in range. This is preferred to unmixing in post processing, which can be ambiguous.

LADAR, or active sensing in general, has clear advantages over passive sensing. These advantages are based on the fundamentals of the techniques and will persist even with revolutionary advancements in vision algorithms and processing technology.

1.1.3.2. Benefits Relative to Spatial-only Classification

Spatial identification of objects and terrain types is, and will remain, a crucial part of a UGV perception system. There are, however, common cases where objects and terrain features cannot be differentiated on the basis of spatial characteristics alone. This may occur when a type of object has significant spatial diversity or when crucial differences in object or terrain physical properties are not indicated by spatial characteristics.

Situations in which there is significant spatial diversity include objects that are reconfigurable or flexible. Human pedestrians fit into this category, and the detection of humans is perhaps the most critical of all perception system objectives so that collision and injury are avoided. Humans may be present in a scene in a variety of postures and physical proportions. They may move about the scene and constantly change their apparent shape or be relatively static. Detecting humans with properties that are independent of these variations can improve the trade-off between the probability of detection and false alarm error rate. Unlike spatial signatures, the spectral signatures of

hair, skin, and clothing can be very specific markers identifying a detected object as a person.

Many other objects may also be present in significantly different shapes and vary with time. Vehicles, for example, may have doors and other compartments open or closed which causes significant variation in shape from some perspectives. Attempts to identify vehicles in all of their many spatial configurations may be possible with a high probability of detection, but the false alarm rate will suffer if the classification criteria of a vehicle are made very broad. Further, damaged objects may be highly distorted in shape which may result in improper classification. Just as in the case of identifying humans, detecting specific spectral markers of vehicles such as tires and paint will decrease the likelihood of false alarms from such things as a similar-looking arrangement of cardboard boxes or wooden crates.

Even objects that are assumed to be in a very narrow range of shapes can be difficult to detect using spatial recognition alone. Objects may be partially obscured by other objects in the scene, such as foliage or camouflage. In this case, spectral signatures may be able to identify an object even when its partial spatial presentation is entirely ambiguous.

Objects and terrain features that lack any spatial differentiation are impossible to detect with conventional LADAR and passive sensors without the aid of spectral information. Terrain features often have little spatial differentiation. Dirt, mud, gravel, sand, and asphalt all have nearly identical spatial characteristics but vastly different physical

properties that have a significant impact on vehicle dynamics and handing. Spectral signatures can differentiate these terrain classes. Successful operation of UGVs over varied terrain requires knowledge of the surface contacting the tires or tracks. Vehicles must adapt to driving over mud so that they do not become stuck. Long range navigation sensors with terrain identification capability like Spectral LADAR can improve mission performance by choosing to avoid inferior surfaces like mud and sand in favor of solid ground.

The identification of friends versus foes (IFF) is difficult when sophisticated and expensive RF transponders are unavailable or impractical. In ground combat situations, this is usually the case. Importantly, friendly forces can not be distinguished from others on the basis of their spatial characteristics. The use of uniforms is a centuries old method of quickly distinguishing allegiances. Almost as old is the forgery of uniforms to misrepresent enemy combatants seeking to infiltrate friendly positions. Since uniforms are overtly displayed and have distinguishing features in the visible spectrum, they are easily copied. However, using special spectral signatures in the invisible portions of the electromagnetic spectrum is far more covert and resistant to forgery. Known friendly agents and objects may be spectrally "tagged" with a spectral signature to distinguish them from others. In these cases forgery is discouraged since the signatures are hard to detect, and practically impossible to duplicate if the chemical composition requires esoteric, hard to find, or hard to formulate materials. Such passive optical tags intended for interrogation by Spectral LADAR may be very inexpensive per unit in large quantities and be an effective means of highly directional friend vs. foe identification.

Spectrally-assisted identification of objects makes a sensor system far more resistant to decoy measures. Decoys may be used by opposing forces as an area denial weapon as effective as mine fields to prevent the use of UGVs. The use of spatial decoys to fool spatial-only sensors may be readily deployed by using mannequins to simulate humans, and perhaps using an arrangement of crates and boxes to simulate hostile vehicles. Thermal signatures* may be simulated using widely available heating elements, including a simple light bulb. Spectral signatures, on the other hand, are more difficult to emulate. Duplicating the spectral response of skin, uniforms, or particular vehicles is more difficult compared to deploying decoys to feign a spatial signature.

In general, spectral signatures as an adjunct to popular spatial sensing techniques allow for more specific identification of objects in a wider variety of circumstances.

1.1.3.3. Unique Advantages

Sections 1.1.3.1 and 1.1.3.2 discussed the advantages of active LADAR sensing compared to passive sensing, and spectrally augmented sensing compared to sensing that is exclusively based on spatial properties. Clearly it is possible to use passive hyperspectral and LADAR sensors simultaneously, and associate a spectral vector with vectors in 3D space by fusing the data into a combined point cloud. This, however, will

* Here, thermal signatures refer to surface temperatures as opposed to spectral signals in the thermal infrared.

still fall short of the imagery produced by a true Spectral LADAR sensor. The critical deficiency is that, unlike LADAR, the hyperspectral image produced by the passive sensor is not range resolved, and does not produce multiple returns per pixel which is needed in highly cluttered scenes or for the recognition of objects obscured by camouflage or foliage. Consequently, multiple LADAR returns may be associated with one passive sensor pixel and the spectra of that pixel will have a mixed constituency. The range resolved operation of Spectral LADAR does not mix range-separated spectra and leads to more accurate spectral classification in highly cluttered scenarios.

Moreover, the spectral capability does not rely on the availability or characteristics of external radiation sources and is instead detected with an active spectral interrogator. Active systems are known to produce better results since they are not susceptible to shadows or the errors resulting from inaccurate assumptions in the inverse sensing (reconstruction) problem [13].

1.1.4. System Requirements

One objective of this work is to construct a demonstrator system as a proof-of-concept. Such prototypes need not meet all requirements for practical use; however it is important to consider these requirements in advance so that there is a clear path towards practical implementation. The requirements presented in this section derive from experience in conventional LADAR system design for UGVs. In many cases, the sensor requirements are imposed by the needs of those working on vehicle navigation software and systems.

Specifics vary from vehicle to vehicle based on a number of factors including end-user requirements.

1.1.4.1. Imaging Speed and Range

An effective LADAR system for high speed vehicle operation must be capable of imaging the environment in real-time, at 10 FPS or more. The frame rate requirement is mainly a function of vehicle speed and the time dynamics of the environment. The field of view also depends on vehicle speed, accounting for the turning capability of the vehicle. At high speeds, a narrow field of view (15^o x 15^o) in azimuth and elevation scanning in the direction of movement at high frame rate may be desirable, whereas a wider, even panoramic, field of view (360^o x 15^o) with slower frame rate may be more appropriate for navigation and situational awareness at a slower speed.

Angular resolution is an important parameter as it determines the spatial granularity at which objects are perceived. Typically, full-angle resolutions for UGV LADAR are approximately 1 mrad* to a few mrad [14]. The military sensing community has generally assumed 4 or 5 pixels on a target as being sufficient for recognition [15].

The product of field of view, angular resolution, and frame rate determines the required pixel rate (pixels/sec). Systems having pixel rates in excess of 20,000 pixels/sec are

---

* mrad is $1x10^{-3}$ radians, sometimes abbreviated as 'mr'

generally considered useful. The high pixel rate imposes constraints on the spectroscopic method; it makes single-pulse spectroscopy necessary and requires the entire spectrum to be captured with each pulse of the laser transmitter. Thus, it is not feasible to use tunable lasers to sweep a broad spectrum due to the settling times being on the order of 1 ms or more. Broadband sources with tunable (scanning) receiver filters would also not meet the pixel rate requirement in addition to being highly inefficient.

The LADAR should have a maximum range of no less than 150 m assuming a 40% reflective target to be useful for high speed driving. The range accuracy should be within several centimeters, and the range resolution should be no more than 40 cm.

1.1.4.2. Size, Weight, Power and Cost (SWaP-C)

Serious attention must be paid to the operational characteristics and practical aspects. The SWaP-C of the instrument has a strong effect on its deployability on various platforms- military, civilian, or commercial. To be practical, the entire system should weigh less than 25 kg and the receiver aperture diameter should be no more than 100 mm.

1.1.4.3. Eye Safety

Eye safety is an absolute requirement that sets an upper bound on performance by limiting the energy density from the laser transmitter. This requirement is particular to autonomous vehicles since the LADAR sensor must be usable in populated settings.

There is no possibility that laser safety goggles could be worn by all personnel in the vicinity of an operating UGV as a means to increase permissible transmission energy.

The region around 1550 nm is exceptionally eye-safe using the definitions of the ANSI standard. At wavelengths longer than that of human vision, lasers become progressively more eye safe up to about 1450 nm where the eye has very high tolerance of pulsed laser radiation. Longer wavelengths are also relatively eye safe as well.

The requirement of eye-safety immediately rules out a number of popular spectroscopic technologies which are fundamentally incompatible with this principle. Among these are Laser-Induced Breakdown Spectroscopy (LIBS) [16, 17, 18, 19, 20] and Raman Spectroscopy [21, 22, 23, 24]. There has been much success using these methods for high spectral resolution substance identification and explosives detection [25, 26]. Success aside, there is no clear route toward transforming common methods into eye-safe variants. LIBS uses a high power, finite focused, laser transmitter to ionize the surface layers of the target of interest and record the plasma's spectral signature. Thus, the intent of surface ionization with high brightness lasers is inextricably opposed to eye-safe operation. Raman spectroscopy favors wavelengths in the visible region (often 532 nm) to probe vibrational transitions with characteristic energies in the infrared. Short wavelengths are used since the Raman cross section has λ^{-4} wavelength dependence. Due to the photochemical activity of the eye at visible wavelengths, the maximum permitted transmitter power in the visible spectrum is extremely limited, exacerbating the challenge

of obtaining high signal to noise ratio (SNR) from the typically small Raman cross sections.

1.2. Technical Approach

Figure 4 depicts the operational concept of a Spectral LADAR system. In this concept, the sensor is mounted to a UGV. A multispectral laser or laser-like beam scans the surroundings. The 3D coordinates are calculated from the time-of-flight (ToF) of the backscatter and scanner parameters. A spectral diversity receiver disperses the backscatter to analyze the object's spectrum. Optionally, this may be done in two orthogonal polarizations to assess the scattering properties of the surface as a means of material discrimination. As the sensor scans the scene, a 3D image is generated with a spectral vector associated with each point in the image.

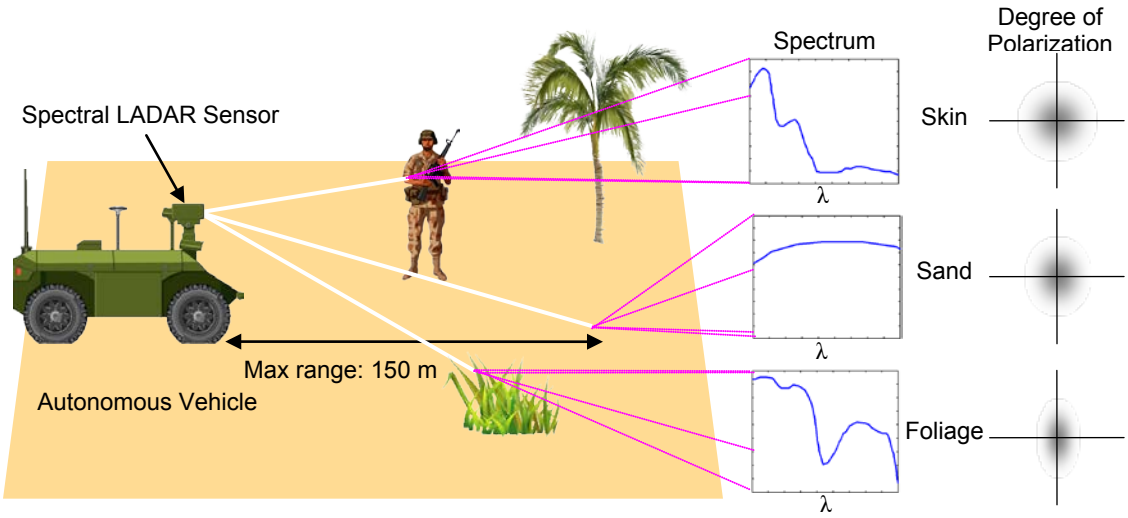

Figure 4: Principle of Spectral LADAR

The technical objectives of this work are to determine the feasibility of the stated technique. The first step taken was to consider a wide range of technologies that could implement the concept shown in Figure 4. Special emphasis was put on the detection of humans since they are both particularly difficult and critical to detect. Specific markers of human presence, including the spectral signatures of respiratory products were considered. Highly specific and popular spectroscopic techniques, such as Raman spectroscopy and LIBS were evaluated. These options proved to be infeasible due to their required high laser intensities, which are impractical for eye-safe standoff detection. Backscatter absorption spectroscopy of diffuse media was one technique that was apparently suitable. The availability of photonic crystal fibers and the pulsed supercontinuum sources that derive from them has recently opened the door to high resolution, wide optical band active sensing. While not the only way to realize the Spectral LADAR concept, supercontinuum sources allow for a large number of spectral bands that would be difficult to achieve using laser or parametric sources.

First, simulations were used to calculate the transmitter power and receiver apertures needed to spectrally distinguish several targets. Spectra used in the analysis were obtained from several databases. The Monte-Carlo simulations used receiver noise estimates and the link budget equation to predict detectability and class separability.

The polarization properties of target scattering profiles are an important means of classification. A monostatic polarimeter was constructed to measure the depolarizing properties of targets important to UGVs. The geometry of this system was identical to that of a LADAR system, however the low power transmitter was only capable of measuring backreflection out to a range of a few meters. The degree of polarization was mapped over a wide range of angles. These tests were performed simultaneously with the spectral simulations.

Following the simulations, which confirmed the feasibility of the technique using a supercontinuum source, a Spectral LADAR experimental prototype was designed to collect data from real-world objects. This prototype – a laboratory demonstrator – was designed to produce imagery at a much slower rate to simplify the architecture and reduce development cost, but would have a clear path toward a full-performance system. Specifically, a slow scanning mechanism and single detector substitute for an APD array were used. Polarization-based classification was not implemented in this version of the demonstrator, but provisions were made for future work using this modality in concert with spectral sensing.

Several classification algorithms were developed to analyze the data collected with the laboratory demonstrator. For the most part, these algorithms were adaptations of common methods including K-Means, K-nearest neighbor, and maximum likelihood routines. Adaptations were made to suit the particulars of Spectral LADAR data, especially the transformation of data to a Spectral Angle Map (SAM), which renders spectral signatures invariant to changes in LADAR cross section.

Test scenes were constructed indoors at a significant distance from the sensor aperture. Some scenes were simple constructions intended to illustrate performance characteristics, such as amplitude linearity and dynamic range. Other scenes were intended to gather training data sets to represent material classes. Finally, scenes were constructed to represent practical scenarios for a comprehensive evaluation of sensor performance. Three dimensional images of these scenes were collected and recorded by the demonstrator unit. The data was processed and analyzed offline, which allowed for parameter tuning and optimization based on a constant data set.

The experimental data demonstrated that Spectral LADAR can plausibly increase the performance of UGV perception and allow more sophisticated vehicle operation at higher speeds and over more complex terrain. The data and experimental observations also suggest future work for improvement, and spinoff applications in other fields such as biomedical imaging and agricultural sensing.

2. Discussion of Prior Work

The general sensing concept expressed in Figure 4 has received considerable interest from researchers over the past 15 years. A number of reports can be found in the literature, using various methods to achieve spectral identification of objects, some of which involve three dimensional imaging of scene objects.

A 2003 report by R. Fogler at Sandia National Laboratories investigated the benefits and challenges of multi- and hyper-spectral imagery for UGV applications [27]. The report concluded that spectral sensing can address some troubling problems for UGV operations, including water hazard detection and foliage evaluation. The report analyzed a variety of spectral signatures and noted that within-class variation needed further study. Fogler suggested that a "multispectral laser radar" was applicable to UGV navigational problems.

To date, there have been no reports of an active 3D multispectral imaging sensor that fully implements the vision in Figure 4 and the requirements discussed in Section 1.1.4 that are relevant to UGVs. The reported sensors have been inadequate in one or more ways, considering adequate maximum range, eye safety, frame rate, or sufficient optical bands and spectral resolution for high confidence classification.

2.1. Passive Spectral Sensors

Using multispectral and hyperspectral imagery for terrain sensing has been used for decades in land use and agricultural studies. These passive sensors are based on satellites or high altitude aircraft. Some of the aspects of this well established application have a significant relation to this work, especially classification algorithms [28]. Many of these ground observing sensors utilize solar irradiance for short wavelength sensing (< 2.5 μm) or blackbody emission in the thermal infrared (> 5 μm). The AVIRIS sensor used on NASA airborne platforms is a recent example [29]. A sample of AVIRIS data obtained by passive methods is shown in Figure 5. The top surface, in the *x*-*y* plane, of the cube is the spatial domain. The depth axis (λ) contains the spectral intensity information.

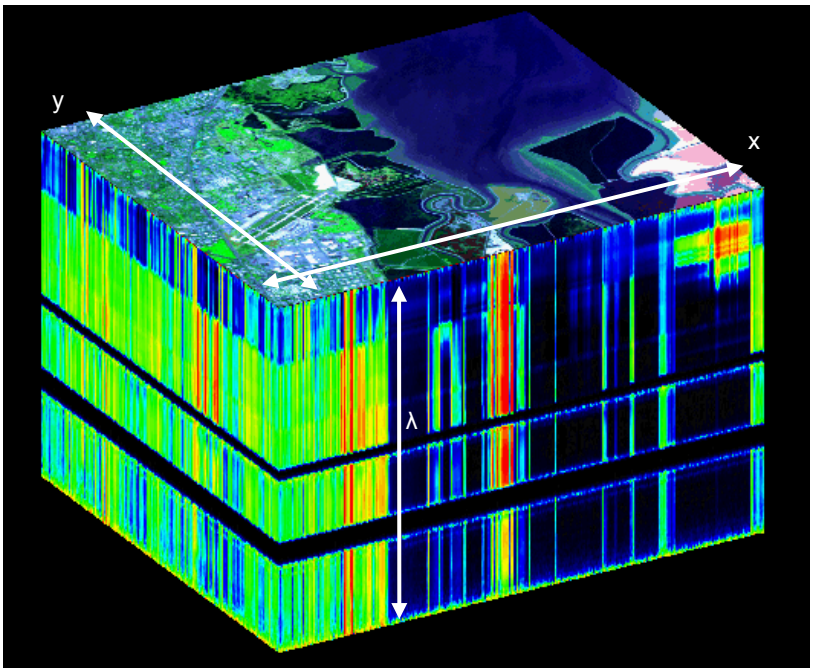

Figure 5: AVIRIS data cube [29]

Work in spectral geosensing has produced copious data for spectral signature databases. This data provides a good starting point, but the differences in stand-off range and scope of interest limits its applicability to UGV applications. These high altitude earth sensing platforms seek to classify imagery on a spatial scale in the tens to hundreds of meters in cross-range. UGV sensing is interested in classification of much smaller-scale objects such as humans and vehicles. At centimeter resolution scales, a tree will have separate signatures for bark and leaves rather than one signature containing a mixture of bark and leaves. The overwhelming emphasis of the large scale spectral features in the geosensing literature does not address the fine detail that is resolvable with UGV LADAR. Specifically, signatures of individual humans, vehicles, and foliage at a detailed, centimeter scale have not been widely studied or reported.

Clearly, each of the many potential applications for Spectral LADAR and active spectral imaging in general – biomedical, agriculture, UGVs, and geoscience – require some degree of application-specific signatures study.

Ground based hyperspectral imagers have recently received growing attention from defense and security specialists. Recently, passive hyperspectral detection has been used at NIR wavelengths to identify humans based on the signature of hemoglobin in the spectrum of skin [30].

2.2. Active Spectral Sensors

Several groups have published results of active sensing of objects in the literature. This section details similar work with an emphasis on spectral classification. Some of these reports include polarization sensing, which will be discussed further in Section 2.3.

M. L. Nischan, J. P. Kerekes, and coworkers at MIT Lincoln Laboratories worked on active spectral imaging with publications ranging from 1999 to 2003 [31, 32]. The objective of their work was to classify scene information to detect mines and other anomalies. Although their system did not involve range-resolved measurements as is important for UGV applications, it did implement a number of unique and interesting aspects. Notably, the sensor system combined multiple aspects including spectral reflectance, fluorescence from chlorophyll, and polarimetry. These aspects were used in concert to identify foreign objects such as shell casings and plastic containers against a

backdrop of natural material such as soil and foliage. Their work stands out as the only instrument to date to make use of a supercontinuum laser source for this type of application. Importantly, the authors concluded that active imaging reduced the false alarm rate by two orders of magnitude compared to the false alarm rate using a passive* illumination. The classification performance is depicted in Figure 6 with red indicating a foreign object. The authors noted that anomaly detection is possible with only two wavelengths.† Despite presenting good experimental results, the work did not address all the characteristics needed for the UGV application considered in this work. Significantly, while their supercontinuum source was broadband, their receiver system was scanned in wavelength by an acousto-optic tunable filter (AOTF). Thus, only a small range of wavelengths was measured at one time, instead of simultaneously. This limitation effectively precludes operation in the situations described in Section 1.1.4, which require high-pixel rate sensors which measure the entire spectral response with a single laser pulse. Additionally the spectral bandwidth of their instrument was limited by the long wavelength limit of their InGaAs detector, which was 1.7 μm. No mention of eye safety was included in their published work and the visible wavelength supercontinuum sources used along with a 0.532 μm laser for fluorescence measurements makes eye safety doubtful. While falling short of suitability for UGV applications, the authors demonstrated that active imagery is useful for object classification with stand-off distances in the tens of meters, and the superiority of active versus passive imaging for these types of applications.

---

* e.g., solar radiation

† Anomaly detection is effectively a two-class system: normal versus anomalous

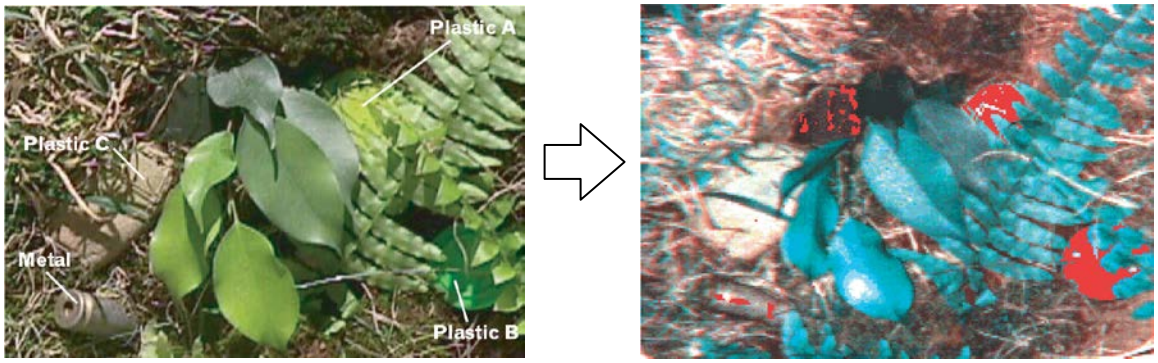

Figure 6: Classification results for the system reported by Nischan et al. [13]

A group at the USAF Wright Laboratory in collaboration with the University of Dayton (M. Vaidyanathan, R. C. Hardie, P. F. McManamon) [33, 34] developed a related scheme toward hyperspectral active LADAR in the late 1990s. The goal of their work was remote sensing from airborne and elevated platforms to ranges from 3 km to 20 km, using an Optical Parametric Oscillator (OPO) as the transmitter. Like the Lincoln Lab work, this method also does not interrogate all bands in a single pulse. Instead, the OPO was tuned over its bandwidth of 1 μm to 5 μm over multiple pulses to acquire the spectral response information. The work was very thorough in its analysis of noise sources, and included a study of some target signatures. The polarization aspect of target signatures was not discussed and it is not clear if any experimental validation was performed. Further, no discussion of the pixel rate capability was included and it is doubtful that an approach using an OPO could achieve high frame rates.

The work of B. Foy et al. [35, 36] at Los Alamos National Lab in 2001 was similar to that performed at Wright Laboratories, however it used a tunable CO_2 laser in the 9 μm to

11 µm window for measurements and classification of terrain at a distance of up to 5 km. The tuning of the transmitter produced the ability to use 44 CO_2 lines at a rate of 113 spectra per second - far below what is required for UGV usage. The authors averaged 128 pulses at each location to increase the SNR. Figure 7 shows the scene and the spectrally classified voxels at a stand-off distance of 4.1 km. Generally, the 9 µm to 11 µm region has been shown to be good for geological sensing since many minerals have spectral features from restrahlen bands (lattice vibrations) at those wavelengths [37].

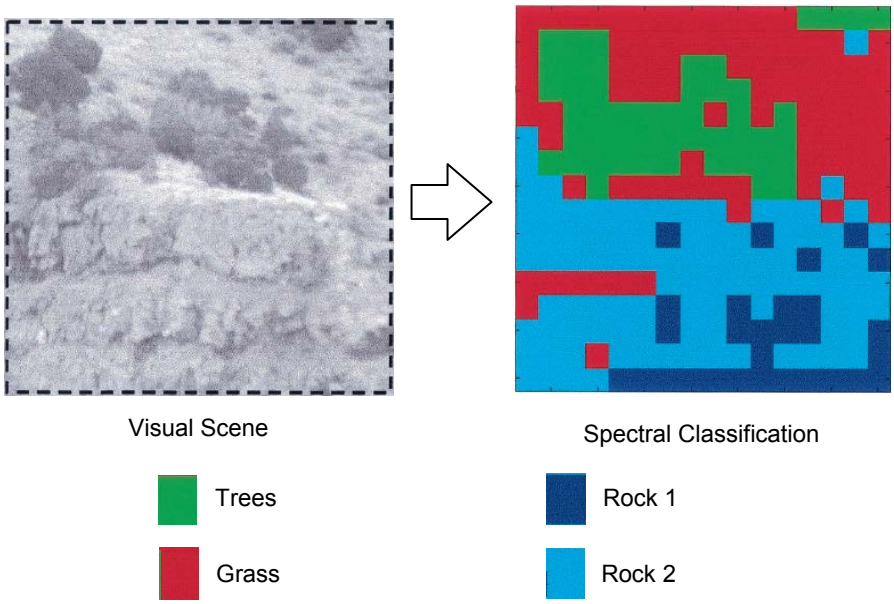

Figure 7: Spectral classification in the LWIR by Foy et al. [35]

Similar systems reported include those utilizing multiple laser lines for sources, one of which uses a streak tube and dispersive element to image in several wavelengths. These systems were limited to only a few optical bands [38, 39].

Two other reports used supercontinuum sources for 3D sensing. In 2007, Kaasalainen et al. used a hyperspectral source to measure the backscatter properties of several materials. They postulated using a supercontinuum to generate 3D images but did not report any results [40]. A 2006 paper by Andersen et al. used a Raman broadened supercontinuum (relatively narrow) in the visible spectrum to create 3D spectral images, however this system was not eye-safe and limited to less than 8 meters maximum range [41].

A. M. Wallace and co-workers took the approach of using 6 diode lasers in parallel as a multispectral source for active ranging and spectral imagery [42, 43]. The diode's center wavelengths ranged from 630 nm to 972 nm. Single photon counting was used for detection with a rather large 200 mm aperture. They published limited performance results without demonstrating imaging operations in 2005.

There have been reports of other LADAR systems combining hyperspectral data with single wavelength 3D range information, some passive [44] and some active [45]. None of them have reported performance figures that meet the requirements for UGVs, and in some cases the method employed does not show promise toward applicability in the situations discussed here.

The work of J. R. Miller stands out as an example of a combined LADAR / passive spectral sensing technique purpose built for unmanned vehicle use, in this case an unmanned helicopter [46]. Miller's multiplexed aperture design combined a LADAR sensor with a visible three color, single-pixel sensor. While not classifiable as a

multispectral sensor, much less a hyperspectral sensor, both the active and passive components use the same aperture and scanning mirror. The work is notable for its combined approach to world modeling that is similar to Spectral LADAR. Figure 8 shows an image generated by this sensor. Since the spectral data is only 3-band and passive, it is limited in classification capability and also does not possess the clutter resistance feature of Spectral LADAR discussed in Section 1.1.3.3.

Figure 8: Passive 3-band colored point cloud from Miller's sensor [46]

Other researchers have also published work dealing with spectral terrain backscatter in some related applications. Numerous publications present spectroscopic data on natural terrain and man-made structures [47, 48, 49]. Few, on the other hand, present data on spectral signatures of particular interest to UGV applications. The spectral signatures of human skin, hair, typical clothing, and others are very limited. Some preliminary work has been done on this in the visible and NIR very recently (2007) by J. M. Cathcart at Georgia Tech [50, 51], and visible bands by others [52], and some discrete lines by still more [53], but a detailed characterization and statistical classification is lacking.

Other researchers have examined the aspects of the wavelength dependent scattering of terrain features using LADAR, mainly to improve downward-looking two wavelength Differential Absorption LIDAR (DIAL) systems used in atmospheric monitoring [54]. DIAL systems use two closely spaced wavelengths, one on a molecular resonance and one off, to quantitatively detect a fine absorption line of a gas species. This is reliable only when the backscatter reflectance is relatively independent of wavelength over the line separation. This approximation of a slowly varying spectral response has been noted as a significant contributor to the uncertainty in a terrain backscatter DIAL measurement [55, 56, 57]. The results from this research can be helpful in this application.

2.3. Active Polarization Sensors

Several authors have conceived of polarimetric active sensors for target identification. For the most part, systems reported in the literature involve a polarized transmitter and a polarization-diversity receiver. In 2000, Breugnot and Clémenceau [58] published their work on both the theoretical analysis and experimental observation of an active polarimetric sensor in the NIR band. As shown in Figure 9, their convincing experimental data was able to show that wood, steel, and paper could be distinguished on the basis of depolarization despite having similar reflectivity. Since the system used a CW laser at 806 nm, range information was absent.

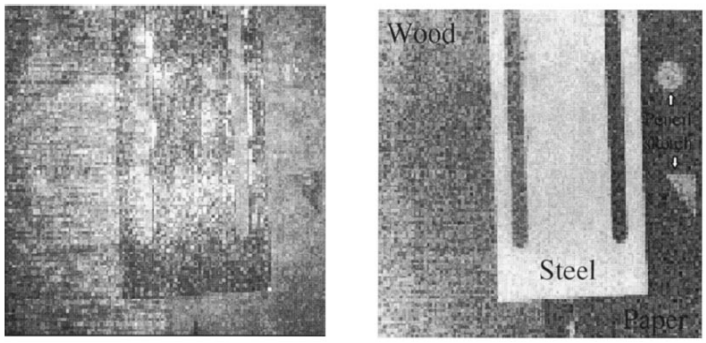

Figure 9: Intensity and polarization images of Breugnot and Clémenceau [58]

The simulations of Chun and Sadjadi [59, 60] in 2005, however, did involve range resolved operation. Using the IRMA simulation package [61] and the Stokes-Mueller formalism used in prior work, the authors were able to show how vehicles (in this case a Soviet T-72 Tank) could be discriminated from foliage. Figure 10 shows the results of their simulation where the range image shows little contrast, but the tank stands out due to its polarization features.

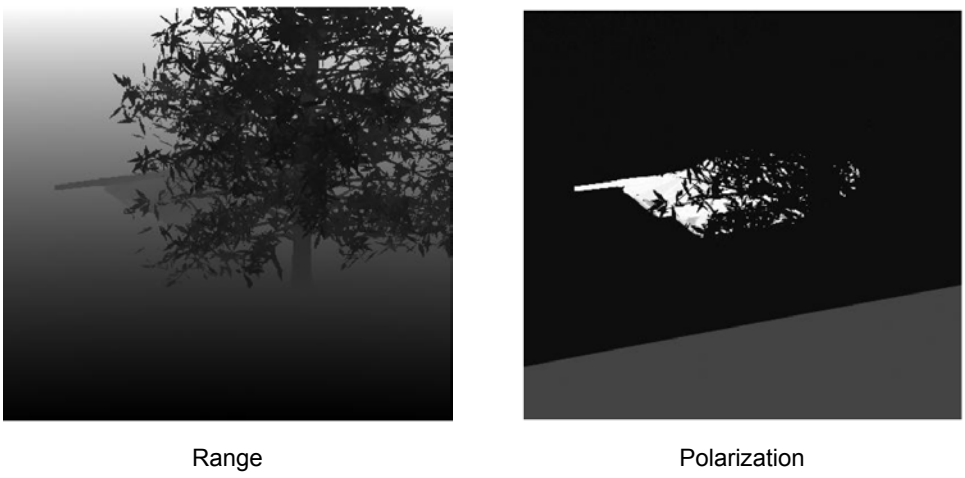

Figure 10: Simulated range and polarization images of Chun and Sadjadi [59]

Goudail and Réfregier have also published their work on active (but not range resolved) polarimetric sensing for target detection [62]. Researchers led by Cathcart at GTRI are currently evaluating polarization signatures for landmine detection [63]. Recently Tan and Narayanan [64] used polarimetric LADAR at 1064 nm and 532 nm to collect data on canopy vegetation. It is doubtful that their airborne system was eye-safe at close range; however its 4 mrad beam divergence and operating altitude of at least 1000 m likely made it eye-safe for people on the ground.

The PILAR program, awarded to Lockheed Martin by the US Air Force Research Laboratory at Wright Patterson AFB, uses polarization sensing to enhance LADAR images of ground targets captured from UAVs [65]. The sensor used a beamsplitter to feed with two orthogonal polarization channels. The system used a 1064 nm laser and a relatively large 150 mm aperture. Intended for long distance standoff target identification, the maximum range is several kilometers. The sensor was first tested in 2005, although well documented images taken with this sensor are not publicly available.

None of the studies summarized above provide an appropriate solution for the challenges and requirements of UGV sensors posed earlier, although they do provide a basis for further work.

3. Background

This section introduces the principles and technologies upon which Spectral LADAR is based. The fundamentals of LADAR, detection of signals in noise, digital signal processing, atmospheric propagation, absorption spectroscopy, supercontinuum sources, APD photoreceivers, and spectrometers are among the topics discussed. In each section, the topic is related to its application to Spectral LADAR. In cases where experimental analysis was performed to verify assumptions, a reference is given to the appropriate section later in this work.

3.1. Fundamentals of LADAR Sensors

LADAR systems are similar to RADAR systems, albeit at much higher carrier frequencies. In contrast to RADAR, the optical frequencies at which LADAR operates are far too high to use classical antenna technology and require different approximations and techniques. One of the most significant differences is that square-law quantum photon detectors are used to convert electromagnetic wave quanta to electric current quanta. Thus, with many (direct detection) implementations of LADAR the emphasis is on electromagnetic power rather than fields. Nevertheless, some of the large volume of RADAR literature is applicable to varying degrees.

The vast difference in wavelength (tens of MHz to hundreds of GHz for RADAR, versus tens to hundreds of THz for LADAR) allows LADAR to have substantially higher diffraction-limited angular resolution versus RADAR at similar apertures. Angular resolution can be approximated by Equation 1 [66, 67]. Angular resolutions (θ_r) of 1 mrad or less are easily achievable with optical frequencies. This allows for high resolution imaging with a single stationary LADAR imager, avoiding the need for synthetic aperture (SAR) techniques.

Equation 1

$$\theta_r \approx 1.22\frac{\lambda}{D} \quad [\text{ radians }]$$

Given:

λ = Wavelength [m]

D = Transmission aperture [m]

Not surprisingly, the much shorter wavelength of LADAR leads to substantially different scattering properties, where microscopic surface structure plays a large role. LADAR (like RADAR) may only detect objects when the material and geometric properties of a distant object produce sufficient backscatter to be detectable by the receiver. This requires that the object (at the LADAR transmission wavelength) have some degree of electromagnetic impedance contrast* with the propagation medium (in many cases air)

* Impedance is a bulk material property, however Rayleigh (elastic) and Raman (inelastic) scattering which are molecular in nature are often used in LADAR to measure gas or aerosol properties.

and that the geometric properties of the object allow for scattering in a direction toward the receiver aperture [68].

Most active sensors with range resolved capability depend on propagation delay to compute a range-to-target (Equation 2). This may be called time-of-flight (ToF) in some modulation formats, but in any case the basic principle is that the time / phase delay of the return waveform is proportional to a propagation velocity. The vacuum phase velocity (relating angular frequency ω and wavenumber k) is almost always assumed for ranging in air, and small deviations from this are usually either ignored or addressed in a calibration process.

Equation 2

$$\Delta r = \left(\frac{c}{2}\right)\Delta t \quad [\ \text{m}\ ]$$

Given:

Δr = Range-to-target [m]

Δt = Time-of-flight [s]

c = Vacuum speed of light [m / s]

3.1.1. Direct and Coherent Detection

LADAR systems fall into one of two categories based on the detection scheme used. Direct detection systems use a photodetector in which the backscattered signal directly

generates a photocurrent proportional to the incident optical power (Figure 11). Coherent LADAR (Figure 12) is more analogous to classical RADAR techniques. In this case the signal is detected by first mixing a local oscillator with the backscattered field. Mixing is realized by the photon absorption process. Since a photodiode is a square-law detector, the photocurrent is proportional to the optical power, which is proportional to the square of the field amplitudes. Systems may be further categorized on the modulation format used. Modulation is necessary to determine range. In many cases the delay of the baseband signal is compared to a timebase signal that establishes a starting time (t_0) to compute range.

The direct detection scheme (Figure 11) can use AM, FM, pulse, or hybrid modulation formats to determine the propagation time. The direct detection scheme does not have a direct analogy to RADAR since it lacks the components corresponding to an RF or IF section. It is possible to use a mixing scheme in the electrical domain, as several interesting implementations have shown [69]. The electrical-domain (modulation) mixing technique, although easier to implement, is not as sensitive compared to the optical-carrier coherent technique, especially when the mixing stage is downstream from the front end amplifier which is the principal noise generator. Direct detection LADAR techniques and components are often closely associated with free space and fiber optic communication systems.

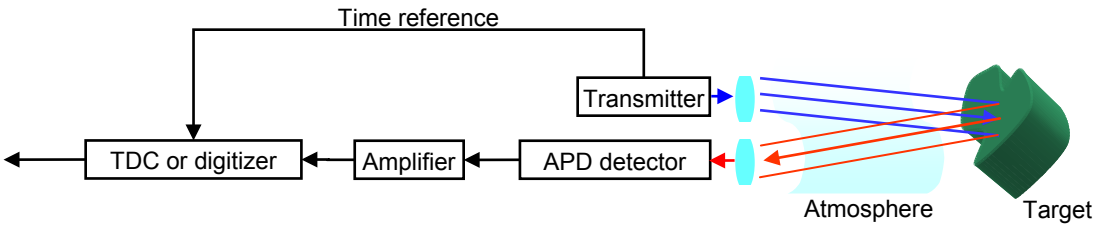

Figure 11: Direct detection LADAR

The optical carrier mixing operation of coherent LADAR (Figure 12) amplifies the signal without excess noise. As with direct detection LADAR, AM, FM, pulse or hybrid modulation formats can be used, with the distinction that frequency and phase modulation may be applied to the optical carrier directly, in contrast to the modulation envelope. Coherent LADAR is distinguished by the use of a local oscillator that may be diverted from the transmitter laser at the same frequency (homodyne) or frequency shifted by a Bragg cell (heterodyne), or from a secondary laser. The square law behavior of a photodiode mixes two optical fields to produce a photocurrent, $i(t)$, given in Equation 3 which represents the current output of a photonic mixer, analogous to the electronic variety. The first two bracketed terms are at optical frequencies, much greater than the electronic response of the detector. A classical approach treats the *sum* frequencies as DC terms, where the second term is much smaller than the first [70]. The third bracketed term is the cross term, where the amplitudes of the signal and local oscillator are factors of a difference frequency term which is typically in the hundreds of MHz, well within the bandwidth of receiver electronics. Under the classical wave approximation and limited electronic bandwidth, the higher mixing frequencies are not shown in Equation 3. The photon (quantum) description of wave mixing demonstrates that these terms are absent

altogether [71]. By the mixing term, the current output is sensitive to changes in frequency, phase, and amplitude of the signal. This property is exploited for Doppler vibrometry and other auxiliary information in LADAR signals, but unwanted fluctuations generate noise in the output. Specifically, target speckle and atmospheric turbulence can scramble the phase of the transmitted and backscattered wavefronts and degrade performance significantly. Also, the receiver optics for coherent LADAR must be diffraction limited to ensure wavefront matching of the local oscillator and signal over the entire surface of the detector.

The multiplication of local oscillator and signal amplitudes in Equation 3 enables the relatively intense local oscillator to amplify the small signal field. Shot noise limited performance is achieved when the shot noise of the local oscillator dominates the input-referred thermal and amplifier noise of the receiver electronics.

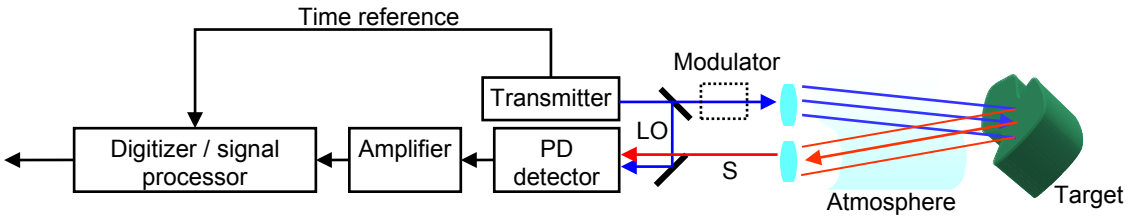

Figure 12: Coherent detection LADAR

Equation 3

$$i(t) = \left(\frac{\eta q}{\hbar \omega}\right) c\varepsilon_0 \left[E_{LO}{}^2 + E_S{}^2 + 2E_S E_{LO} \cos\left(\left(\omega_S - \omega_{LO}\right)t + \varphi_S - \varphi_{LO}\right)\right] \quad [\ \text{A}\ ]$$

Given:

η = Detector quantum efficiency

q = Fundamental charge [C]

$\hbar$ = Normalized Plank constant [J s]

ω = Optical angular frequency of signal ($_S$) or local osc. ($_{LO}$) [rad / s]

ε_0 = Permittivity of free space [$c\,\varepsilon_0$ = admittance of free space, 1 / Ω]

E_{LO} = Local oscillator field [V / m]

E_S = Signal field [V / m]

φ_S = Signal phase of optical carrier [radians]

φ_{LO} = Local oscillator phase of optical carrier [radians]

While coherent detection was more popular in the early days of LADAR, direct detection has been receiving more attention recently due to the availability of very low noise Avalanche Photodiodes (APDs). Operated at or beyond the optimum avalanche gain value, the sensitivity of APD-based LADAR receivers is limited by the shot noise of the photocurrent and multiplicative gain noise as this noise term dominates the thermal noise of the pre-amplifier. The sensitivity of APD direct detection is comparable to that of coherent receivers, but without the need for long coherence length lasers, diffraction-limited receiver optics and interferometric alignment, and the phase scrambling limitation of the speckle penalty. The reduced complexity of direct detection APD-based LADAR is often worth the cost of additional noise from the APD gain excess noise factor.

3.1.2. Spectral LADAR Concept

The Spectral LADAR concept is an active multispectral system where the target reflectance spectrum is reconstructed using a single optical pulse. Figure 13 is the overall scheme of this approach. The key components are a multispectral laser or laser-like source and spectrally-dispersed optical receiver.

In Figure 13, a short pulse containing a broad spectrum of optical frequencies is represented at the top of the figure in blue. In general, this could be a broad optical continuum or several time synchronized laser lines. A set of transmitting optics projects this beam through the atmosphere to a distant target. A "flying spot" beam scanning mechanism, not shown in Figure 13, scans the beam in azimuth and elevation to image the target. This concept could easily be extended to a one dimensional line scan, or a frame-at-once "flash" LADAR system with greater difficulty.

The backscatter from the target, represented in Figure 13 (red), propagates back through the atmosphere to the photoreceiver which performs an optical to electrical signal conversion. High speed electronics digitize the electrical pulse in a number of separate spectral bands which sample the reflectance spectra of the target. The time delay indicates target range, and a comparison of the transmitted spectrum to received spectrum indicates the optical properties of the target material.

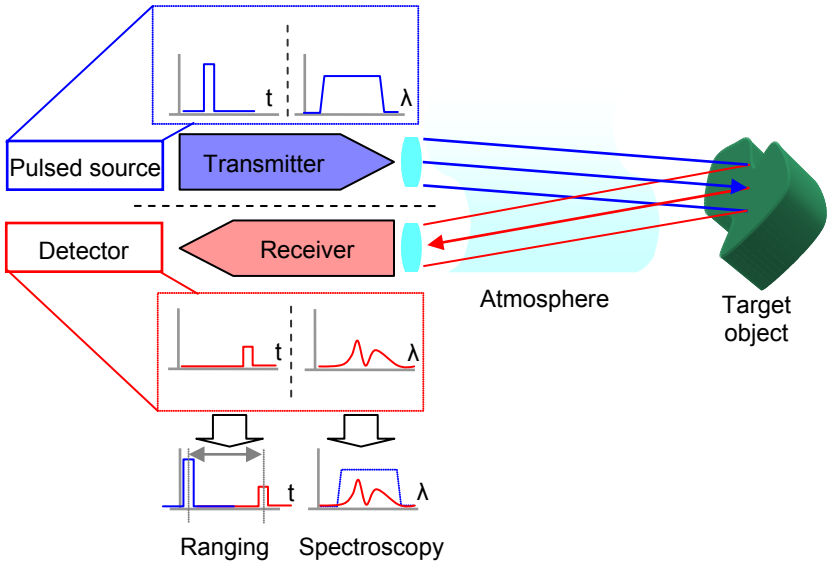

Figure 13: Spectral LADAR technique

It is important to note that the optical pulse is not necessarily transform limited. Therefore, the optical spectrum and time domain pulse envelope are not strictly related by the Fourier transform.

In this scheme, direct detection is used since there is no straightforward way to implement high speed coherent detection of an optical continuum spanning an octave or more of optical frequency. Pulse modulation is preferred in this case, especially when the transmitted radiation is generated by nonlinear phenomena which are most practical when used to generate high intensity light in short bursts. Correspondingly, APD-based receivers often have the highest sensitivity in this scheme.

3.1.3. Range Equation

The optical power received by the target is found by using the well known direct detection range equation (Equation 4) [72, 73, 74]. It is essentially equivalent to the RADAR range equation, with different assumptions in some cases owing to the large differences in wavelength [75]. Figure 14 is a graphical illustration of the significance of Equation 4. The received power term, P_r, is the power integrated over the entire receiver focal plane. Terms in Equation 4 which have wavelength dependence (as indicated) are assumed to be integrated over the extents of a single optical band.

Equation 4

$$P_r(t,\lambda) = \left(\frac{P_T(t,\lambda)}{r^2\Omega_T}\right)\Gamma(r,\lambda)\left(\frac{\pi D^2}{4r^2\Omega_r}\right)T_A(r,\lambda)^2\,\eta_p(r,\lambda) \quad [\ \mathrm{W}\ ]$$

Given:

t	=	Time coordinate [s]
λ	=	Wavelength [m]
$P_T(t, \lambda)$	=	Transmitted optical power [W]
$P_r(t, \lambda)$	=	Received optical power [W]
r	=	Range [m]
Ω_T	=	Transmitter far-field solid angle [steradians]
$\Gamma(r, \lambda)$	=	Laser radar cross section (LCS) [m^2]
D	=	Receiver aperture diameter [m]
Ω_r	=	Target scattering solid angle [sr]

$T_A(r, \lambda) =$ Atmospheric transmission [dimensionless]

$\eta_p(r, \lambda) =$ Tx - Rx pixel coupling factor [dimensionless]

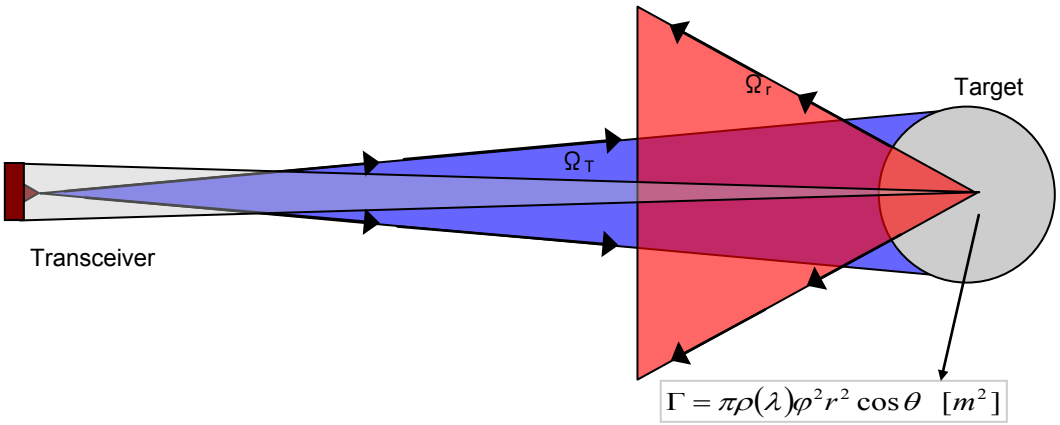

Figure 14: Geometry of the LADAR range equation

The above expression assumes that all photon scattering is elastic, and that the laser cross section (LCS) is constant over the time scale of one pulse width* [76]. The LCS of a target is defined as the corresponding cross sectional area of a specular, reflecting sphere that produces an equivalent return signal. The LCS has a wavelength dependence which usually varies mildly with geometric scale properties, but often strongly with material properties. The shorter wavelength of LADAR vs. RADAR, as discussed earlier, results in most targets producing diffuse (Lambertian, see Section 3.2.1.2) rather than specular backscatter since most ordinary targets have roughness much greater than the laser wavelength. Additionally, the wavelength of LADAR results in most targets being larger than the diffraction limited far-field divergence angle. It is useful to express the range equation in a simplified form for extended (larger than beam) Lambertian reflectors, by

* For fluorescent targets, time dependence is required.

substituting Equation 5 which is the cross section (Γ) for an extended, Lambertian target. Making this assumption reduces Equation 4 to Equation 6 at normal incidence which is applicable in many practical situations. The transverse profile of the transmitted beam is a factor in a completely general case, but not when extended targets are concerned. Target signatures and cross sections will be discussed further in Section 3.2.

Equation 5

$$\Gamma = \pi\rho(\lambda)\varphi^2 r^2 \cos\theta \quad [\ \mathrm{m}^2\ ]$$

Given:

$\rho(\lambda)$	=	Bulk reflectivity [dimensionless]
φ	=	Transmitter divergence angle [radians]
θ	=	Incident angle [radians]

Equation 6

$$P_r(t,\lambda) = \frac{P_T(t,\lambda)\rho(\lambda)D^2\eta_p(r,\lambda)T_A(r,\lambda)}{4r^2} \quad [\ \mathrm{W}\ ]$$

In direct detection systems, the signal is directly proportional to the received power, assuming that this may be approximated as a small signal which does not saturate the detector or receiver electronics.

3.1.4. Fundamental Noise Processes

Noise in the receiver sets a fundamental limit to the sensitivity of the LADAR system and determines the minimum amount of received optical power for a target to be detected. It also can distort the perceived target spectrum and establishes a noise-equivalent delta reflectivity (NEDR) parameter, which is the spectral reflectivity difference equal to the per-band noise fluctuations. A high NEDR can cause classification errors or reduce the sensor's ability to distinguish two targets with highly similar spectral reflectance.

Noise in electronic systems is typically described as power per unit bandwidth, W / Hz. Quantum optical detectors are square law devices where optical power is proportional to current. However, the electrical power is proportional to the square of current *or* voltage. When noise spectral density in the electrical domain is extracted to the optical domain, the noise units become W $Hz^{-1/2}$ to reflect the square law property. Because of this, the SNR in the electrical domain is the square of that in the optical domain. This numerical difference does not improve the detection statistics but it makes it important to clearly specify whether the SNR is in the electrical domain (SNR_E) or optical domain (SNR_O). The fact that the electrical power is the square of the optical power does not violate conservation of energy or thermodynamic laws. When a photodiode is operated in photoconductive (reverse-bias) mode, additional power is supplied by the bias circuit which constrains the voltage across the diode at a constant value.

The two fundamental sources of noise are shot noise in the photodiode and thermal noise generated in the amplifier and other conductors. Other sources of noise, such as temperature fluctuations or electromagnetic interference, are not fundamental since they may be eliminated with design techniques, operating environment control, or shielding.

3.1.4.1. Shot Noise

Shot noise is a fundamental source of noise that arises from the fact that electrical current is carried by discrete unit charges and an electromagnetic field is quantized in photons. The current fluctuates due to the random arrival / generation times of photoelectrons. The distribution of photoelectron arrivals follows Poissonian statistics, which is approximated by Gaussian statistics for a large rate parameter (large numbers of expected events). It should be noted that shot noise is generated by electrons crossing a potential barrier – such as in a diode – and that shot noise is not generated in resistors [77].

By describing the noise process as a series of elementary current pulses with random arrival times described by Poisson statistics, it can be shown that shot noise has a uniform spectral density [78]. Shot noise is generated by signal photoelectrons, dark current photoelectrons, and background photoelectrons. Its current amplitude variance (σ_s^2) when approximated by Gaussian statistics is given in Equation 7 [79].

Equation 7

$$\sigma_s^{\,2} = \left\langle i_s^{\,2}(t) \right\rangle = 2qI_p\Delta f \quad [\ \mathrm{A}^2\ ]$$

Given:

I_p = Noise generating current [A]

Δf = Receiver effective noise bandwidth* [Hz]

i_s = Noise current random variable [A]

$\langle \ldots \rangle$ = Mean value

3.1.4.2. Thermal (Johnson / Nyquist) Noise

Electronic noise from the thermal agitation of conductors was first determined theoretically and experimentally by H. Nyquist [80] and J. Johnson [81] and is also referred to simply as thermal noise. The noise originates from the random thermal motion (Brownian motion) of charge carriers in a conductor, analogous to the atomic or molecular constituents of a gas [82]. This is also consistent with the absorption and emission fluctuations of blackbody radiation at thermal equilibrium [83]. By considering resistors with identical values attached to a transmission line, it can be shown that the spectral density is uniform through adaptation of Plank's blackbody radiation law to a one-dimensional cavity. It is important to note that thermal noise is inherent in all dissipative circuit elements and not in purely reactive elements. Although some elements can have noise in excess of the thermal noise limit due to other effects (1/*f*, generation-recombination), thermal noise *power* density depends only on the temperature of the

* The effective noise bandwidth is, assuming a uniform spectral noise density, the frequency extent of a rectangular transfer function having the same integral noise power as the receiver's frequency transfer function magnitude integrated over all frequency.

element. The resistance of the element enters into consideration when current and voltage quantities are considered.

The random charge motion creates a random electrical current that, like shot noise, has a uniform spectral density and time-voltage properties described by Gaussian statistics. Its current variance (σ_T^2) is given in Equation 8. The spectral power density is uniform to a good approximation up to very high frequencies, greatly exceeding the signal bandwidth.

Equation 8

$$\sigma_T^{\,2} = \left\langle i_T^{\,2}(t) \right\rangle = (4k_B T / R_L)\Delta f \quad [\ \mathrm{A}^2\ ]$$

Given:

k_B = Boltzmann constant [J / K]

T = Temperature [K]

R_L = Load Resistor [Ω]

Unlike shot noise, thermal noise is independent of current through the element. Additionally, it is also completely independent of the material of the resistor / conductor, although some materials have thermally dependent noise in excess of the fundamental Johnson / Nyquist noise.

Since this noise arises from the receiver front-end circuitry and amplifier, it is customary to specify thermal noise as input-referred or output-referred. A specification of input-referred noise would lump all of the front-end noise into one current source placed in

parallel with the input terminals of the amplifier. By doing such, the amplifier and all other circuit elements would be considered noiseless. Conversely, output-referred noise lumps all noise sources in a parallel voltage source (input-referred current source through transimpedance gain) on the output of the amplifier. Amplifier noise in excess of Nyquist / Johnson noise may be specified as an amplifier noise figure (F_n) coefficient in Equation 8.

3.1.5. Solar Background Noise

Somewhat related to thermal noise is background noise, produced by the photo-thermal emission of all objects at finite temperatures. At SWIR wavelengths, the thermal emission of objects at ordinary temperatures (~300K) as calculated by Plank's blackbody radiation law is small. Thermal emission is not negligible for Spectral LADARs operating in the MWIR and LWIR bands, however.

The dominant source of background radiation in SWIR Spectral LADAR is solar radiation reflected from objects within the system's instantaneous field of view – which is the field of view of a single detector element. The solar spectral irradiance outside of the atmosphere (extra-atmospheric) and at ground level after propagating through the vertical atmosphere is shown in Figure 15 [84].

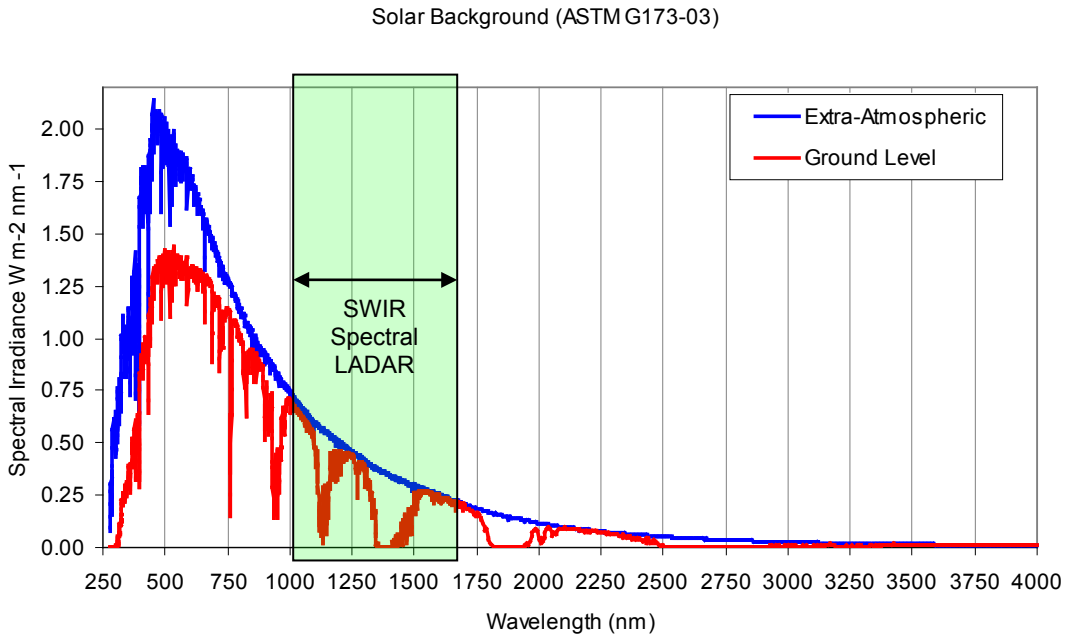

Figure 15: Solar spectrum from standard ASTM G173-03 and US standard atmosphere

A convenient way of estimating the collected solar background uses the camera equation (Equation 9) to relate the spectral irradiance of the object to the spectral irradiance in the image plane of the receiver [85]. The two major factors that influence this are the instantaneous field of view (iFOV), F/# of the receiver lens, and solar angle relative to the target surface. Equation 9, when multiplied by the photodetector active area, equals the optical power from solar background sources, both direct and diffusely scattered from the atmosphere. The iFOV is not included directly in Equation 9, but implicitly when multiplied by photodetector active area.

Equation 9

$$I_{image} = \frac{\pi I_{object}}{4(F/\#)^2} \quad [\text{ W m}^{-2} \text{ }]$$

The spectral reflectivity directly affects the magnitude of the solar background, but since this is directly proportional to the signal it will be neglected. It is important to note that the angle of the object surface normal with respect to the sensor is irrelevant when Lambertian scattering is assumed. A larger subtended target surface area exactly counterbalances the cosine falloff when the surface is uniformly illuminated and is larger than the iFOV at that (or all) observation angle(s). The angle of the target with respect to the sun is important, since the cosine of this angle affects the surface irradiance term. This situation contrasts with the target angle dependence explained later in Section 3.2.1.2 since in that case the illumination angle necessarily changes with observation angle (extended objects are also assumed in this case). Also, it is important to note that the calculation of solar background power is independent of range for extended targets. Although the fraction solid angle subtended by the receiver aperture decreases with the inverse square of range, this is counterbalanced by the increase in viewed target area, which increases with the square of the range.

Solar or thermal background is present in the signal at a DC, or close to DC, level. Since most receivers are AC coupled, this DC level is filtered out. What remains is the shot noise created by the background radiation, with a white spectrum (Section 3.1.4.1). Excess noise from APD gain is also created by background radiation.

As a numerical example, the solar background power is computed to be 44 nW continuous, using the parameters in Table 1. Note that Equation 9 is independent of

range, provided that the target is extended (i.e., larger than beam size) at all ranges under consideration.

Table 1: Solar background calculation parameters

Parameter	*Value*
Spectral receiver optical bandwidth	1225 – 1250 nm (25 nm)
Receiver F/#	1.3
Detector diameter	100 μm
Solar angle to object surface normal	0^o (worst case)
Reflectivity at test wavelength	60%

This amount of power, representing a worst-case-scenario in terms of sun intensity and position, is about 3 times the minimum noise equivalent power of the receiver, calculated later in Section 5.6. Although not negligible, the solar background is quite small for the iFOV (cross range resolution) and bandwidth considered for Spectral LADAR.

3.1.6. Detection and Estimation of Signals in Noise

The performance of LADAR or any active sensor system is fundamentally limited by the processes that induce fluctuations in the received signal. Unfortunately, a myriad of phenomena can affect signal reception and the estimation of signal parameters. Some of these are systematic errors correctable with calibration or compensation, however others are truly random fluctuations, which set an upper bound to system performance. This section will discuss endogenous sources of noise inherent in the receiver system. Other sources of noise resulting from exogenous effects such as atmospheric propagation and target scintillation (speckle) can be significant, and merit separate discussion in Section

3.1.7. Background radiation from solar or target self-radiance, while not internal to the LADAR system, will be discussed since its analysis is similar.

Thermal noise is generated in all electrical conductors due to Brownian motion induced electron collisions in the material. This source of noise, discussed in detail in section 3.1.4.2, usually dominates in RADAR systems at the amplification stage. A key difference between LADAR and RADAR is the large difference in photon energy, hv. LADAR frequencies are typically at least 1000x greater than that of RADAR. Given a return signal with power equivalent to the thermal noise of a pre-amplifier, LADAR systems will have photon flux numbers much less than that of a RADAR system. Consequently, the quantization noise due to random photon arrival times, shot noise, is much more significant in LADAR and is often more significant than thermal noise sources. This is detailed in Section 3.1.4.1.

Background radiation from the sun or from target thermal self-emission can be significant, especially for Spectral LADAR that may not have the narrowband optical filtering of monochromatic systems. The background radiation is essentially CW, lacking any modulation characteristics. Although most receivers are AC coupled and will electronically block the DC background radiation, the shot noise generated by the background is additive to the total noise.

These effects can be accurately characterized as white noise with a Gaussian amplitude distribution in most cases. The spectral power density of these noise components are

additive, therefore the noise voltages and currents are additive in quadrature (Equation 10). Quadrature addition of rms voltages and currents is simply addition of mean squared voltages and currents, or voltage and current variances.

Equation 10

$$\sigma_{total}^{\ 2} = \sigma_s^{\ 2} + \sigma_T^{\ 2} + \sigma_{bg}^{\ 2} \ldots \quad [\ A^2\ ]$$

The detection of LADAR signals can be analyzed as a channel corrupted with Gaussian noise, having the SNR (Equation 11) as a key performance parameter. The remainder of this section analyzes the influence of noise on the detectability of the signal and the estimation of range and intensity parameters. The spatial resolution of the system is related to these issues.

Equation 11

$$SNR = \frac{I_s^{\ 2}}{\sigma_T^{\ 2}} \quad [\ \text{dimensionless power ratio}\ ]$$

The definitions of range accuracy and range resolution of LADAR systems are not consistent in the literature and industrial specifications, especially among LADAR and RADAR sensors despite their similarity. This section defines these terms in a manner most consistent with historical RADAR definitions expressed by Skolnik [86]. In particular, precision and accuracy in a typical measurement context is defined as the variance of multiple measurements and the difference of the mean of those measurements to accepted values, respectively. Here, range accuracy refers to both systematic errors and random errors.

3.1.6.1. Detection Statistics

Detection of a return pulse is a statistical determination in which one of two mutually exclusive outcomes occurs per voxel. A trial tests a pair of hypothesis – H_0 and H_1 – where the null hypothesis, H_0, represents the absence of a target and H_1 is the alternative hypothesis representing the presence of a target.

D_0 and D_1 represent the mutually exclusive selections (decisions) of one hypothesis with the respective subscript. With each trial, there are four possible outcomes representing the pairings of hypothesis (H_x) to decision (D_x). The probabilistic detection of a target can be described by the probabilities of each of the four possible outcomes.

Two of the four possible outcomes are correct decisions and their probabilities are $P(D_0 \mid H_0)$*, the probability of selecting the null hypothesis given that the null hypothesis is true, and $P(D_1 \mid H_1)$, the probability of selecting the alternative hypothesis given the alternative hypothesis is true. The other two outcomes are errors. $P(D_1 \mid H_0)$ is known as an error of the first kind (type I), or more colloquially as a false alarm since the alternative hypothesis was selected given the null hypothesis is true. The error of the second kind (type II) is $P(D_0 \mid H_1)$ is a miss since the null hypothesis was selected given the alternative hypothesis is true. Clearly the sum of the probabilities of like hypothesis

---

* The conditional probability of D_0 *given* H_0

subscripts is unity since the target must be present or absent. The joint probabilities $P(D_x, H_x)$* also sum to unity [87].

The probabilities $P(H_1)$ and $P(H_0)$ are *a priori* probabilities based on knowledge of the signal before the trial. It is not always, and usually is not, possible to estimate these probabilities in a LADAR sensor. In digital communications, however, the mark (H_1) and space (H_0) probabilities are equally likely since both digital values are equally likely. In other cases involving sensors, the consequences of type II errors may be substantially greater than type I errors. In such cases cost parameters may be assigned to reflect the disparity in error severity to determine an optimal balance. The Bayes decision rule, along with the maximum likelihood decision rule, handles these cases where *a priori* estimates of hypothesis likelihood are available and the error types may have quantifiably different costs. In these cases, a decision threshold is chosen such that the cost is minimized. In the case of many active sensing systems the *a priori* probabilities and cost coefficients are unknown or completely arbitrary.

The goal of this analysis is to develop the criterion that leads to the selection (D_x) of the most likely outcome (H_x). Consider a continuous random variable x which represents the amplitude value of a digitized waveform at a particular time. The main interest is in the *a posteriori* probabilities – the probabilities of a hypothesis being true after an observation of the random variable is made. The conditional probabilities for each hypothesis, given x, is $P(H_0 \mid x)$ for the null and $P(H_1 \mid x)$ for the alternative. Equation 12 describes the

---

* Probability of D_x *and* H_x

Gaussian PDF for the random variable x, given the null hypothesis where only zero-mean noise is present in the signal (Equation 12a), and the alternative hypothesis where the presence of the average signal level s creates additional noise (Equation 12b). By Bayes' rule, the posterior probabilities may be related to the prior probabilities, e.g. the probability of x given H_x.

Equation 12

$$p(x \mid H_0) = \frac{1}{\sqrt{2\pi\sigma_T^{\,2}}} e^{\frac{-x^2}{2\sigma_T^{\,2}}} \qquad \text{(a)}$$

$$p(x \mid H_1) = \frac{1}{\sqrt{2\pi\left(\sigma_T^{\,2} + \sigma_s^{\,2}\right)}} e^{\frac{-(x-s)^2}{2\left(\sigma_T^{\,2} + \sigma_s^{\,2}\right)}} \qquad \text{(b)}$$

The Neyman-Pearson decision rule applies best in the situation where *a priori* or cost information is lacking [88]. This approach maximizes the probability of detection (P_D) by setting a threshold at a fixed but arbitrary acceptable false alarm (P_{FA}) rate. P_{FA} and P_D are defined by Equation 13 [89].

Equation 13

$$P(D_1 \mid H_0) = P_{FA} = \int_{x_{thresh}}^{\infty} p(x \mid H_0)\,dx \qquad \text{(a)}$$

$$P(D_1 \mid H_1) = P_D = \int_{x_{thresh}}^{\infty} p(x \mid H_1)\,dx \qquad \text{(b)}$$

Finding the threshold which maximizes P_D subject to the constraint of P_{FA} involves determining the value of a Lagrange multiplier (μ), to maximize P_c, the probability of making a correct decision in Equation 14, where α is the false alarm constraint [90].

Equation 14

$$P_c = P_D + \mu(\alpha - P_{FA})$$

When substituting Equation 13a and b into Equation 14 for P_D and P_{FA}, the maximum value of Equation 14 is obtained with the proper choise of threshold (x_{thresh}) that defines the limits of integration. The Lagrange multiplier turns out to be the value of the likelihood ratio* (Equation 15) at the optimum decision threshold ($\mu = l(x_{thresh})$). [91]

Equation 15

$$\ell(x) = \frac{p(x|H_1)}{p(x|H_0)} > \mu \quad H_1 \text{ Selected}$$

$$\ell(x) = \frac{p(x|H_1)}{p(x|H_0)} < \mu \quad H_0 \text{ Selected}$$

The probability of the other two outcomes, $P(D_0 \mid H_0)$ and $P(D_0 \mid H_1)$ are the differences of Equation 13a and Equation 13b and unity, respectively. Figure 16 is a graphical representation of the threshold selection criteria. Although Gaussian noise is assumed in this analysis, the technique is also applicable to other statistical distributions. The integrated area of the magenta curve, $p(x \mid H_1)$, to the right of the threshold represents P_D.

---

* Ratio of PDFs

The integrated area to the right of the threshold of the blue curve, $p(x \mid H_0)$, represents the P_{FA}. In this figure zero-mean noise is assumed. Variations in signal level will shift $p(x \mid H_1)$ to the right or left and affect P_D while P_{FA} remains constant. A receiver operating characteristic (ROC) curve may be plotted to demonstrate the trade-off of P_D and P_{FA}, with movement along the curve corresponding to movement of the decision threshold [92].

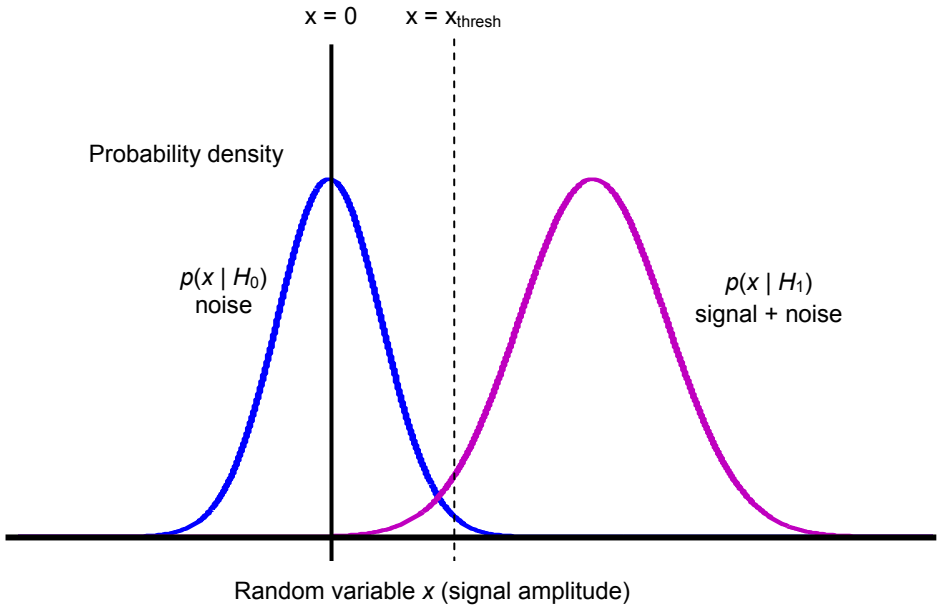

Figure 16: Probability density and detection threshold

It is important to note that P_{FA} is the probability of a false alarm in a voxel, not a pixel. Even with a low P_{FA} false returns may be common since there are many voxels along the path of a single transmitted pulse [93]. A key advantage of the Neyman-Pearson criterion versus the Bayesian criterion is that P_{FA} is a controlled parameter. In the Bayes' criterion, the probability of making a correct decision is maximized, but this may lead to an intolerably high P_{FA} [94].

3.1.6.2. Matched Filter Receiver

Maximizing the receiver SNR with a proper filter is a major concern in achieving optimal performance in terms of both signal detection and parameter estimation. The received signal is wideband in a channel with added Gaussian (white frequency) noise.* A receiver filter that is excessively wide will reproduce the signal with high fidelity in terms of preserving its original shape and amplitude. It will, however, include far more noise than is necessary over the uniform spectral noise density and diminish the SNR. A filter that is too narrow will distort the signal by cutting off high frequency components, diminish range resolution, and yield poor performance. Early RADAR experimenters found that for approximately rectangular pulses, a bandwidth of approximately $B\tau = 1$ yielded good results, where B is the band-limited frequency and τ is the pulse duration [95]. The matched filter receiver, developed first for RADAR applications, seeks to maximize SNR and achieve the proper roll-off in the transition region to maintain high signal throughput and low noise throughput. The matched filter is typically part of the IF section of a RADAR system. Since direct detection LADAR does not have a segment analogous to a RADAR IF, the LADAR matched filter would be analogous to a video band (or baseband) filter in RADAR. This analysis is appropriate in either case [96].

* Excess noise from APDs is multiplicative

The name matched filter is apt since the filter is specific to the frequency and phase content of the transmitted pulse. Thus, this technique is only applicable to the detection of known signals. Consider a transmitted pulse with optical power $s(t)$ and a Fourier transform of the optical power envelope as $S(\omega)$. The transfer function of the matched filter is represented in the frequency domain as $H(\omega)$. The noise power per unit frequency is a constant N_0. Equation 16 provides the formalism for choosing a transfer function $H(\omega)$ to maximize the peak output signal $s_o(t)$ at a time t_m as a ratio to the mean noise power N_f. The numerator in the LHS of Equation 16 is the instantaneous peak power at time t_m, taken here as the pulse maximum. The equivalent frequency domain expression in the numerator of the RHS is formulated from the inverse Fourier transform of the filtered input signal and evaluated at the time t_m. The denominator of the RHS is the post-filter noise power taken from the noise spectral density integrated over all frequency (N_0 is a white noise and frequency-independent).

Equation 16

$$\frac{|s_o(t_m)|^2}{N_f} = \frac{\left|\int_{-\infty}^{\infty} S(\omega)H(\omega)e^{i\omega t_m}d\omega\right|^2}{\frac{N_0}{2}\int_{-\infty}^{\infty}|H(\omega)|^2 d\omega} \quad [\text{ dimensionless }]$$

Utilizing either the Cauchy-Schwarz inequality or the calculus of variations, it can be shown that the ratio of Equation 16 can be maximized with the transfer function of Equation 17, where K is a constant and a phase shift term is added as a time domain delay of t_0 [97]. A delay is necessary for a matched filter to be realizable as a causal system, which is only significant for the relatively rare case of truly real time processing [98].

Equation 17

$$H(\omega) = KS^*(\omega)e^{-i\omega t_0} \quad [\ 1 / \text{Hz}\ ]$$

Equation 17 demonstrates that maximum SNR is achieved with a filter whose transfer function is the complex conjugate of the signal, i.e., the impulse response of the filter is the time-reversed signal pulse shape. The output of the matched filter is in general the cross-correlation of transmitted and received signals. Under the assumption that the received signal has sufficiently low noise so as to not significantly perturb the pulse shape, the output is the time-shifted autocorrelation of the transmitted signal.

Applying the Cauchy-Schwarz inequality and Parseval's theorem reveals that the maximized SNR of the system is limited by Equation 18 where E is the signal energy integrated in either the time or frequency domain [99]. The maximum SNR is limited by the ratio of signal energy to noise spectral density (N_0).

Equation 18

$$SNR \leq \frac{2E}{N_0} \quad [\ \text{dimensionless}\ ]$$

It is important to note that a matched filter receiver maximizes the SNR subject to this limit, but makes no effort to reproduce the signal's shape with high fidelity. Moreover, it requires knowledge of the pulse shape prior to reception to be effective. These characteristics are suitable for active imaging systems based on echoes of transmitted pulses, but less so for communications systems.

The matched filter, while primarily analyzed here in the frequency domain, is implementable in either the frequency or time domain. This technique is often referred to as a cross-correlation receiver in a time domain context. Time-domain implementations may be preferred in cases where the hardware is better suited to correlations rather than Fourier transformation.

3.1.6.3. Range Resolution

Range resolution is defined as the system's ability to distinguish closely separated consecutive returns along the direction of beam propagation. Occasionally, some sources refer to range resolution as the time resolution of the digital counter used to calculate delay. This usage is inconsistent with RADAR terminology but the effects of digital counters can be included in range accuracy, which will be discussed next.

Like resolution in an optical imaging system, there is no strict mathematical definition of range resolution although criteria similar to the Rayleigh criterion have analogs for range resolution in LADAR and RADAR systems. The Rayleigh criterion assumes that two diffraction-limited image points are resolved when the maximum of one Airy disk function corresponds in space with the minimum of the other, and vice-versa. Since most LADAR pulse waveforms are strictly monotonic about their centroid, this criteria does not apply directly. Figure 17 shows just-resolved Gaussian pulses. The red and blue

curves correspond to two objects with equal return strength, and the purple curve represents the sum of the two returns as it would appear to the receiver.

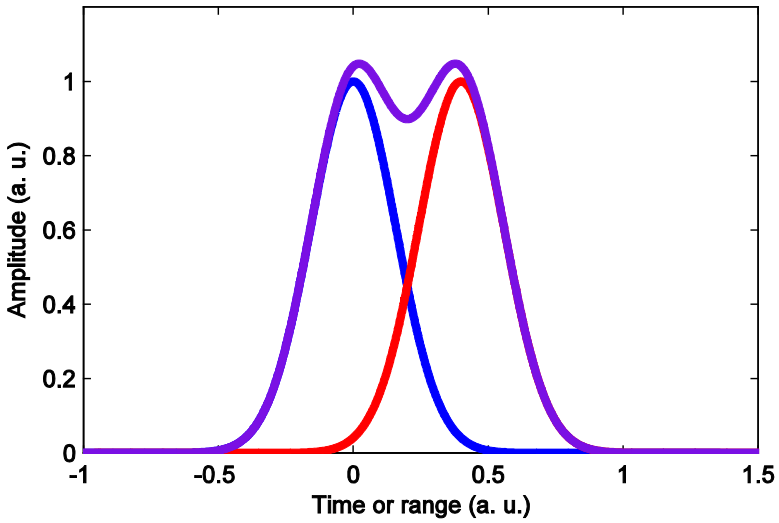

Figure 17: Just-resolved Gaussian pulses

Typically the specification of range resolution assumes equal strength signal returns from the two (or multiple) scattering points. Clearly the range resolution depends on the pulse width, but it also depends on the shape of the pulse. The characteristics of the pulse discriminator are also key, since thresholding systems will have a range resolution that depends on the threshold amplitude. A universal definition is impossible to specify, although 0.8 pulse width range separation is a generally accepted rule of thumb for range resolution when using approximately rectangular pulses with a matched-filter receiver [100].

The frequency domain implications of range resolution are straightforward. Increasing the range resolution by narrowing the pulse shape increases the central lobe of the

frequency content. This requires greater electrical bandwidth and allows for increased noise and noise spectral density.

3.1.6.4. Range Accuracy

Range resolution deals with the system's ability to discern two closely spaced scattering features, however range accuracy describes the system's precision in computing the range value of a single scattering feature. Fundamentally, range accuracy is the consistency between the perceived range and the actual range of a target.

This term, although widely used in RADAR contexts, conflicts with common application of the term in other measurement contexts. If an instrument were to produce measurements with little variance about the mean, it would be said to be "precise." If an apparatus were to produce measurements that had a mean value closely corresponding to the actual or accepted value of a known quantity, it would be described as "accurate." Thus, in a scientific context accuracy refers to systematic errors and precision refers to random fluctuations affecting the measured value. This is opposed to the usage of accuracy in a RADAR context, where accuracy describes the magnitude of random fluctuations affecting range measurement. The conflict in these definitions can sometimes lead to confusion, but both definitions are well entrenched in their respective contexts.

It is fair to associate range accuracy with timing jitter, a familiar concept in digital electronics. Range accuracy could also be termed range jitter, although usage of this term is less common. The analysis presented here will exclude jitter from digital timing circuits and focus on that which comes from Gaussian noise on the receiver front end. The following will also assume that all sources of systematic range error are insignificant.

The derivation for LADAR systems here follows that of Skolnik, [101] who applied these principles to RADAR sensors in cases of adequate SNR where the return pulse shape is not significantly distorted by receiver noise. The "video pulse" or "video bandwidth" parlance used in RADAR contexts is analogous to the electrical receiver output in a direct detection system. Here in this analysis, as in many practical systems, the rising edge threshold crossing will be used to determine target range. In the adequate SNR approximation, the slope of the received pulse is about the same as that of the transmitted pulse. Errors in range occur from noise induced fluctuations on the rising edge that cause the threshold to be triggered slightly earlier or later than the nominal threshold crossing time. These small perturbations cause fluctuations in threshold crossing time, and time delay is linearly proportional to target range. The greater the slope of the pulse, the less a given amount of noise will cause fluctuations in the trigger time. For an ideal square pulse, with infinite slope, the range accuracy will be perfect – containing zero error. This is true regardless of the pulse height (energy). This is, however, clearly impossible since infinite slope (zero rise time) requires infinite bandwidth. Realizable pulses will have finite rise time, and a slope that depends on bandwidth. Thus, specific characteristics are desirable in the frequency domain of the pulse. Faster rise times affect the shape of the

spectrum by shifting energy out from low frequencies to higher frequencies, and higher amplitudes are reflected in the magnitude of the spectrum.

Several forms of analysis yield the same expression, Equation 19, for the rms error (δr_{rms}) in a leading edge time delay measurement [102]. Measurement of two threshold crossings, such as the rising edge and falling edge, can reduce the rms error by a factor of $\sqrt{(2)}$, or $\sqrt{(n)}$ for n independent threshold crossings.* As in previous expressions, E is the received pulse energy and N_0 is the noise power spectral density.

Equation 19

$$\delta r_{rms} = \frac{c}{\beta}\left(\frac{1}{\frac{2E}{N_0}}\right)^{1/2} \quad [\text{ m }]$$

The parameter β in Equation 19 is known as effective bandwidth, and is given in Equation 20. It has a form highly similar to the second moment of inertia and is normalized to the total signal energy. This definition of bandwidth is unusual in the respect that it is not referenced to 3 dB power points but is instead highly dependent on the shape and distribution of the frequency content of the signal.

* Provided these measurements are statistically independent. Measurements made with separation time greater than the inverse bandwidth are required.

Equation 20

$$\beta^2 = \frac{\int_{-\infty}^{\infty} \omega^2 |S(\omega)|^2 \, d\omega}{\int_{-\infty}^{\infty} |S(\omega)|^2 \, d\omega} = \frac{1}{E} \int_{-\infty}^{\infty} \omega^2 |S(\omega)|^2 \, d\omega \quad [\ \mathrm{Hz}^2\ ]$$

An important conclusion may be drawn from the effective bandwidth concept. As a second moment definition, frequency content far from the mean (zero in the baseband) is weighted much more heavily than that near the mean. This is consistent with the earlier discussion of range accuracy being highly dependent on rise time and less so on pulse width.

Equation 19 and Equation 20 unite the concepts of range resolution (Section 3.1.6.3) and range accuracy. Shorter pulses have higher range resolution, and shorter pulses are constrained to have rise and fall times no greater than half the pulse width. In the frequency domain picture, a shorter pulse will shift more energy away from the mean, thereby increasing the second moment of the pulse spectrum. Therefore, systems with high spatial resolution must necessarily have high range accuracy. The converse, however, is not true. Systems with high range accuracy may not necessarily have high resolution. This means that LADAR systems can achieve range accuracy that is shorter than the pulse width. An extreme case is when the frequency content of a pulse is consolidated in delta functions at $+f / 2$ and $-f / 2$. This provides the highest moment possible for a given bandwidth and pulse energy. Notably, the return in this case would be an infinite sine wave and returns would be completely irresolvable.

Figure 18 plots the energy spectral density for a single trapezoidal pulse of 1.2 ns width. The rise time is varied between 100 ps and 800 ps. It is clear from the figure that the short rise time diverts greater energy to higher frequencies and increases the second moment of the distribution. Comparing β^2 values for these cases indicates an rms range error reduction of a factor of about 3.5 for the 100 ps rise time case. It is important to note that potential increases in thermal noise spectral density (N_0), which are likely to accompany the increased receiver bandwidth necessary to encompass the larger signal bandwidth, were not considered.

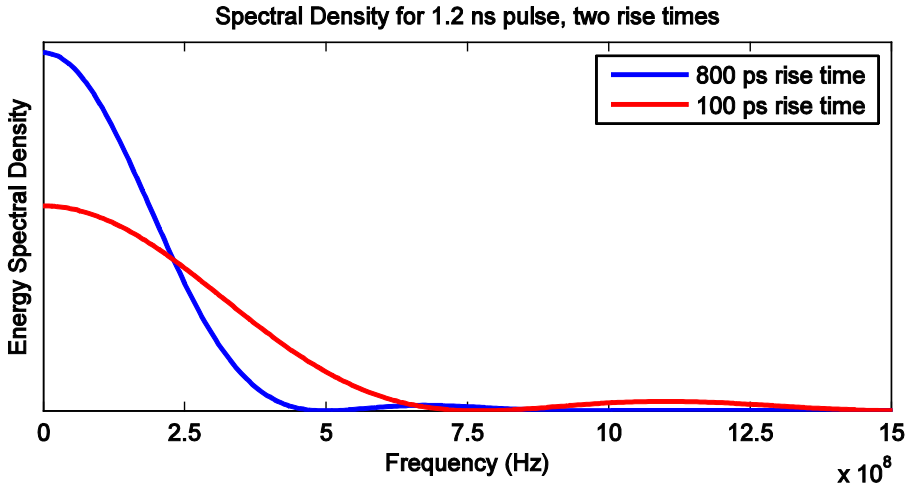

Figure 18: Spectral comparison of a 1.2 ns trapezoidal pulse width for 800 ps and 100 ps rise times (resaccuracy.m)

3.1.6.5. Amplitude Accuracy

The previous sections discussed pulse detection, filtering and localization. Accurate estimation of pulse amplitude has unusual significance to Spectral LADAR, compared to often peripheral concern in conventional LADAR imagers where spatial accuracy of 3D points is paramount.

Accurate representation of pulse energy (or amplitude) is critical when the pulse energies in each band determine the target spectrum. It is possible to estimate the target spectrum from the peak voltages, in which the statistics of Section 3.1.6.1 would apply. The pulse detection and localization calculations require high bandwidth for high fidelity 3D reconstruction of a scene. Estimating the energy of the return pulse does not require high temporal-electrical bandwidth. To improve spectral accuracy, the pulses are integrated over a fixed time period, approximately equal to the pulse width at 2% of the pulse maximum. The integration process effectively lowers the bandwidth. This is similar to how the integration time determines the noise and signal bandwidth on CMOS and CCD imagers [103].

Assuming that all noise sources are of a band-limited white spectrum type and have a Gaussian amplitude distribution, the variance in pulse energy (σ^2_{energy}) can be estimated from noise power density ($A^2\ Hz^{-1}$) and integration time (T_i). Considering numerical integration as a Riemann sum likens it to an averaging process. It should be noted that variance does not decrease by $N_s^{1/2}$ with N_s being the number of digital samples, since the samples are not necessarily independent.

Equation 21: Pulse energy variance

$$\sigma^2_{energy} = N_0 \Delta f = \frac{N_0}{T_i} \quad [\ A^2\ ]$$

3.1.7. Atmospheric Propagation and Speckle

Several atmospheric propagation effects are of general concern for remote sensing systems, including absorption, scattering, and turbulence-induced scintillation. Detector noise may set the ultimate limit on sensitivity, however exogenous effects relating to the intervening atmosphere may also reduce sensitivity and distort spectral measurements. Light makes a double-pass through the atmosphere from the sensor to the target. Along this path, absorption and scattering cause the beam to lose intensity. Atmospheric turbulence, which creates a dynamic refractive index variation in air, may also distort the transmitted and returning wavefront causing distortions in the image plane. The beam is also subject to random de-phasing by the rough surface of the target, leading to the observation of speckle.

The next two sections discuss atmospheric loss from absorption and the speckle phenomenon. These two effects were deemed to affect the performance of Spectral LADAR significantly, while turbulence is not expected to have a significant effect at ranges of about 100 m.

3.1.7.1. Atmospheric Propagation and Absorption

Predicting atmospheric propagation of optical beams in turbulent and heterogeneous atmospheres is a complex topic, requiring assessment of Mie and Rayleigh scattering as well as optical absorption of gaseous species. For this analysis, only the nominal

atmospheric conditions will be considered, neglecting weather effects such as rain, fog, dust, and other effects that contribute to loss.

Absorption is a significant effect, even at short ranges. Although the atmosphere is nearly transparent at visible wavelengths, many resonances chiefly from water and carbon dioxide molecules break up the near- mid- and far- infrared spectrums into usable regions, which will be referred to as windows. Traditionally, atmospheric windows in the infrared are considered to be from 0.8-2.5 μm in the NIR/SWIR, 3-5 μm in the MWIR, 8-12 μm in the LWIR.

The atmospheric transmittance over a 300 m path (representing the round-trip at a range of 150 m) is plotted in Figure 19 [104]. SWIR Spectral LADAR, with InGaAs detectors, extends out to 1.7 μm, and possibly as far as 2.5 μm. In this region, water vapor may be a significant factor by absorbing radiation along the line of sight in some spectral bands, as indicated by dips in the transmission plot. Ordinarily, conventional LADAR designers are concerned with signal loss when transmitting in these regions that reduce the SNR. The relative change in band atmospheric absorption is an additional factor with particular relevance to Spectral LADAR. These changes may be caused by varying weather conditions. Absorption lines or regions in the intervening atmosphere change the relative appearance of target spectra, which can lead to classification difficulties. Significantly, spectrally dependent fluctuations in atmospheric transmission are not removed by the SAM projection, as discussed in Section 3.3.

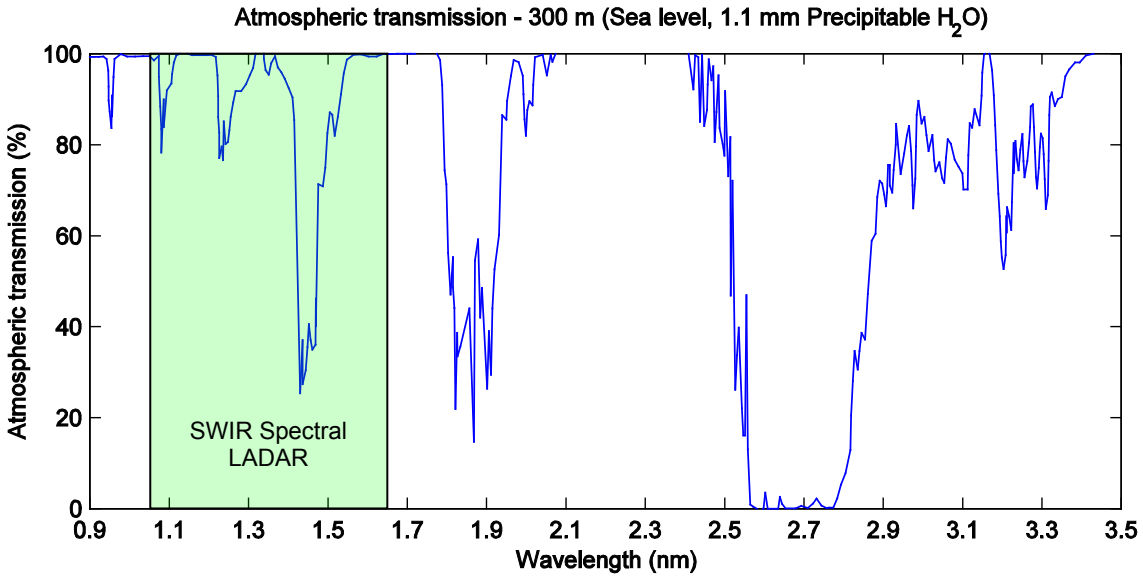

Figure 19: Atmospheric transmission over 300 m propagation distance

3.1.7.2. Speckle

An effect known as speckle arises from the scattering of waves from randomly textured surfaces. This can be observed in LADAR, RADAR, and even SONAR (medical ultrasound) systems, practically any time a coherent beam of finite diameter is reflected from a surface with random topographic perturbations having a characteristic roughness amplitude and lateral dimension on the order of a wavelength or more. This phenomenon results from the interference of multiple wavefronts with random phase perturbations. It is related to atmospheric scintillation where atmospheric turbulence creates random phase delays, and also to the interference patterns observed from multimode fiber when illuminated with a monochromatic source.

The wavelength scale dependence is important when differentiating a mirror-like specular return without speckle to a diffuse return which will exhibit speckle. A painted wall is

rough in optical terms, however in low frequency RADAR terms is smooth (RMS roughness < λ / 20). The short wavelength of LADAR results in most objects being at least partially diffuse (rough at optical wavelength scales) and exhibit speckled reflection, whereas most objects can be treated as specular scatterers in the RADAR domain. This has implications in calculating return cross sections (Section 3.1.3).

The speckle phenomenon commonly observed with reflections from laser illumination is not due entirely to the monochromaticity of laser radiation (temporal coherence), but in large part to its diffraction limited nature (spatial coherence) [105]. The path differences for the interaction of randomly de-phased waves are typically small and thus highly temporally coherent sources are not required to produce a speckle pattern. In fact, speckle patterns are observable from solar radiation in specially arranged conditions.

For ordinary natural and manufactured surfaces, the surface roughness and multiple scatterings near the surface of the material introduce random phase fluctuations greater than 2π. Speckle statistics are independent of surface roughness when the roughness is much greater than $\lambda/2\pi$, with the phases of contributory scatterers becoming uniformly distributed over the modulo 2π phase interval.[*] Several researchers have characterized speckle as a random walk problem, with individual scattering centers contributing to random steps in the complex plane [106]. It can be shown that intensity statistics of points in an image plane follow a negative exponential probability density, which implies

[*] This is true for most surfaces relevant to the Spectral LADAR concept of operations discussed in the introduction.

a contrast ratio of unity since the mean of the negative exponential distribution equals its standard deviation for the negative exponential distribution [107].

The spatial distribution of the speckle has a spatial frequency limited by the diffraction limit of the optical system. Consequently, the size of a speckle correlation cell is, on average, approximately the size of the airy disk for the system without aberrations. This is apparent if the random corrugation of the scattering surface is imagined as the superposition of sinusoidal gratings and the aperture of the imaging lens forms a band-stop filter. The speckle size then scales with the system F/#, with small F/# systems having small speckle cell size in the image plane [108].

The deleterious effects of speckle in imaging systems are clear, causing an unwanted variation of intensity in the focal plane. In a LADAR system, the concern is how the speckle pattern causes variations of signal level with respect to random microscopic variations of the scattering surface, *ceteris paribus* [109]. Thus, it is important to estimate the limitation of SNR as a ratio integrated optical power (I_0) to its variance (σ_I) of the over the active area of a single pixel. Unlike coherent techniques which are phase sensitive, only the irradiance (W m^{-2}) is of consequence for direct detection systems. Goodman has shown that the statistical signal-to-noise level of a lens system viewing a target uniformly illuminated with monochromatic radiation is proportional to the square root of ratio of detector area (A_d) to speckle cell area (A_s), and consequently the square root of the number of speckle cells integrated over the detector active area (s_p) (Equation 22) at the limit of the speckle cell size being much smaller than the detector active area

[110]. Speckle noise can be reduced by using large detectors, or systems with low F/#, essentially with an imaging system with focal plane resolution far from the diffraction limit. This analysis is for a uniformly illuminated target and therefore it is understood that the image plane is uniformly illuminated to a good approximation. Equation 22 will underestimate the SNR to the degree that the detector is under-filled or is illuminated with an irradiance that is non-uniform and decreases towards the edges of the detector active area. Since these things are usually true in a LADAR system, this estimation can be treated as a worst-case scenario. Using parameters that will be discussed later for a laboratory demonstrator system (Section 5), a worst case electrical SNR at the speckle limit is quite high and unlikely to be a limiting factor relative to receiver noise.

Equation 22

$$\left(\frac{S}{N}\right)_{rms} = \frac{\langle I_0 \rangle}{\sigma_{I_0}} = \sqrt{\frac{A_d}{A_s}} = \sqrt{s_p} \quad [\text{ dimensionless }]$$

It follows that speckle can be reduced by averaging uncorrelated speckle cells on an intensity basis (not an amplitude basis, which would be like adding more steps to a random walk). Averaging a diversity of aspect angles, polarization orientations, reducing the spatial coherence (equivalent to varied aspect angles) can decrease the rms value of the speckle based fluctuation by a factor of $N_m^{1/2}$ for N_m uncorrelated measurements.

The reduction of speckle also depends on the spectral broadness of the illuminating source compared (Δv) to the rms height excursions (σ_z) of the target surface. An approximate expression (Equation 23) shows that the spectral separation of two lines

required to produce uncorrelated spectral images is related to the coherence length [111, 112, 113].

Equation 23

$$\Delta\nu \cong \frac{c}{2\sigma_z} \quad [\ \text{Hz}\ ]$$

3.2. Fundamentals of Spectral Imaging

Spectroscopy, as a basic science, probes the structure of matter by its response to radiation of varied energy. In order of decreasing characteristic energies, atomic, molecular, and intermolecular forces have electronic and vibrational resonances that are characteristic of the material's chemical structure. Specific substance identification is often possible with laboratory prepared samples using instruments that observe a single, well defined sample volume or area. Optical transmission, reflection, or emission are typical methods for analyzing the spectral response of materials.

Spectral imaging is the combined spectral-spatial mapping of objects where spectroscopic data is collected at multiple points in an area or volume. Samples in this case may be expected to have spatially varied, heterogeneous composition. The combined spectral-spatial images obtained with these techniques elucidates structural, functional, and chemical information which has many applications in military, biomedical, and basic science contexts [114].

Polarization sensing is frequently used in combination with spectral imaging. When applied to rough surfaces and disordered media, polarization sensing can provide information about the surface structure of an object. This additional discriminator is significant, especially when spectral signatures are ambiguous.

Spectral band terminology is arbitrary and considerable variation can be seen in the literature. For the purposes of this discussion, the Near IR (NIR) will be assumed to extend from 0.6 μm to 1.1 μm, the Shortwave IR (SWIR) from 1.1 μm to 3 μm, the Midwave IR (MWIR) from 3 μm to 8 μm, and the Longwave IR (LWIR) from 8 μm to 15 μm.

3.2.1. Reflectance Spectroscopy

Reflectance spectroscopy, especially that which involves natural granular and unprocessed samples, is significantly different from, and in many ways more challenging than, gas spectroscopy or spectroscopy in pure, homogeneous solids or liquids. In the latter cases, transmission measurements are frequently employed and the absorption is related to an extinction coefficient by the application of the Lambert-Beer law. Reflectance spectroscopy, on the other hand, usually deals with disordered and heterogeneous media where the structure, size, and distribution of particles can play a very significant role in the spectral content of the backscattered radiation. Moreover, the

structural variation of the material can have dimensions on the order of the wavelength of incident radiation leading to wavelength dependent scattering properties. Figure 20* depicts three different scattering types, that of surface, volume, and volume multi-scatter. The amount of absorption depends on the interaction length in the disordered media, which by its nature is inconsistent and difficult to predict.

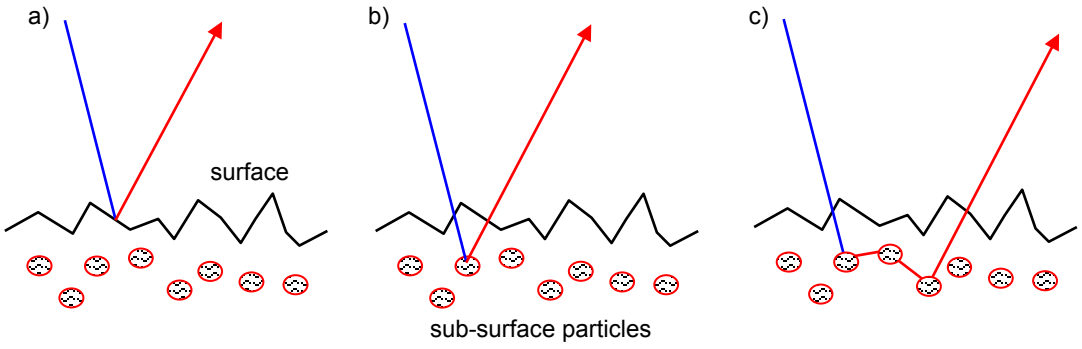

Figure 20: Backscattering from rough surfaces: surface scatter (a), volume single-scatter (b), volume multi-scatter (c)

The dependence on the arrangement of the material, in addition to chemical composition, leads to considerable variation between observations of the same type of sample. Soil provides a good example of this dependence. Although two soil samples may have the same chemical composition, their microscopic structure could be significantly different. Both soil samples will absorb at the same wavelengths, but the magnitude of the absorption is strongly dependent on the morphology. Thus, two samples of dirt with similar chemical composition can have different spectral signatures if the samples have been formed differently or exposed to different conditions. It is also important to note

* Note Spectral LADAR as considered here is a monostatic system, and the backscattered ray as depicted in the figure would have to closely retrace the path of the incoming ray to be collected by the receiver aperture.

that porous media, such as soil, can contain a varying content of water that affects spectral signatures [115].

3.2.1.1. Light-Matter Interaction

While the concept of Spectral LADAR is applicable over a wide range of the electromagnetic spectrum (UV, VIS, SWIR, MWIR, LWIR, and even THz), the sensor considered in this analysis and in the experiments described later operates within the portion of the SWIR spectrum, 1 μm to 2.5 μm (10000 cm^{-1} to 4000 cm^{-1} in wavenumbers[*]). The photon energies in this region are often too low to excite electronic resonances in atoms, so observed spectral features are due mainly to vibrational resonances in molecules.[†] A simple yet illustrative model considers a diatomic molecule as a mass-spring system (Figure 21) [116, 117]. The fundamental resonant angular frequency, ω_0, is $(k / m_r)^{(1/2)}$, where k is the force constant and m_r is the reduced mass of the two atomic masses, m_1 and m_2. The system oscillates about an equilibrium distance d_{eq}.

---

[*] Wavenumbers ($1 / \lambda$) are more commonly (and historically) used in mid-infrared spectroscopy, since the unit is proportional to photon energy under an assumed dispersion relation (ω - k). More accurately, wavevectors are proportional to photon momentum ($\boldsymbol{p} = \hbar \boldsymbol{k}$).

[†] Rare-earth ions, e.g. Er^{3+} are one exception, having electronic resonances in the SWIR.

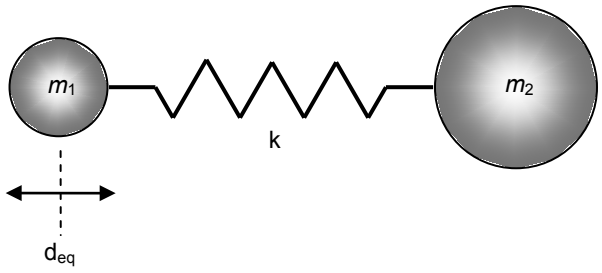

Figure 21: Mass-spring diatomic molecular system

When the system in Figure 21 is considered as a harmonic oscillator, where the attractive force is directly proportional to displacement, the potential energy versus molecular displacement is quadratic, and the laws of quantum mechanics allow for the system to be in any one of equally-spaced energy levels (v), equivalent to $\hbar\omega_0(v + ½)$. Real molecules are to some degree anharmonic oscillators, where the expression of attractive force contains higher order terms [118]. The associated potential energy function, the so-called Morse potential, is shown in Figure 22 with U as the potential energy and d as the interatomic distance. This is shown in the context of three techniques for optical probing of vibrational resonance, Raman, fundamental infrared absorption, and overtone infrared absorption. The Raman effect is a scattering process, where a photon is emitted. Fundamental absorption results in the molecular system transitioning from one state to the next higher state. Overtone absorption occurs when a single photon is absorbed with energy equivalent to any higher vibrational state. The absorption processes considered here are non-radiative, i.e. the absorbed energy adds to the thermal energy of the system.

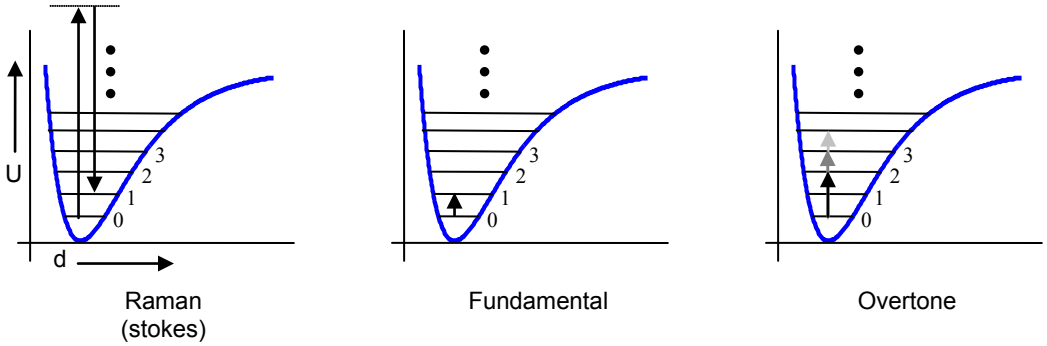

Figure 22: Energy diagram of photon - molecule interactions

In principle, each molecular bond in a complex molecule will be represented by a vibrational resonance, which together comprise a molecule's specific signature. The vibrations may be of a stretching, rocking, or other motion, having $3N_{vib}$-6 modes for N_{vib} degrees of vibrational freedom.* The signature of a particular molecule will have peaks that can be associated with specific chemical structures, such as a C-H bond.

The Raman technique involves probing molecular resonances with relatively high energy photons. Photons are scattered inelastically, involving a virtual energy level in the system. While having some advantages, such as a reduced diffraction limit, the very low scattering cross sections (inelastic scattering is 70 dB to 80 dB down from the excitation energy) and high Rayleigh (elastic scattering) background are significant disadvantages. The main limitation is that the scattering cross section is proportional to λ^{-4}. Wavelengths

* $3N_{vib}$-6 modes are available in a non-linear molecule, i.e. where constituent atoms are not in a line (where $3N_{vib}$-5 modes are available). Not all vibrational modes are "IR active," which requires a change in molecular dipole for displacement along the axis of vibration. Raman active vibrations must have change in polarizability with displacement.

longer than 1.064 μm are not commonly used for Raman excitation, making eye safe operation difficult if not impossible.

Fundamental infrared absorption involves the photo-absorption induced transition from one energy level, usually the ground state, to the next higher energy level. These transition energies are characteristically in the thermal infrared, the so-called molecular fingerprint region.

Shortwave, or near infrared, spectroscopy probes vibrational overtones where the absorption of a photon excites the system from the ground state to levels above the adjacent level. It is the anharmonic character of the molecule that allows transitions of more than one level [119]. The anharmonicity also causes the spacing of the energy levels to be uneven to some degree. Although such transitions are allowed, the transition probabilities are much lower than that of fundamental resonances, making overtone absorption much weaker than fundamental absorption. Anharmonicity is enhanced by greater dissimilarity in atomic masses in the diatomic system of Figure 21. For example, C-H, O-H, and N-H absorption lines are among those featured prominently in overtone spectroscopy [120]. In polyatomic molecules, excitation of combination vibrations may occur, where multiple modes are excited into a next-higher vibrational state.

Fundamental IR spectroscopy is often preferred for chemical analysis in laboratory environments. Fundamental resonances often appear in the spectrum as distinct and well isolated peaks that can be attributed specifically to a chemical structure in the material.

The weaker overtones in the SWIR region are seldom so distinct; they are usually broader and overlapping. This, combined with reduced cross sections, makes specific chemical identification challenging using overtone spectroscopy.

Overtone IR spectroscopy maintains some advantages over fundamental resonance spectroscopy. The shorter wavelengths allow an improved diffraction limit for higher resolutions with same-sized apertures. The reduced overtone absorption allows for deeper penetration of the transmitted beam into the target surface, increasing the contribution of deeper layers of the materials. This can be an advantage when imaging natural scenes, since light layers of accumulated debris will have less impact on the spectral signature of an object. Additionally, working at SWIR wavelengths does not require cryogenic cooling of detectors and optical elements and is not sensitive to the thermal background of an object.

Aggregated into a bulk medium, the molecular resonance characteristics are represented in the complex-valued permittivity. When considering the interaction with waves at optical frequencies, it is often useful to use the refractive index, which is complex-valued and derived from the square root of the product of the relative permittivity and permeability [121]. The real part of the refractive index is the relative phase velocity at a particular frequency, while the imaginary part describes the absorption, specifically the exponential decay of intensity with propagation distance. The absorption term is usually adequate when measuring absorption by transmission in a laboratory setting, with non-turbid medium. Backscatter spectroscopy, however, involves both the absorption

properties and the reflective properties of the medium. The reflective properties for a slab of material are described in the Fresnel equations, which depend on the complex refractive index and polarization [122].

The spectral signature of a particular material depends on these absorption and reflection relations applied to a rough surface with random geometry at optical wavelength scales and mixed material constituents. The geometric properties of the media highly influence the relative contributions of reflection and absorption. A full analysis would require vector diffraction theory and is beyond the scope of this work.

3.2.1.2. Backscatter Geometry

Reflections from surfaces are often grouped in two categories, specular and diffuse, which is determined by the surface roughness. Surfaces that are smooth in comparison to the wavelength (roughness less than $\lambda/4$) are specular reflectors while surfaces with greater roughness (peak-to-valley or rms) are diffuse.

A complete description of the reflectance is described by a Bidirectional Reflectance Distribution Function (BRDF). This function relates the incident distribution of radiance to the reflected distribution of radiance. In its most general form it is a function of polarization and wavelength. The accepted geometry and notation as promulgated by Nicodemus [123] for describing BRDF functions is given in Figure 23. The definition of BRDF is the fractional target radiance ($W\ m^{-2}\ sr^{-1}$) of the incident target irradiance ($W\ m^{-}$

^{2}) and has dimensions of inverse steradians (sr^{-1}). This is expressed in Equation 24 with dN_r and dN_i denoting infinitesimal radiances centered about the given polar coordinates. The irradiance at a sensor's aperture follows when an appropriate transformation of coordinates is taken and the BRDF is integrated over the solid angle of the aperture.

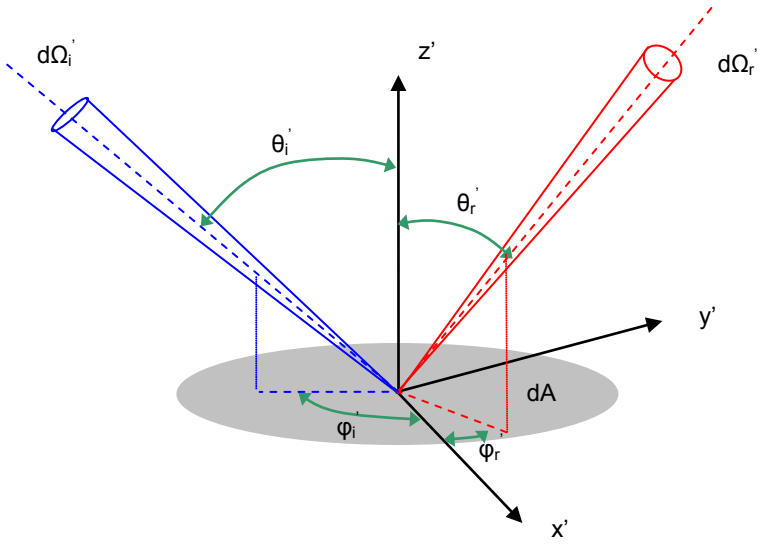

Figure 23: BRDF geometry

Equation 24

$$f_r(\theta_i',\varphi_i';\theta_r',\varphi_r';\lambda)_{dA} \equiv \left(\frac{dN_r(\theta_r',\varphi_r',\lambda)}{dN_i(\theta_i',\varphi_i',\lambda)d\Omega_i'} \right) \quad [\ sr^{-1}\ ]$$

Surfaces which are perfectly diffuse are said to have a Lambertian scattering pattern, shown in Figure 24 [124]. The backscattered intensity per unit solid angle falls off as the cosine of the viewing angle relative to the surface normal, however the viewed area of an extended target increases inversely proportional to the cosine of the angle. If an extended

target were illuminated uniformly, the observed intensity would consequently be invariant to the observation angle if the illumination angle were constant. However, for monostatic LADAR, the illumination angle is fixed with respect to the observation angle. The target irradiance is proportional to the cosine of the illumination angle. The balance of these cosine factors cause a cosine proportionality of observed intensity. Some well respected sources conclude LADAR observation angle independence for perfectly Lambertian surfaces in error [125].

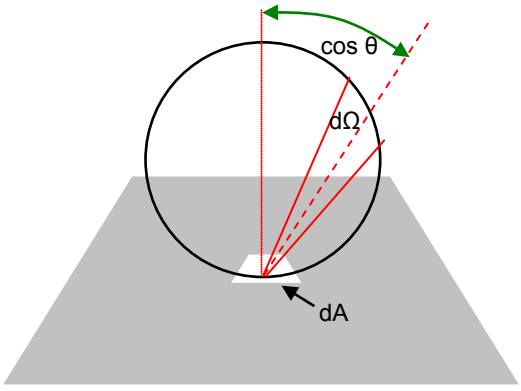

Figure 24: Lambertian scattering

Perfectly Lambertian (diffuse) and perfectly specular surfaces are extreme cases that are seldom, if ever, seen and represent more of a mathematical convenience. Diffuse media which have lower absorption at a given wavelength provide a closer approximation to Lambertian behavior due to deeper penetration and increased scattering. Realistic surfaces have both specular and diffuse characteristics. In theory, if the scattering material structure was known then the BDRF could be calculated using radiative transfer theory; however this is seldom done due to the complexity of electromagnetic wave

propagation through disordered media. Closed-form solutions to the radiative transfer equation are often impossible, and numerical solutions are often impractical, even considering the use of high performance computers. Some authors, most notably Hapke [126, 127] and earlier Kubelka and Munk, [128] have proposed simplified models of reflectance functions, however these are lacking in exactness, generality, or both. Empirical measurements of BDRF are often relied upon as a result [129].

3.2.2. Spectral Signatures

The efficacy of Spectral LADAR depends upon more than the accurate and precise reconstruction of object spectra. The spectra of natural objects themselves must be sufficiently dissimilar so that they may be identified uniquely from others. The high fidelity reconstruction of object spectra is important to accurate identification, but accuracy is moot if the statistical spread of target signatures is much greater than instrumental error, making differentiation impractical in a statistical sense. Consequently, it is important to have spectral discriminants that are both sensitive and specific. Discriminants must be sensitive in the sense that they have an appreciable contribution to the overall reflectance spectrum of a target. Specificity is desired in the sense that a particular observed spectrum should uniquely identify a target material and exclude all other possible identifications. Some sample spectra of typical objects are plotted in Figure 25.

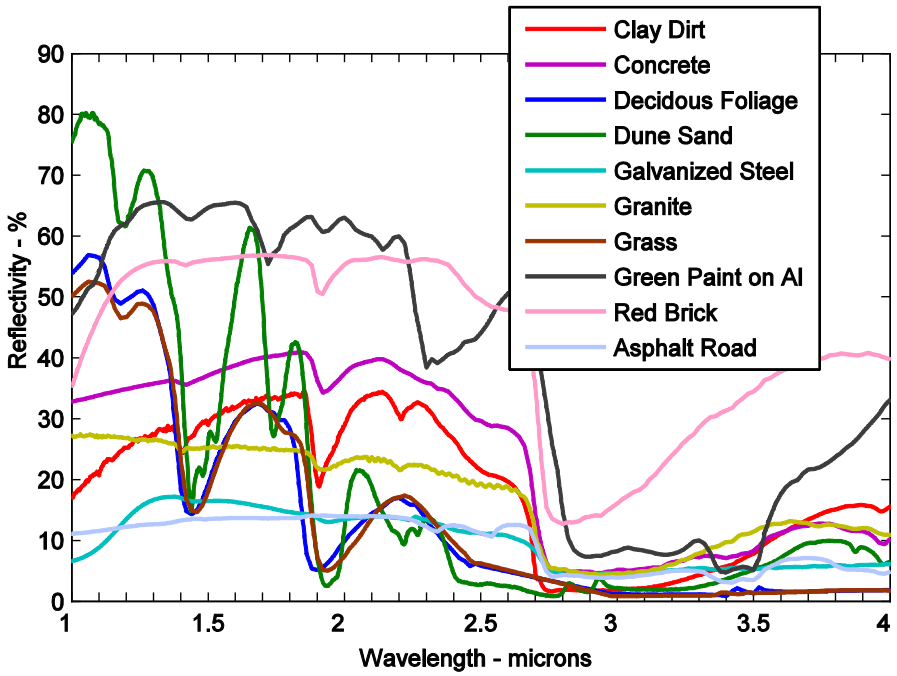

Figure 25: Spectra of natural and common outdoor materials obtained from library data

A major problem in the design of spectral imaging equipment that involves classification of pixels / voxels into several categories is the selection of wavelength bands, both in number, spacing, and size. Identifying specific spectral markers warrants investigation into the chemical basis of spectral signatures. A successful detection scheme is able to correlate spectral observations for each class with a specific and invariant material and chemical composition which have a high contrast to the background and other classes. A specific signature is a spectral feature unique to a class, while an invariant signature is that which does not have significant differences among class observations at different times, locations, or environmental conditions. Finding such signatures is not trivial considering the range and bandwidth of the measurements. Often, there is considerable overlap in spectral signatures between different classes due to common composition. The C-H stretch line at 3.5 μm is a good example, since it is present in many materials,

especially those with high concentrations of hydrocarbons. Spectral lines from water are an example of a feature that could be highly dependent on the exposure history of a target and environmental conditions, leading to unpredictable variability between observations.

Table 2 lists several object classes and their significant chemistry. The right column provides a few spectral features in the SWIR, mainly including those above 2.5 μm, based on available data.

Table 2: Chemical resonances

Target Type	*Significant Chemistry*	*Some IR Resonances*
Skin	Collagen	3.0, 3.2, 6.0 μm
	Elastin	3.0, 6.0, 6.4 μm
	Lipids	1.71, 1.78 μm
	Water	0.94, 1.14, 1.38, 1.88, 15 (broad)
		2.90, 3.11, 6.08 μm
Clothing	Polyester	3.5, 5.7 μm
	Cotton	(cellulose)
Foliage	Cellulose	2.90, 3.28, 3.4 to 3.55, 4.66 μm
	Lignin	2.92, 3.42, 3.48, 5.76 μm
	Water	(above)
Construction Materials	Tar	2.7, 3.5, 5.5 μm
	Cement	2.6, 3.5, 4.2, 4.7, 5.2, 5.6 μm
Terrain	Soil	Varies
	Sand / Rock	Quartz – 8.3, 9.0 μm

The reflection from skin has been examined by some groups in the NIR and SWIR out to approximately 2.0 μm, due to interest in this band for optical coherence tomography and photodynamic therapy [130, 131, 132, 133, 134]. Collagen, elastin, and lipids are biochemicals that are unique to the skin class. Water, however, is a dominant feature and is thought to be overwhelming beyond 2.5 μm. Notably, most of the resonances in Table 2 are beyond the spectral range of the prototype system to be discussed in Section 5.

Unlisted overtones of the spectral lines in Table 2 may be represented and observable with the prototype sensor, consistent with the discussion of 3.2.1.1.

Typical clothing consists of natural fibers (cotton), and synthetic fibers (polyester). The synthetic fibers will exhibit many hydrocarbon resonances while the cotton cellulose may be distinguished by pigment additives. A recent report observes cotton resonances at 1210, 1488, and 1935 nm, and polyester resonances at 1135, 1389, and 1665 nm [135].

Cellulose and lignin have similar spectra and are materials unique to foliage. Water has a very strong spectral impact [136]. It is well known that the spectra of foliage changes rapidly (within hours) due to water stress from cut branches, etc. It is possible on this basis to distinguish living foliage from fresh cut and dead material. A challenge will be to distinguish foliage from clothing fiber due to the similarity between cotton cellulose and cellulose of other plants. The PROSPECT leaf model is notable for its representation of leaf signatures with relatively few parameters [137].

Construction and building materials are represented by a broad and varied range of optical signatures. The spectral signature of tar has an abundance of hydrocarbon resonances and is very dark across the entire spectrum. Asphalt is an amalgam of tar and stone aggregate, and has a mix of those signatures based on weathering and age. The spectrum of cement is dominated by calcium silicates and calcium aluminate. Two mineral silicates, alite and belite, are formed in the curing process. It is interesting to note that belite is seldom found naturally and could be a distinguishing feature of man-

made structures. Paint can be distinguished on the basis of its pigments as well as its binding agents, of which there are few in common use, including linseed oil, and polymers (polyurethane, fluorocarbons). The transparency of the pigments and binding agents at some wavelengths in the infrared will allow spectral contribution from the substrate.

Terrain refers mainly to the bare ground surface in vehicle contexts. Typical surfaces may be man-made (asphalt, cement, tar and crushed stone, stone) or natural composition (dirt, mud, sand, rock, decaying plant matter). The composition of soil may be mixed and varies according to location. This presents significant spectral identification challenges and is one case where the location the voxel aids in identification. Constraints may be used to assure that any voxel to be classified as a terrain type must be spatially located on the ground.

3.2.3. Polarization Signatures

Although the polarized (transverse) nature of electromagnetic waves has been known for a considerable length of time, the use of polarization imaging for object classification and discrimination is surprisingly recent in its development [138, 139]. Human eyes are nearly insensitive to polarization, while some animals, especially insects, obtain vital information from polarization sensitive eyes [140].

Reflection at a surface can affect the state of polarization (SOP) of incident radiation in a few ways. Depolarization occurs when the reflected wavefront no longer has a coherent SOP due to scattering. Diattenuation results from the reflectance in one orthogonal direction of polarization being more reflective than the other, and retardance occurs when the target applies a relative shift in phase between the two orthogonal directions. Since most targets of interest are usually not birefringent, only depolarization is significant.

Frequently the SOP of a wave is described by the so-called Jones formalism, which is a matrix representation of the magnitude and phases of the orthogonal components of the electric field. This technique, however, only applies in cases of polarized light and is unsuitable for cases of partially polarized or randomly polarized light. Since targets will have some degree of depolarization to the incident field, the Stokes-Mueller formalism is appropriate to describe these circumstances [141]. Accordingly, lacking a coherent state of polarization, the Stokes-Mueller convention of the SOP is described in terms of intensity. The polarization of a field is given by the Stokes vector, and the target's action on the incident radiation is given by the Mueller matrix, as shown in Equation 25. In the Stokes vector, I represents the total intensity as Q, U, and V represent the horizontal/vertical linear, +/-45^{o} linear, and right/left circular polarizations, respectively.

Equation 25

$$\tilde{S} = \begin{bmatrix} I \\ Q \\ U \\ V \end{bmatrix}$$

$$\mathrm{M} = \begin{bmatrix} M_{00} & M_{01} & M_{02} & M_{03} \\ M_{10} & M_{11} & M_{12} & M_{13} \\ M_{20} & M_{21} & M_{22} & M_{23} \\ M_{30} & M_{31} & M_{32} & M_{33} \end{bmatrix}$$

$$\tilde{S}_{reflected} = \mathrm{M}\tilde{S}_{incident}$$

The surface's interaction with the incoming SOP, as described by the Mueller matrix, is affected by the roughness of the surface, the material and its absorption properties and also the angle of incidence. In general it is wavelength dependent. To fully determine the Mueller matrix of a target, 16 measurements would have to be made for the 4x4 matrix, with 4 different incident states and 4 received states. Performing 16 measurements per pixel incurs a significant penalty in signal-to-noise, pixel rate, or both. It is fortunate that, lacking diattenuation and retardance, only the diagonal components of the Mueller matrix are nonzero due to depolarization. Furthermore, M_{11} and M_{22} are effectively degenerate since they represent a rotation about the axis of propagation, and no fixed orientations are assumed in a practical setting. Thus, only three elements of the reduced matrix remain: M_{00}, M_{11}, M_{33}. M_{00} represents the backscattered intensity, while M_{11} and M_{33} represent the linear and circular depolarization, respectively.

Depending on the incident polarization vector, the linear and circular depolarization can determine the reduced Mueller matrix with two measurements. This can be done simultaneously with a polarization diversity receiver having two orthogonal channels. Experiments from numerous researchers have shown that the depolarization for man-made objects (M_{11}, M_{33} large) is generally and significantly less than that of natural objects (M_{11}, M_{33} small). Combining spectral and polarimetric information is expected to provide greater discrimination than if the techniques were used separately.

Often, a LADAR with polarization capability only measures the degree of polarization (DOP) of the received backscatter (Equation 26). The DOP represents the extent to which the diffuse reflection process scrambled the transmitted polarized state. This alone can yield important target information. It is widely known that natural materials are more depolarizing (lower DOP) than artificial or synthetic materials.

Equation 26

$$DOP = \frac{\sqrt{Q^2 + U^2 + V^2}}{I} \quad [\text{ dimensionless }]$$

The scattering properties and spectral absorbance of diffuse media are somewhat related. Light which is absorbed less rapidly penetrates deeper into the medium. With greater penetration comes greater opportunity for multiple reflections, which further scramble the incoming state of polarization. Therefore, reflectivity and the degree of backscatter polarization have a degree of positive correlation [142].

3.3. Spectral Space

The conventional approach for spectral classification maps an *N*-band voxel into an *N*-band space. This is what is known as spectral space: a Euclidean set of *N* mutually orthogonal axes with each axis corresponding to a spectral band. Thus, for each volume element in physical space, there is an associated vector in *N*-space that contains its band-intensity spectral information. Figure 26 depicts how a spectrum is divided into orthogonal components to form a vector space.

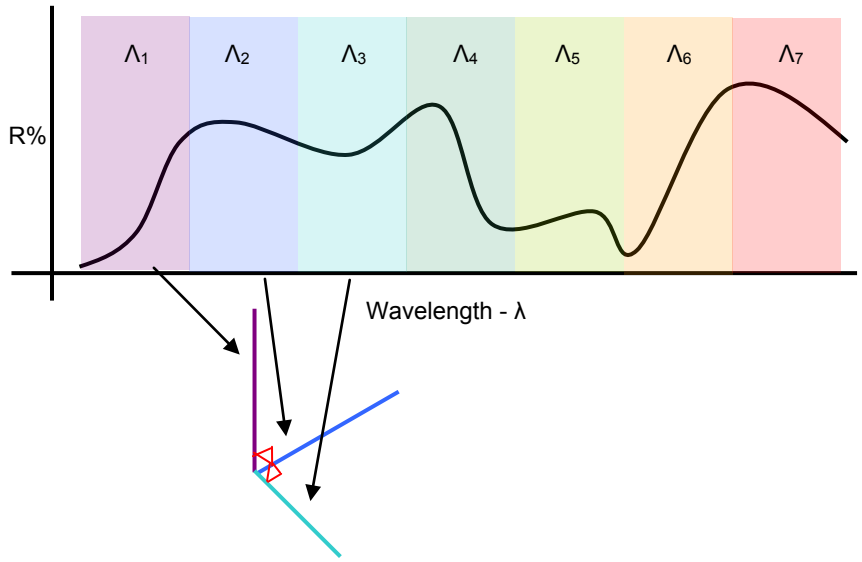

Figure 26: Orthogonal spectral bands form a Euclidean space

Spectral space representation in the presence of instrumental noise is an important issue. For every class there is an expected measurement vector, $\boldsymbol{\mu}_i$, and every measurement

vector contains a random noise vector ***n***. These vectors in *N*-space add as in Equation 27 to produce the observed vector, ***f***.

Equation 27

$$\vec{f} = \vec{\mu} + \vec{n} \quad [\text{ dimensionless }]$$

Vectors in spectral space can be classified in the Euclidean space to which they are originally mapped, where each axis is a linear function of spectral intensity. Distances between two points (***a*** and ***b***) are measured by their Euclidean distance, Equation 28.

Equation 28

$$\left\|\vec{a} - \vec{b}\right\| = \sqrt{\sum_{n=1}^{N} (a_n - b_n)^2} \quad [\text{ arbitrary distance }]$$

For some spectral imaging applications, especially active sensing and Spectral LADAR, mapping and analyzing spectral vectors in Euclidean space has some significant drawbacks [143]. Since mapping to Euclidean space is proportional to the optical intensity in each band, the mapping is highly sensitive to target range and cross section.* For vectors to be classified, they must be transformed to represent the target surface reflectivity regardless of range or cross section, which requires the solution of the inverse problem. The inverse problem attempts to compute the target reflectivity, ρ, by making assumptions on the parameters in Equation 4. The computation of the inverse problem is often inaccurate. It is useful, therefore, to project the vectors in Euclidean space to a

* All of Equation 4, including incident angle and partial obscurations

space that is invariant to the absolute intensity of the backscattered energy, thus making the inverse problem trivial. The spectral angle map (SAM) projection is sensitive only to the direction of spectral vectors, not their magnitude (Equation 29). While the SAM projection is insensitive to target range and cross section, all information on the absolute reflectivity which could be useful in classification is lost by the transformation.

Equation 29

$$\angle(\vec{a},\vec{b}) = \arccos\left(\frac{\vec{x}\bullet\vec{y}}{\|\vec{x}\|\|\vec{y}\|}\right) \quad [\text{ radians }]$$

Geometrically, SAM is the projection of the Euclidean space vectors onto the unit hypersphere in *N* dimensional space. This is shown graphically in Figure 27. Thus, SAM effectively reduces the dimensionality as it projects the data into an *N-1* subspace on the hyperspherical surface.

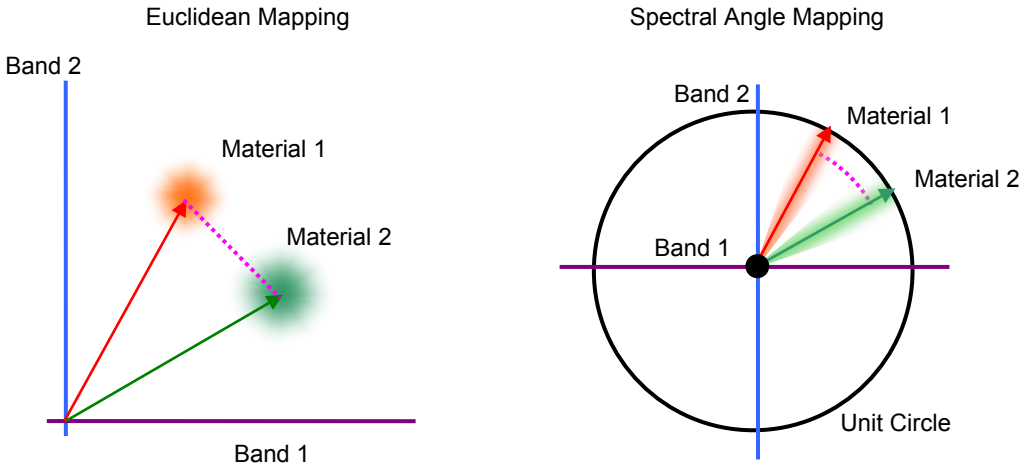

Figure 27: Euclidean mapping and Spectral Angle Map (SAM) for a two-band sensor

Whether the SAM mapping is superior to Euclidean mapping depends on factors relating to the inversion problem in remote sensing – that is reconstructing the scene from available data. The SAM metric depends only on the relative reflectivity, while, if properly inverted, the Euclidean map can measure the absolute reflectivity. Classification based on the absolute reflectivity as measured in Euclidean space would provide the best performance in an ideal situation, provided that the assumptions made in the inversion problem are accurate. Two effects that cause the apparent reflectivity to deviate from the absolute reflectivity are very prevalent. If the target was at an angle with respect to the receiver's axis, for instance, or the intervening atmosphere had wavelength independent scattering from fog or haze, it would cause changes to the apparent reflectivity that would cause the magnitude of the measurement vector in *N*-space to change. In order for Euclidean space classifiers to work properly, both the target angle and atmospheric attenuation would have to be well known to avert those effects and have an accurate measure of absolute reflectivity. The SAM projection is unaffected by any wavelength independent fluctuations, variations, or phenomenon. It is likely that a combined metric will ultimately prove to provide the best performance.

Since the proposed instrument analyzes an image in 4 dimensions – 3 spatial and 1 spectral – it is possible to correlate spatial data with spectral data for classification and recognition. The identification of a person would correlate the spatial observations of a human form with the spectral observations of skin and clothing. Identifying a vehicle would correlate the observation of a vehicle-like shape with a painted metal surface.

Furthermore, using spatial data allows spectral averaging across surfaces identified in 3D space to reduce the effects of noise.

The high dimensionality of spectral space often results in large datasets that are difficult to transmit, process, and archive. Further, it is also common to have correlated bands that are redundant indicators of underlying signatures (e.g. a single material constituent absorbing proportionally in two different bands). Reducing the dimensionality of multi- and hyperspectral datasets while preserving the most information content possible is the goal of principal components analysis (PCA, also known as the Karhunen-Loève or Hotelling transform), a common technique in spectral imaging [144, 145]. The variation in a large number of spectral vectors can be expressed by a covariance matrix, where the diagonal elements represent the band variance and the off-diagonal elements represent the covariance, or (indirectly) the correlation between two bands. The covariance matrix of a datasets with fully independent band representations will be a diagonal matrix, while correlated bands are indicated to the extent that the covariance matrix is not diagonalized.* Eigenvalue factorization may be performed on the covariance matrix to find a transform under which the covariance matrix is diagonal. Large eigenvalues indicate a high degree of uncorrelated variance (associated with information content) in the data when expressed in the new eigenvector basis as opposed to the original identity

* Independence results in zero correlation, however zero correlation does not indicate independence

basis.* The original spectral vectors may be transformed to the eigenvector basis by an associated rotation matrix.

The transformation itself does not reduce the dimensionality of the dataset. Dimensionality may be reduced arbitrarily by dropping dimensions associated with low eigenvalues, since little uncorrelated data variance is represented in these axes. Depending the nature of the data and the underlying properties of the spectral bands, a few principle component axes may represent the majority of variation in the spectral observations. PCA is also useful for reducing the dimensionality to 3-space so that multispectral images may be displayed in RGB or other tri-color system (Section 9.1.1).

3.4. Spectral Classification Algorithms

Spectral classification algorithms seek to partition spectral space into regions that correspond to a particular material type. The spectral mapping process takes each voxel in the world space point cloud, and associates it with a one-to-one corresponding vector in a high dimensional spectral space as described in Section 3.3. The spectral vectors are then assigned classes based on the partitioning of spectral space. The class labels are then applied to the world space vectors, leading to augmented understanding of objects in the scene. Spatial classification can also be applied to the point cloud and reconciled

* The degree to which noise influences the observed variance is a concern. Noise in each band is usually assumed to be independent, and therefore has uncorrelated band observations, but carries no information.

with the spectral class labels. Spectral classification algorithms can be organized into distinct groups: supervised and unsupervised, parametric and non-parametric.

Supervised classifiers rely on a supplied set of data, known as training data, to establish the class boundaries in spectral space. The training data is created by a human operator on the basis of known ground truth or controlled samples. This is shown in Figure 28. Each material type has a statistical spread representing variations in training data observations. In the context of Spectral LADAR, this data may be obtained from sample images of a scene containing many different objects of interest (e.g., skin, clothing, dirt, foliage). The pixels of the scanned image are then manually selected and grouped based on target type. Thus, a large grouping of pixels representing the clothing class would be separated from pixels representing the foliage class. The mean vector of all class observations represents an exemplar spectrum. In obtaining these data sets, it is essential that the natural variations of these classes be represented and that all classes are reasonably distinct in the scope of natural variations. It would be important, therefore, to represent bush, tree, and grass samples in a general foliage class, and not in separate classes if the spectral signature of the shrub class overlaps substantially with that of the grass class (Figure 28). In some cases it may be unimportant, or impossible, to distinguish between sub types with high confidence (e.g., Figure 28). In other cases, it may be possible to distinguish classes with very high confidence, and sub-classes with lower confidence. The selection of classes also must reflect the operational requirements of the sensor.

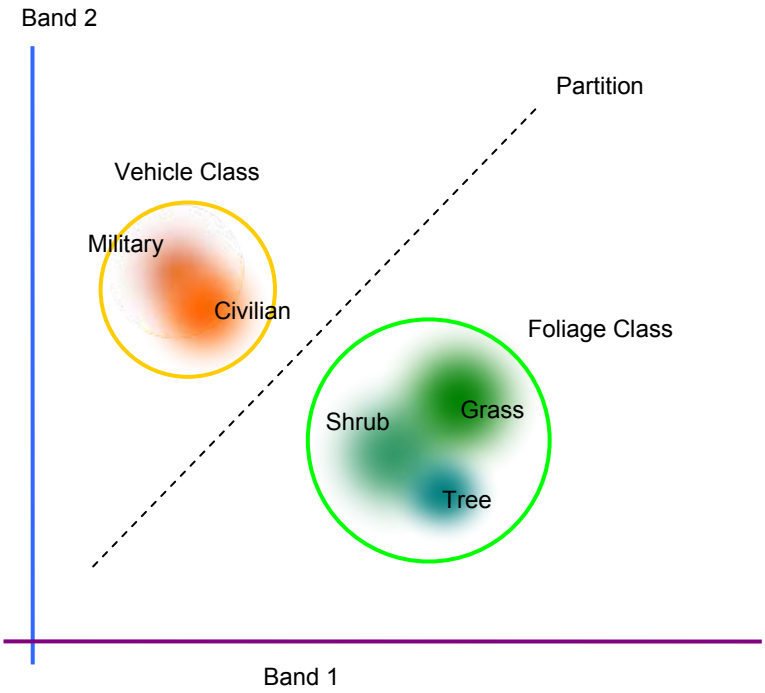

Figure 28: Class boundaries in a two band spectral space (example)

Unsupervised classifiers are a fully automatic approach to spectral classification and do not require a set of manually created training data. Instead, these algorithms look for natural grouping in the data and choose partitions based on observed similarities. It is not always possible for unsupervised classifiers to associate a class with a particular feature type (e.g. conclusively associate a cluster with foliage). So-called clustering algorithms are unsupervised.

The parametric / non-parametric attribute of a classifier describes how it defines the partitions of spectral space. A parametric classifier describes a partition in statistical terms (i.e., parameters) using the first, second, or higher moments of a distribution (i.e., mean, variance, etc.) in multidimensional spectral space to define the location and

boundaries of a class. The statistical parameters are derived from training data, and are only an accurate representation of the class to the degree that the training data is accurate and comprehensive. Non-parametric classifiers partition the spectral space using points and point-distances rather than statistical metrics.

Clearly, hybrid approaches are possible. It is possible for an unsupervised classifier to "seed" a supervised classifier, or vice versa. It also could be possible to use parametric and non-parametric approaches simultaneously. The scope of classification algorithm work in this project is to adapt existing classification approaches to the specifics of this application and leave the development of advanced algorithms to future work.

The classification approach taken here is categorized as hard and pure. The classification is hard in the sense that only one class association is applied per spectral vector (and its one-to-one corresponding voxel). In soft or fuzzy classification schemes, a voxel can be assigned multiple classifications, each with an associated confidence level. The approach taken here is to classify points based on their single most likely class membership. The classification is pure in the sense that it is assumed that only one object type is represented in the spectrum of a return. A mixed pixel, in contrast, contains some combination of spectra such as that which occurs if a pixel straddled a junction between two material types with range separation below the range resolution in the sensor. Sub-pixel detection algorithms are often used to classify pixels with multiple spectral constituents, but this is less important in Spectral LADAR since the range resolved nature of each pixel (voxel) performs some unmixing when multiple returns are present. The

classification methods to be used in this study of Spectral LADAR are described in the following sections.

3.4.1. K-Means and ISODATA

K-means is a clustering algorithm, implying that it is unsupervised and non-parametric. The algorithm partitions the multi-dimensional space into a pre-determined number of clusters (classes in the K-Means sense) by an iterative process that converges to a set of cluster centroid vectors that have the lowest sum of point-to-centroid distances over all clusters. This algorithm is widely used in remote sensing and other applications.

The algorithm is seeded with a fixed number of centroid vectors, equal to the number of clusters desired in the final classification. The seed vectors could be random or representative of certain exemplar spectrum. An initial classification is performed, associating each point with the nearest seed vector (nearest-mean classification). A new set of cluster centroid vectors is then chosen based on the seed vectors, seeking to minimize the sum of point-to-cluster-centroid distances over all clusters. After reclassification based on the new centroid vectors, the process repeats until the iterative change of all cluster centroids between iterations is below a specified threshold.

The resultant centroid vectors do not depend on the initial seed vectors if a sufficient number of iterations are allowed. Choosing seed vectors based on expected clusters may allow the algorithm to converge faster.

The K-Means algorithm is very effective if there exists some natural clustering in the data, that is, if the data is not dominated by random noise. The classification method easily adapts to novel observations automatically and does not depend on training data to find patterns. There are some significant disadvantages, however. As an unsupervised algorithm, the output is a set of centroid vectors defining the observed classification, and the nearest mean classifications of all points with respect to the centroids. The centroids themselves do not represent meaningful object types *per se*; they must be associated with an object type (e.g. foliage) in a separate process. K-means is thus a solution to the spectral segmentation problem (and by extension can be useful for spatial segmentation) but not to the classification problem without further interpretation.

Perhaps the most significant inadequacy of traditional K-Means clustering is the fact that the number of clusters must be pre-determined. Rarely, if ever, is this practical. Overestimating the number of clusters usually is not serious, but underestimating the number of spectral clusters in a dataset can produce very poor results. Moreover, since the nearest-mean method is used to associate points to cluster centroids, multiple centroids may be needed to adequately encapsulate clusters that have a highly nonuniform distribution in spectral space (high aspect ratio, for instance). The ISODATA algorithm partially addresses these shortcomings. It adds the feature of class fission or fusion, the splitting or merging of centroid vectors if distances to adjacent centroids are too great or small, respectively. This feature requires additional parameters that must be tuned and evaluated for optimal operation.

K-Means classification was used in the multispectral LADAR work of Foy et al. at Sandia National Labs, while Wang et al. used the ISODATA algorithm for classification of multispectral active sensing data [146, 147].

3.4.2. K-Nearest Neighbors

The K-Nearest Neighbors (KNN) algorithm is a straightforward nonparametric classification algorithm that is based on training data (exemplar set) that is assumed to be an accurate and comprehensive representation of a class of scene material (e.g. for foliage, representative of all within-class variations of foliage) [148].

A relatively naive nonparametric classifier is the parallelepiped classifier. In this situation, a multidimensional parallelepiped is defined in a region of spectral space corresponding to the expected range of class vectors. Vectors inside a particular parallelepiped are classified according to the class label. The drawbacks of this approach include an arbitrary determination of the extent of the parallelepiped, a simple shape not corresponding to the distribution of class exemplar vectors and a high likelihood of overlap among class parallelepiped volumes.

The KNN classifier addresses these concerns in a convincing way. The implementation of such a classifier is straightforward. A large number of exemplar pixels must first be obtained to represent each class in spectral space. A data point is then classified in a

spectral space populated with these exemplar points. A class determination is made by assigning the class of the nearest exemplar point to the data point – in the 1NN case. Variations on this theme are extended to include a majority rule of the k nearest neighbor exemplar points, or a distance weighted average of the k nearest neighbors.

Thus, by defining the class volume by nearest-neighbor properties, the classification region can assume arbitrary shape and extent based on the exemplar data. In fact, the classification volume can consist of a central region and multiple non-contiguous satellite regions if so defined by the exemplar data. Thus, the KNN method is highly robust since it makes no assumptions about the underlying shape or statistical distribution of the class variability. These properties clearly set it apart from parametric methods that are based on an assumed multivariate PDF (Probability Density Function).

A disadvantage of this technique is that it is computationally intensive since a distance metric must be computed for every exemplar point in spectral space.

The classifier's adaptability to oddly distributed data makes it difficult to predict the performance of the algorithm with analytic techniques. In contrast to the maximum likelihood classifier, discussed next, it is not straightforward to find overlap in the parameter-based PDFs of two classes and calculate P_D and P_{FA} using multivariate statistical techniques. Along those same lines, the KNN method does not always result in separable classes, and lack of separability may not be immediately evident as it would be with parametric classifiers or K-Means. Two exemplar data sets can be so thoroughly

mixed and overlapping that the classification of a data point, perturbed by Gaussian noise, is essentially random.

3.4.3. Maximum Likelihood Classifier

As a parametric classifier, the maximum likelihood assumes that the natural variation of class signatures has a PDF that can be represented with an analytic function and parameters relating to the statistical moments. Typically, signature variation is represented by a Gaussian PDF, however the maximum likelihood classifier and parametric classification in general work with other analytic distributions [149]. The maximum likelihood classifier chooses, from a composite hypothesis (H_0, H_1, … $H_{M\text{-}1}$), the most likely class of which a noise-perturbed vector $\boldsymbol{f}$ is a member.

Training data collected from known samples determines the parameters of the statistical distributions that will later define the class boundaries in spectral space. Just as with the KNN classifier (Section 3.4.2), using adequate training data that fully represents the spread of class signatures is essential for robust operation. The training data defines the conditional probabilities for the class distribution, for instance $p(\boldsymbol{f} \mid i)$ is the probability density vector of $\boldsymbol{f}$ given that the represented voxel is of class i. A class is then represented by a multivariate Gaussian distribution, as in Equation 30.[*]

[*] A superscript T indicates matrix or vector transposition

Equation 30

$$p\left(\vec{f} \mid i\right) = \frac{1}{(2\pi)^{N/2}\left|C_i\right|^{1/2}} \exp\left(-\frac{1}{2}\left(\vec{f} - \vec{\mu}_i\right)^T C_i^{-1}\left(\vec{f} - \vec{\mu}_i\right)\right)$$

Given:

N	=	Dimensionality of spectral space
$\boldsymbol{\mu_i}$	=	Expected value vector for class i
$\boldsymbol{C_i}$	=	Class i covariance matrix

The key parameter for computing the maximum likelihood is the *a posteriori* probability, $p(i \mid \boldsymbol{f})$, which is the probability of the object belonging to class i given an observation of vector $\boldsymbol{f}$. Bayes's rule relates the class distribution PDFs to the *a posteriori* probability given the *a priori* probabilities (Equation 31).

Equation 31

$$p\left(i \mid \vec{f}\right) = \frac{p\left(\vec{f} \mid i\right)p(i)}{p\left(\vec{f}\right)}$$
$$p\left(\vec{f}\right) = \sum_i p\left(\vec{f} \mid i\right)p(i)$$

The expression $p(\boldsymbol{f})$ is a normalizing constant, and is the same for all classes. It expresses the probability of the observation vector $\boldsymbol{f}$ from any of the G classes. The values of $p(i)$ express the *a priori* probabilities of a vector belonging to class i. Often, these prior probabilities are unknown. Assuming equal prior probabilities and ignoring the normalizing constant allows for the posterior probabilities $p(i \mid \boldsymbol{f})$ to be directly related to the training data sets. This allows for the formulation of an intuitively satisfying decision

rule (Equation 32), as a special case of Bayesian theory [150]. This rule selects class *i* if the likelihood of that class is higher than all others, and it is based on the training data distribution.

Equation 32

$$\vec{f} \in i \quad if \quad p(\vec{f} \mid i)p(i) \geq p(\vec{f} \mid j)p(j) \quad for\,all \quad j \neq i$$

As a mathematical convenience, a monotonic transformation may be applied to Equation 32. The probability densities, transformed by taking the natural logarithm, become the discriminant functions which are compared. Assuming Gaussian probability definitions for class distributions, the discriminant function is Equation 33, where the constant factors, including prior probabilities, have been eliminated. Only the second term (the Mahalanobis distance) must be calculated per-voxel.

Equation 33

$$g_i(\vec{f}) = -\ln|C_i| - (\vec{f} - \vec{\mu}_i)^T C_i^{-1} (\vec{f} - \vec{\mu}_i)$$

The decision surfaces formed implicitly by the set of Equation 33 (from $i = 1 \ldots G$) are quadratic in the N dimensional spectral space. Integration of the probability densities using the decision surfaces as limits can determine the probability of correct and erroneous classification, in a manner similar to Section 3.1.6.1 and Figure 16.

3.4.4. Voxel Rejection

In some cases a particular voxel may have to be rejected rather than be classified. Rejecting a voxel may be done in a classification sense only, and assigned an unclassifiable status in the point cloud rather than removing the voxel from the spatial point cloud entirely.

Voxels may be rejected if they satisfy at least one of the following criteria. The first is low SNR. Low SNR which causes high statistical uncertainty in the SAM spectral space representation will likely lead to misclassification. If the SNR in one or some predetermined number of bands is below a particular threshold the voxel will be labeled unclassifiable. Spectrally unclassifiable voxels may still contribute to spatial recognition.

The second criterion is low likelihood or similarity, and the application of this criterion varies according to classifier method. In the maximum likelihood classifier, voxels may be rejected if the likelihood of all classes (Equation 32 or Equation 33) is below a certain threshold. In this case the voxel is deemed to be an outlier and there can be little confidence in even the most likely class assignment. Similarly, if the spectral representation of a pixel is greater than a certain distance to a training vector in the kNN classifier, the voxel may be rejected for the same reason.

3.5. Eye Safety

Any sensor onboard a UGV must be eye-safe to bystanders and must not require specific practices or equipment on the part of the bystanders to assure safety (e.g., gaze aversion, laser goggles, etc.). Eye safety is helpful in other applications of Spectral LADAR as well (e.g., agricultural sensing).

Laser hazards to eyes are based on any one or combinations of three mechanisms: photoacoustic, photochemical, and thermal. The activity of each damage mechanism is spectrally dependent and contributes to the maximum permissible exposure (MPE). The spectral dependence is based largely on the optical absorbance of the involved tissues of the eye, including vitreous humor, cornea, and the retina. The retina is highly susceptible to photochemical and photoacoustic damage at wavelengths that are not absorbed by the preceding structures (cornea and vitreous humor). Photochemical damage arises from high intensity absorption by pigments in the retina, while photoacoustic damage occurs from pulsed radiation that, with absorption, creates damaging acoustic waves. These effects are mitigated at 1.4 μm, beyond which the cornea and vitreous humor are opaque and focused light does not reach the retina. At longer wavelengths, thermal effects are dominant. The authoritative ANSI Z136 Standards [151] set MPE limits for laser pulse exposure. The standard is separated into a number of regimes based on modulation and wavelength. For nanosecond pulses, several spectral regions are defined. Wavelengths from 1.5 μm to 1.8 μm have the highest permissible exposure, at 1.0 J cm^{-2} while, with the exception of that band, wavelengths from 1.4 μm – 2.6 μm have an MPE of 0.1 J cm^{-}

^{2}. Beyond 2.6 μm, the MPE is 0.01 J cm^{-2}. This is very high compared to the permissible exposure of 5x10^{-7} J cm^{-2} at visible wavelengths from 400 nm to 700 nm and makes the SWIR a good choice for active remote sensing.

Figure 29 plots the eye safe limits for single nanosecond duration pulses defined by the ANSI standard with a bold gray line. The different regions are separated by narrow vertical lines. It is assumed that only one pulse will be absorbed by the eye over a relatively long time interval compared to the pulse width. Many practical LADAR systems for UGVs are only eye safe when the beam is scanned rapidly.

The ANSI standard does not directly address supercontinuum radiation, rather it only addresses narrow band laser radiation. Some interpretation of the standard was necessary to apply it to Spectral LADAR sensors using a spectral continuum. It is assumed that spreading out a laser line to cover a broader spectrum within a particular ANSI defined region would be at least as safe as a laser line of equivalent energy. This is a reasonable assumption since the thermal eye damage mechanisms are not strong functions of wavelength. Therefore, if the spectral energy density of the supercontinuum as integrated over the spectral limits of one region is less than the permissible laser line energy in that region, the supercontinuum should also be eye safe. The spectrally integrated irradiance of the supercontinuum (specifications in Section 5.2) is shown per-ANSI defined region in Figure 29 by a series of colored circles. It is further assumed that supercontinuum radiation is eye safe over multiple regions simultaneously if it is eye safe in each spectral region defined by the ANSI standard. Figure 29 shows that, by this definition, the

supercontinuum is eye safe in all but the shortest wavelength region at 2 meters. Since the exposure limit is based on energy surface density (J cm^{-2}), the safety margin increases with distance. Wavelength selective attenuation could be applied to a beam if needed.

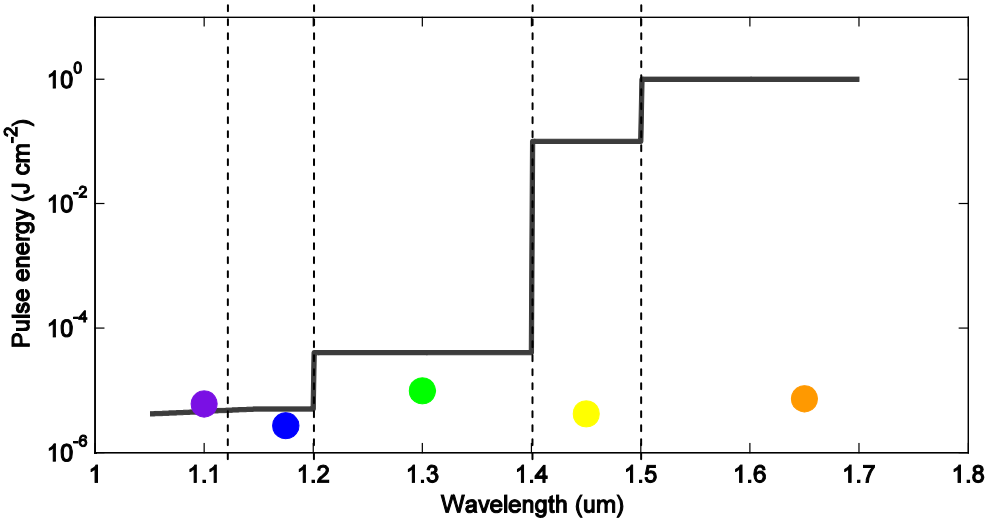

Figure 29: Eye safe limits according to ANSI Z136, at 2 m range

3.6. Optical Transmitters

Spectral LADAR requires a spectrally diverse, modulated laser or laser-like beam of sufficient power to enable long-range imaging with small receiver apertures. The fundamental issue is the selection of spectral region needed to adequately distinguish important target types with a high level of confidence. The transmitter can address this with a spectrum consisting of a number of laser lines chosen at wavelengths motivated by target studies, or a spectral continuum that spans a broad optical spectrum.

If a few several spectral lines are adequate to classify scene objects, a parallel combination of lasers or frequency shifted lasers is likely an optimal configuration. Alternatively, if more than a few spectral lines or continuous spectral sampling is required for adequate classification, a spectrally broadened beam is best. The focus of this work is on Spectral LADAR using broad continuous spectral sources. Choosing this as a starting point is an effective experimental strategy since a multispectral laser line source is, by filtering, a special case of a broad continuum. Experimentation with a broad continuum can collect comprehensive data and perhaps point the way toward a multispectral line-based system, but not vice-versa.

A number of compact and inexpensive sources exist that can address the requirements of a laser line or broadened continuum system. Q-switched microchip and fiber lasers are sources well suited to direct detection LADAR applications. Microchip lasers can easily accommodate a passive or active Q-switch, and have photon cavity lifetimes suitable for mid picosecond to nanosecond pulse widths. Repetition rates are typically in the single to double digits of kHz, and kW peak power levels are readily achievable [152, 153]. Fiber lasers, utilizing either single or double-clad fiber are also appropriate for LADAR applications. Although photon cavity lifetimes of fiber lasers tend to be too long for adequate range resolution, using a MOPA (Master oscillator, power amplifier) configuration with a modulated seed laser source can produce very high peak power pulses at repetition rates in the hundreds of kHz [154, 155]. Mode locked fiber laser sources can achieve higher repetition rates, but with very short pulses. Several parallel

fiber or microchip lasers can be used as a multispectral line source, or a single laser can be used to pump a supercontinuum generator (Section 3.6.2).

3.6.1. Multispectral Laser Line Sources

Figure 30 depicts a multispectral laser source using master laser oscillators seeding gain fiber in the MOPA configuration. The pump sources are not shown. In this situation, narrowband emission from several lasers is combined into one beam to be transmitted as a time synchronized pulse. It is not necessary that all spectral lines be generated by laser sources in the strictest sense. Rare-earth doped fibers can be used for gain in the SWIR spectrum; commercially available doped fiber candidates include Er^{3+} (1.53 – 1.63 μm) [156], Pr^{3+} (~1.3 μm) [157], Tm^{3+} (~2.0 μm) [158], Nd^{3+}, Yb^{3+} (1.0 – 1.1 μm), Ho^{3+} (2.2, 2.8 μm) [159, 160]. Parametric conversion or Raman shifting can be used to access spectral regions where laser gain media does not exist or is difficult to use at high peak powers [161, 162].

This technique is likely only feasible for several spectral lines, likely 5 or fewer. The number of pump and seed lasers, plus fiber and free space optical components will cause the size, weight, and cost to scale dramatically upwards with the number of bands. In spite of this, one advantage of this technique include greater resistance to solar background radiation since the receiver bands can be very narrowly filtered (optically) to match the linewidth of the source lasers. This also means that the greater coherence in each spectral band will make the system more susceptible to speckle and related effects.

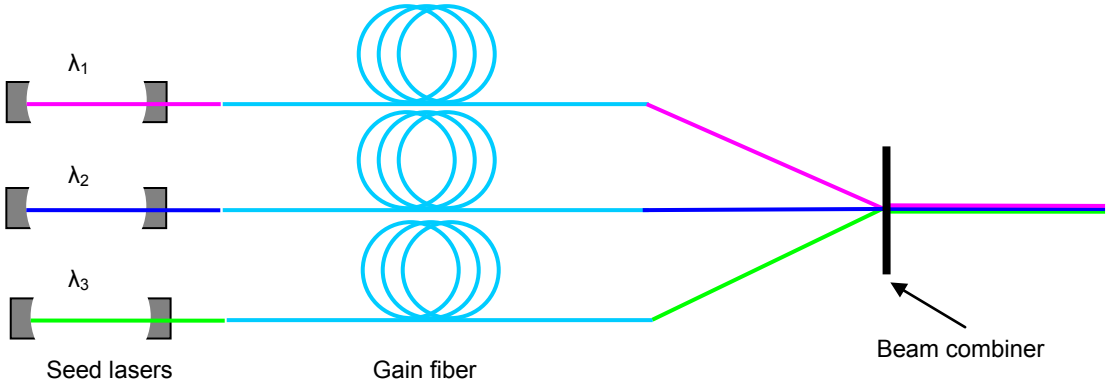

Figure 30: Multispectral source with parallel lasers

3.6.2. Supercontinuum Sources

Spectral continua can be generated by the broadening of high intensity radiation by nonlinear wavelength conversion processes. This process of supercontinuum generation (SCG) involves a complex and chaotic interaction of a number of cascaded nonlinear interactions. An optical supercontinuum (SC) was demonstrated as early as the 1970s, however recent advances in the fabrication of microstructured optical fibers and compact, high intensity pump lasers have enabled this technology to be practical for a wider range of applications.

Clearly, SCG is not the only way to generate broad spectral radiation. The distinguishing characteristics of an optical SC is the laser-like spatial coherence and spectral radiance

(or brightness, W m^{-2} sr^{-1} Hz^{-1}) that exceeds that of thermal sources by orders of magnitude and its suitability to short pulse modulation (intrinsic in its generation).

Although SCG can be achieved in any medium with appreciable nonlinear response, guided wave generation in optical fiber has been a major focus of recent developments since it enables high optical intensities (W m^{-2}) over very long interaction lengths when compared to bulk media. Although silica glass does not have a particularly high third order nonlinear coefficient, the favorable geometric properties of waveguide confinement and reasonable damage thresholds have made SCG in silica glass fiber a relatively inexpensive and popular method. Figure 31 shows the major components of a typical fiber based SCG system.[*] In the figure, a high power laser pumps a length of nonlinear fiber. As the wave propagates through the fiber, a number of nonlinear processes combine to broaden the beam from a laser line to spanning over an octave in optical frequency. The temporal power envelope of the emerging beam is similar to that of the pump beam.

[*] The horizontal scales of the input and output spectra in Figure 31 are not the same; the spectral width of the pump is enlarged greatly.

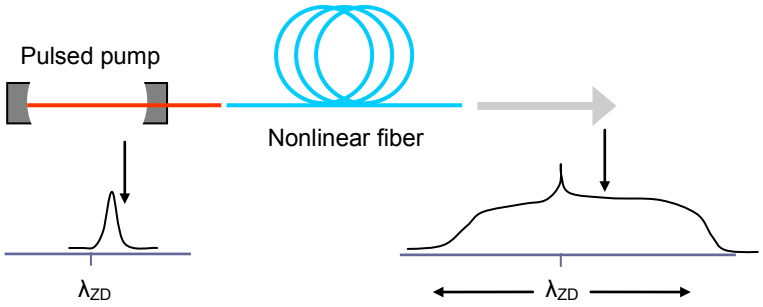

Figure 31: Supercontinuum source

Although SCG is possible using pump sources that range from femtosecond pulses to CW, pulse operation is common since it is easier to produce the high optical flux necessary for nonlinear interactions in pulses for a number of practical reasons. The abundance of research of pulsed supercontinuum is fortunate for Spectral LADAR since pulse modulation is a suitable format. Moreover, the modulation of an octave-spanning CW supercontinuum using pulse, AM, or FM formats at high speeds would be difficult and does not relate well to established optical fiber communication devices that can be leveraged to support LADAR technology.

The SCG process in optical fiber is strongly dependent upon a number of factors, including the fiber material, spatial mode distribution and intensity, propagation length, fiber dispersion properties, and temporal shape of the pulse.

3.6.2.1. Fiber Properties

There are many published demonstrations using silica glass as the fiber material, despite silica's unremarkable nonlinear properties compared to materials specifically utilized for

nonlinear interaction. The amorphous nature of these fibers obviates the concern of crystal orientation, which is critical to many nonlinear conversion devices. The main limitation of using silica glass for SCG is mainly due to its long wavelength absorption limit as opposed to other factors. The key technology behind the success of silica glass optical fiber for SCG is the development of microstructured fiber, often called Photonic Crystal Fiber (PCF). Photonic crystals are formed by the periodic variation of permittivity of a material to create a photonic bandgap, similar in concept to an electronic bandgap in semiconductor materials. Photonic crystals are the extension of a Bragg mirror (1D photonic crystal) to three dimensions. All microstructured fiber does not exhibit a photonic bandgap, making PCF somewhat of a misnomer. Microstructured fiber used for SCG is of the solid core type, and this geometry does not achieve waveguiding through a bandgap effect but by an effective index effect. Guided waves in fiber of this type can be described through a modified total internal reflection effect, similar to traditional optical fibers. The geometry of such a fiber contains holes of constant diameter, spaced on a hexagonal grid, with a particular pitch. Omitting a hole at the center of the fiber produces a region of localized, elevated refractive index which guides a single transverse mode.

A number of PCF structures exist for a variety of purposes. Purpose-built fibers for SCG seek two properties: tight guidance of the fundamental transverse mode for small mode field diameter (MFD), and specifically tuned group dispersion. The benefits of a small MFD are clear in the context of nonlinear interactions, as smaller MFD increases the peak field strength for a given input power. Tuned group dispersion is critical to SCG.

The dispersion properties of the fiber relative to the pump wavelength determine the extents of phasematching and thereby the degree to which parametric processes are involved in the broadening of the pump beam [163].

3.6.2.2. Nonlinear Effects and Dispersion

The physical processes behind SCG differ in accordance to the regime in which the SC is generated. A significant amount of contemporary work in SCG research and development is in the femtosecond regime in which the physics of ultrashort pulse propagation is involved. Femtosecond SC sources require modelocked pump lasers which tend to be expensive, and have repetition rates in the MHz regime. For these reasons, and the fact that electronic receivers cannot resolve ultrashort pulses, femtosecond SCG is not applicable to Spectral LADAR without fundamental changes in approach. Instead, Spectral LADAR is in the picosecond to nanosecond regime, and the broadening not *directly* described by Self Phase Modulation (SPM) and soliton-related effects as it is in the femtosecond regime. SCG in the "long" pulse regime is described with a combination of degenerate four-wave mixing (FWM) and stimulated Raman effects.

Picosecond to nanosecond SC sources can be categorized into three regimes according to the pump wavelength relative to the fiber's zero dispersion wavelength (ZDW or λ_{ZD}), under the condition that the fiber has only one ZDW [164]. The group velocity dispersion (GVD) is zero at this point ($\partial^2\beta / \partial\omega^2 = 0$). The first region is pumping far below the ZDW, where $\lambda_{pump} << \lambda_{ZD}$. In this regime, there is no significant

phasematching since the GVD around the pump is high. In the absence of such phasematching, the Raman effect dominates since the parametric processes require phasematching unlike Raman scattering [165]. The hallmark of such a SC spectrum is the fact that it is one-sided with only wavelengths downshifted from the pump to lower energies.* The first several Raman lines stand out from the continuum, producing an uneven broadening at wavelengths close to the pump that then merge to a continuum at longer wavelengths as the spectral intensity tapers off. For pumping at slightly lower than the ZDW ($\lambda_{pump} <\sim \lambda_{ZD}$), phasematching causes degenerate FWM to dominate the process since FWM has higher gain than Raman scattering in such situations. In this case a SC forms around the pump, and parametrically (FWM) generated signal and idler waves. The spectrum is stronger around these lines and weaker in between. The spectral broadening is usually less than the first case. The third case ($\lambda_{pump} > \lambda_{ZD}$), where the fiber is pumped in the anomalous dispersion region, produces wide and smooth broadening, which is favorable for Spectral LADAR. In this case, some phasematching is achieved, but the most significant effect is that a cascade of FWM effects breaks the nanosecond pump pulse into a pulse train of femtosecond solitons with a nanosecond envelope close to the original pump envelope.† This breakup is caused by modulation instability (MI), the time domain equivalent of FWM. Following MI breakup, the dynamics of femtosecond SC generation act on the elements of the random pulse train, including SPM and soliton effects [166]. The actual breakup of the pulse is influenced by noise, which inevitably leads to some pulse fluctuations. These fluctuations are, in contrast to the

---

* Anti-Stokes scattering will be comparatively small

† Solitons may only exist in the anomalous dispersion regime where nonlinear effects can counterbalance dispersion

other features of anomalous region pumping, an issue for Spectral LADAR since they may necessitate pulse-by-pulse source compensation.

A crucial feature of PCF intended for SCG is that the ZDW can be tuned to match wavelengths of powerful, compact, and inexpensive pump lasers. In standard single mode fiber, the ZDW is about 1.31 μm from the combined effect of material dispersion (ZDW of 1.27 μm in bulk silica glass) and waveguide dispersion. Dispersion shifted fibers utilizing specialized core doping profiles can shift the ZDW to longer wavelengths, such as those matching the dispersion minimum with the loss minimum in silica fibers at 1.55 μm. Due to the limitations imposed by the material dispersion, it is not possible to shift the dispersion minimum much below 1.3 μm. The advantage of PCF over standard doped fiber is the much greater influence of waveguide dispersion over material dispersion [167]. The microstructuring and effective index guidance allows the ZDW to be decreased to a wavelength lower than that of the bulk material. The wide ZDW tuning range allows for this critical parameter to be matched to laser sources. Fibers with a ZDW slightly less than the Nd^{3+}:YAG wavelength of 1064 nm are commercially available. When pumped by a kW peak power microchip laser, a very compact and high power supercontinuum transmitter can be attained.

3.7. Photoreceivers

Photodiode detectors are frequently used for LADAR because of their high sensitivity and high speed operation. Photomultiplier tubes may have adequate sensitivity and bandwidth, but cannot be used conveniently in an array for parallel spectral read-out. Other common detector types such as photoconductors, bolometers, thermopiles, and pyroelectric detectors have nowhere near the response time required for accurate and high resolution ranging. Exotic types like photoelectromagnetic detectors and infrared superconductor detectors have interesting properties but are not suitable for this application due to lack of commercial or near-commercial availability. Avalanche photodiodes, with an internal electron gain mechanism, are well suited to Spectral LADAR since they combine high sensitivity with high bandwidth and can eventually be fabricated in linear and two dimensional arrays for simultaneous spectral and spatial read-out. A Spectral LADAR receiver is distinct from a CMOS imager or CCD since it is a proper photodiode array in that each detector is directly and continuously read-out by a full bandwidth analog channel, instead of a charge-integration and multiplex read-out.

3.7.1. Optical Processes in Semiconductors

Semiconductor photon detectors convert photons into electrical signals by the photoionization of an electron-hole pair, a type of photoelectric effect. Electrons in the valence band are promoted to the conduction band when a photon of energy greater than

the bandgap energy of the semiconductor is absorbed. This process, sometimes supported by phonons to satisfy momentum conservation, leaves a hole in the valence band corresponding to an unoccupied electron state. Semiconductors can be of a direct bandgap type where the minimum bandgap energy transition corresponds to no change in electron momentum, or the indirect type where the minimum bandgap energy transition requires a shift in momentum.

Photodiodes, which use pair generation in the depletion region of a diode, achieve their high speed operation in reverse bias by the fast transport of holes and electrons across the depletion region of the diode. Charge carriers are accelerated by the electric field in the depletion region to the n and p regions, respectively. This minority carrier injection results in rapid recombination allowing current to flow through the device.

3.7.2. Fundamentals of Photodiodes

Photodiodes operate on the same principles as ordinary p-n junction diodes, with some modified structures to optimize their characteristics for the generation of photocurrents. In contrast to a typical p-n junction, photodiodes are constructed with a p-i-n junction that adds an intrinsic layer in between the p and n doped regions.[*] The intrinsic region, which has neutral charge density, effectively lengthens the depletion region. This separates the

[*] The intrinsic region is referred to with the letter π in some references

space-charge depletion regions in each doped region and makes the electric field approximately constant over the length of the intrinsic region. This imparts two advantages. The first is higher quantum efficiency resulting from longer high-field absorption depth in which to generate photocarriers.* The second is reduced junction capacitance, which increases bandwidth and also decreases the thermal noise spectral density by allowing higher input impedance at a fixed bandwidth of the receiver system. Some photodiodes utilize a heterostructure design where lattice matched materials with different bandgaps are used. This type of structure can be engineered to selectively absorb photons in the desired layer, with other layers transparent to the incoming radiation.

The responsivity (R) of a photodiode is based mainly on its quantum efficiency (η). Quantum efficiency is the ratio of incident photons on the active area to photocurrent electrons (Equation 34). The absorption of photons in the intrinsic region is described by the Beer-Lambert law. The absorption coefficient and layer thickness must be sufficient to absorb nearly all photons, but not be so thick as to increase the transit time of the carriers and decrease bandwidth. It is important for the absorption region to have a sufficiently strong electric field to sweep the carriers into the opposing doped regions for recombination.

Equation 34

$$R(\nu) = \frac{\eta(\nu) q}{h \nu} \quad [\ \text{A / W}\ ]$$

* Or a wider region allowing for a larger active area, if light is incident laterally

The wide optical bandwidth of Spectral LADAR makes it important to consider quantum efficiency and responsivity as functions of optical wavelength. Typically, photodiodes are designed so that the quantum efficiency is relatively constant over the device's optical bandwidth but the responsivity monotonically increases with wavelength. This is due to the quantum (or square-law) nature of semiconductor photodetectors. Each absorbed photon results in one electron hole pair, regardless of how much the individual photon energy exceeds the bandgap. Photon energy exceeding the bandgap energy is dissipated through lattice vibrations (phonons). The band-edge transition has the highest electrical yield versus incident energy. Consequently, photodiodes have relatively lower responsivity for higher energy photons.

3.7.3. Avalanche Photodiodes (APD)

Avalanche photodiodes (APDs) are an enhancement of p-i-n junction photodiodes which, when properly adjusted under certain conditions, can increase the SNR of a photoreceiver. APDs utilize avalanche multiplication to amplify the photocurrent. The multiplication (gain) is achieved through impact ionization by photocarriers as they are accelerated through a high field region. At some point, they accumulate sufficient kinetic energy to create electron hole pairs on impact with electrons at lattice sites. The impact ionized carriers can also ionize secondary pairs in subsequent impacts. The following

description of APDs applies mainly to silicon devices, but the principles discussed apply to InGaAs based detectors with some modifications.

Most high speed, low noise APDs follow a reach-through structure, which Figure 32 depicts in simplified form. Other alternatives, such as a beveled edge or guard ring structure, usually have slower response times due to long transit times or significant photocurrent transport through diffusion (reach-through structures can also have guard rings to suppress unwanted currents) [168]. The remainder of this discussion will be specific to reach-through devices. Reach through devices are called such due to the growth of the depletion region as reverse bias is applied. As the reverse bias voltage increases, the depletion region at the p-n^+ junction expands to reach through the p region entirely, and ultimately stretches into the p^+ region. This fully depleted mode of operation is most common and useful. Operating a reach-through APD below the reach-through voltage will significantly degrade the frequency response, first due to the high capacitance at the p-n^+ junction and later due to the insufficient field strength in the intrinsic region which is needed for fast transport.

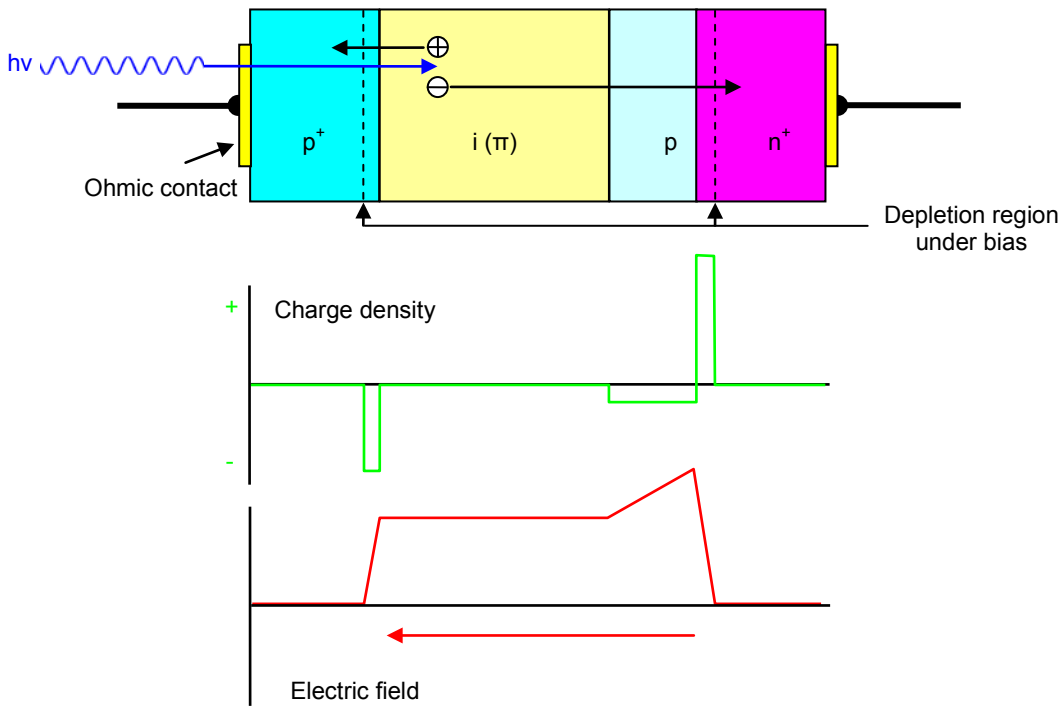

Figure 32: APD structure, space charge, and electric field properties

The noise characteristics will be explained quantitatively in Section 3.7.5, however the structure of the device has significant influence over the excess noise of the multiplication process. For low noise operation, it is necessary to inject only one carrier type into the multiplication region. In the InP family, electrons have a higher ionization coefficient. Thus, it is desirable to inject only electrons into the high field region for impact ionization. Most APDs implement a Separate Absorption and Multiplication (SAM*) structure so that only one carrier type is injected. Heterostructure APDs often contain an additional grading region (SAGM) to smooth out bandgap discontinuities that can slow carrier transit and decrease bandwidth.

---

* Not to be confused with SAM, referring to Spectral Angle Map

When electron injection is desired, the device is structured such that photons enter through the p^+ side and are absorbed in the intrinsic region. Since this region has a moderately high electric field, electrons are quickly swept to the right while holes are swept to the left, in the orientation of Figure 32. Photons absorbed in the p^+ region or outside the transverse extent of the intrinsic region will be transported by diffusion, which is significantly slower than the drift induced by the electric field. Carriers transported by diffusion will not contribute to the photodiode's responsivity to a high speed modulation. These effects often present "long tail" impulse responses [169]. The primary holes created by the photoionization are collected in the p^+ region without encountering electric fields strong enough to impart ionizing energies. Electrons, on the other hand, drift toward the very high electric field at the p-n^+ junction. Here, electrons gather sufficient energy to ionize secondary carriers, and these carriers can ionize further pairs in succession.

The avalanche gain is a sensitive function of temperature and bias voltage. Highest gain is obtained by operating the device slightly below the reverse breakdown voltage. When biased beyond the breakdown voltage, dark current flows unabated, regulated only by external circuits and bulk resistances. A representative curve is shown in Figure 33. Reach-through occurs at the voltage where the dark and signal current are observed to dramatically increase. When biased well beyond reach-through the APD is capable of its full bandwidth. At the breakdown voltage, the gain approaches infinity along with the signal and dark current. The current may be physically limited by compliance resistors.

The optimum reverse bias voltage and hence the optimum gain to maximize the photoreceiver's SNR is usually close to the breakdown voltage but depends on the thermal noise characteristics of the receiver circuit.

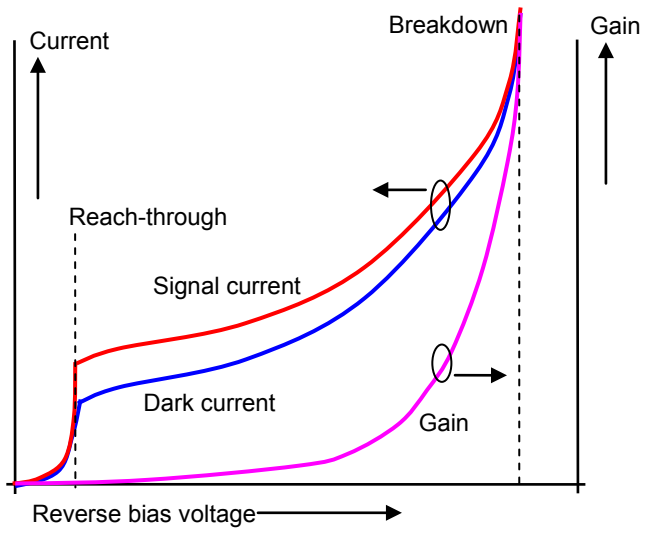

Figure 33: Representative I-V curve at constant light input

3.7.4. Limitations of APDs

The potential SNR benefits of APDs are not without trade-offs. Stability is a challenge both in the design and operation of these devices. APDs are operated on the brink of destructive breakdown so adequate control is necessary. Frequently a compliance resistor is put in series with the APD to limit the current in a reverse breakdown situation to a value that will not cause irrevocable damage to the device. Temperature control is a major concern since the breakdown voltage has a temperature dependence of about 0.03 V / K. The design of the high field region is especially critical. It is important to keep

the electric field as uniform as possible (with a consistent doping profile and control of edge effects) so that the entire cross section of the device has approximately the same gain. Since the device is operated close to breakdown, a highly nonuniform electric field could cause some localized regions of the device to go into breakdown at lower voltages. The result is a weakest-link problem. A device that must be kept at lower bias voltage to avoid localized breakdowns will have lower average gain over the active area. Along the same lines, it is also necessary to operate the device with a very low noise high voltage power supply to avoid avalanches caused by transient bias voltage disturbances.

The gain mechanism decreases the temporal bandwidth of the device simply because the avalanche process increases the transit time [170]. Higher gains and higher values of the ionization ratio (to be discussed later) increase the degradation of bandwidth. This ultimately leads to a familiar gain-bandwidth trade off.

Most APDs are designed and operated for applications where monochromatic, near monochromatic, or a relatively narrow range of wavelengths are used. Although APDs have a wide optical responsivity spectrum, using this entire spectral range at once is uncommon. It is notable that the avalanche gain is wavelength dependent because the absorption depth in the intrinsic region is a function of wavelength. The absorption depth affects the gain because the kinetic energy of the charge carriers is a function of position in the intrinsic region. Thus, all spectral bands will not see the same APD gain and it may be possible to observe a higher excess noise due to hole injection with wavelengths that penetrate beyond the multiplication region. This may prove to be important in

Spectral LADAR either with a single-APD laboratory demonstrator (Section 5.6.1) or an array of APDs.

Diffusion current is a problem of particular importance in LADAR applications using planar type APDs. Many LADAR architectures directly illuminate a receiver focal plane from the receive lens, and many systems have some degree of parallax from slight departures from a quasi-monostatic configuration. This parallax can cause returns at close ranges to be laterally mis-aligned with the active area of the APD and create photocarriers in a field-free region where the only transport mechanism is diffusion. Depending on the severity of the problem and the pixel rate, the diffusion current could cause interference between received pulses, or adjacent APDs. These effects can be reduced by using mesa-type APDs or utilizing other means to decrease the mean diffusion length outside of the active area.

3.7.5. Excess Noise in APDs

The gain of an APD is not noise-free. Shot noise, discussed in Section 3.1.4.1, is the result of discrete charges crossing the potential barrier of a photodiode as a stochastic process. Amplification from impact ionization is also a statistical process and this imparts additional noise, in excess of the shot noise, on the output signal. Ionization is a random process which occurs at random locations in the multiplication region. The multiplication factor M is the average gain, whereas it is important to realize that the gain

for one generated pair is a random variable, m_g. The noise from the amplification process, F_A, is a multiplicative factor to the native shot noise and is referred to as the excess noise factor. Equation 35 is the shot noise variance including the gain excess noise and contributions from dark current and background to be discussed in Section 3.7.6.

Equation 35

$$\sigma_s^2 = \left\langle i_s^2(t) \right\rangle = 2qM^2F_A\left(RP_{sig} + I_d + I_{bg}\right)\Delta f \quad [\ \mathrm{A}^2\ ]$$

Given:

R = Fundamental APD responsivity, M = 1 [A / W]

P_{sig} = Return signal power [W]

I_d = Dark current [A]

I_{bg} = Background photocurrent [A]

As a first approximation, the excess noise in an APD is a function of the mean gain (M) and the ionization ratio (k). The ionization ratio is usually approximated by the ratio of the electron ionization coefficient (α_e) to the hole ionization coefficient (α_h). These coefficients represent the probabilities that an electron or hole, respectively, will ionize a new carrier pair over an infinitesimal distance. These factors are, of course, dependent upon the ionization mechanics which are determined by the electric field profile, injection properties, and bandgap profile. Their ratio, k, is independent of gain so it can be assumed to be constant and applies to a wide range of operating parameters. Most APDs can be approximated with the assumption of pure electron injection. A derivation

for the excess gain is presented in the classic paper by Webb, McIntyre, and Conradi, [171] with the result of Equation 36 (valid only for electron injection).

Equation 36

$$F_A = kM + (1-k)\left(2 - \frac{1}{M}\right) = \frac{\langle m_g^{\,2} \rangle}{\langle m_g \rangle^2} = \frac{\langle m_g^{\,2} \rangle}{M^2} \quad [\text{ dimensionless }]$$

The excess noise is equivalent to the ratio of the gain variance (mean-square gain) to the mean gain squared (M^2). It is clear from Equation 36 and the plot of excess noise factor in Figure 34 that lower values for the ionization ratio enable amplification with much less excess noise. Low values of k indicate the majority of ionizations are from electrons versus holes. High values of k (close to infinity) represent situations where holes exclusively initiate impact ionizations. Excess noise is minimized with very low or very high values of k. The value of k in an APD depends on the material properties, structure, and injection type. The material used as the multiplication regions differ in various material systems. Bulk silicon has a k value of 0.02 for electron injection. This low value makes silicon very favorable for APD development, among other reasons. The InP family of detectors is well suited for SWIR bands. Bulk InP has a k value of 0.4, which is considerably higher than silicon. Nevertheless, intrinsic InP is used as the multiplication material in many SWIR APDs. Recently, InP based APDs have utilized InAlAs multiplication regions, which are lattice matched to InP and have a k value of 0.2.

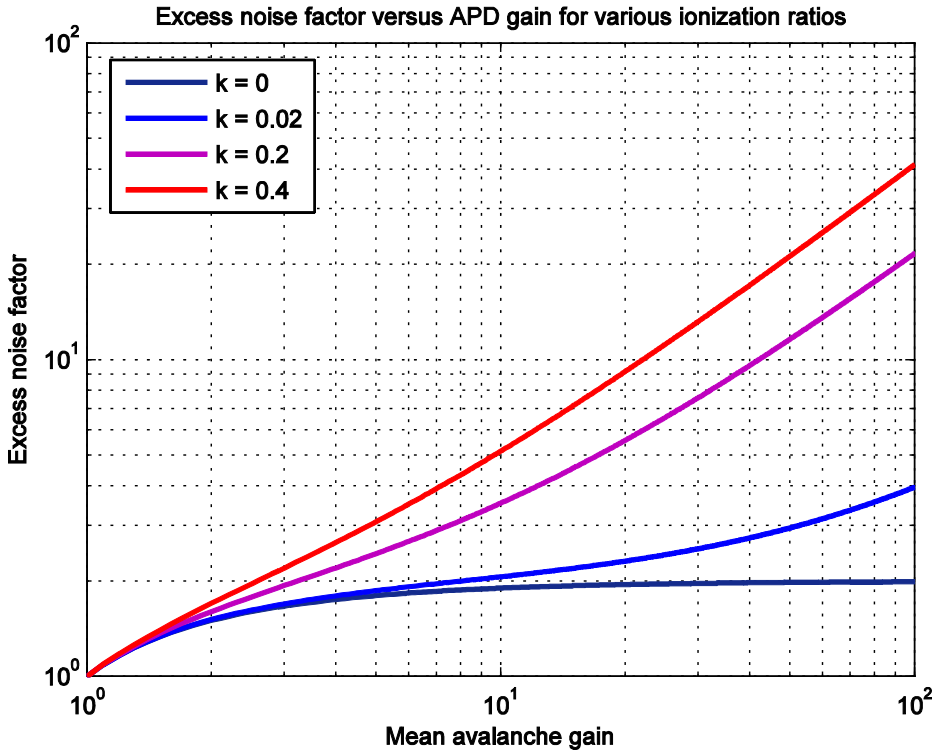

Figure 34: Excess noise factor as a function of gain

The APD depicted in Figure 32 represents a simplified approach. Recently, staircase [172] and superlattice [173] APDs have been demonstrated as a means to reduce the effective value of *k* with an engineered material structure. The disadvantages of these structures include higher dark current due to the presence of narrow bandgap materials, tunneling, defects, and band discontinuities. Another approach is utilizing an impact-engineered structure. In general, impact engineered structures use a modulated bandgap and electric field profile to localize impact sites, and discourage secondary ionization from undesired carriers (usually holes). The work of Campbell and others [174, 175] has led to impact-engineered structures in the InP system to obtain *k* values as low as 0.02, about the same as silicon.

3.7.6. APD Equivalent Circuit Model

An APD is always operated in reverse-bias, the so-called photoconductive mode.* In this mode, the APD acts like a current source, with current dependent on the incident optical power. An I-V curve for the photoconductive mode with a photodiode is depicted in Figure 35. The load line (dashed) reflects the photodiode driving a near zero impedance load.

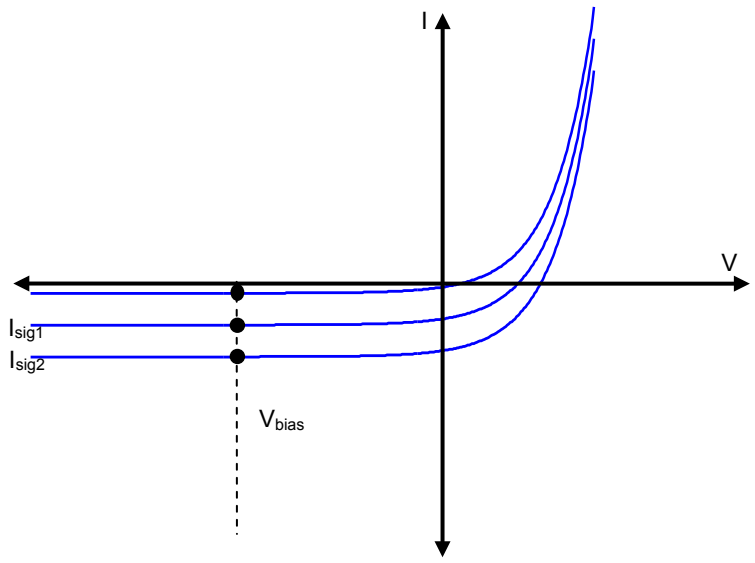

Figure 35: Notional photodiode I-V curve

* Not to be confused with photoconductors, which have a resistance which is affected by photo-generated carriers. Photoconductor detectors are not diodes.

An APD may be modeled with linear circuit elements and is shown driving a load in Figure 36. Three photocurrent sources are in parallel, with I_{sig} representing the signal current, I_d the dark current, and I_{bg} the background photo current from sunlight or other sources. The capacitance of the diode is represented by a parallel capacitor. Similar to a varactor diode, the capacitance results from the depletion region and is a function of the detector's active area, doping profile, and reverse bias.

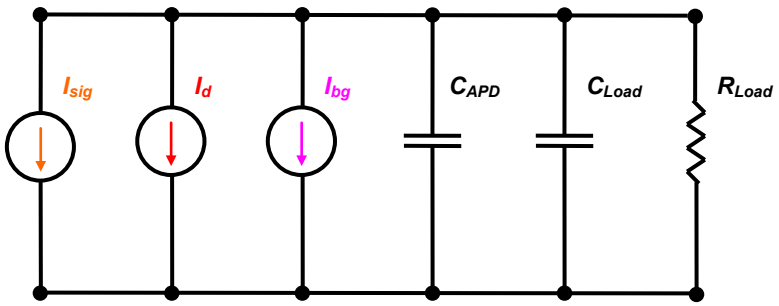

Figure 36: APD equivalent circuit driving a load

The signal current (I_{sig}) is given in Equation 37 where P_r is the power received by the APD's active area. The fundamental photocurrent in an APD is multiplied by the gain factor (M) over what it would be for a p-i-n photodiode with unity gain. Like the responsivity (R), the current is also a function of wavelength.

Equation 37

$$I_{sig} = MR(\lambda)P_r(\lambda) \quad [\ \text{A}\ ]$$

The dark and background photocurrent sources generate noise in the system while not contributing to any useful input (Equation 38). The DC level presented by background and cark current is commonly removed by utilizing AC coupling, but the white noise

generated from the DC component will still be present in the output. The dark current (I_d) has two components: surface current (I_{dsurf}) and bulk current (I_{dbulk}). The surface current is mostly innocuous at high gain factors since it is not amplified in the multiplication region. The bulk dark current component, however, is multiplied and remains significant. The dark current arises from the thermal generation of carriers from lattice defects and can be reduced by operating at lower temperatures. Typically the dark current is reduced by half for every ~15 K of temperature decrease.

The background photocurrent (I_{bg}) is not generated from within the photodiode as the dark current but affects generates shot noise in the same way. The background optical power (P_{bg}) comes chiefly from solar sources that illuminate the FOV of the receiver system, as discussed in Section 3.1.5.

Equation 38

$$I_d = I_{dsurf} + MI_{dbulk} \qquad [\ \text{A}\ ]$$
$$I_{bg} = MR(\lambda)P_{bg}(\lambda)$$

The total APD noise variance (σ^2_{total}), including signal, dark, and background currents and their contributions to the shot and excess noise is given in Equation 39. The independent noise sources add in quadrature (i.e. their powers, not amplitudes, are additive).

Equation 39

$$\sigma_{total}{}^2 = \sigma_s{}^2 + \sigma_T{}^2 = 2qM^2F_A\left(RP_r + I_d + I_{bg}\right)\Delta f + 4\left(\frac{k_BT}{R_L}\right)F_n\Delta f \qquad [\ \text{A}^2\ ]$$

The impulse response of an APD receiver depends on the transit time of photocarriers across the depletion region, the contribution of any slow diffusion carriers, the RC time constant of the diode and load, and the bandwidth of the following amplifier [176]. Operation at moderate gain and good alignment with suppression of diffusion driven carriers makes the last two factors dominate the impulse response.

3.7.7. Transimpedance Amplifiers

As shown in Figure 36, an APD may be modeled in a circuit by a current source with a parallel capacitance. The small current from an APD must be pre-amplified by a low noise amplifier and, usually, converted into a voltage signal to drive following circuits. A straightforward but naive approach would be to convert the APD current to a voltage simply by using a load resistor. By Ohm's law, a larger voltage drop will occur across the terminals for a larger valued resistor under the constraint of constant current. This concept, known as a high-impedance front end, has the advantage of relatively low current noise (Equation 8) but since the bandwidth of the electronic front end is determined by the RC time constant of the APD capacitance and load resistor, GHz bandwidth with high sensitivity is almost never achieved in this way.

A transimpedance amplifier (TIA) seeks a compromise between high gain, high bandwidth, and low noise. It is commonly used in lightwave communications and

LADAR receivers. A basic implementation of a TIA is an op-amp*, with a single current-driven input into the inverting terminal, and the output fed back into the inverting terminal through a resistor. The non-inverting input is grounded. This circuit topology makes use of the virtual ground behavior of op amps to essentially present very low load impedance to the APD so that the RC time constant becomes very small. Thought of another way, the TIA is a virtual short to ground, and the voltage swing on the capacitor is very small [177]. The transimpedance gain comes from the feedback resistor. The noise is also dominated by the relatively high resistance feedback. Additional noise is contributed by the op amp's noise figure, which is a multiplicative factor (F_n) in calculations such as Equation 41.

Often, TIAs are designed for AC coupled, 50 Ω outputs. Adding a second stage of gain using an IF band amplifier is useful to overcome the input noise of a digitizer or following electronics. It is important to note that AC coupling necessarily means zero average voltage over a comparatively long interval. The positive (or negative) pulses on the front end will have some degree of negative (positive) voltage swing following the pulse on the output side of the AC coupled output. The voltage swing will be shallow and long for a low cutoff frequency on the low side (e.g. 100 kHz), or deep and short for a comparatively higher low cutoff frequency (e.g. 10 MHz).

* Some other techniques such as ones based on Current Feedback Amplifiers are also used (as a current dual to the conventional op-amp, a Voltage Feedback Amplifier).

Bandwidth, transimpedance gain, and input-referred noise current are the most important TIA parameters concerning LADAR receivers. Usually these parameters will depend on the input capacitance from the APD itself, so calculations should assume a value for APD junction and stray capacitance. Bandwidth and gain are subject to a trade-off. The input referred current noise is the noise of the amplifier (thermal noise multiplied by a noise factor) expressed as an equivalent input current. This virtual current source reflects internal noise sources at the input and is a typical point of reference when evaluating TIA noise. Figure 37 is a general representation of a direct detection front end with several noise sources: background radiation, dark current, and input-referred amplifier noise (I_T with zero mean and variance σ_T^2). Amplifier noise with multiplicative factor F_n is included in the input-referred amplifier noise current (Equation 40).

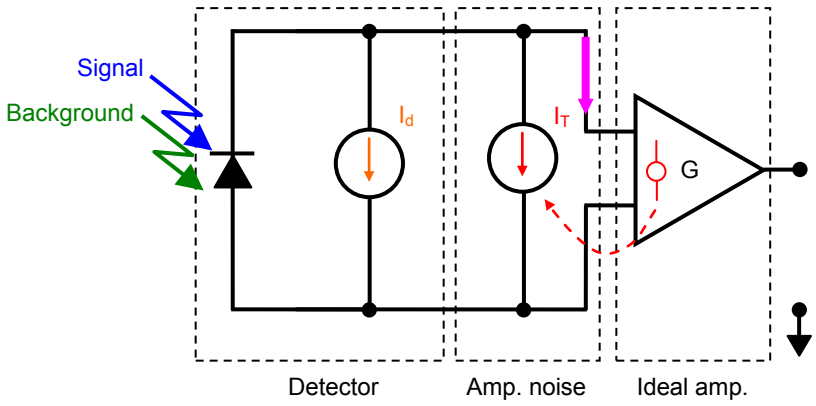

Figure 37: Photoreceiver AC-equivalent front end and noise sources

Equation 40

$$\sigma_T^{\,2} = \left\langle i_T^{\,2}(t) \right\rangle = F_n \left(\frac{4k_B T}{R_L} \right) \Delta f \quad [\ \mathrm{A}^2\ ]$$

3.7.8. Optimization of SNR with an APD

Using an APD in lieu of a p-i-n photodiode increases the sensitivity of a receiver only in certain conditions, and in those conditions only a particular gain value optimizes the SNR of the system. Equation 41 approximates the SNR of an APD based receiver, including noise contributions from shot noise, excess noise, and thermal noise, using the symbols explained earlier. The avalanche gain term, M, is squared in the numerator but is only present in one term of the denominator to equal degree. The consequence of this is that as long as the first noise term (representing shot noise from the signal and dark current) remains small relative to the second noise term in the denominator (representing thermal and amplifier noise) the overall SNR can be enhanced by the M^2 term in the numerator. This is usually true when the bandwidth of the system is large.

Equation 41

$$SNR = \frac{{I_{sig}}^2}{{\sigma_s}^2 + {\sigma_{therm}}^2} = \frac{\left(MRP_s\right)^2}{2qM^2F_A\left(RP_{sig} + I_d + I_{bg}\right)\Delta f + 4\left(\frac{k_BT}{R_L}\right)F_n\Delta f} \quad [\text{ dimensionless }]$$

The value of M that maximizes the SNR is thus dependent upon a number of factors, including the thermal noise spectral density and bandwidth, excess noise factor, dark current, and signal power. LADAR signal power fluctuates wildly for different target types and ranges. Therefore, the gain must be adjusted to typical conditions with the

understanding that the SNR is only maximized at some optical power levels and compromised at others.

Figure 38 plots the SNR for LADAR returns at 100 m and 200 m range using parameters of a commercially available InGaAs APD. The thermal spectral noise density is 11 pA / $Hz^{1/2}$, with an ionization ratio of 0.02 and 0.65 μA dark current (at $M = 10$). Other parameters used were typical of Spectral LADAR, 20 W peak per band, 74 mm aperture, and a target reflectivity of 0.60. The dashed lines in the figure indicate the SNR-maximized avalanche gain.

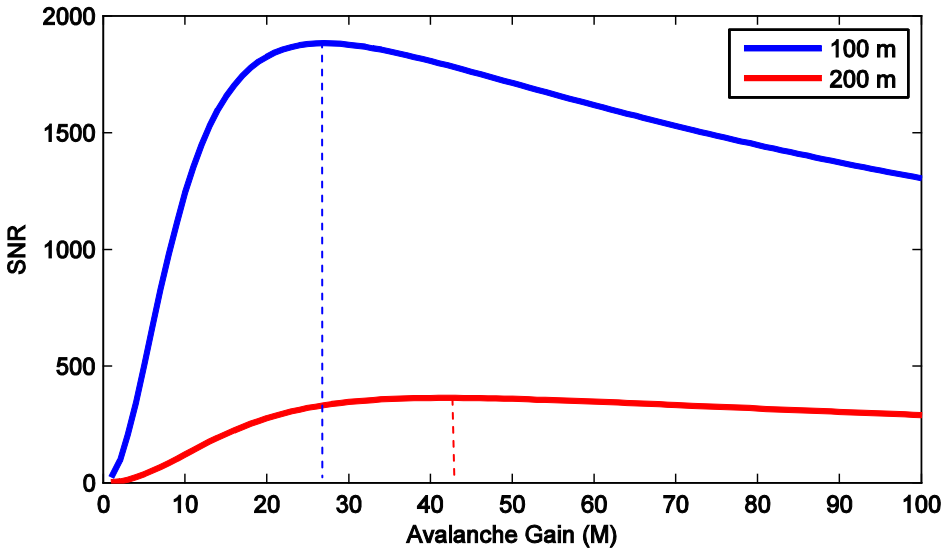

Figure 38: APD SNR versus avalanche gain

The curves of Figure 38 show the typical behavior of a steep increase in SNR followed by a relatively gentle fall off. The optimum gain for the target at 100 m range is about 27, while that of the target at 200 m is about 42. Increasing the thermal noise will shift

the peaks towards higher gain, while increasing the dark current or ionization ratio will shift the optimal gain towards lower values.

When the optimal SNR determined in a plot like Figure 38 is greater than unity, an APD makes an optical receiver system more sensitive versus a p-i-n photodiode. For the most part, the GHz to multi-GHz electronic bandwidths of contemporary LADAR result in front ends with high thermal noise making APDs justified, especially when the ionization coefficient of the APD is low. Systems needing large active areas or high bandwidth require small front-end resistances,* which leads to high thermal noise current. For systems with sufficiently low thermal noise, an APD will hurt performance. APDs also have hidden performance penalties difficult to express in analytic terms. The dark current of APDs tends to be higher per unit active area than that of p-i-n structures owing to the more complicated and numerous layers of the APD. Multiplication regions can be leaky in themselves. Also, APDs require a high voltage supply that could contribute noise into the system or fluctuate in a way that affects the device performance. These additional measures make APD based systems less stable and harder to calibrate on a radiometric basis. Finally, APDs are more expensive, especially when fabricated in monolithic array forms. Breakdown voltage (and, consequently gain) can fluctuate across an array leading to uniformity issues. Finally, it is commonly observed that APDs are more prone to failure when compared to p-i-n diodes.

* The front-end resistance is the effective impedance of the TIA input, which is determined by the op-amp gain and feedback resistor.

InGaAs APDs are suitable for Spectral LADAR due to their high sensitivity from 0.9μm to 1.7 μm. With different substrate choices the short wavelength limit can be extended well into the visible spectrum, and with strained absorption layers the long wavelength limit can be stretched beyond 2 μm with some compromise in dark current levels. InGaAs / InP technology has benefited from years of telecommunications industry investment since the material system has high responsivity at 1.31 μm and 1.55 μm, which correspond to the minimum dispersion and minimum absorption wavelengths of single mode silica fibers, respectively.

3.8. Spectroscopic Instruments

An essential part of the receiver is the dispersive element which separates the panchromatic signal into a number of time-resolved wavelength bands. This part of the system is often the component with the highest insertion loss, making proper design crucial to the operation of the system.

When a spectrometer tunes to one small range of wavelengths at a given time it is often referred to as a monochromator. If capable of simultaneous read-out of a number of wavelength resolution bands, the term spectrograph is often used. There are many techniques for spectroscopic instrumentation, each having particular advantages and disadvantages relative to a given application. One of the distinguishing characteristics of a spectrometer for Spectral LADAR is that the spectral resolution requirement is

relatively modest when compared to other common applications. Identification of typical terrain and objects can be adequately sampled with resolution in the tens of nanometers, whereas many other spectroscopic studies require resolution at fractions of nanometers.

While not demanding in a resolution sense, the high temporal bandwidth and circular detector aperture geometry* sets this instrument apart from the majority of spectral sensing devices. Relatively small area detectors must be used since this benefits electrical bandwidth and reduces dark current. This contrasts with most commercially available spectrometers, which use high aspect ratio CCD linear arrays with detector integration time on the order of 1 ms, 10^6 times too long for LADAR. Consequently, this imposes unusual requirements on imaging aspects of the spectrometer. The imaging system must have close to diffraction limited point spread function (PSF) over its optical bandwidth so that oversized detectors are unnecessary. Circular detector apertures require low astigmatism, in contrast to slit-like detector apertures in common spectrometers.

Low insertion loss is a positive attribute in any application, but the extremely low signal levels (and wide bandwidths) in active remote sensing make high throughput spectroscopy a very imposing requirement for Spectral LADAR.

---

* Circular detectors, and therefore exit slits, are necessary when using APDs to minimize the effect of fringing fields that could induce localized breakdown at small radii corners and lower the maximum gain of the detector as a whole.

Finally, the spectrometer system must have adequate free spectral range (FSR), the spectral separation between unambiguously resolved wavelengths, to cover the optical bandwidth of interest. The need for large FSR effectively rules out the use of Fabry-Perot Etalon spectrometers, which have high resolution but poor FSR, usually requiring extensive filtering to avoid ambiguities.

For LADAR, it is necessary to measure all wavelength components of a single pulse with a spectrograph type device. This multiplex capability is usually more expensive and difficult to implement than tunable monochromator-like devices, often due to the requirement of imaging over a large field and the need for a detector array.

Although spectrographic operation is needed in a practical system, it is not needed for a proof of concept demonstration that makes some sacrifices in pixel rate for considerable cost savings and complexity reduction. A rapidly tunable monochromator may use segments of several pulses to build up a complete spectrum (i.e., quasi-single-pulse operation) that has the same detection statistics of a single-pulse spectrograph. Of the various spectrometer varieties, an ideal technique will support tunable operation while also having straightforward adaptability to a multiplex configuration.

3.8.1. Alternatives

Several spectrometer types were considered, including fiber dispersion, waveguide FTIR, lateral FTIR, acousto-optic, liquid crystal, diffraction grating, and prism.

3.8.1.1. Liquid Crystal Tunable Filters

Liquid crystal tunable filters (LCTF) are essentially Lyot filters using liquid crystals as dynamically birefringent elements. Unlike a diffraction grating or prism which disperses a wave in angle, a LCTF absorbs all but a small range of wavelengths. Thus, a LCTF is not an inherently parallel architecture, though their structure makes their integration in optical systems relatively straightforward, comparable to interference filters. Unfortunately, these devices have high polarization sensitivity. LCTFs are commercially available at SWIR wavelengths for microscopy applications [178]. Perhaps the most disqualifying property of LCTFs is their slow tuning times, which can be up to 150 ms at room temperatures, which is comparable to mechanical tuning of grating instruments. The disadvantages of LCTFs outweigh relatively few substantial advantages for this application.

3.8.1.2. Fiber Dispersion

One compelling spectroscopic technique is to use the dispersive properties of optical waveguides to create a time to wavelength mapping of a short optical pulse. If a very short optical pulse propagates in a dispersive medium or waveguide, the dispersion

properties can transform the shape of the pulse to represent the constituent spectral content as a time waveform that is much longer than that of the undispersed pulse. Consider two transform limited pulses of different mean frequencies simultaneously launched into a single mode fiber with engineered dispersive properties. If the dispersion (ps km^{-1} nm^{-1}) as a function of frequency and propagation distance are chosen properly, the two pulses will arrive at the distal end of the fiber with a delay that is associated with a particular mean frequency difference. This technique has been demonstrated for gas optical absorption analysis [179]. The advantage of this technique is that it can be very compact and inexpensive since only a length of fiber and a single detector are necessary. Unfortunately, the electronic bandwidth of the detector will be increased, along with a trade-off between spectral and spatial (longitudinal) resolution. Moreover, coupling the received light into a single mode fiber is likely to be inefficient due to the speckle phenomenon.

3.8.1.3. Fourier Transform Infrared (FTIR)

Fourier transform infrared (FTIR) spectrometers utilize the interference of waves to measure spectra [180, 181]. FTIR spectrometers typically consist of a Michelson type interferometer* with a movable mirror, fixed mirror and a single detector element. As the movable mirror is translated longitudinally, a sinusoidal interference pattern will appear if the input to the spectrometer is a single frequency (temporally coherent). If another spectral line is simultaneously present, it too will create another sinusoidally varying

* Specifically, a Twyman-Green variation where plane waves are used

interference pattern at the detector with another spatial frequency. The interference patterns from all components form a superposition at the detector, and the spatial pattern sampled by displacements of the moving mirror is known as an interferogram. The key idea behind FTIR is that the interferogram and spectral intensity form a Fourier transform pair. FTIR systems are common equipment in chemistry labs since they possess high spectral resolution and high spectral range. The resolution and long wavelength limit of this spectrometer are determined by the maximum scan displacement while the short wavelength limit is determined by the Nyquist sampling criteria of the spatial interference pattern. FTIR systems are also preferred because they have a favorable étendue-resolution trade off (Jacquinot advantage) and the multiplex (Felgett) advantage. The multiplex advantage over monochromator type spectrometers since all of the input power is used over the entire integration time, versus a monochromator which blocks most of the input energy at a given time. This advantage, however, does not confer any benefit to a Spectral LADAR an application. Classical FTIR instruments are not suitable for single pulse spectroscopy since they require mechanical scanning, which would necessarily be much longer than the pulse duration. An FTIR instrument that could simultaneously measure interference patterns at all displacement points could be a solution. Recently, some parallel (or stationary) FTIR approaches have been discussed in the literature. Winters et al. have reported on their split-mirror FTIR configuration that overlaps two beams laterally to produce an interference pattern that could be sampled by a linear detector array [182]. The disadvantage of this approach is the high spatial coherence required, which limits the light collection of the system. Le Coarer et al. have disused a stationary wave FTIR concept where the interference pattern is created by

counterpropagating waves in a waveguide [183]. The longitudinal interference pattern is sampled along the length of the waveguide via collection of energy from the evanescent field. This technique could be useful if sensitivity issues are addressed. Low coupling efficiencies from speckled backreflections into a single mode waveguide could limit efficiency [184, 185].

3.8.1.4. Acousto-Optic Diffraction

Acousto-optic devices involve the interaction of an acoustic wave with an electromagnetic wave at optical frequencies in a medium. The acoustic wave is usually produced by a piezoelectric crystal coupled to an optically transparent medium. Fundamentally, an acousto-optic tunable filter is very similar to a diffractive phase-type grating since the acoustic wave sets up a periodic modulation of refractive index from the compression and rarefaction of the acoustic medium. Unlike a grating, the acousto-optic cell (or Bragg cell, in contrast to operation of an acousto-optic cell in the Raman-Nath regime) imparts a small frequency shift of the acoustic frequency to conserve momentum in the photon-phonon interaction since the grating is usually a propagating wave. This frequency shift, typically in the MHz range, is insignificant in Spectral LADAR applications. The advantages of this technique are that the grating period can be dynamically adjusted to suit different situations and target types. For a laboratory demonstrator, the tuning time can be very fast, approximately the transit time of the acoustic wave through the beam diameter. The downside of this technique is that it is much more difficult to construct and operate than a plane grating. The frequency drift and EMI generated by the RF oscillator and amplifier can be troublesome and distort

measurements. Since a Spectral LADAR with objective level performance will use a linear or 2D array detector which does not need rapid tuning, the advantages of an acousto-optic spectrometer are unlikely to outweigh the disadvantages and cost of its development.

3.8.1.5. Prism

A prism is a compelling option for Spectral LADAR systems despite a long decline in use in common laboratory spectroscopy. Prism spectrometers are relatively rarely used for spectroscopy in the classic sense since, for the most part, they are trumped by grating and FTIR equipment [186]. The étendue and resolution capabilities are usually inferior to grating and FTIR counterparts (Section 3.8.13). The requirements of Spectral LADAR, especially the modest resolution requirements, are such that prisms are a viable, and perhaps superior, choice. Their key advantage is a very large FSR. Prism spectrometers do not suffer from aliasing problems, and their FSR spans the useful transparency region of the prism material. With the proper coatings their efficiency can be very high, and all input light at a particular frequency has one and only one exit vector (no multiple orders). Because the refractive index of the prism material is not linear over a wide spectral range ($dn / d\lambda$ not constant), calibration can be more challenging than the calibration of a grating spectrometer where the grating period is uniform and known to a high degree of precision.

3.8.2. Diffraction Grating

Diffraction gratings are the dispersive element of choice for this application due to their highly efficient operation, relative polarization insensitivity, applicability to both tuned and spectrograph implementations, and fast tuning time. The following sections describe the theory, operation, and applicability to Spectral LADAR.

Diffraction gratings have a periodic structure comparable to the wavelength of incident radiation. They work on the combined principle of multiple-slit interference and diffraction. Several types exist, classified by their modulation (phase or intensity) and optical operation (reflective or transmissive). Optical properties vary among the varieties. Phase gratings have higher efficiency than intensity modulated gratings, and transmission gratings tend to be less polarization sensitive than their reflective counterparts. Various groove phase profiles are useful, among which sinusoidal and triangular (blazed) are most common. Monochromatic radiation incident on a grating is divided into numerous diffractive orders (… -2, -1, 0 1, 2 …) according to the grating equation (Equation 42).

Equation 42

$$\frac{m\lambda}{d} = \left(\sin\alpha + \sin\beta\right) \quad [\ \text{dimensionless}\ ]$$

Given:

m = Diffractive order

d = Grating period [m]

α = Incident angle [radians]

β = Exit angle [radians]

Angles α and β are measured from the grating surface normal in the plane perpendicular to the grooves. Diffractive orders occur when the conditions for constructive interference are satisfied. This is evident in the simple geometric construction used to arrive at Equation 42. Over the grating period d, the $d \sin \alpha$ and $d \sin \beta$ are the optical path differences at the incident and transmitted angles, respectively. These must add up to an integral number of wavelengths to interfere constructively in the far field where m is the order of the interference, the number of integral wavelengths shifted. Importantly, diffractive orders can only exist when $m\lambda/2d \leq 1$, i.e., when λ is no more than twice the grating period. Only a finite number of diffractive orders may exist.

Of the various subtypes, blazed reflective phase gratings are highly efficient at dispersing light into one spectral order, and thus are suitable for Spectral LADAR. Gratings can be etched on planar or curved surfaces. Planar gratings were chosen due to their commercial availability in a wide number of groove frequencies and for image quality. Figure 39 depicts the geometry of a blazed reflective phase grating. The common sign convention establishes positive diffractive orders to be on the same side of the grating normal as the incident beam, while negative orders are on the opposite side.

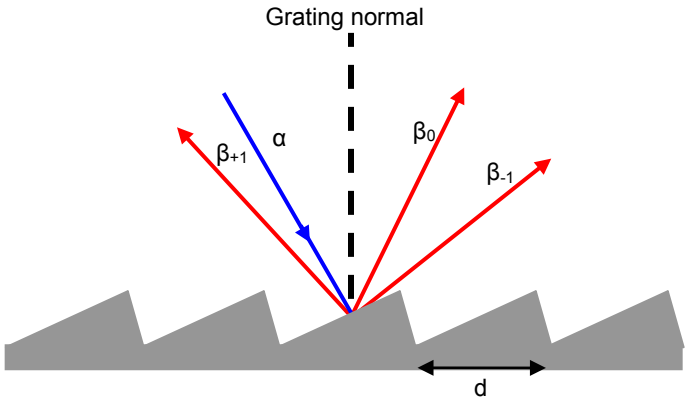

Figure 39: Blazed planar reflective phase grating

In most applications, the incident beam lies in a plane perpendicular to the direction of the grooves. This is a favorable situation known as planar (classical) diffraction since all diffracted orders at all wavelengths and the incident beam will be mutually coplanar. When the incident beam is not in a plane perpendicular to the grooves, conical diffraction results where the diffracted light lies along the outer surface of a cone. This poses difficulties, since the smile-like bending of the diffracted spectrum is hard to couple to a linear array or single pixel with grating rotation.

The polarization of the incident radiation is often important. When describing reflection and transmission of waves at isotropic boundaries the geometry is referenced to a plane of incidence which contains the incident, transmitted, and reflected beams. In this case, two polarization modes refer to this plane: TE (S-plane), where the E-field is perpendicular to the plane of incidence, and TM (P-plane) where the E-field is parallel to the plane of incidence. When considering diffraction from a grating, the presence of grooves at the interface break the symmetry of this situation, polarization may be

referenced to the direction of the grooves instead of the plane of incidence. In the usual case of classical diffraction (plane of incidence perpendicular to the grooves) the TE mode is said to have the E-field polarized parallel to the groves, but instead is referred as p-plane polarization, while the TM mode is referred to as s-plane polarization in contrast to incidence on isotropic surfaces* [187]. Polarization can be very significant when estimating and measuring the diffraction efficiency of gratings and also plays a role in the stability of the Spectral LADAR system.

3.8.3. Grating Mounts

A grating "mount" refers to the overall geometry of the optical system that contains an entrance slit to accept incoming light and an exit slit or array of exit slits that transmit or transduce the dispersed beam. There are many different mounts used in practice. The Littrow, or autocollimated, mount is often used as the standard for measuring the properties of gratings since the resolution and efficiency depend on the mount configuration. A true Littrow mount ($\alpha = \beta$) has the exit slit coincident with the entrance slit and is often used as the tuning element in tunable lasers. Operating a grating in the Littrow configuration or near-Littrow (small deviation angle, $\alpha \approx \beta$) is preferred in applications that require high efficiency.

---

* This is the convention used by the Richardson Grating Handbook [187]

The Czerny-Turner mount (Figure 40) is another often used configuration and is used when the spectrometer is not reciprocal – where the exiting beam does not re-trace the path of the entering beam.

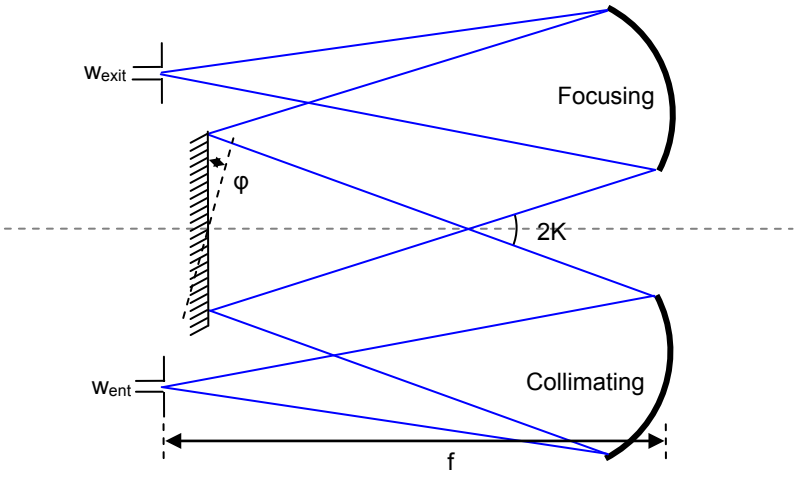

Figure 40: Czerny-Turner mount

It is often useful to re-formulate the angles α and β of Equation 42 in terms of the deviation angle (K) and the scan angle (φ) in the above figure. The terms w_{ent}, w_{exit}, and f are the full width of the entrance and exit slits and focal length (assumed symmetric), respectively. Using the sum to product of sinusoids trigonometric identity, Equation 42 is expressed in terms of the deviation (K) and scan (φ) angles which results in Equation 43.

Equation 43

$$\frac{m\lambda}{d} = 2\cos(K)\sin(\varphi) \quad [\text{ dimensionless }]$$

Where $K = ½(\alpha - \beta)$ and $\varphi = ½(\alpha + \beta)$. This expression now yields the tuned wavelength as a function of grating scan angle and deviation scan angle. Most systems operate at constant K and varied φ, the constant deviation configuration, or at varied K and constant φ, the constant scan configuration.

The choice of mount and optics plays a very large role in the efficiency and resolution of the system. A reflective collimating and focusing mirror is the common choice, as shown in the Czerny-Turner configuration of Figure 40. Reflective optics are free of chromatic aberration, which is significant for spectrometers since they operate over a wide spectral range. Most of the time, however, reflective optics must be used in off-axis fields which permit the other third order Seidel aberrations – coma, astigmatism, and field curvature to corrupt the image in the exit plane. Refractive optics can be used on axis, and though they may suffer from chromatic aberrations (axial and lateral color) they may offer improved performance if the off-axis aberrations are more difficult to control than chromatic aberrations. This can be true at low F/# where reflective optics must be used at high field angle.

3.8.4. Grating Dispersion

The dispersion of a grating (D) is the change in exit angle β with infinitesimal changes in wavelength at a constant entrance angle α (Equation 44). This dispersion relates only to

the angles and is independent of any focusing optics that transform dispersion angles to lateral distances in a focal plane.

Equation 44

$$D = \frac{d\beta}{d\lambda} = \frac{m}{d\cos\beta} = \frac{\sin\alpha + \sin\beta}{\lambda\cos\beta} \quad [\ \mathrm{m}^{-1}\ ]$$

The linear dispersion is the lateral variation of the focused beam with respect to wavelength in the focal plane. In the small angle approximation ($tan\ \theta \approx \theta$) which is usually observed, the linear dispersion is the product of the angular dispersion and the focal length of the focusing lens.

3.8.5. Free Spectral Range (FSR)

From Equation 42 it is clear that overlap can occur between spectral orders. In other words, a wavelength λ_1 in order $m = 1$ can exit the grating at the same angle and be imaged to the same point in the focal plane as a different wavelength λ_2 in order $m = 2$. The maximum optical bandwidth that can be imaged in the focal plane without overlapping with other orders (aliasing) is the FSR. This is a critical consideration for Spectral LADAR since exceeding the FSR can cross-correlate the bands and produce results that are hard, if not impossible, to interpret.

Solving the grating equation to find the FSR reveals that the FSR depends on the diffractive order, and is equal to λ / m. This restricts single-grating spectrometers to a maximum FSR of one octave in the first order, and significantly less in higher orders. In some cases crossed gratings can be used to separate ambiguous orders by diffraction in a perpendicular plane, with some loss of SNR. This solution is not likely to be acceptable for the low light levels of Spectral LADAR, and would be very difficult to implement in a "line-scan" LADAR system in which a 2D pixel array uses one axis for spectral dispersion, and an orthogonal axis for spatial scanning, leaving no degree of freedom for disambiguation of spectral orders. Thus, a grating spectrometer is a good solution for a one octave Spectral LADAR but for broader optical bandwidths another dispersion method or parallel grating spectrometers would have to be considered.

3.8.6. Optical Bandpass

The bandpass (B) of a spectrometer (Equation 45) refers to the spectral width of the exit slit considering the dispersion of the grating and the focal length of the focusing lens.

Equation 45

$$B = \frac{wd\cos\beta}{mf} \quad [\ \mathrm{m}\ ]$$

Bandpass is an important consideration for Spectral LADAR with a supercontinuum source since the power received per-band is proportional to the instrumental bandpass.

Thus, the bandpass influences both the resolution and the SNR of the instrument. A narrow bandpass will yield high spectral resolution but low band integrated power and low SNR, while it is clear that a wide bandpass will have low spectral resolution and high SNR. Striking the right balance is critical for optimizing performance.

3.8.7. Grating Efficiency

For a grating, efficiency is defined as the fraction of incident light redirected into the desired order. Equation 42 determines the angular positions of the diffracted orders given the periodicity of the grating, wavelength, and incident angle. The optical intensity for each order and fine spatial structure is determined by a multiple slit interference treatment. Blazing is often used in phase gratings to maximize power in a particular order by shifting the diffraction envelope maximum to coincide with an interference peak of the desired order at a particular wavelength. The blaze equation (Equation 46) defines the appropriate blaze angle θ_b (the facet normal relative to the grating normal) at which the diffraction peak corresponds to the interference solution of order m at the wavelength λ_b and grating period d.

Equation 46

$$\frac{m\lambda_b}{d} = \left(\sin\alpha + \sin\left(2\theta_b - \alpha\right)\right) \quad [\ \text{dimensionless}\ ]$$

It is interesting to note that when the grating is configured for on-blaze operation at a particular wavelength, the angles of incidence and reflection are equal and opposite relative to the normal of the groove facets. This would correspond to specular reflection from the facets *if* ray optics were to apply. The diffraction maximum corresponds to the conditions of ray optics where the far-field path difference is zero.

Gratings are polarization sensitive, and a complete description must involve a full vector electromagnetic wave calculation. In some situations, however, a scalar wave approximation is valid. This is especially true for TE polarizations where the electric field runs parallel to the grating grooves and does not see a periodic modulation in permittivity. Deviations from scalar wave theory in optical diffraction gratings are often referred to as anomalies and appear as sharp changes in grating efficiency. Anomalies may be categorized into two groups – Rayleigh anomalies and resonance anomalies. Rayleigh anomalies occur when the exit angle (β) of an order transition over the cutoff angle ($\pm \pi/2$). By conservation of energy, the incident radiation must equal the reflected radiation less any losses. The redistribution of energy among the remaining orders causes some abrupt changes in efficiency (a particular order). Resonance anomalies occur as a result of surface plasmon resonances in the periodic structure, and can cause substantial shifts in efficiency when light resonantly couples into the plasmon wave. For blazed gratings, there are several classes of blaze angle values that have common anomaly characteristics. Since Spectral LADAR has very modest requirements for resolution, and thus typically low groove frequencies, the blaze angles are often very low. Very low blaze angles, nominally from 0^o to 5^o, correspond to a region of very mild anomalies and

behavior that is well approximated by scalar wave theory and consequently independent of polarization.

3.8.8. Scalar Wave / Huygens-Fresnel Approximation

For gratings with relatively small blaze angles ($< 5^o$), the scalar wave approximation is a good representation of grating performance. The Huygens-Fresnel principle is an approximation of wave propagation, and a further approximation of scalar wave theory [188]. In this case a propagating wavefront may be computed based on a superposition of infinitesimal Huygens wavelet emitters. Integrating the coherent field of Huygens emitters with the amplitude and phase response imparted by the grating yields a solution for an arbitrary grating profile. For a blazed planar grating, the solution is a function containing the diffraction envelope of a single grating period multiplied by the "multiple-slit" interference pattern of many such periods over the extent of the grating.

Figure 41 is the result of such calculation, carried out for a grating with 150 groves / mm and a first-order blaze wavelength of 1.25 μm. The grating is illuminated and positioned on-blaze for 1.25 μm. It is clear that the blaze condition aligns the minima of the diffraction envelope with all but the intended interference order.

To show some of the fine interference pattern detail, the top plot spanning +/- 60^{o} has a grating diameter of 0.5 mm, while the inset diffraction-interference product is plotted with a more practical grating diameter of 50 mm.

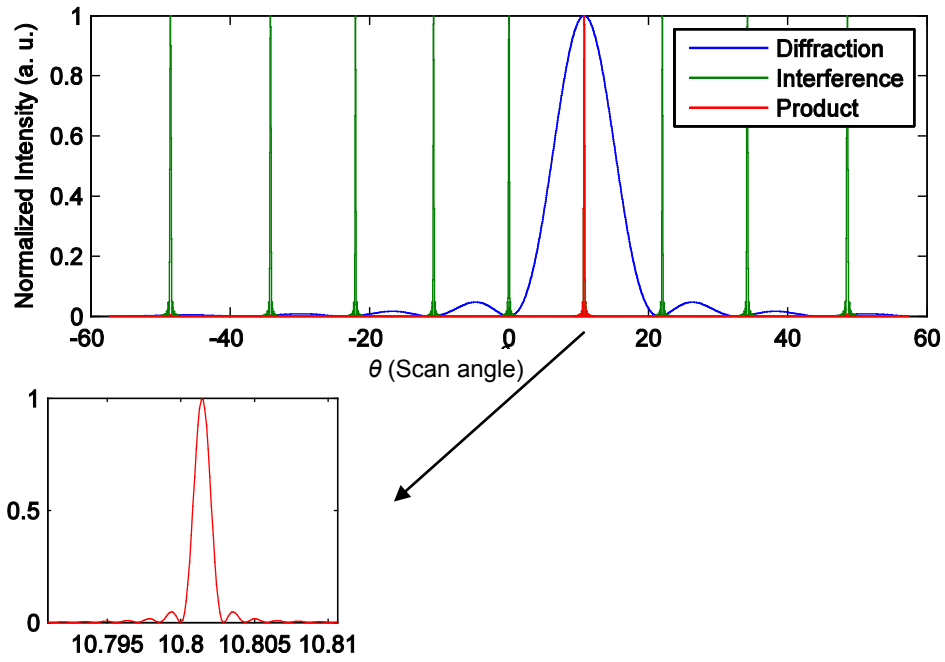

Figure 41: Blazed grating diffraction - interference plot

The inset image of Figure 41 shows a close-up of what may be called the spectral impulse-response (or linespread) of the grating itself. If significant compared to the lens impulse responses (PSFs) or exit / entrance slit dimensions, it must be included in the computations of Sections 3.8.11 and 3.8.12. Often, the spatial extents of the grating response are much smaller and the grating response may be approximated by a delta function.

The grating response may also be calculated using the principles of Fourier optics. This, in addition to Figure 41 makes it clear that it is the number of grating periods intersected by the beam that determines the grating resolving power, discussed next.

3.8.9. Resolving Power

Resolving power is a dimensionless number often used to describe the ability of a grating to disperse two closely spaced wavelengths.* It influences but does not specify resolution directly, since resolution also depends on the collimating and focusing properties of the spectrometer. The resolving power is a function of grating parameters alone. The key concept of the resolving power (Equation 47) is its dependence on the number of grooves illuminated (N_g), and not their pitch, profile, or period. The Rayleigh criterion is the standard for discerning resolvable peaks which must be no closer than the first minima of one airy function coinciding with the maxima of the other.

Equation 47

$$R = \frac{\lambda}{\Delta\lambda} = \frac{N_g d(\sin\alpha + \sin\beta)}{\lambda} = mN_g \quad [\text{ dimensionless }]$$

* This may be regarded as a poor terminology since it does not involve the definition of power in the classic sense (J / s).

3.8.10. Anamorphic Magnification

Gratings, even when planar, have anamorphic magnification which is evident from simple geometric analysis (Equation 48) where a and b are the incident and reflected beamwidths, respectively. With the exception of the zero order which obeys the law of specular reflection ($\alpha = -\beta$) and in Littrow mount ($\alpha = \beta$) all classically diffracted orders will experience some magnification only in the plane of diffraction.

Equation 48

$$\frac{b}{a} = \frac{\cos\beta}{\cos\alpha} \quad [\text{ dimensionless }]$$

Consistent with the conservation of radiance (brightness) and the Lagrange invariant, the decrease in beamwidth when $\beta > \alpha$ will produce an increased spot size in the diffraction plane at the exit slit, and the opposite when $\beta < \alpha$. A small deviation angle makes Equation 48 close to unity since K is the half difference of β and α.

3.8.11. Dispersed Image Formation

At a particular wavelength and for fixed parameters (e.g. K, φ), the imaging properties of grating spectrometers are approximately linear and spatially invariant. This allows for a convolution model of imaging to determine the image of the entrance slit in the exit slit plane (Equation 49) [189]. The initial image is the intensity distribution of the entrance

slit ($I_{entrance}$). The spatial impulse response (or kernel) of the imaging system is the mutual convolution of several imaging elements, including the collimating optic, focusing optic, and grating spatial response (G_{lens}, G_{lens}, $G_{grating}$, respectively). Scaling by the anamorphic magnification factor may be necessary if the ratio b / a is not close to unity. The grating spatial response can be found from the scalar wave approximation, and taken as the product of the diffraction and interference components in a *local* region around the desired order, assuming that the desired order is aligned to the vicinity of the exit slit. For gratings utilized at high resolving power, the spatial impulse response of the grating is likely well approximated by a delta function.

Equation 49

$$I_{exit}(x,y) = I_{entrance} \otimes \left[G_{lens} \otimes G_{lens} \otimes G_{grating} \right] \quad [\ \mathrm{W\ m^{-2}}\ ]$$

By integrating I_{exit} over the bounds of the exit slit or detector and normalizing to the integrated irradiance of the entrance slit, the insertion loss due to the imaging errors can be estimated. Insertion loss due to scattering at surfaces (AR coatings, grating losses) can be accounted for with the multiplication of scalar factors.

The convolution of the entrance slit and exit slit determines the instrumental broadening function (linespread*) if all else is negligible. With a large grating and diffraction limited lens performance, this is a reasonable approximation. The convolution of the slits has a

* Spectral impulse response

trapezoidal profile in one dimension across the diameter of the circle.* This trapezoid line spread function reaches a limiting case of a triangular profile if the slit widths (including the effects of anamorphic magnification) are exactly the same.

Most spectrometers are designed to have a triangular linespread function. This situation is typically favored since it maintains full throughput† and maximizes spectral resolution [190]. In cases where the exit slit is smaller than the entrance slit image, a spectra containing an infinitesimal spectral line will be broadened to a trapezoid with limited throughput. Conversely, using an exit slit wider than the image of the entrance slit will also result in a trapezoidal profile but will have full throughput. The resolution will be lower than the limiting case of a triangular linespread.

The third case is preferred in Spectral LADAR for several reasons that justify the loss of spectral resolution. First, a circular aperture wider in width is also wider in height. This allows for increased pixel coupling and tolerance of defocus as well as covering more area that would not be overlapped with adjacent circles of the same size (discussed further in Section 5.5.2). Second, the larger exit slit increases the orthogonality of adjacent bands since the band overlap may be reduced while keeping the sampling relatively uniform.

---

* In this one dimensional case, the convolution of two "top hat" functions

† Defined as the ratio of input spectral line power to maximum tuned output power

3.8.12. Spectrometer Resolution

The resolving power of a grating (Section 3.8.9) is useful in describing the dispersive capabilities of a grating itself, however the true spectral resolution is determined by the complete imaging system with which the grating is used. Resolution is often defined by the Rayleigh criterion, however this choice is somewhat arbitrary.

The actual resolution of the instrument is dependent upon the image quality of the system in addition to the grating dispersion, magnification, and slit widths. The final spectrum (S_{out}, Equation 50, with some notational liberties) scanned at the output is subject to the convolution of the entrance slit's image in the exit focal plane and the exit slit transmission function ($G_{exitslit}$). The scan angle variation is implicit in Equation 50.

Equation 50

$$S_{out}(\lambda) = S_{in}(\lambda) \otimes \int \left(I_{exit}(x,y) \otimes G_{exitslit}(x,y) \right) dy \quad [\ \text{W nm}^{-1}, \text{ qualitative }\ ]$$

Consider two spectral impulses (spectral lines) fed into the spectrometer. The convolution of the entrance slit, exit slit, and spatial impulse response of the lens system determines the spatial extent of the spectral impulses in the exit slit plane. The grating dispersion defines the separation of the centroids of the images. In the case of perfect geometric imaging, with a point source at the input imaged to a point in the exit slit plane, the optical bandpass (Equation 45) defines the resolution. To the extent that this imaging is not perfect, the resolution will be reduced. In this way, the optical bandpass sets a lower limit on the resolution. Since imperfect lens performance and alignment

affect resolution, it is important to measure resolution experimentally. The resolution of the spectrometer used in the laboratory demonstrator will be experimentally verified in Section 5.5.3.

3.8.13. Spectrometer Étendue

Since Section 3.8.12 noted that resolution depends on input slit width, it is important to consider the tradeoff of étendue (sometimes referred to as Luminosity [191]) to the resolution of a spectrometer. The optical bandpass limited resolution only occurs for a point source as the entrance slit, which has zero étendue.

The étendue of a spectrometer (Φ) is defined by the product of the slit area, solid angle subtended by the grating and/or lenses, and n^2, where n is the refractive index surrounding the system, usually assumed to be 1 [192]. For a spectrometer with a round entrance slit, and using the small angle approximation for the cone apex, solid angle, and numerical aperture (NA), Equation 51 results.

Equation 51

$$\Phi = \pi^2 \left(\frac{w_{ent}}{2} \right)^2 \left(\frac{D}{2f} \right)^2 = \pi^2 \left(\frac{w_{ent}}{2} \right)^2 (NA)^2 \quad [\ \mathrm{m^2\ sr}\ ]$$

A constant figure-of-merit for grating spectrometers is the étendue – resolving power product. Following a similar procedure used by James and Sternberg, the product can be found to be Equation 52, which has units of solid angle multiplied by area, as expected since resolving power is dimensionless [193].

Equation 52

$$\Phi R = \frac{\pi^2}{4}\left(\frac{\sin\alpha + \sin\beta}{\cos\beta}\right)D^2 \quad [\ \mathrm{m}^2\ \mathrm{sr}\ ]$$

Analysis by Moore, Davis, and Coplan which follows work by Jacquinot shows that the spectral Luminosity for a grating is often greater than that of a prism by a factor of 10 or more [194].

4. Loop-back Surrogate

Several experiments were conducted using a loop-back surrogate system prior to the construction of the laboratory demonstrator prototype discussed in Section 5. This surrogate simulated the transmission and reception of the supercontinuum pulse from a target at constant range from the sensor. The main goal of this testing was to establish the feasibility of components and measurement techniques to suit the purposes of the prototype apparatus. Additionally, the loop-back arrangement provided a means to test the control software, signal processing, and other components prior to obtaining all necessary materials for the laboratory demonstrator.

4.1. Spectral Stability

The magnitude and spectral dependence of fluctuations are both important factors when considering the effects of source stability on accurate reconstruction of target spectra. Figure 42 shows a panchromatic pulse in the time domain with some degree of intensity fluctuation. These fluctuations can arise from a large number of factors, including ambient temperature. Although the pump laser itself is temperature stabilized, there are other ways in which temperature can influence the coupling of the pump and the generation of the supercontinuum. Intensity fluctuations can be manifested in two ways.

The first, in the upper right hand corner of Figure 42, represents intensity fluctuations that affect the overall power but not the spectral shape since each wavelength maintains its proportionality. The second, in the lower right, represents polychromatic intensity fluctuations. The first case is easier to handle for two reasons: a single compensation coefficient can be computed from a panchromatic reference, and that the Spectral Angle Map transformation (SAM, discussed in Section 3.3) is inherently immune to proportional spectral shifts. Fluctuations containing variations of the second type require a compensation coefficient for each of *N* spectral bands.

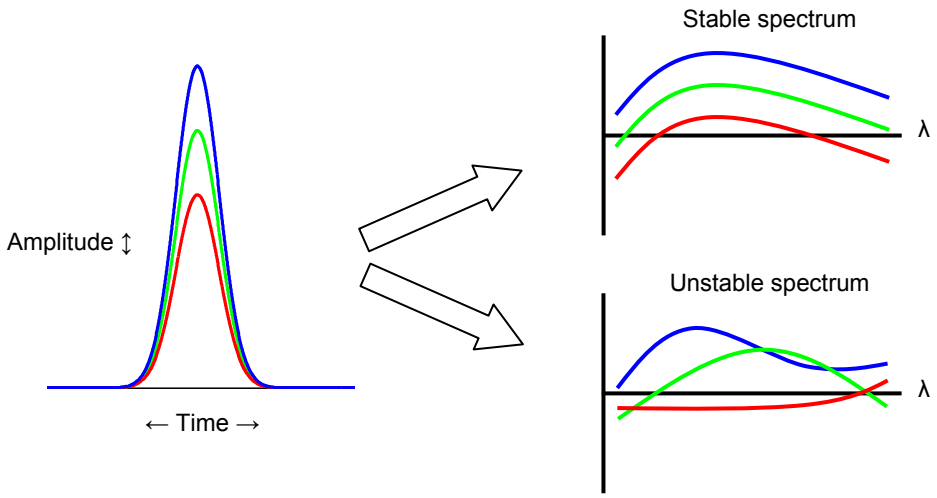

Figure 42: Types of instability

4.2. Layout and Construction

The layout of the loop-back system is shown in Figure 43. The supercontinuum is delivered from a non-polarization maintaining photonic crystal fiber (PCF) into a "Fiber

Bench" modular breadboard sold by Thorlabs (previously OFR). This compact unit has four ports; each coupling a free space beam to a fiber using identical aspheric lenses. The breadboard is configured with two beamsplitters and attenuators, which separate a fraction of the pulse energy, delay it through a fiber, and then recombine the time-shifted and attenuated pulses to an output fiber connected to a spectrometer. The delay and attenuation module works best when it is achromatic and polarization insensitive so it does not distort the spectrum of one pulse relative to the other or have some preferred polarization orientation.

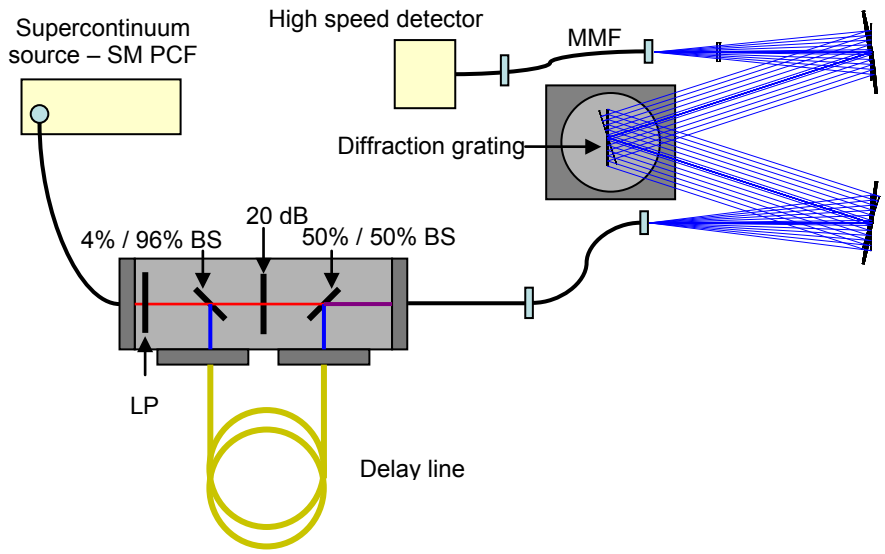

Figure 43: Loop-back test system (SM PCF: single mode photonic crystal fiber, MMF: multi mode fiber, LP: linear polarizer, BS: beamsplitter)

In Figure 43, the supercontinuum enters the delay and attenuation module and is collimated by an aspheric lens with a focal length of 11 mm. A linear polarizer may be included as the first element encountered by the beam so that all subsequent elements operate in a polarization state with stable orientation. The pulse is then split by a plate

with an AR coating on one side and the other side uncoated. The Fresnel reflection from the uncoated side makes for a spectrally flat beamsplitter with about a 4:96 ratio of reflected to transmitted optical power. The reflected light is coupled into the delay fiber to be reintroduced later. The transmitted light is attenuated by a 20 dB inconel metal neutral density (ND) filter. This attenuation reduces the transmitted light to about the same intensity as that diverted into the delay line. Following the attenuator, the two beams are recombined on a 50:50 beamsplitter that is coated on both sides. The beams are then coupled into the output fiber, with one having a delay equal to the propagation time in the delay fiber relative to the straight-through beam. The delay and attenuator module requires some focusing and alignment for low loss. In general, loss is not a problem since the source is relatively high power. Some dispersion from the single-glass aspheres creates spectrally variable coupling losses depending on fine focus. Other attenuators can be added following the second beamsplitter to reduce the optical power to within the linear range of a detector down the line. The delay and attenuation module is shown in Figure 44 with some components removed for clarity.

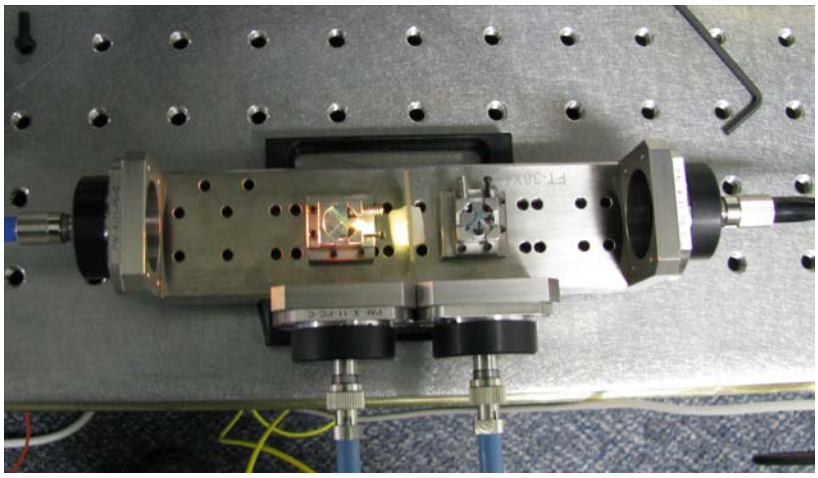

Figure 44: Delay and attenuator module

The output from the delay and attenuator module is coupled to a surrogate Czerny-Turner spectrometer using nearly all off-the-shelf components (Figure 45). The utilization of these components restricted the design space of the spectrometer. Specifically, an optical bandpass of 2 nm was implemented despite a preference for a wider bandpass. Also, some vignetting was unavoidable at the collimating mirror and grating. These components were somewhat smaller than the beam diameter at their respective points in the system. The setup and construction of this system paved the way for the spectrometer described in Section 5.5.

The optical fibers used in the delay and attenuator module varied depending on the testing goals, however the output of the spectrometer always utilized a standard Infinicor 300 fiber, a graded index 0.22 NA 62.5 μm core fiber. The distal end of this fiber was connected to either a power meter, New Focus 1647 APD receiver module (1.3 GHz bandwidth), or a 5 GHz bandwidth unamplified photodiode.

The smaller than desired optical bandpass of 2 nm divided the spectrum into 268 bands ranging from 1100 nm to 1600 nm, the high responsivity region of the photodiodes. The testing results show that this high level resolution presents the issues of grating motor precision, coherence driven instability, and low tolerance alignment that without adequate design precautions can be limiting factors in Spectral LADAR performance.

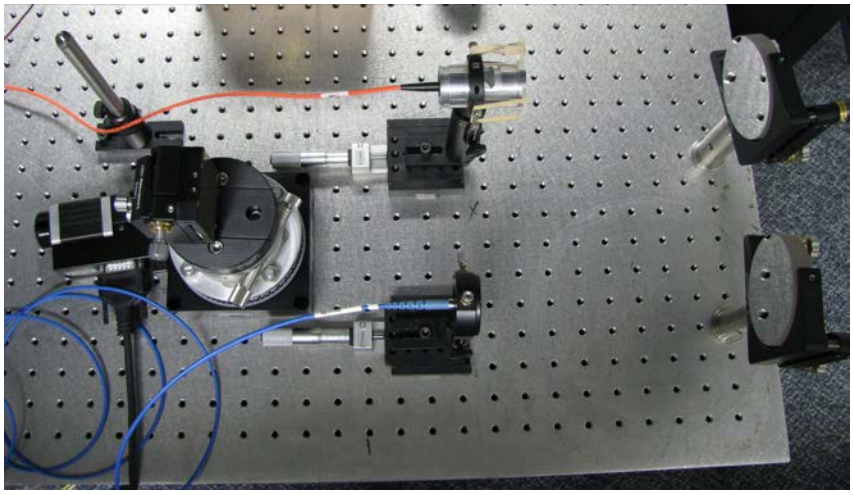

Figure 45: Surrogate Czerny-Turner spectrometer

4.3. Source Stability Tests

The spectral source pulse energy stability was typically measured as the ratio of two standard deviations from the mean (Equation 53), expressed as a percentage in each optical band (Λ_n). The mean and standard deviation were calculated with at least several hundred samples per band for robust statistics. Lower numbers reflect greater stability and small standard deviations with respect to the mean.

Equation 53

$$stb(\Lambda_n) = \frac{2\sigma(\Lambda_n)}{\mu(\Lambda_n)} * 100$$

The first measurements utilized standard multimode communications grade fiber for the delay line and connection between delay and attenuator and spectrometer. These initial tests demonstrate a stability value of about 8% to 30% without a consistent trend with respect to wavelength (Figure 46). The stability was practically unchanged by increasing the optical power and SNR by 10 dB at the receiver. Applying 100 sample averaging to the time domain waveform traces did not improve the stability by an appreciable amount. The polychromatic pulse stability was also measured, and at high receiver SNR the fluctuation was approximately 3.75%. This suggested a significant amount of second-type spectral fluctuation (discussed in Section 4.1), and that the fluctuation occurs on a timescale greater than that needed to acquire 100 samples for averaging.[*]

[*] i.e., the 100 samples over the time interval were highly correlated and not independent.

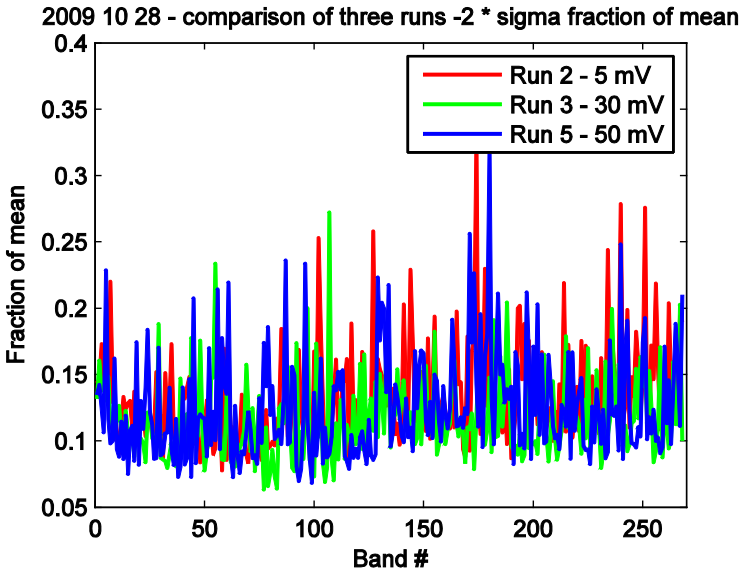

Figure 46: Initial stability tests with MMF (091028)[*]

To investigate further, tests were performed to assess any time dependent fluctuation behavior in one or a few spectral bands. Figure 47 shows the time evolution of several bands and the evidence of periodic variation. The periods were found to correspond to the HVAC unit in the laboratory switching on and off to regulate temperature. The fluctuations were less serious but still present to some degree with the HVAC unit disabled.

[*] Alphanumeric codes in figure captions are references to the data sets used to construct plots, or index codes for photographs.

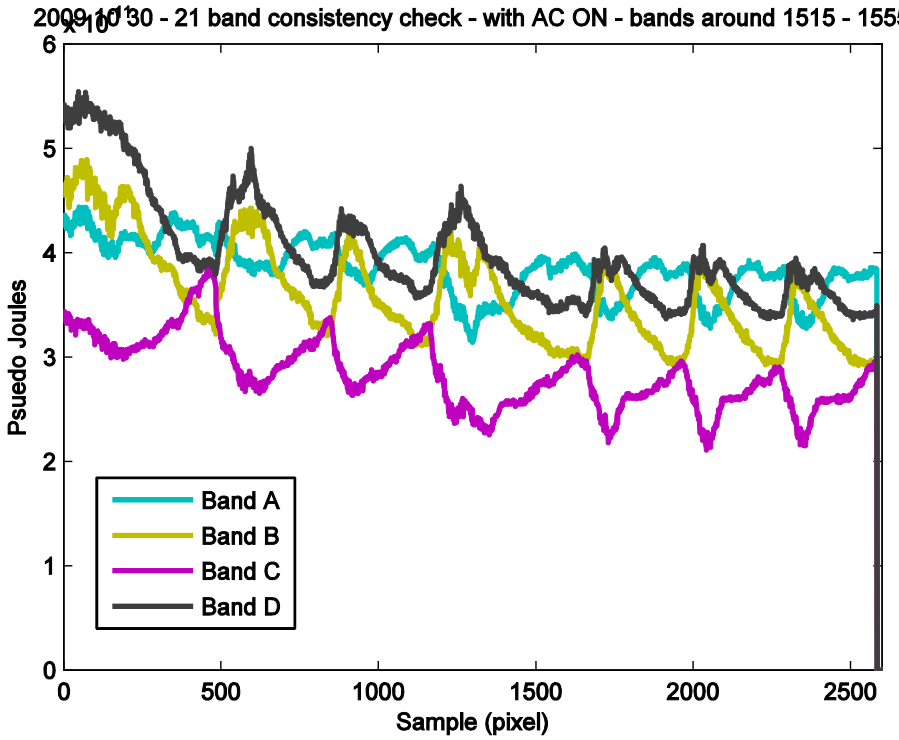

Figure 47: Time evolution of detected band energy (091031)

The fluctuations shown in Figure 47 would not be serious if it were not for the observations depicted in Figure 48. Thermal fluctuations could be compensated with a reference beam but only if the reference and signal beams experience exactly the same fluctuations. Figure 48 shows that the ratio of the delayed and straight through beam fluctuates with temperature. The variations are severe when the laboratory HVAC system is active (Figure 48a, left) but are still sufficiently severe to cause measurement distortions when the system is disabled (Figure 48b, right).

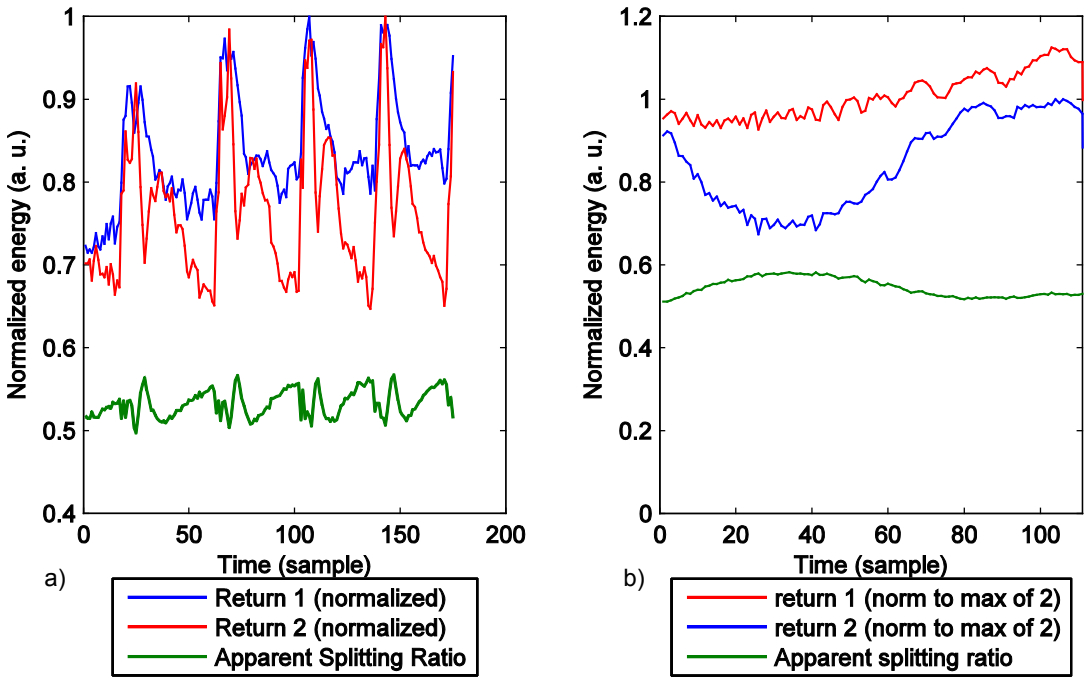

Figure 48: Time dynamics of splitting ratio with time waveform averaging (091104)

Solving this problem requires detailed consideration of how thermal variations affect the delayed and undelayed beams differently. At least two factors could cause significant variations in the beam splitting ratios.

The first is thermally induced changes in the beamsplitters. Although it is highly unlikely that small changes in temperature could affect the splitting ratio, the first beamsplitter has a higher polarization dependence than might be expected. The first beamsplitter is a Fresnel reflector at 45 degrees angle of incidence. The Fresnel equations for an uncoated glass surface show that the difference in reflectivity between TE and TM polarizations is about a factor of 10. Although polychromatic average power measurements of the supercontinuum source revealed a very limited degree of polarization, the large reflection polarization sensitivity coupled with small spectral bandwidth and other factors can make

this a significant effect. Unpolarized single mode fibers can maintain a high degree of polarization over several meters if a highly polarized source is launched into the fiber. The orientation of the polarization, however, is highly unstable.

The second possibility is modal interference. The speckle-like output from multimode fibers results from the interference of many modes with various propagation constants. The interference pattern is highly dependent on the fiber launch conditions and small perturbations in the bending and orientation of the fiber. The pattern can also be affected by thermal variations that effect the modal distribution. Propagation over several meters is not sufficient to achieve equilibrium modal distribution in many fibers. A beam delayed in multi-mode fiber will experience random interference which is not present in the undelayed (straight through) beam. Furthermore, the launch conditions of the delayed and undelayed beams into the output fiber are different. The effects of this may be small if the insertion loss of subsequent components is independent of a random modal pattern. This may be true when the total intensity of the beam is measured as an integration of the intensity of the entire wavefront. This is not the case in the surrogate spectrometer, where some apertures are overfilled. The vignetting that occurs at these surfaces effectively causes mode-dependent insertion loss. The modal distribution of multi-mode fibers is sensitive to many factors, including minute temperature changes.

To solve these problems, the multi-mode fiber for the delay and output lines was replaced with single-mode polarization maintaining fiber on the delay line, and single mode fiber (SMF-28) on the output. This configuration, combined with a linear polarizer as the first

element in the module, improved the overall stability, but some individual spectral bands were found to be much more unstable than others. Figure 49 shows that some improvement was realized by using normalization to the first return, compared to Figure 46. Variation of the splitting ratio was still apparent. The most significant improvement was realized when SM-PM fibers were used for both the delay and output lines. This is shown in Figure 50.

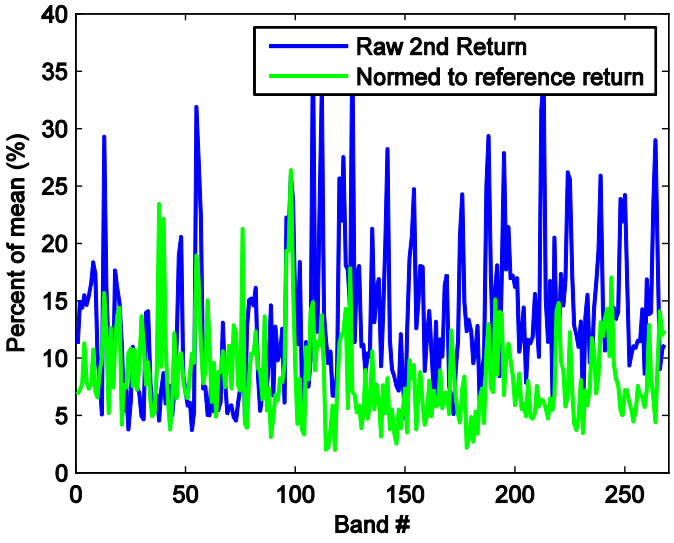

Figure 49: Stability results with SM-PM delay and SM output with time waveform averaging (091125)

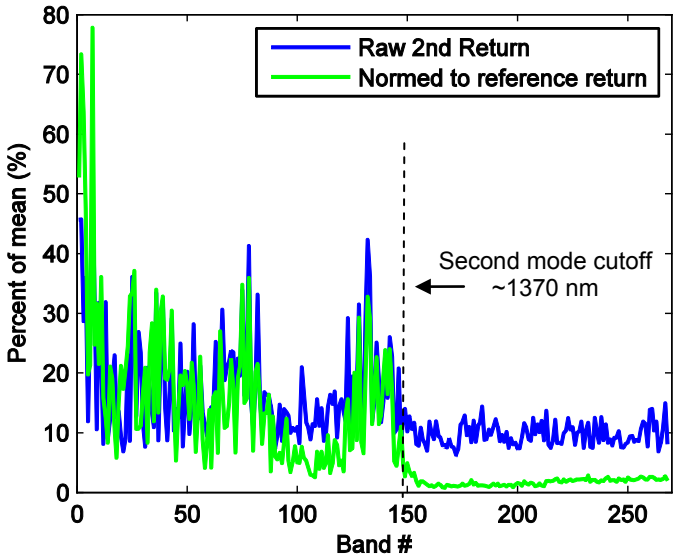

Figure 50: Stability results with all SM-PM fiber with time waveform averaging (091221)

Figure 50 demonstrates that the variations are significantly reduced at wavelengths beyond the second mode cutoff of the SM-PM fibers, which is at about 1370 nm. Operating in single mode with stable polarization orientation reduces thermally induced mode partitioning and polarization scrambling. The second return, normalized to the first return, shows a fractional stability metric (Equation 53) of only 1-2% at wavelengths propagated in a single mode. It is important to note that time waveform averaging was applied to look only at fluctuations at long time scales. Pulse-to-pulse fluctuations are effectively filtered by the averaging. These tests suggest that when multi-mode fiber propagation is necessary, vignetting and aperture occlusions should be avoided. It further suggests that the use of Schmidt-Cassegrain optics* in the laboratory demonstrator spectrometer (which is fed by a multi-mode fiber) is not likely to produce the best results.

* Schmidt-Cassegrain reflective optics have centrally occluded apertures

The spectrometer constructed for the laboratory demonstrator was also tested to see how spectral stability may behave with a larger 24 nm optical bandpass. Using the same configuration (SM-PM fiber) used to obtain Figure 50, the laboratory demonstrator spectrometer was used in lieu of the surrogate spectrometer to produce Figure 51.

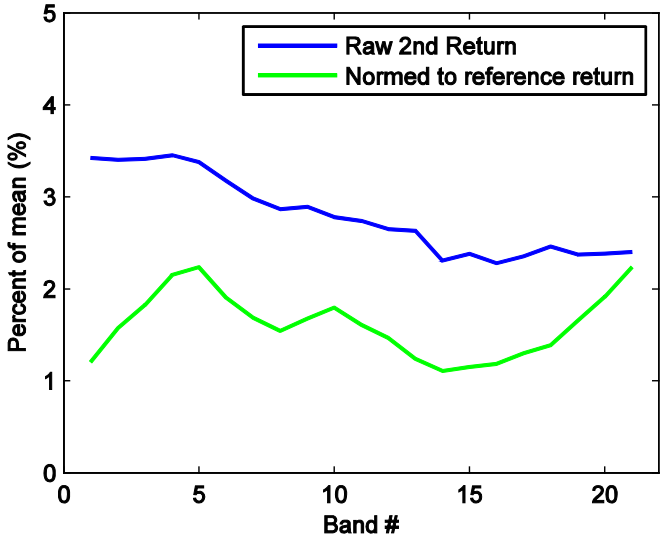

Figure 51: Stability with laboratory demonstrator spectrometer with time waveform averaging (100126)

In this situation, source compensation (normalization to the reference return) decreased the variation by over a factor of 2 in some cases. Also notable is the relatively even chromatic fluctuations (under averaging) that can be seen by looking at the time evolution of band energy (Figure 52), where the time waveforms were averaged to eliminate detector noise and pulse-to-pulse fluctuations. The periodic fluctuations evident here are believed to be from the pump laser intensity. As the system approaches thermal equilibrium, the period of the fluctuations gets longer.

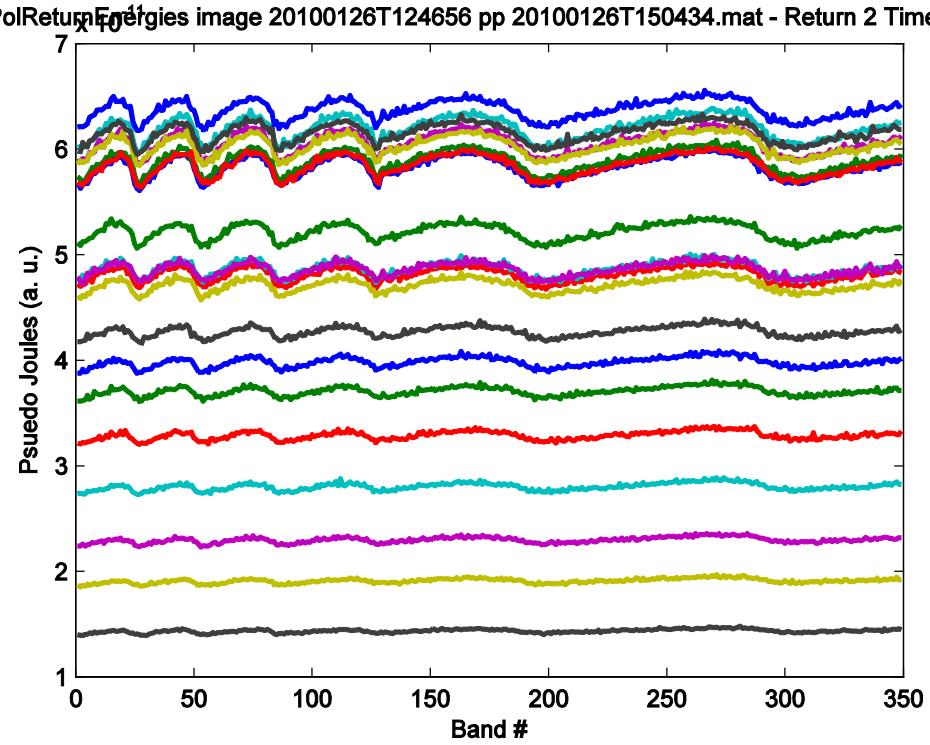

Figure 52: Band energy time evolution computed from time averaged waveforms (100126)

Stability analysis and source compensation are revisited in Section 7.1, in the context of actual measurements made of a remote target with the laboratory demonstrator.

5. Spectral LADAR Laboratory Demonstrator

An experimental approach was taken to evaluate the feasibility of Spectral LADAR where theoretical analysis is inadequate due to the unknown expanse of natural target signatures. The implementation of the Spectral LADAR concept with practical performance levels requires considerable funding and labor effort. The key cost and timeline driver is primarily the linear or two-dimensional detector array and corresponding read-out electronics. A full performance photoreceiver requires custom development of an InGaAs APD array, with appropriately designed microlenses, and hybridization (bonding) of that detector array to parallel pre-amplification and read-out electronics implemented in a custom ASIC*. At the time of this writing, the development and first-run cost of such custom components could easily exceed $1M USD and a year of development time. In addition, a fast scanning mechanism would also require substantial development of control electronics and optical components. Recognizing these economic barriers, a "Laboratory Demonstrator" prototype was developed, which functions in the same manner as a system with objective-level performance yet obviates the need for high cost components. Using off-the-shelf substitutes for the detector, read-out electronics, and optical scanner requires significant compromises in the pixel rate (and consequently frame rate) of the laboratory demonstrator, but allows the collection of true 3D spectral data from static scenes. The results from experimentation with this

* Application Specific Integrated Circuit

limited system refine the requirements and techniques for a Spectral LADAR with objective-level performance while reducing risk and justifying a larger follow-on development program.

The first point of technical compromise, lacking a linear or two dimensional receiver array, has very significant performance consequences and also some impact on the interpretation of the data recorded by the laboratory demonstrator. As discussed earlier, the defining concept for Spectral LADAR is the sensing of spectroscopic signatures with a single broad spectrum optical pulse. This usually requires a receiver with dispersion in the spatial domain and an array of optical detectors simultaneously covering the dispersed spectrum.* For the laboratory demonstrator a single detector element is used in lieu of an array, and a spectrometer is tuned to each of the optical bands in a time sequence. Consequently, the laboratory demonstrator does not implement *true* single-pulse spectroscopy in the strictest sense since it amalgamates spectral sections from several broad spectrum pulses, referred to as quasi-single-pulse spectroscopy. In a practical proof-of-concept sense, the tunable receiver records data equivalent to a single-pulse system since the SNR and pulse characteristics are identical in the two cases. In fact, evaluating the feasibility with a tuned-receiver system may yield an overly conservative estimate of performance compared to a true single-pulse system since pulse-to-pulse instabilities effect a tuned receiver in a more significant way. It is important to note that a tuned receiver system is effective at establishing technical feasibility of the Spectral LADAR technique while some tuned-transmitter systems would not be. A laboratory

* Dispersion in the temporal domain is also possible

demonstrator utilizing a tuned OPO* as a transmitter would not demonstrate that ample transmitted pulse spectral energy could be produced *simultaneously as a single pulse*. Using a supercontinuum source and a tuned receiver is a more effective demonstration since the fundamental technique is easily extensible by parallelization.† Although there are several ways to build a tunable receiver, utilizing a mechanically tuned grating in the laboratory demonstrator provides a straightforward path toward future full-performance systems by simply making the grating stationary and adding pixels in the exit focal plane.

The second compromise is the beam scanning mechanism. A LADAR that can image a wide iFOV with near-video frame rates (~ 24 FPS) requires a fast scanning mechanism (flying-spot or line scan) or an entirely parallel architecture (FLASH LADAR). The complexity of developing these or similar rapid scan architectures is deliberately avoided in favor of a straightforward solution – a large mirror in the object space of the lens. The gimbal mount is capable of a very wide scan angle, albeit at a relatively slow scan rate. Significant increases in the scan rate require the development of a low inertia beam scanner, possibly a line scan system, and a receiver lens well corrected for off-axis performance. All of these elements complicate the goal of demonstrating the feasibility of the technique and are left for later work. Moreover, the tuning time of the spectrometer dominates the pixel acquisition time and therefore makes high speed operation of the scanning system relatively moot.

---

* Optical Parametric Oscillator

† Extra pixels merely need to be added to the spectrometer, a straightforward extension when compared to a laboratory demonstrator using a tunable transmitter system.

The laboratory demonstrator was constructed with commercially available components to the extent possible. The custom designed subsystem components includes the lenses, mechanics, fixturing, and support electronics. The following sections discuss the technical characteristics and function of the system and its components.

5.1. System Function

The functional layout of the laboratory demonstrator system is depicted in Figure 53. The figure includes the most significant optical and electrical connections, but neglects electrical control, synchronization, power, and high voltage bias lines. Not shown is the electrical trigger from the supercontinuum source to the digitizer, as well as the Ethernet and RS-232 data / control connections from the computer system to the gimbal, rotation stage, digitizer, and high voltage supply.

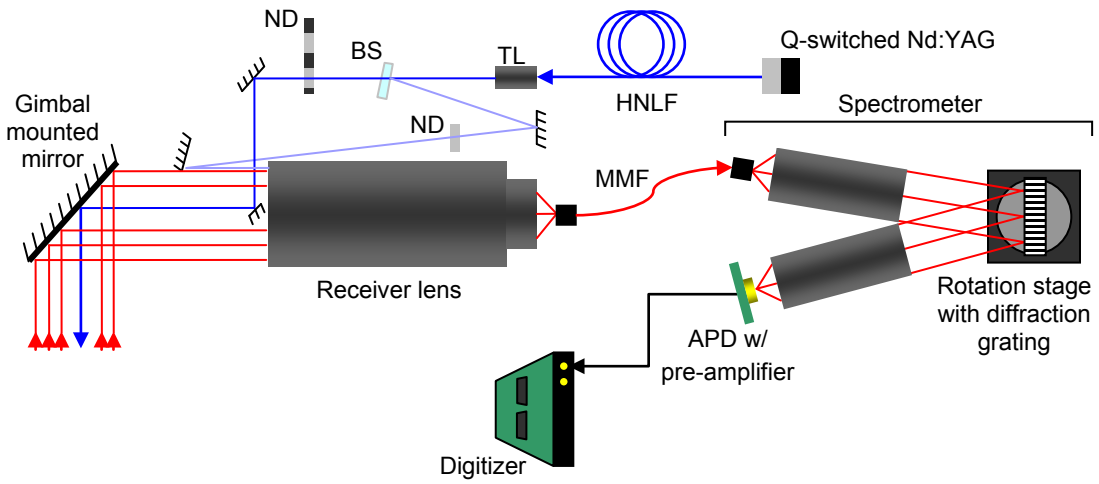

Figure 53: Functional layout of the laboratory demonstrator. (ND: neutral density filter, TL: transmitter lens, BS: beamsplitter, HNLF: highly nonlinear fiber, MMF: multi-mode fiber)

The Q-switched laser is the transmitter optical source and produces a 1 ns to 2 ns duration, high power optical pulse (1064 nm) at a repetition rate of about 20 kHz. An electrical synchronization signal sent to the digitizer serves as the t_0 reference for the time-of-flight measurement. The optical pulse is frequency broadened in the photonic crystal fiber that follows.

The fully developed supercontinuum is collimated by an achromatic doublet lens. The collimated beam is split by a 30 arcmin wedged silica glass beamsplitter with an AR coating on one side and an uncoated surface on the other for a splitting ratio of about 14 dB. The high power beam propagates forward as the transmitted beam, while the low power beam becomes the reference beam. The splitting angle of the reference beam is small to minimize polarization effects, which could become as strong as 10 dB at 45^{o}

incidence. Both the reference and transmitted beams are attenuated using variable inconel metal neutral density filters and absorbed by beam stops not shown in the figure.*

The reference beam is reflected from a pair of mirrors and is fed into and focused by the receiver lens into the receiver fiber. The transmitted beam reflects from a small, steerable mirror located on the axis of the receiver lens and propagates toward the beam steering mirror. Co-axial operation of the transmitter and receiver minimizes parallax error. A two-axis motorized gimbal steers the transmitted beam in a wide field of view. The instantaneous field of view (iFOV) of the system, defined by the lesser of the transmitter beam divergence and the receiver fiber core field of view in object space, is 1 mrad full angle.

The gimbal steers a 152 mm diameter silver coated mirror that reflects the beam toward the target in two axes with two stepper motors. The stepper motor phasing is controlled by a commercially available controller unit with a RS-232 interface. The step time for 0.5 mrad increments needed to place pixels in an adjacent grid was found to be 200 – 250 ms.

The transmitted beam reflects from the target, back onto the gimbaled mirror, and is focused onto the receiver fiber core by the receiver lens. The receiver lens is aligned to

---

* The transmitted beam attenuators are adjusted to fall within the linear range of the detector, depending on the range scale and reflectivity of the target. The reference beam attenuator is adjusted to have the highest SNR within the linear dynamic range of the receiver as well. The attenuation of metallic beamsplitters must always be verified experimentally as they are frequently out of published specification and vary with wavelength.

operate on axis, and the transmitted beam is aligned to coincide with the receiver axis. A 0.37 NA, 100 μm core fiber connects from the receiver lens to the spectrometer and photoreceiver subsystem. This fiber is technically unnecessary for the operation of the system but greatly simplifies the alignment, test, and calibration operation discussed in Section 5.10.4.

The spectrometer consists of two identical lenses, a collimating lens on the input side, and a focusing lens on the output side. Together they form a 1:1 relay system with a planar grating in the collimated (infinite conjugate) image space. Both lenses are used in the axial field, with the fiber core serving as the entrance slit for the spectrometer. The focusing lens images the spectrally dispersed optical pulse on an APD, which serves as the exit slit. Adjustments in the grating angle tune the exit slit (APD) to a particular optical band.

The APD is packaged in a windowed TO can and includes a transimpedance pre-amplifier, the MAX 3277. The combined unit is referred to as the photoreceiver module and is mounted to a small board, the receiver board, that includes electronic filtering and cable connectors.*

The digitizer is the acquisition board of an Agilent 54854A oscilloscope. Three channels are used, two for the differential mode signal from the receiver board, and one for the

---

* A modified version of the receiver board includes a second stage amplifier with modest gain (~17 dB) to elevate the output of the receiver module significantly above the EMI cable pickup and digitizer input port noise.

trigger (synchronization) signal from the laser source. All ports are configured for standard 50 Ω input impedance. The Agilent scope supports an SCPI command interface over Ethernet. A session of MATLAB connects to the oscilloscope data buffers using this interface over a gigabit Ethernet connection.

The control of the instrument components is coordinated by a set of MATLAB functions running on a Windows XP based PC. MATLAB directly controls the gimbal system, spectrometer rotation stage, and digitizer. The timing of the system components is orchestrated in software, with the exception of the digitizer trigger, which is synchronized to the laser.

Figure 54 and Figure 55 are photographs of the actual hardware assembly configured for imaging operations. Figure 54 depicts the transmitter and receiver assemblies. The optical path for the transmitter (blue) and reference (green) beams are indicated. The very small (3 mm x 3 mm) turning mirror that allows the transmitted beam to be coaxial with the receiver axis is suspended in the center of the receiver lens by two articulating rods. Figure 55 shows the spectrometer and photoreceiver components which are connected to the receiver lens by optical fiber. In these images the grating is mounted to a stage with adjustable pitch, roll and forward translation. The stage is mounted to a relatively large direct drive motor.

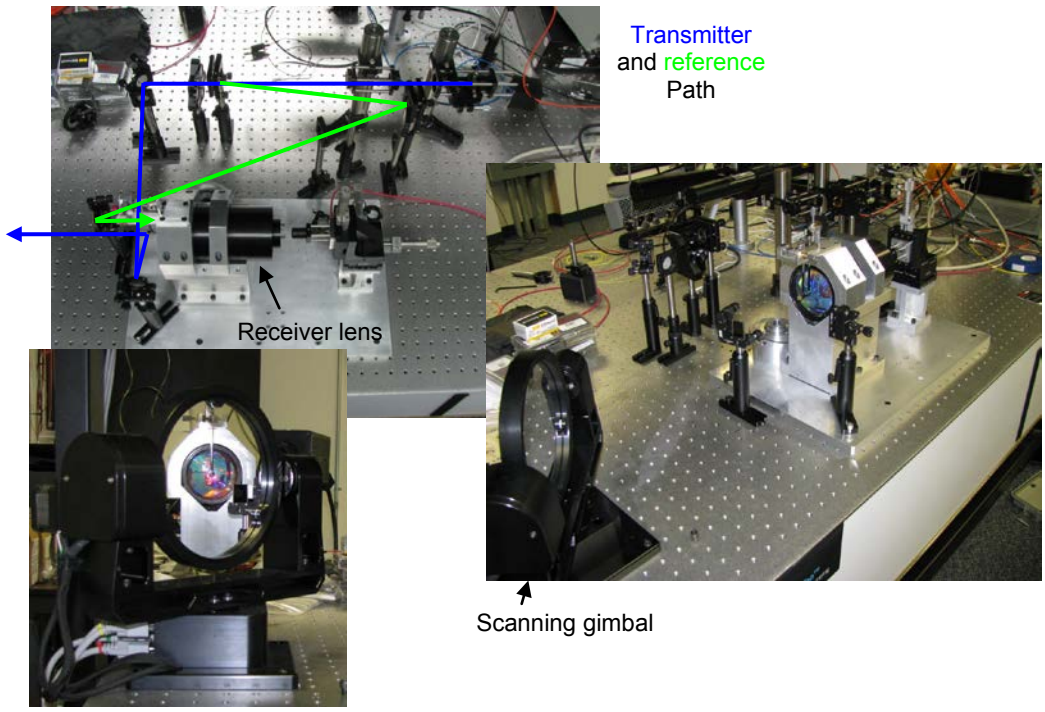

Figure 54: Receiver / transmitter optics assembly

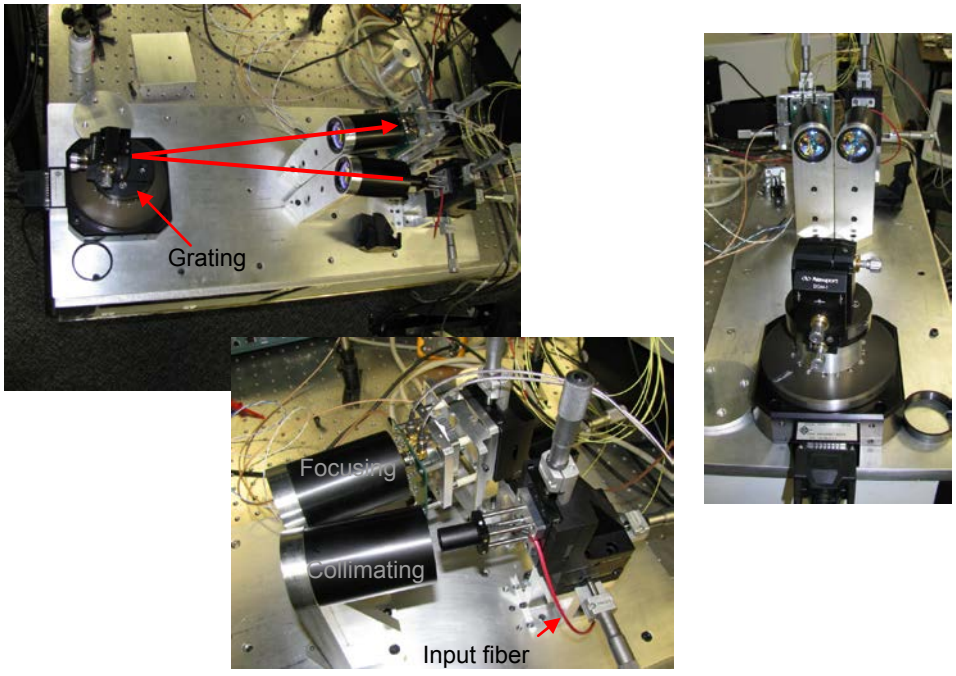

Figure 55: Spectrometer and photoreceiver assembly

5.2. Multispectral Source

The supercontinuum transmitter consists of a Q-switched Nd:YAG laser pumping several meters of photonic crystal fiber (PCF). The fiber has a Mode Field Diameter (MFD) of about 3.9 μm at 1064 nm with a 0.17 NA. The MFD increases monotonically to about 4.2 μm at 1650 nm with an NA of about 0.30. The small MFD diameter, combined with the customized zero dispersion wavelength (λ_{ZD}) at 1040 nm make this fiber well suited for supercontinuum generation using high peak power microchip lasers as a pumping source. The small MFD diameter increases the power density for high nonlinearity, while the λ_{ZD} is appropriately matched to put a powerful Nd:YAG emission line in the anomalous dispersion region, close to the zero dispersion wavelength.

The generation of supercontinuum radiation is discussed in Section 3.6.2. Figure 56 shows the output at the distal end of the PCF. The image is overexposed (saturated) to show some of the sidelobe features inherent in the PCF design. These low intensity sidelobes are neglected in further analysis. The beam has an approximately Gaussian profile.

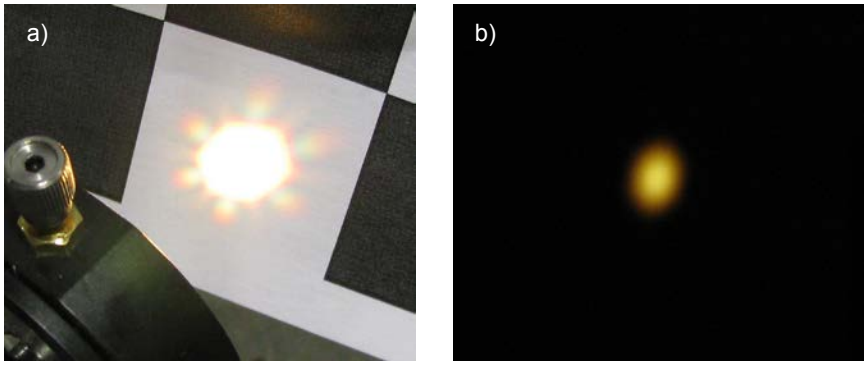

Figure 56: Supercontinuum output showing sidelobe detail (a, left) and central lobe detail viewed at an angle (b, right)

The pump laser operates at around 20 kHz pulse repetition frequency (PRF). The pulse timing is indicated by a TTL signal which is used as a trigger for the digitizer and to establish the time delay start (t_0). The PRF is used as a timing signal for the rest of the system including the control software running in MATLAB. Since the acquisition process for one pulse takes longer than the 50 μs repetition period, most pulses are skipped. The source used in this work is a pre-configured model that is commercially available.

5.2.1. Pulse Shape

The temporal properties of the supercontinuum pulse are wavelength dependent. Figure 57 plots the pulse shape at several center wavelengths (CWL) with a bandpass of about 24 nm in each case. These differences require different matched filters to be used for each. The noise level, range accuracy, and resolution are slightly different among the 25

optical bands. These variations in pulse shape are expected and have been reported in the literature [195].

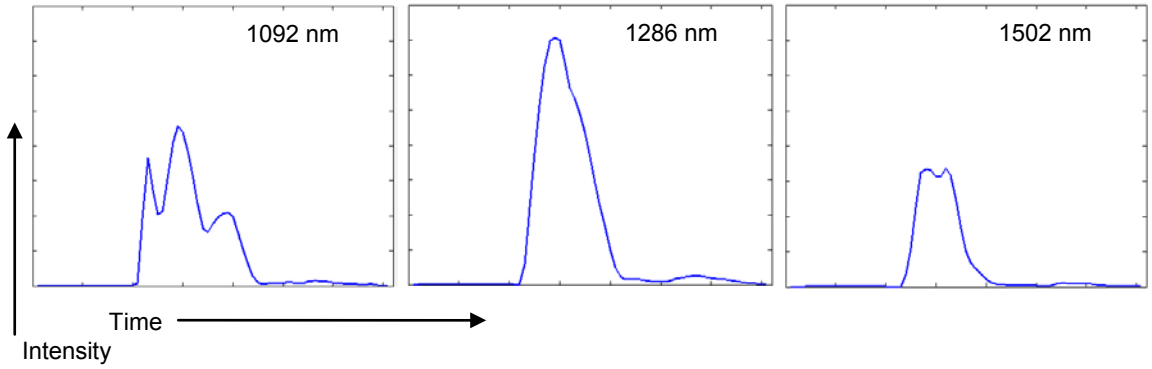

Figure 57: Pulse shapes at various CWLs and 24 nm optical bandpass

5.2.2. Power Output

Figure 58 plots the spectral density of the supercontinuum source. The average power is given in units of dBm / nm. The average power spectrum was measured by an independent lab with a telecommunications type optical spectrum analyzer (OSA). Although the spectral extent of the supercontinuum extends from about 450 nm to 2300 nm, the limitation of the OSA only allowed the range of 700 nm – 1750 nm. The spectrum is mainly flat, with a peak appearing at the pump wavelength.

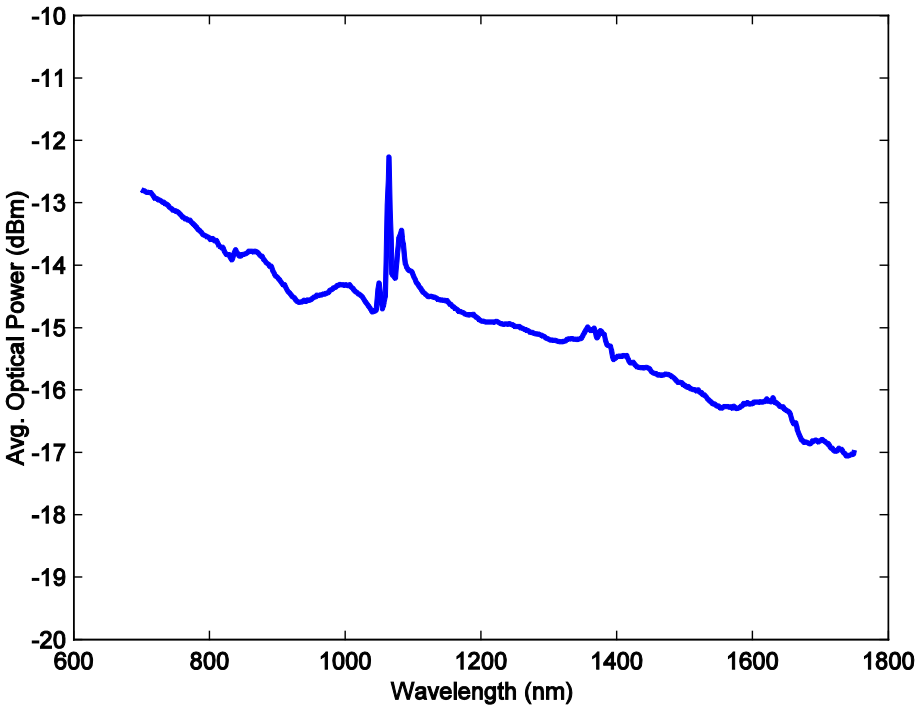

Figure 58: Supercontinuum spectral density

5.3. Transmitter Lens and Assembly

The supercontinuum beam from the PCF is collimated (focused at infinity) to a nominal 1 mrad full angle divergence by a chromatically corrected lens with effective focal length f_{tx}. The lens is mounted in a three axis (translational) stage for alignment to the fiber. Off-axis aberrations are avoided by centering the fiber on the axis of the lens.

Collimation is achieved by imaging the new beam waist following the lens at infinity. An expression for relating the output divergence angle to input beam waist (w_0) at a wavelength of λ can easily be found in or derived from a number of sources to yield

Equation 54 [196, 197]. Since the squared term under the radical is typically much less than 1, this can be simplified to show that the divergence angle of the beam emerging from the lens (θ') is approximately the ratio of the waist of the input beam to the focal length of the collimating lens (The output beam waist is w_0'). The reduced expression at the right of Equation 54 is within the limit of geometric optics in the small angle approximation.

Equation 54

$$w_0 = \frac{\frac{f_{tx}\lambda}{\pi w_0'}}{\sqrt{1+\left(\frac{\lambda f_{tx}}{\pi w_0'^2}\right)^2}} \approx f_{tx}\theta' \quad [\text{ m }]$$

The value θ' is the divergence half angle of the $1/e^2$ intensity point, which must be less than the receiver's field of view by some margin. Targeting 0.7 mrad full angle for this value requires a focal length of 6 mm at 1550 nm (for a fiber MFD of 4.1 μm). The Rayleigh range ($\lambda / \pi\theta^2$) for a beam with a divergence angle of 0.7 mrad at 1550 nm is much shorter than the minimum range of the LADAR, so geometric optics can be used to approximate the beam diameter downrange.

The lens first selected was an achromatic bonded doublet lens (Thorlabs AC050-008-C) with a focal length of 7.5 mm and clear aperture diameter of 5.0 mm. The focal length is slightly longer than required, however the selected part is the best match to stock catalog lenses. Analysis of this lens in ZEMAX shows that the geometric aberrations are

significant compared to the asymptotic beam divergence. This leads to an aberrated beam with some coupling loss. The object space location of the fiber (calculated using paraxial optics) that focus the waist (at 1550 nm) at infinity results in the ray fan in Figure 59a, while the focal distance of the fiber in object space that minimizes ray aberrations at all wavelengths results in the ray fan in Figure 59b. Figure 59b shows that defocus is used to partially correct ray aberrations, however this departs from paraxial collimation (Figure 59a). Using the physical optics* routines in ZEMAX to compute the intensity at a 40 m distant target (Figure 59c) results in predicted fractional encircled radiance (1 mrad) to be 0.48, 0.41, 0.30, and 0.28 at 1700 nm, 1550 nm, 1310 nm, and 1000 nm respectively when optimized to the correct divergence angle at 1550 nm. The choice of a stock lens for this application results in significant performance compromises in terms of coupling efficiency, but also leads to other more serious effects discussed in Section 7.5.

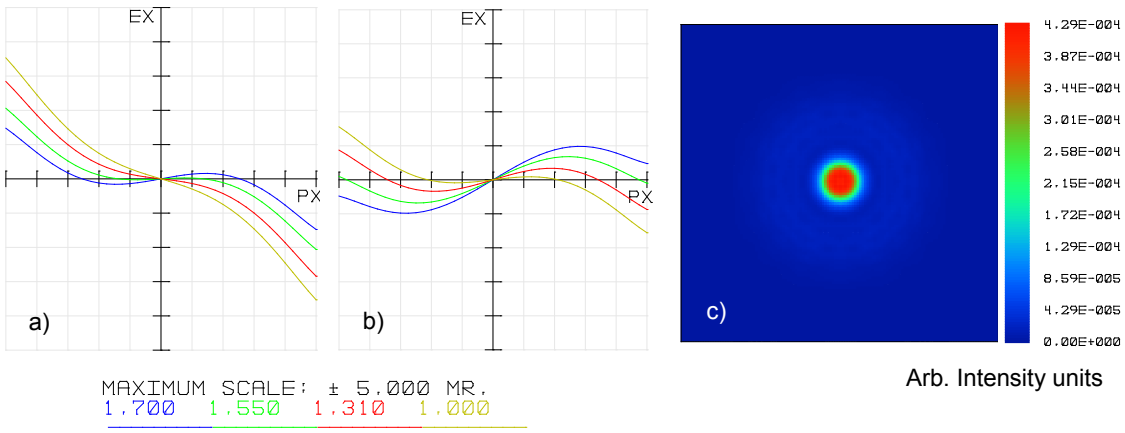

Figure 59: Ray fans for stock doublet lens (a, b) and physical optics intensity computation (c)

* Computation including diffraction and geometric aberrations

A detailed version of the transmitter optics assembly is shown in Figure 60. This includes more components than the broad overview depicted in Figure 53. The supercontinuum beam is delivered to the transmit lens focal plane by the PCF in which it is generated. The fiber is attached to an x-y mount behind the collimating lens which is adjustable with a micrometer in the z-axis. Following the collimating lens, all subsequent optical surfaces are planar, making translational alignment trivial.

Two filters immediately follow the collimating lens. First, a 1064 nm notch filter is used to eliminate the excess pump radiation. This is a rugate type filter, having very low ripple and high transparency in the passband. The filter blocks a small region around 1064 nm with about 40 dB attenuation. The purpose of this is to prevent the excess pump beam from overloading the APD. The second filter is a RG850 glass substrate with an AR coating on both sides. This colored glass filter cuts off short wavelengths (< 850 nm) to ensure eye safety, and also serves the purpose of guarding against aliasing in the spectrometer. When aligning the system, it may be useful to have the visible wavelength components of the supercontinuum in the beam for convenient visualization. Both filters can be removed easily since they are on magnetic mounts. During the alignment process (Section 5.10.4) a 10 dB or 20 dB visible ND filter can be used for eye safety and removed for actual device operation.

Following the first filter bank, the beam is split with a Silica glass plate with a slight (0.5 deg) wedge. The side toward the beam has no AR coating, so the Fresnel reflection is reasonably strong, in the range of 4%. This reflected beam is used as the reference beam

to implement source compensation, and is shown in green in Figure 60. The other side of the beamsplitter has an AR coating. It is important, and sometimes difficult, to select the beam from the Fresnel surface (which has a flat spectrum) from that reflected by the AR coated surface. In addition, the filters and beamsplitters have stray beams generated from multiple reflections that can be distracting, even hazardous without proper precautions. Beam stops are used to block these beams, although these are not shown in Figure 60. The transmit beam continues mostly without deviation through the beamsplitter. The beam has some very slight deviation due to the small wedge in the beamsplitter. This is evident in some color separation during the alignment process (Figure 95) but does not have a serious effect on performance.

The high power transmit beam is attenuated by a variable attenuator to both avoid saturation of the receiver and simulate longer range operation than the test range allows. This variable attenuator is of the filter wheel type and provides attenuation in the single digit decibel range. Since it contains discrete filters and is not continuously variable, it can be measured for repeatable results. The transmit beam then reflects off several alignment mirrors.

Following the beamsplitter, the reference beam transits one or more variable ND filters. These filters are of the continuously variable type, and are able to apply attenuation of up to 50 dB to bring the reference beam into the linear range of the receiver.

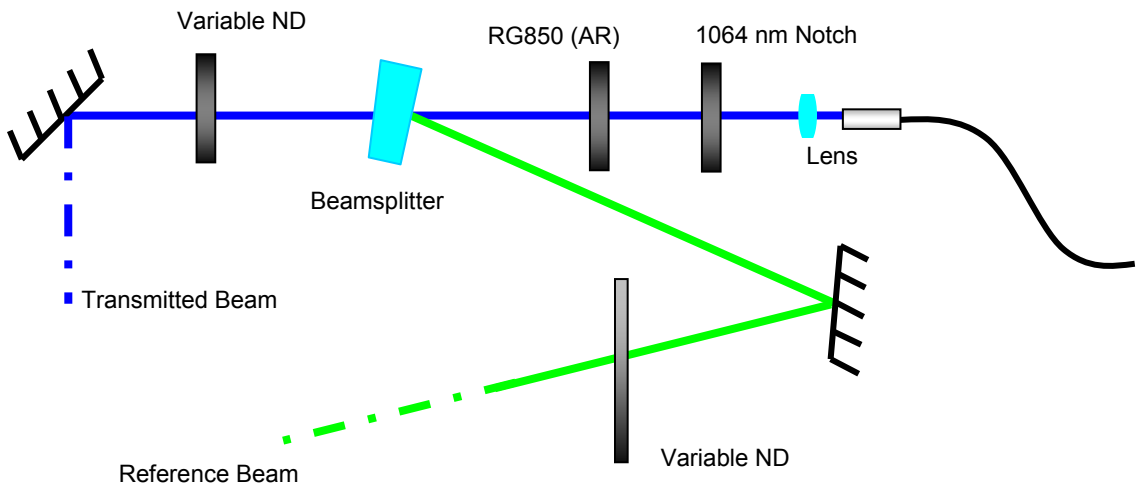

Figure 60: Detailed transmitter layout

5.4. Receiver Lens

The receiver lens collects the backscattered radiation and reference beam and couples both to a multi-mode fiber. As an option, a linear polarizer can be accommodated between the last lens element and the fiber for polarization sensing. The receiver lens and axial turning mirror of the transmitter lens are combined into one common assembly (Figure 61).

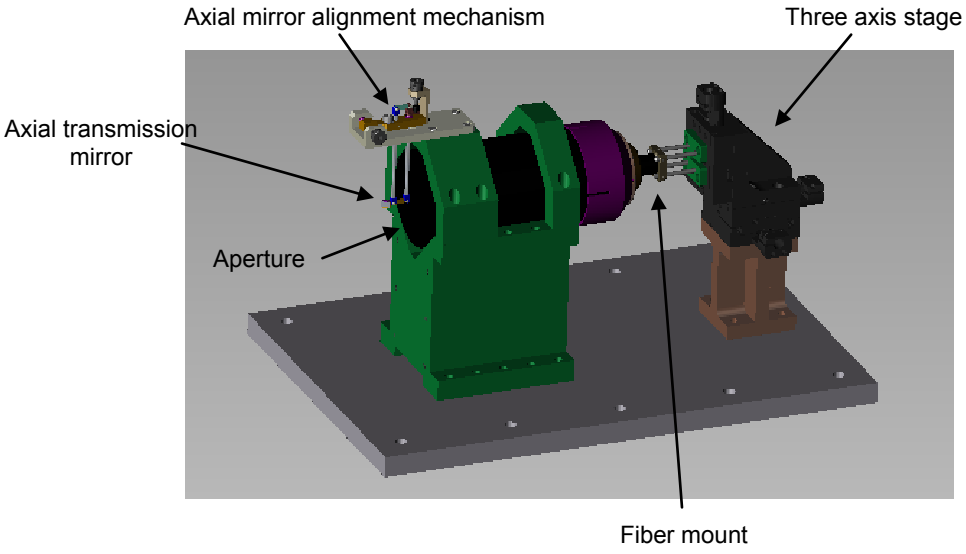

Figure 61: Receiver assembly with axial transmitter mirror

5.4.1. Lens Design

Figure 62 is the lens design. Four elements are required to achieve good coupling (low insertion loss) into the fiber. A front group and rear group consist of a positive ultra low dispersion element and a negative flint glass element. Since a positive crown and negative flint is the requisite combination for an achromatic doublet, this lens can be thought to be a double doublet, with air spaced elements. All surfaces have spherical curvatures. Aspheric surfaces have significant performance advantages, but the diamond turning manufacturing process used to create them in small volumes is not applicable to all material types, such as silica glasses. Limiting the field of material choices to those compatible with diamond turning is not a good approach for a lens that must be highly

achromatized. Although aspheres can be created with glass using other methods (e.g. injection molding) these options are infeasible for economic reasons.

The lens was designed using the ZEMAX design code. An initial, rough design was incrementally improved by using the Global Search optimization algorithm included in ZEMAX. Manual intervention was frequently necessary to eliminate dead end designs that were not feasible from a manufacturing or material property basis.

The use of calcium fluoride (CaF_2) was instrumental in reducing chromatic aberrations. This ultra-low dispersion coefficient crystal has an Abbe number of 95, which is substantially higher than most crown silica glasses. Low dispersion occurs in regions far from material resonances, which unfortunately also implies lower refractive index. Lenses of lower refractive index must have higher curvatures at a given refractive power.* The need for higher curvatures implies increased aberrations, including spherical aberration, since higher incidence angles cause more deviation from the small angle approximation under which ideal diffraction limited imaging is achieved. The use of four elements was found to satisfy the balance of imaging performance versus cost and reflective losses.

A broadband AR coating (1000 nm – 1700 nm) was applied to all lens surfaces to reduce the Fresnel reflection from about 4% per surface to 0.5%. Coating the doped silica glass elements (N-LAK33A and N-SF66) followed typical recipes. The coating for the

---

* Refractive power defined as 1 / EFL, where EFL is the effective focal length

calcium fluoride elements was slightly more challenging since in less demanding applications calcium fluoride is routinely used without optical coatings since its low refractive index has low Fresnel losses. Its low index is also less compatible with ordinary coating materials. The coating operation was performed by a specialty coating vendor.

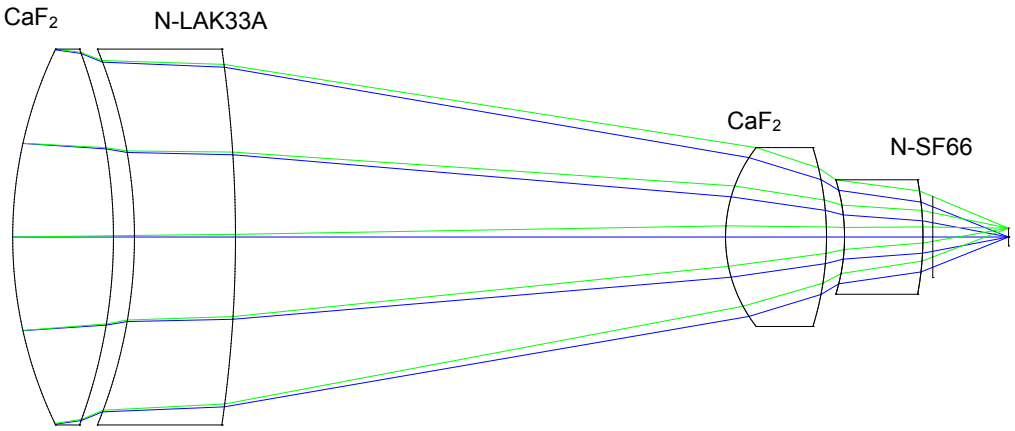

Figure 62: Receiver lens optical design

Figure 63a plots the ray fan for the receiver lens in its nominal construction and focus. The lens was designed with two field points, one axial and one at 1^{o} which is a lateral displacement of 1.75 mm in the focal plane. The receiver lens is expected to operate with the fiber centered in the axial field only, however the optical design software was configured to optimize a 1^{o} off-axis point so that the imaging performance versus field radius would be forgiving to misalignment and not drop off too rapidly. The ray fan shows the image plane intersection relative to the chief ray versus normalized pupil coordinates (x axis). A perfect diffraction limited lens would have a horizontal line as its

ray fan, indicating that all rays intersect the image plane at a single point regardless of pupil zone and rotation [198]. The lens is limited by geometric aberrations to the extent that the ray fan error exceeds the airy radius. Several lines are plotted in each ray fan for sample wavelengths. In the axial field, the most significant feature is a quadratic undulation of the ray fan which indicates higher order spherical aberration. Coma and astigmatism are never present in the axial field, only off axis. The deviations between wavelengths are indicative of chromatic aberration. The slope of the ray fan indicates defocus, and astigmatism is the variation of defocus in the orthogonal axes. In the off axis field, some astigmatism can be observed since the tilt of the fan differs in the x and y directions. Some coma is visible in the asymmetry of the y ray fan. Lateral color is mild and can be seen in the vertical offset of the fans representing different wavelengths. Axial color in the off-axis field point is about the same as the on-axis field point. These ray fans represent the nominal performance of the lens as designed, which amounts to a best case scenario. Manufacturing errors are not included, and are accounted for in a statistical tolerance analysis.

Figure 63b is the result of an image simulation analysis. Unlike the ray fans which represent the point-to-point mapping of rays from object space to image space over the entrance pupil, the image analysis represents a sort of finite element simulation of an extended source in object space mapped to the image plane. In this case, the image plane, entrance pupil, and extended object are spatially quantized and some large number of rays, each of finite intensity, is mapped from the extended source to the image plane. The intersection of these finite intensity rays in the image plane generates an intensity

image. Although the ray fan is an important tool to assess the nature and magnitude of geometric aberrations, the image analysis can provide a quantitative coupling efficiency and predict insertion loss by integrating the irradiance over the spatial extents of the fiber core and limits of the numerical aperture. Neglecting reflective losses from the fiber facet or other optical elements, the geometric efficiency was shown to be 98%.

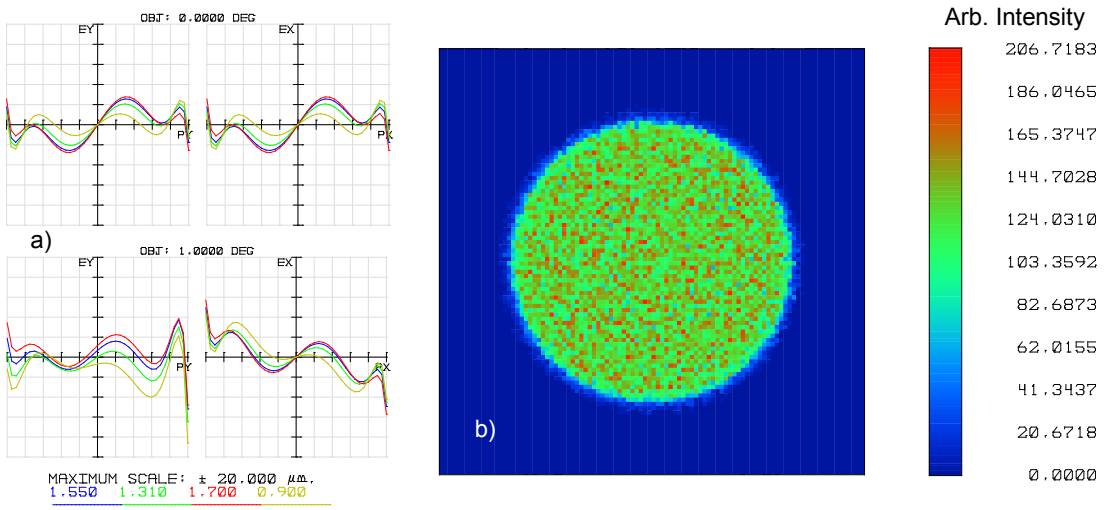

Figure 63: Geometric ray fan (a, left) and image analysis (b, right) (LENS A – RC1 – RTM.ZMX)

The point-spread function (PSF) for the axial field is shown in Figure 64a. This represents the spatial impulse response in the convolution model of imaging, including diffraction effects [199]. The Strehl ratio compares the peak of the PSF to the diffraction limited ideal PSF. The Strehl ratio varies from 0.5 to 0.7 over wavelength, indicating that the lens has very good performance rivaling the polychromatic diffraction limit. The polychromatic Strehl ratio shown in the PSF of Figure 64a is 0.65. Figure 64b is two views of the manufactured and assembled lens elements and body.

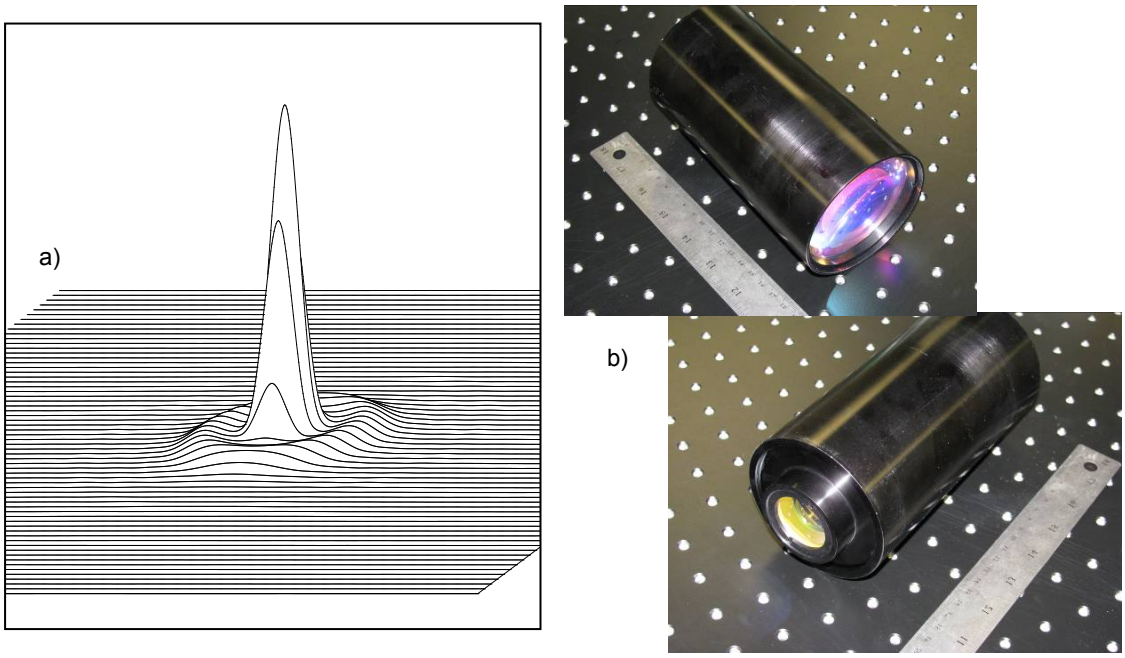

Figure 64: (a, left) Diffraction point-spread function and (b, right) lens assemblies

The receive lens also couples the reference beam into the multi-mode fiber. Since the reference beam has a very small diameter relative to the focal length, diffraction effects play a large role in determining the coupling efficiency. Since the reference beam has a power greatly in excess of what is needed, a detailed analysis of this coupling is unnecessary since a very high degree of coupling loss is acceptable.

5.4.2. Coupling Fiber and Insertion Loss

The fiber used to couple the receiver lens to the spectrometer is a large core, step index, silica-silica glass fiber. The core size is 100 μm and fluorine doping is used to reduce the index of the cladding, which has an outer diameter of 110 μm. The large NA (0.37)

combined with the large core allows for a high étendue, which is important for high sensitivity in direct detection LADAR. The length of fiber is approximately 1 m.

Figure 65 shows the mode pattern of the unfiltered reference beam exiting the distal end of the coupling fiber. The ring pattern is due to the underfilling of the fiber NA in conjunction with a large incident angle. The propagation length (1 m) and low microbending or scattering defects in the fiber prevents the mode distribution from achieving equilibrium in such a short length of fiber. This can be a serious issue in situations of a partially obstructed pupil or vignetting, since the mode structure's fluctuation over time (due to temperature, position, and other variations) can lead to variable insertion loss.

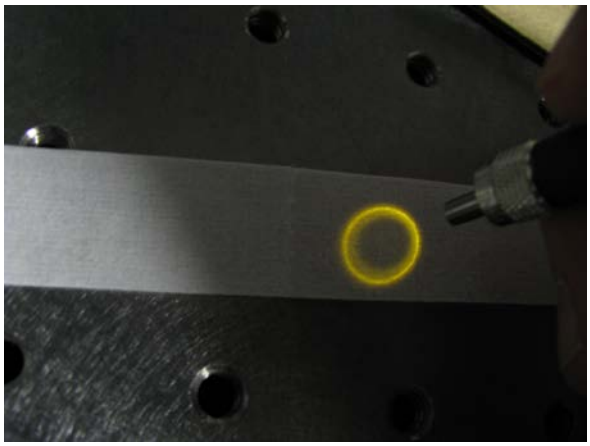

Figure 65: Reference beam exiting distal end of coupling fiber demonstrates non-equilibrium mode distribution (100216)

Assuming an AR coating loss of 0.5% per surface, a geometrical efficiency of 98.0%, and no loss from vignetting, overfilling apertures, or misalignment, the total as-designed throughput of the lens from aperture to distal end of coupling fiber is 93.2% (insertion loss of 0.3 dB). A more detailed estimate would take statistical tolerancing of the lens system into account, and also include full polarization and pupil analysis of the AR coatings. In practice, there will be some degree of focus and alignment error and some degree of aperture obstruction from the reference beam and transmit mirrors. A good estimate for link budget purposes is 85% efficiency (0.7 dB loss).

5.5. Spectrometer

The spectrometer (Figure 66) utilizes refractive optics, which is unusual for a spectrometer since they operate at a wide range of wavelengths and are thus susceptible to the chromatic dispersion in refractive media. As discussed in Section 3.8.3, refractive optics yield better performance in this case due to an exit slit with near-unity aspect ratio. This condition favors on-axis refractive operation with corrected chromatic aberration over off-axis reflective systems, which are devoid of chromatic aberration but present partially compensated off-axis aberrations.

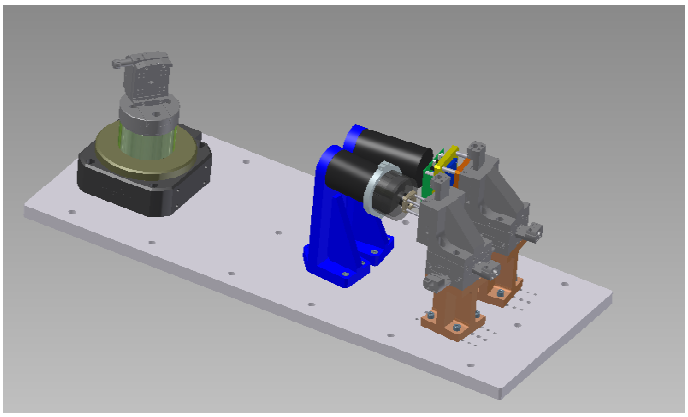

Figure 66: Spectrometer design model

The spectrometer itself consists of an entrance aperture*, collimating lens, grating on a rotating stage, focusing lens, and exit aperture defined by the active area of an avalanche photodiode (APD, Section 5.6). The spectrometer used in the laboratory demonstrator is tunable to a narrow range of wavelengths at one time (the optical bandpass), in contrast to a spectrograph which has multiple exit slits, perhaps defined by an APD array, and is tuned to multiple center wavelengths simultaneously. Spectrometers are less expensive and easier to construct compared to spectrographs since the single exit slit utilizes only one detector and the focusing lens system operates only in the axial field.

The entrance aperture is defined by the core of the multi-mode fiber connected to the receiver lens. The entrance aperture is 100 μm in diameter and has a 0.37 NA, which defines the étendue of the spectrometer.

* It is common to refer to the entrance aperture as the entrance slit, however, slit implies a rectangular opening with high aspect ratio; not found on this spectrometer. These terms will be used interchangeably.

5.5.1. Spectrometer Lenses

The collimator and focusing lenses were designed as a symmetric pair, with an infinite conjugate space for the diffraction grating. This forms a 1:1 relay pair to image the entrance slit in the exit focal plane with dispersion applied by the diffraction grating. The focal length of one side is 55.58 mm, a value driven by the other system characteristics including commercially available gratings, fiber diameters, and APD diameters. That value of focal length gives the spectrometer an optical bandpass of 24 nm. The NA of the system matches that of the multimode fiber. The optical design is pictured in Figure 67. It follows from the design of the objective lens, but reduced to three elements. Low dispersion CaF_2 and N-SF66 elements are used to match the glass types selected in the design of the objective lens. Although operated in the axial field, an off-axis field point was optimized to provide some slack in the alignment process. The lens surfaces are all spherical.

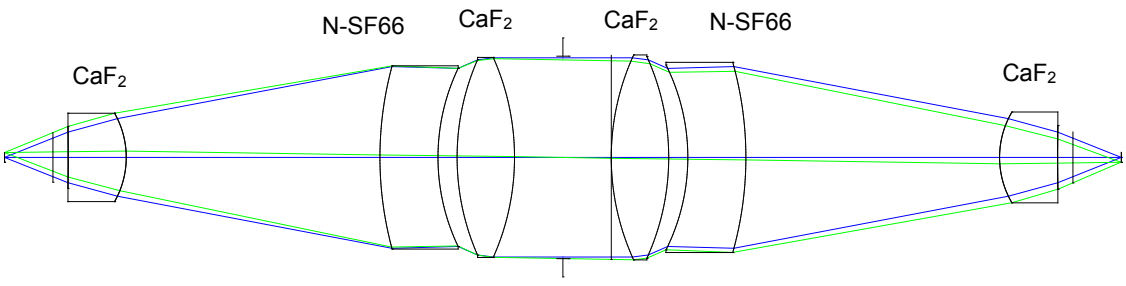

Figure 67: Spectrometer relay optical design

Figure 68a is the ray fan for the relay lens. It is clearly evident that the aberrations in the axial field contain spherical and axial chromatic aberration, where chromatic aberration is slightly greater. In the off-axis field, astigmatism and axial color are dominant, with some small contribution from coma. The geometric aberrations are well controlled in this three element symmetric relay, but it can not be considered close to the diffraction limit. The most important performance metric is that of encircled energy, derived from the image analysis (Figure 68b). At best focus and nominal design parameters, the encircled energy in an exit aperture with a diameter of 100 µm is 89%. For several reasons, an oversized 200 µm exit slit is used, which is double the size of the entrance slit with a 1:1 relay ratio.

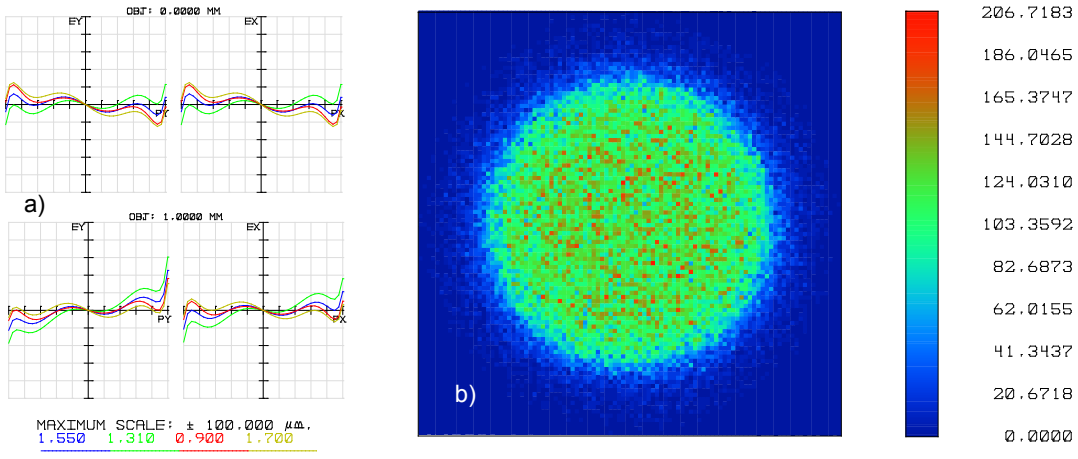

Figure 68: Ray fan (a, left) and image analysis (b, right) of the spectrometer relay (LENS B – RC3.ZMX)

The fabricated lenses are pictured in Figure 69. The same AR coatings that were applied to the receiver lens were also used for the respective glass types in the spectrometer lenses.

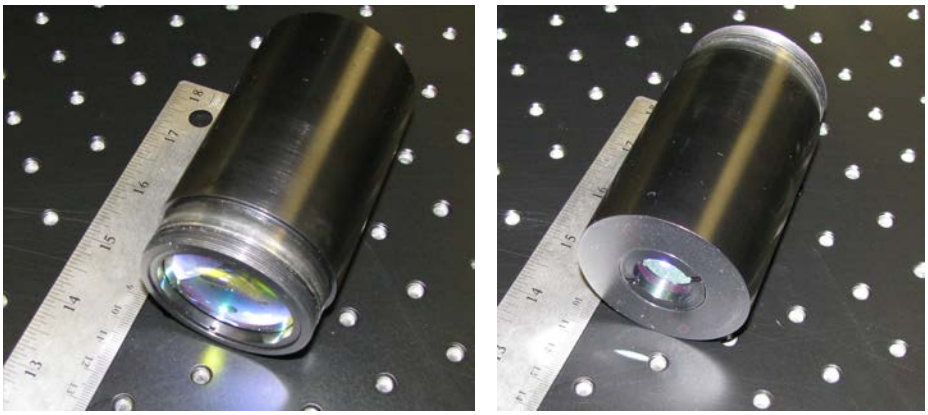

Figure 69: Spectrometer lens

5.5.2. Grating and Dispersion

A diffraction grating was selected on the basis of diffraction efficiency and polarization insensitivity. Polarization insensitivity is beneficial since it simplifies polarization calibration and also reduces the impact of fluctuations in source polarization. As discussed previously, low polarization sensitivity gratings are those well approximated by scalar wave theory, having relatively low spatial frequency and small blaze angle. The stock grating that best meets this criteria has a groove frequency of 150 grooves / mm and a blaze angle of 5.4^{o}, corresponding to a first order blaze wavelength of 1250 nm. The gold coating has high reflectivity in the SWIR versus aluminum, but not quite as high as silver. Figure 70 plots the diffraction efficiency in the first positive order for the selected grating.[*] The dips in the curve for the TM polarization (relative to the plane of incidence,

[*] Measurement performed by C. Palmer, Richardson Gratings, a division of Newport Corporation. The Richardson Gratings convention of referencing polarization to groove direction is used here.

but TE in the Richardson grating convention) are due to surface plasmon resonance phenomena or Rayleigh anomalies. Overall, the polarization dependence is low compared to gratings with large blaze angles.

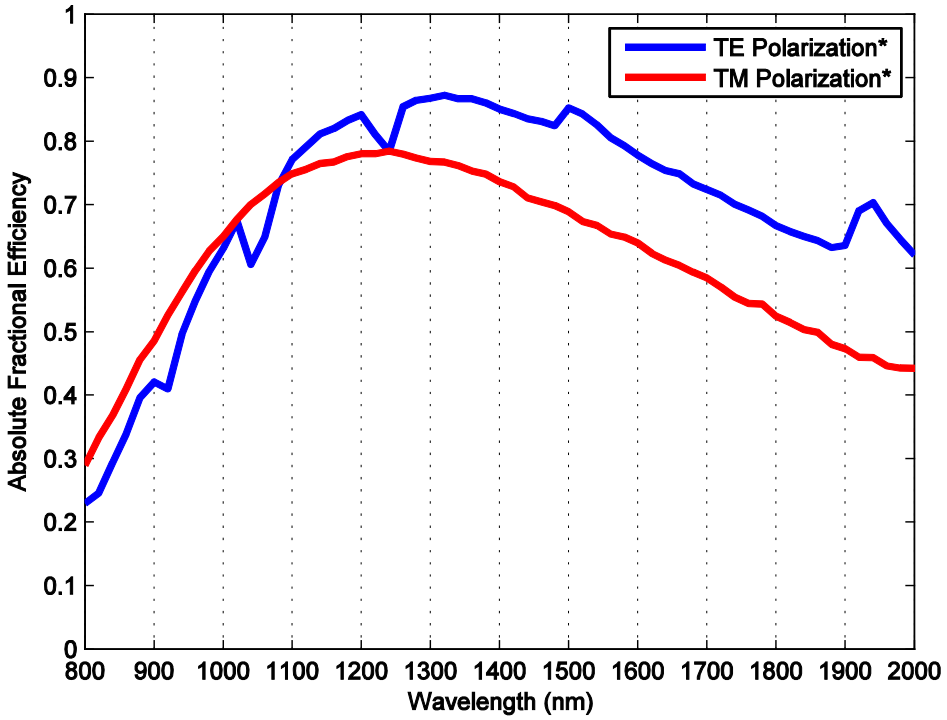

Figure 70: Absolute diffraction efficiency of grating (measured by Richardson Grating Lab, a division of Newport Corp.)

Figure 71 shows how the dispersed entrance slit is sampled by an exit slit of equivalent diameter (a) and twice the diameter (b) assuming optics of unity magnification. For an equivalent exit aperture diameter, the spectrum cannot be sampled uniformly with any degree of overlap between samples. When the exit slit is doubled in diameter, the spectrum can be uniformly sampled with some small degree of overlap. It is important to note that doubling the exit slit does not inescapably double the optical bandpass of the spectrometer since the dispersion of the grating can be doubled to compensate for the larger exit slit. The cost of this arrangement is a larger detector, which has greater dark

current and capacitance by about a factor of 4. This adversely affects the sensitivity and electrical bandwidth of the receiver. The coupling performance, however, is improved by using a larger detector, and is approximately 100%. This is an increase from the 89% coupling efficiency if the exit slit were the same diameter as the entrance.

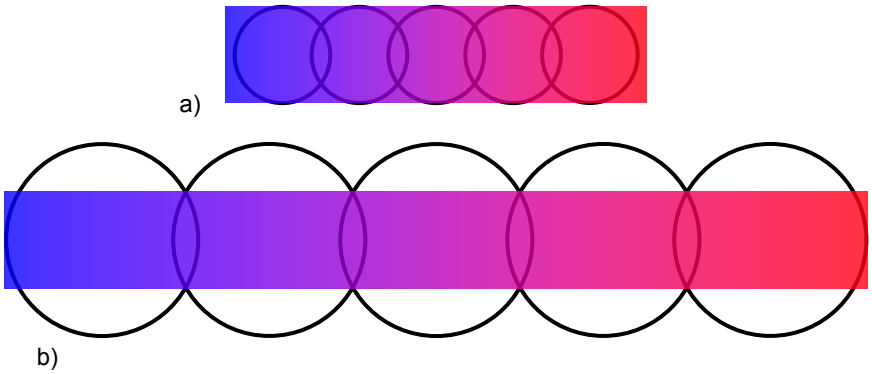

Figure 71: Spectral sampling using a 1:1 exit slit (a) and a 2:1 exit slit (b)

5.5.3. Spectrometer Performance

The key performance parameters for the spectrometer include resolution and insertion loss. These parameters are, in general, wavelength dependent. Étendue is also important, but as a design parameter and is not usually measured.

The spectrometer line spread function is the convolution kernel (impulse response) applied to the input spectrum and represents instrumental broadening.* Effectively, this is the spectral line broadening that is the result of the finite bandpass of the spectrometer. The line spread function is measured by configuring the spectrometer in a calibration mode, and applying a narrowband laser to the input. The focus was validated by first focusing onto a 100 μm core diameter fiber in the exit focal plane and then observing approximately the same power when focused and aligned onto a 200 μm fiber, indicating that the image of the entrance slit is not much greater than about 100 μm diameter. The grating is then scanned over a number of very small steps, each shifting the center frequency by much less than the bandpass. In this way, the image of the entrance slit (containing an approximate spectral impulse function) is scanned over the exit slit. The output of a spectral impulse is obtained, representing the impulse response of the system. Figure 72 plots the linespread at 1550 nm and two lines at 1525 nm and 1550 nm that are resolvable. Finding the resolution to be close to the expected value confirms that the focus of the system is near ideal.

* Not to be confused with a similar concept of line spread in an imaging system as a tool for evaluating the modulation transfer function (MTF).

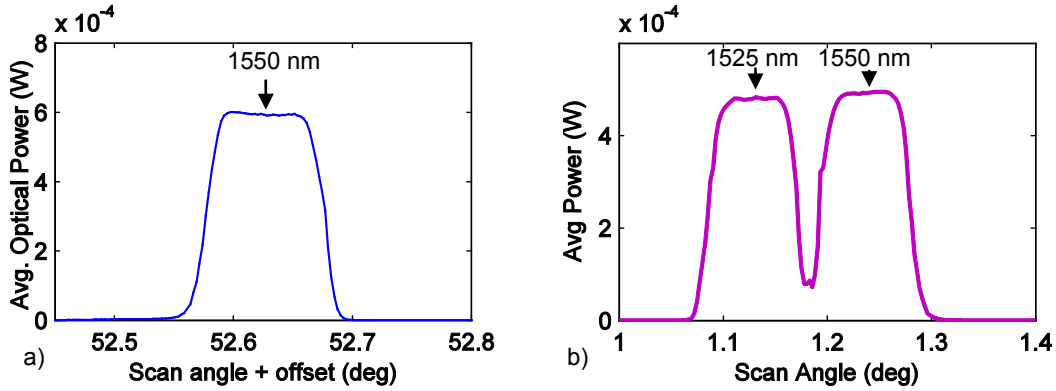

Figure 72: Line spread (a, 100615) and resolution plots (b, 100112)

The other significant performance aspect of the spectrometer is the insertion loss. The most significant component of loss should come from the grating if all other components have been adequately designed. The theoretical efficiency for a randomly polarized input at 1550 nm for the selected grating is about 67%, with up to 80% efficiency at the short wavelength limit and less at longer wavelengths. The three surfaces of the two lens elements are AR coated to about 0.5% reflectivity, for a throughput of 94%. Not including the detector window or the detector itself, the throughput is 63% equivalent to an insertion loss of 2 dB. In practice, an insertion loss of 1.7 dB at 1550 nm was measured, which is consistent with the predicted value within the margin of error. An insertion loss of less than 3 dB is generally recognized as good spectrometer performance.

5.5.4. Scan Motor and Control

The scan angle of the grating is actuated by a rotational stage, with about 0.1 degrees scan angle spacing between each band. The stage is driven by a motor controller that connects to the control PC via a RS-232 (at first) or Ethernet connection (later). The motor controller receives move commands from the computer via the control bus, energizes the motor coils to perform the move operation, reads an encoder as position feedback (in some cases) and reports the actual position or position error to the control PC.

Two different motors were tried in the lab demonstrator setup. The first was a worm-gear driven stage powered by a stepper motor. Torque was applied to the worm gear by a gear reduced stepper motor. This arrangement has reasonable dynamics (40 deg / s angular velocity, and 160 deg / s^2 angular acceleration), but some drawbacks. The most significant drawback was the lack of a position encoder on the stage itself. This introduced some uncertainty caused by the backlash of the worm gear system. In the course of stability testing it was noted that abrupt jumps in band energy occurred while making observations of a fixed target, especially in the first band (Figure 73). Grating position error was found to be the cause. This backlash was undetectable from the position feedback since there was no encoder feedback mounted to the stage itself.

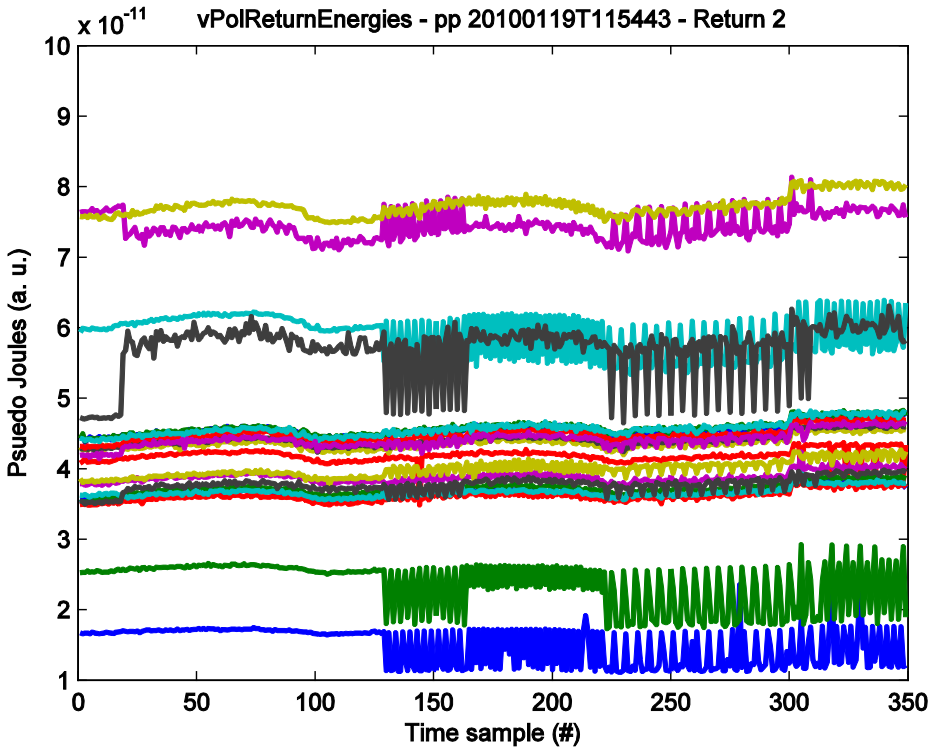

Figure 73: Jump discontinuities in stability analysis (100120)

To solve this problem, a direct drive motor replaced the worm gear unit. The direct drive motor has substantially greater performance (3600 deg / s), but also had a very high resolution encoder mounted directly to the stage for position feedback. Direct drive rotational stages typically outperform their worm-driven counterparts both in speed and precision since the stage itself is the rotor of the motor assembly and no gearing is needed. The disadvantages of direct drive include generally higher cost and a more complicated control architecture. Unlike a stepper motor drive in which the electronics synchronously step through several periods to achieve the desired position and then hold it with a steady state current, a direct drive motor must always have the motor coils energized with AC currents for holding torque, with the coil phases continuously

controlled by a feedback-PID* style controller. This poses the possibility of EMI effects in the photoreceiver amplifier. This controller also requires tuning of the P, I, D parameters to match the inertia of the load and the velocity profile, as shown in Figure 74.

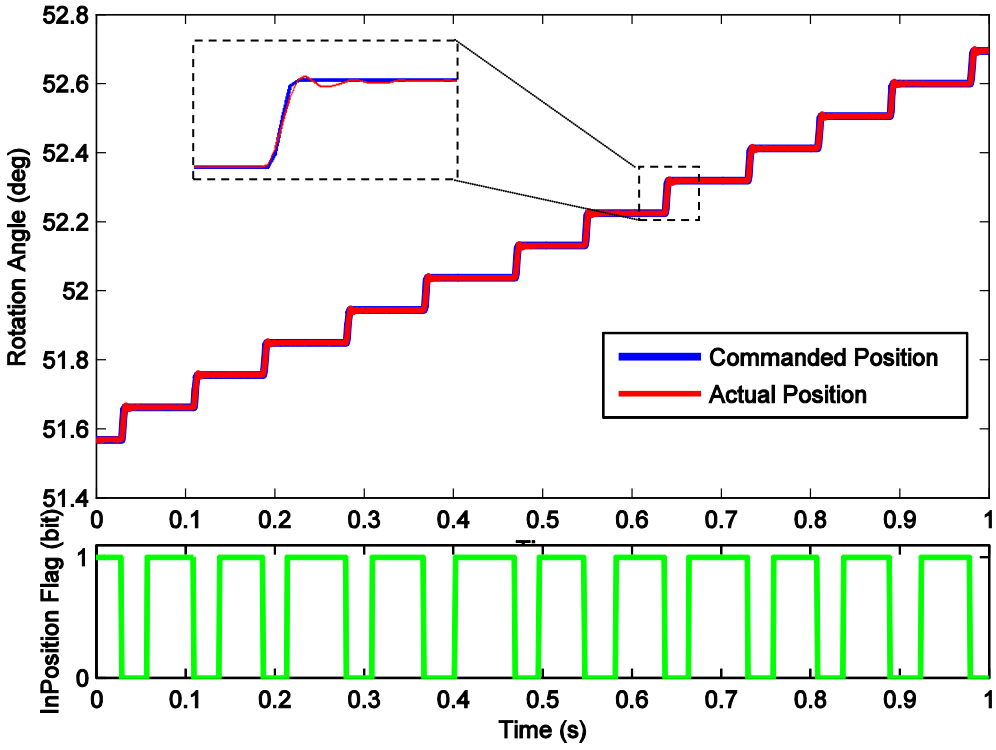

Figure 74: Grating stage: commanded and actual position profiles, signaling (100616)

The control parameters include extensions to the basic P, I, and D. An automatic tuning routine included in the controller software provided an initial approximation to the control parameters, but further manual adjustment was needed to produce the optimal step response time. Decreasing the proportional term was found to allow relatively

* Proportional, Integral, Derivative (PID)

aggressive tuning without appreciable ringing. Two key parameters, the "INPOS" time and error threshold, specify the time over which the position feedback must be within the error threshold for the stage to be considered in the commanded position. When this condition is satisfied the controller system asserts the "INPOSITION" flag which allows the data acquisition process to begin.

The direct drive stage was measured to perform the 0.1 degree moves for band-to-band tuning in less than 65 ms. The total tuning time for a single pixel, taking all grating movements into account including reset, is 1.6 seconds.

5.6. Photoreceiver Electronics

The photoreceiver electronics consist of an APD and transimpedance pre-amplifier (TIA) integrated on a ceramic substrate packaged in a TO – style can, mounted on an interface board. The can includes an AR coated window for optical transmission and is mounted on a purpose built 50 cm x 50 cm two-layer printed circuit board containing headers, RF connectors (SMA type), passive components for filtering (ferrite beads and capacitors), and mounting bolt patterns. The board has a clearance hole centered on the TIA module that allows low thermal resistance conduction to a heat sink, sprung on the backside of the board.

The receiver must have the electrical bandwidth to amplify the high frequency components of the transmitted waveform power envelope. Figure 75 shows the power spectral density of the panchromatic supercontinuum pulse. The frequency content shows that an analog bandwidth of 600 MHz is needed to fully amplify and digitize the return signal. For additional margin and since some bands have more high frequency content than others, a 1 GHz bandwidth was the design goal.

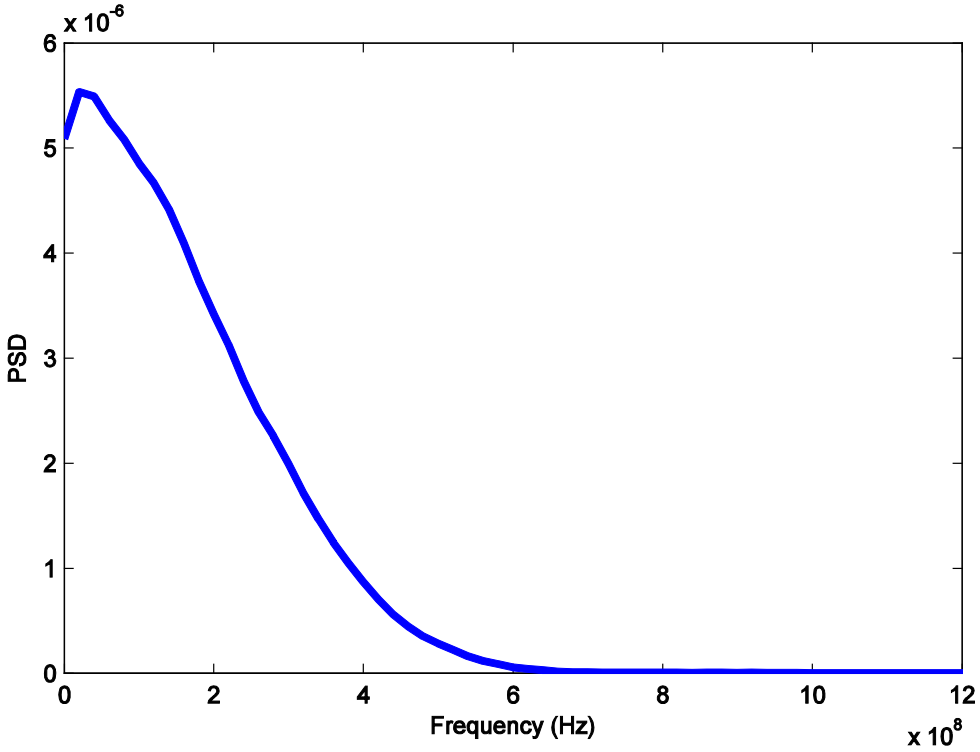

Figure 75: Electrical bandwidth of pulses in three bands (090717, 090624)

5.6.1. APD Receiver Module

A diagram of the major components of the photoreceiver electronics is shown in Figure 76. The module has an input pin to apply high voltage from an external source to reverse bias the APD. An inline current limiting resistor (R_{CL}) clamps the current below that which would damage the APD. The current from the APD is fed into a transimpedance amplifier (TIA) with a differential gain of about 3.3 kΩ into equal 50 Ω loads. An external 3.3 V bias is applied to the differential mode TIA. Signal line AC coupling capacitors are populated on the external receiver board to which the receiver module is mounted. Not shown in Figure 76 are the internal temperature sensor and thermoelectric cooler (TEC), both used to regulate the APD at constant temperature. Also not shown are decoupling capacitors to filter unwanted interference from DC lines. The MAXIM MAX3277 is used as the TIA pre-amplifier; in combination with the relatively large 1.5 pF APD parallel capacitance the bandwidth is about 1 GHz.

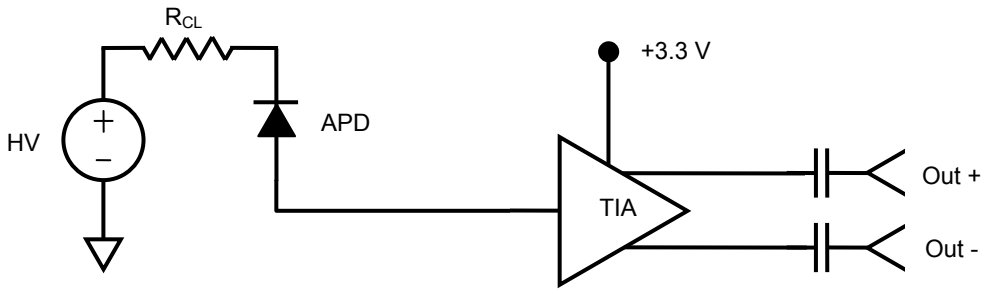

Figure 76: Major components of the APD photoreceiver

Table 3 provides the operating parameters for the APD module. The active area of 200 μm, in combination with the 1 GHz electronic bandwidth, yields a state-of-the-art bandwidth étendue product.* Figure 77 is a photograph of the receiver module as attached the receiver board.

Table 3: Receiver module parameters

Parameter	*Value*
APD active area diameter	200 μm
APD and TIA electrical bandwidth (3 dB)	65 kHz – 1 GHz
Responsivity at 1550 nm (M = 1)	1.05 A/W
Transimpedance gain (differential)	3300 Ω
Output coupling	50 Ω
TIA supply voltage	3.3 V
APD punch-through voltage	~43 V
APD dark current	~ 0.7 μA at M = 10, ~ 3.7 μA at M = 40
APD operating bias range	65 V – 72 V
APD operating temperature	285 K
TIA input-referred current noise	300 nA

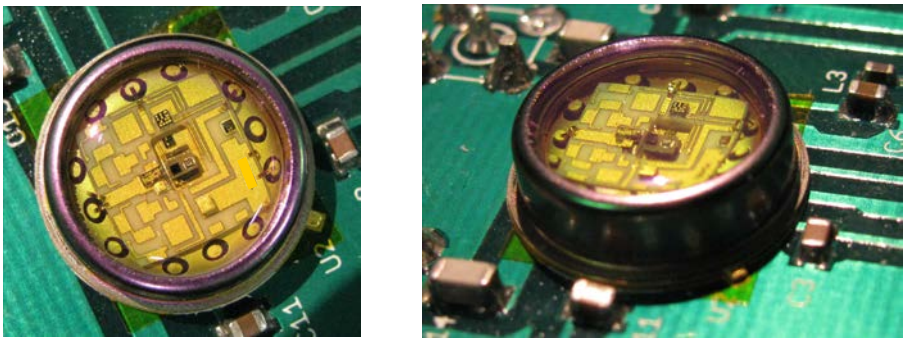

Figure 77: APD receiver module

* Since the bandwidth strongly depends on the capacitance of the APD, which is driven by the active area, the bandwidth and étendue are subject to a trade-off. The receiver board developed for Spectral LADAR may be compared to the bandwidth, étendue, and NEP of contemporary, commercially available APD receivers such as the New Focus model 1647.

5.6.2. Linear Dynamic Range

While photoreceivers for direct detection LADAR are similar to photoreceivers in optical fiber communications and free space laser communications, the need for linear dynamic range is a critical difference. Pulse-to-pulse variations in backscattered intensity can vary over several orders of magnitude in the brief pulse repetition period of tens of microseconds. Receiver power fluctuations are also present in the communication systems mentioned, but to a lesser degree, and less abruptly. Automatic gain correction (AGC) is often built into transimpedance amplifiers for optical communication, but this scheme is not an effective means of managing the abrupt variations in LADAR.

Spectral LADAR is even more demanding than conventional, monochromatic LADAR. Since the latter is mainly concerned with detection and location of targets, accurately measuring intensity is a secondary concern. In conventional LADAR, dynamic range issues are mainly focused on avoiding strong saturation that can disrupt the operation of the receiver for a long period of time and possibly effect subsequent returns. In Spectral LADAR, the *true* linearity of the receiver is of paramount concern when it comes to reconstructing the backscattered spectrum with high fidelity.

Table 4 shows the total dynamic range needed to accommodate returns from diffuse targets that may be at a range of 10 – 150 meters, intersecting at least ¼ of the beam, and having an angle of incidence less than 60 degrees. The total dynamic range required, assuming a transmitted pulse energy that is constant and non-adaptive, would require 16

bit digitization at 2 GSa / s which is a formidable challenge with the contemporary ADC technology at the time of this writing. Some analog pre-processing may be used to alleviate the ADC requirements. It must be noted, however, that Table 4 only accounts for most diffuse targets (having a Lambertian BRDF). Accommodating specular or retroreflective objects would require extremely high linear dynamic range.

Table 4: Dynamic range requirements for diffuse targets

Variability	*Typical Magnitude*
Intrinsic reflectivity (ρ)	10 dB
Range, 10 – 150 m (r)	24 dB
Cross-section, diffuse (Γ)	10 dB
Total	44 dB

Assuming a transmitted power of 20 W per band and a 75 mm receiver aperture, the received optical power can vary from 280 μW down to 16 nW at the extremes of reflectivity, range, and cross section. For 2 ns pulses in photon terms, the number of received photons can vary from 44,000 down to 25 at 1550 nm.

The linear dynamic range of the receiver, as constructed, is discussed in Section 5.10.2.2.

5.6.3. Receiver Board

The TO-style package of the receiver module mounts to the receiver board. This two layer board, approximately 50 mm square, was purpose built to the electrical

specifications of the receiver module and the mechanical requirements of the spectrometer. The first revision of the board is populated with entirely passive components, except for the receiver module itself. The receiver board mainly serves as a mechanical mount to the x-y-z stage of the spectrometer and electrical interface to the power supply, signal, and monitoring cables.

The receiver board maintains SMA connectors to the positive and negative signal output lines, 3.3 V TIA bias, and APD high voltage bias. Coaxial cables of 50 Ω characteristic impedance are utilized with these connectors. Regardless of the impedance matching, the signal stripline is sufficiently short (< 1 cm) in comparison to the shortest wavelength component of the signal such that any reflections will have a negligible impact on the signal transmission. Additionally, a 4-pin connector services the TEC power and diode temperature sensor interface.

Each of the low frequency lines, including the bias and temperature control, is coupled through an onboard pi-filter. This capacitor and ferrite bead filter attenuates signals in the passband of the pre-amplifier and reduces conducted EMI noise. The high speed signal lines are AC coupled to the coaxial cable through DC-blocking capacitors on transmission lines with a characteristic impedance of 50 Ω. The coaxial cable has a tin-soaked outer braided conductor to reduce EMI pickup.

The receiver board is pictured as mounted in the spectrometer in Figure 78. The cables are shown mounted to the board as they are during operation. An EMI shield may be optionally connected to the housing to shield the unit.

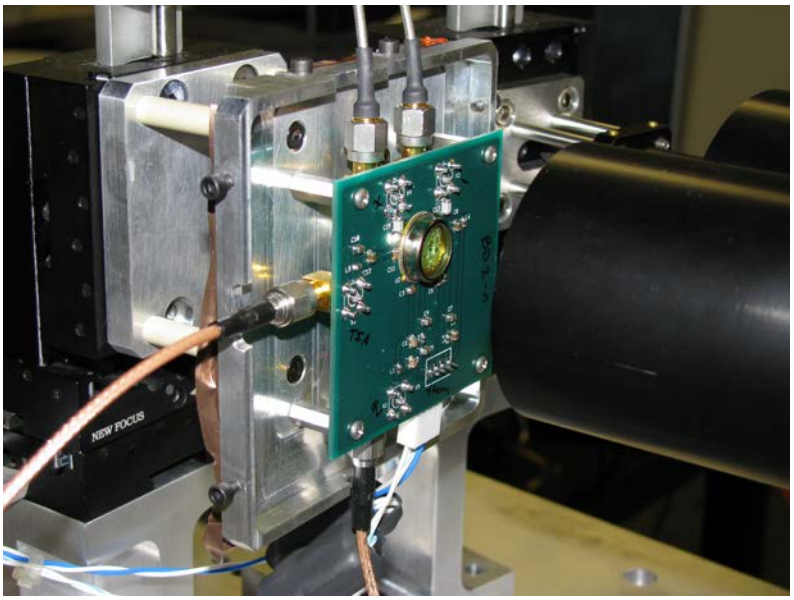

Figure 78: Receiver board

5.6.4. Mounting and Thermal Control

The receiver board mounts to a custom machined mounting plate. This plate is visible in Figure 78 and Figure 79 as the non-anodized aluminum plate with its mounting hardware. The right side of Figure 79 is a CAD model of the mounting plate. The first plate (from left to right in Figure 79, right side) mounts to a three axis translational stage. Ceramic standoffs connect this plate to a second plate to the right. Another set of standoffs connect the receiver board to this plate. The purpose of the second plate is to support a

piston-like spring-suspended heat plate contact that reaches through a hole in the receiver board to contact the backside of the receiver module TO can. The springs apply sufficient force to make contact but not excessive force that may bend the board or lead to focusing irregularities. A thin coating of thermal grease allows for good contact between the bottom of the TO can and the heat plate contact. A heat sink is attached to the backside of the heat contact and dissipates heat through natural convection.

Adequate thermal control is necessary in the APD receiver since the breakdown voltage, and hence the gain, is a sensitive function of temperature. Temperature regulation allows for consistent responsivity regardless of the ambient temperature. Lower temperatures also decrease the dark current of the APD and the thermal noise of the TIA. Temperature control is maintained by a thin film TEC mounted inside the TO can. The APD and a diode temperature sensor are attached to the (nominally) cold side of the TEC, while the hot side of the TEC is connected to the metal TO can substrate. TEC devices have low efficiency, making a heatsink on the hot side necessary to dissipate the excess heat and keep the temperature difference across the TEC as small as possible relative to ambient temperatures. A SRS PTC10 temperature controller, using a standard PID control loop is used to maintain a constant temperature of 285 K on the cold side of the TEC.

The mounting plate includes a provision for an EMI shield to cover the receiver board with the exception of small hole centered on the APD to allow light to enter the window of the receiver module. The shield includes small cut-outs for the cables, and a grounding wire. Gaps in the shield may be closed with adhesive backed copper foil. The

most significant EMI sources within the passband of the pre-amplifier were found to be the CDMA cellular band around 840 MHz, noise around 150 MHz from the temperature controller, and similar noise from the motor controller. Also noticeable, but outside of the passband of pre-amplification, was interference from WiFi transceivers (IEEE 802.11) at around 2.4 GHz.

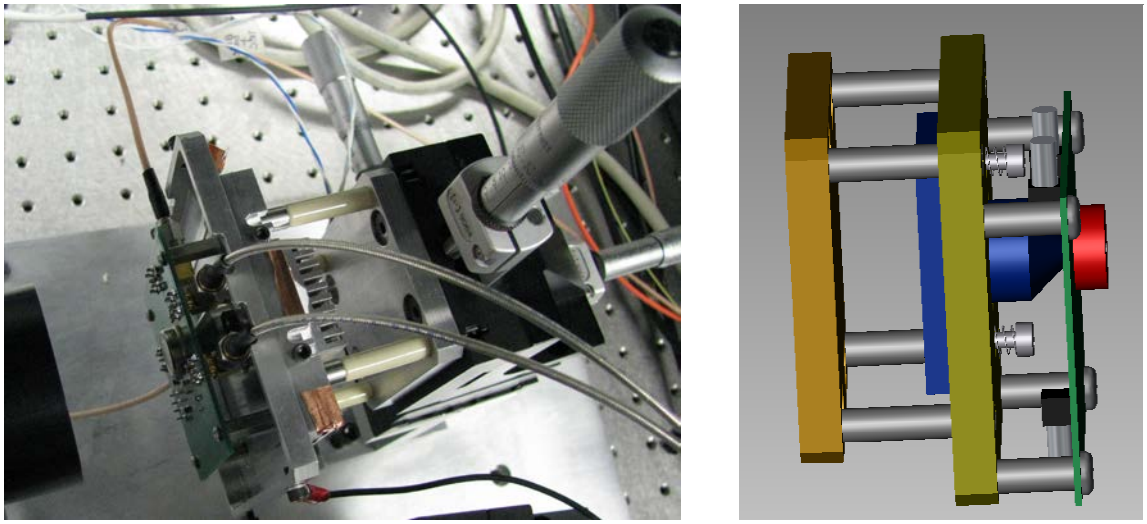

Figure 79: Receiver board mounting and thermal management

5.7. Digitizer

The signal processing approach implements digital signal processing in software to the extent possible. This reduces the complexity and expense that would otherwise be required using hardware, and also allows flexible re-configuration for experimental evaluation of various processing methods. To realize this, the output of the receiver module is digitized directly.

The digitizer is the data acquisition board of a PC-based Agilent 54854A digital storage oscilloscope (DSO) running the Windows XP operating system. The oscilloscope has an application programming interface (API) accessible via Ethernet connection which enables program control over digitizer settings and transfer of waveform data. MATLAB R2007a running directly on the oscilloscope can interface with the instrument API by way of the TCP/IP loopback address. Alternatively, MATLAB can be run on another system and interface with the oscilloscope instrument API over a properly configured TCP/IP network.

The receiver board is connected to the digitizer by two equal-length (1 meter) coaxial cables. Oscilloscope channels 1 and 3 are connected to the positive and negative outputs of the differential pre-amplifier, respectively. Channel 2 is connected to the pulse trigger of the supercontinuum source and serves as the indication of t_0. The acquisition is triggered by a rising edge at 0.5 V on channel 2. All channels have 50 Ω input impedance and are configured to acquire data at 5 GSa / s. This provides sampling well above the Nyquist rate of the 1 GHz bandwidth of the receiver module. The digitizer has 8-bit vertical resolution, with interpolation to 16 bits if averaging is turned on. The waveform data is downloaded to MATLAB as 16-bit words following the internal application of calibration adjustments on the raw 8-bit digitized values. An internal waveform math function computes the difference of the positive and negative waveforms so that only one waveform must be downloaded per-pixel, per-band.

The MATLAB acquisition script controls all aspects of the data acquisition process, including the setting of vertical range (v / div), re-setting of vertical range and offsets when out-of-range signals are detected. The memory depth of the acquisition board is sized to hold the digitized points corresponding to a pre-defined minimum range, which is usually a few meters, and end at a maximum range of 100 meters or more.

The quantization of the ADC contributes to the uncertainty of the intensity measurement. Assuming an 80 mV full scale range, the 8-bit ADC has a resolution of 0.3 mV. This is below the noise level of the digitizer. When the digitized signal is several times the resolution unit, the quantization noise can be assumed to be additive, with a white spectrum and rms value of $1 / 12^{1/2}$ ADU, where ADU is the voltage resolution unit. [200]. This is small compared to other sources of noise. To some degree, dithering from other noise sources may reduce quantization noise when uncorrelated samples are averaged or integrated with respect to time.

5.8. Software and Signal Processing

The acquisition, pre-processing, and post-processing software was designed with a modular architecture so that routines may be added, removed, or substituted to address experimental goals. Importantly, the entire data record is saved to a file at each major step so data can be re-processed with different parameters at a later time. Figure 80 shows the major processing stages in dark boxes, with the major operations of each stage

listed below in a bulleted list. The auxiliary input data to each stage are shown above in lighter boxes.

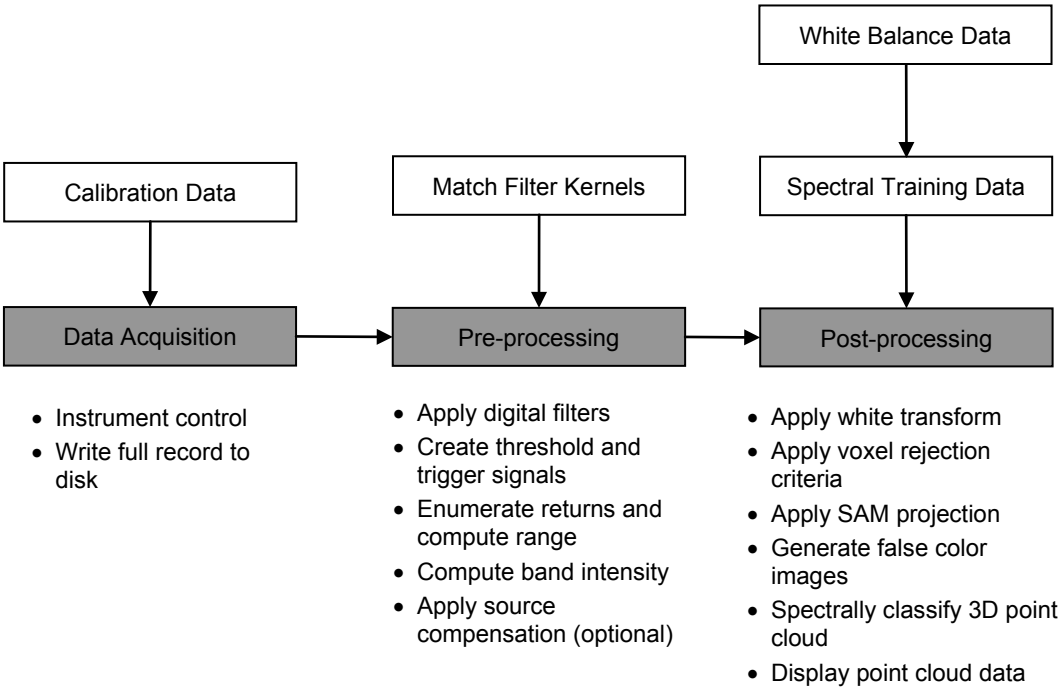

Figure 80: Signal processing flow and function

5.8.1. Data Acquisition

The data acquisition routine performs all instrument control and raw data recording functions. It consists of some initialization instructions that set parameters and configuration of equipment in preparation for a loop sequence that records data for each pixel and band. The procedure takes a number of parameters, the most important of which are enumerated in Table 5. A filename of a .mat file containing spectrometer

calibration information (Table 7) is also supplied and the contents loaded into the base workspace.

The initialization code opens communication and sets configuration parameters for the data acquisition unit, spectrometer (motor controller), and gimbal controller. An important part of initializing the spectrometer is the configuration of the optical bands. The center wavelengths for the bands are determined by the maximum and minimum wavelengths, divided by the optical bandpass. A small overlap factor is also specified (shown in Figure 71). Similarly, the gimbal vector map is determined by the FOV divided by the cross range resolution.

Following the allocation of memory, the procedure enters a nested looping structure to acquire the data. The outer loop scans the gimbal in both azimuth and elevation directions. The inner loop acquires an oscilloscope trace for each spectral band. The inner loop first commands the grating to the proper center wavelength, confirms that the grating is in position, and then sends a digitize command to the data acquisition unit. The acquisition unit then waits for the timebase (t_0) trigger from the supercontinuum laser, then starts the digitization and fills the waveform buffer. This trigger establishes the time reference for the time-of-flight measurement. Diagnostic and error data is also recorded, such as the spectrometer center wavelength error for later analysis.

Once data for every pixel in the image has been recorded, the entire raw dataset is saved to a .mat file for later processing. Saving the raw data allows for changes in signal processing to be considered after the fact and allows for re-analysis of data.

Table 5: Data acquisition routine parameters

Parameter	*Typical Value*
Various TCP/IP and RS-232 communication parameters	various
Minimum wavelength	1080 nm
Maximum wavelength	1625 nm
Elevation FOV	various (degrees)
Azimuth FOV	various (degrees)
FOV bias (defines center view)	various (degrees)
Cross range resolution	1 mrad
Maximum range	75 m
Minimum range	4 m
Receiver linearity limit	80 mV
Averaging	1 (No averaging)
Sample rate	5 GSa / s
Start trigger level	0.5 V

5.8.2. Pre-processing

The pre-processing script takes the raw time series data from the data acquisition file, applies digital filters, detects return pulses, and processes the time waveforms into spectral point cloud data. The principal output are two arrays, one containing the range or ranges of each identified return per pixel, and another containing the spectral energy vector of each return.

The pre-processing routine has several configurable parameters (Table 6), and requires one data set as input. A set of canonical pulse shapes is stored in a separate file. These pulses represent the frequency content of the transmitted signal in each band. The pre-processing routine uses this data to generate the matched filters that are specific to each band.

Table 6: Pre-processing parameters

Pre-processing parameter	*Typical value*
Trigger voltage level	2.5 mV
Calibration trigger level	4 mV
Dropout range	60 m

The routine first computes the matched filters in the frequency domain according to the discussion in Section 3.1.6.2. The centroids of each of the canonical pulses are compared and a calibration factor (usually just an adjustment within few samples) is computed so that each band will register at the same range in the absence of noise.[*] Next, the matched filter is applied to the time waveforms. A digital trigger-arm signal is generated from each waveform that becomes asserted when the signal is above a specified threshold.[†] Early versions of the code triggered on zero crossings of the waveform's derivative under the assertion of an arm signal based on the pulse height, but this proved problematic in the presence of noise. The rms noise is also estimated for each waveform by taking the voltage rms value of points beyond the specified "dropout range," beyond which no true return signals should exist.

---

[*] Using the "calibration trigger level"

[†] Using the "trigger voltage level"

Next, a trigger signal is generated per-pixel, based on the many trigger-arm signals that are generated on a per-pixel, per-band basis, i.e. for each waveform. The trigger signal has a rising edge (t_r) and falling edge (t_f) for each voxel with a return. There are several ways to do this with the N trigger-arm signals, where N is the number of bands. The system could trigger when trigger-arm is asserted in any one spectral band (OR trigger), all spectral bands (unanimous, or AND trigger), or some defined quorum of spectral bands.

The OR trigger is clearly the most sensitive since it indicates the detection of a target in a particular voxel when adequate SNR (i.e. a threshold crossing) is achieved in *any* band. Since the albedo of a target can vary significantly among the many bands, some bands may have a strong return signal while others are well below the noise floor. The OR trigger will indicate the presence of a target in these cases, however spectral classification using all bands is not possible since one or more bands may not have an appreciable signal.

The AND trigger is asserted at times when *all* trigger-arm signals are asserted at a given time. When the trigger-arm threshold is set at a value with very low P_{FA}, and the trigger is asserted, the condition exists where all bands will have adequate SNR for spectral classification. Clearly this means that some non-classifiable returns will be missed by the system despite having high confidence detection in one or more, but not all, spectral bands.

An optimal approach may be to trigger on some quorum of signals, or have adaptive classification based on the number of bands triggered. Another possibility is to use OR triggering to recognize objects, but only perform spectral classification on those returns which satisfy the AND trigger. The laboratory demonstrator takes a simplified approach and uses the AND trigger exclusively. Although a practical system may work best with a hybrid approach, the AND trigger is suitable for evaluating the effectiveness of spectral classification.

Clearly the P_D and P_{FA} detection statistics are affected by the logic of the trigger signal. Assuming the noise in each band is identically distributed and independent and that the trigger level is the same for each, the OR trigger increases the false alarm rate by a multiple close to the number of bands. The AND trigger decreases the false alarm rate at a given threshold level by raising the false alarm rate in one band by the power of the number of bands. Similar statistical logic applies to the P_D rate, where the OR trigger increases P_D while the AND trigger decreases that metric.

Following the generation of the trigger signal, the ranges of the positive return voxels are identified. The center-of-mass (Equation 55) is calculated for each band subject to the interval of the rise and fall of each trigger assertion (t_r to t_f). The center-of-mass time coordinate (R_t) for each trigger event is calculated per-band, and then averaged to compute the range to target. Up to 16 trigger events may be recognized per pixel based on the current code configuration, however there is no fundamental reason why this limitation cannot be increased.

Equation 55

$$R = \frac{\sum_{t_r}^{t_f} s[t]t}{\sum_{t_r}^{t_f} s[t]}$$

The spectral energy distribution is then calculated for each return. This is performed by trapezoidal numerical integration over a fixed interval around the identified centroid in each return. It is important to note that the integration interval is computed by the accessory functions to the matched filter kernel generating functions. The limits of integration are about the centroid and do not depend on the trigger rising and falling edges which are based on fixed thresholds. If the limits were determined by the trigger edges, the fraction of the integrated pulse energy would depend on the pulse amplitude, leading to nonlinear errors. The spectral energy is stored as a vector in *N*-space and has units of volt-seconds. Since optical power is proportional to TIA output voltage fed to the digitizer, the spectral vector is related to optical energy by a constant factor.

Aside from the computation of some diagnostic information, the final function of the pre-processing code is to produce a spectral vector for each return that is source-compensated to the reference return which is present in every waveform. The ratio of the reference return and a fixed reference spectrum (determined by the match filter kernels) is found for each return. This normalization ratio is then applied to the actual returns to adjust them to cancel fluctuations in the source (or detector).

5.8.3. Post-processing and Display

Unlike the data acquisition and pre-processing routines, which consist of one procedure, the post processing and display pipeline is a collection of several routines that accept the same data from previous stages but produce results for different purposes. The various post processing and display routines produce output for performance analysis such as that shown in Section 7. Other routines display images, point clouds, and classified point clouds. Various transformations are applied in the post-processing stage as appropriate to the particular visualization, classification, or analysis method desired. A key part of the post-processing operation is the classification process, described in Section 5.9. The graphics results shown in Section 9 demonstrate some image output of the collection of post-processing routines. The operation of various routines will be discussed alongside the results produced in later sections.

One key function found in most post-processing routines is the application of a white-balance correction factor. Prior to the collection of data, a spectrally flat (white) calibration target at the range of the scene to be imaged is sampled by the system with averaging to eliminate random noise. The white calibration targets are typically a diffuse PTFE-like material. This is done to calibrate the spectral responsivity of the system to some known standard. Each time the system is assembled and aligned, the spectral shape of a white target is slightly different. By applying the white-balance calibration, data obtained with slightly different setups is mutually comparable.

5.9. Classification Algorithms

Several classification algorithms were implemented for use with Spectral LADAR data. The emphasis of this effort was not to develop new algorithms, but adapt existing ones and add minor modifications and adjustments to the particulars of the situation. In every case, the input to the classifier was SAM-projected spectral data. This eliminated the need to compute the inverse LADAR problem to find target reflectivities and make (likely poor) assumptions about object cross-sections and aspect angles. The fundamental details of the classification algorithms are discussed in Section 3.4.

A standard K-means classifier was implemented and based on the K-means algorithm included in MATLAB's Statistics toolbox. K-means is an unsupervised classifier that seeks to partition the data points into a fixed number of clusters. Two supervised classifiers were implemented, k-Nearest-Neighbor (KNN) and maximum likelihood. As with all supervised classifiers, training samples of selected materials were captured in separate test runs. The training data defined the partitions of spectral space for each material type.

5.10. System Construction and Operation

This section describes the construction of the laboratory demonstrator and the testing and evaluation of subsystem components. The construction and testing of the photoreceiver and spectrometer will be discussed. The section concludes with a discussion of the operating procedure.

5.10.1. Link Budget Estimation

During the experimental design process, an estimation of the system's link budget was carried out to ensure ample SNR and to compare observations against expected values. The calculations included noise contributions from APD shot and excess noise, and amplifier thermal noise. These values were extracted from component data sheets. The noise component of solar background radiation was estimated from the calculations discussed in Section 3.1.5. The peak transmitted optical power was estimated to be 20 W per band at around 1550 nm, based on testing with thin film bandpass filters.

The multiplicity of losses due to reflection and absorption at optical surfaces in the system are not negligible. Manufacturer supplied data is used to determine losses due to Fresnel reflections and losses due to finite conductivity metal mirrors. The overall throughput of the receiver lens was estimated to be 85% as calculated in Section 5.4.2. In calculating the link budget, perfect alignment of transmit and receiver FOVs is not assumed. To the extent that the fields of view are mismatched in divergence, focus, or

angular alignment, the received power and SNR will be diminished from an ideal assumption. Based on experimental testing, a spectrometer insertion loss of 2.5 dB is assumed. Some loss parameters were estimated based on typical or expected results.

These assumptions of loss, transmitted optical power, and receiver sensitivity are wavelength dependent. To simplify the analysis, calculations were made for a single band only with parameters representing the average band parameters in the region of high APD responsivity.

In the figures below, a 60% diffuse reflectivity target was assumed. Other parameters, e.g. receiver aperture, are discussed elsewhere in Section 5. The plots of SNR neglect digitizer analog noise and do not consider digital filtering. The link budget was only calculated at ranges greater than 20 m. Closer ranges require an estimation of defocus, which causes the peak power to roll off at short ranges due to coupling loss.

Figure 81 is the estimated peak optical power versus range in a single band. Plotted on a log scale, it is clear that considerable linear dynamic range (over 10 dB) is needed merely to accommodate changes in range from 20 m to 100 m. Because of this, the laboratory demonstrator imaged scenes with less than 10 m of range depth,[*] and attenuation was applied to make targets at 40 m appear to have backscattered intensities as if they were at 60 m or more.

---

[*] Distance from closest target to farthest target

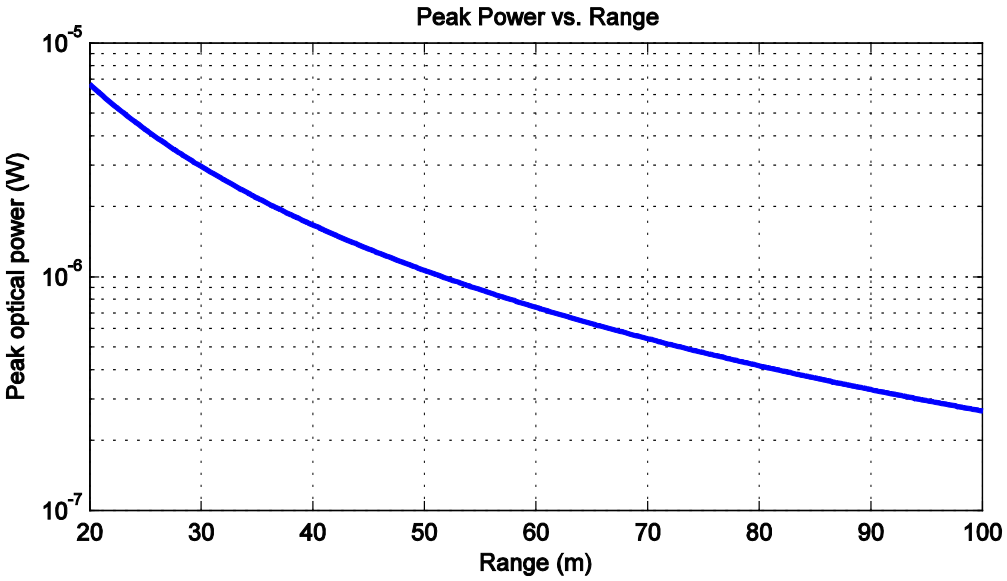

Figure 81: Estimated optical power versus range in a single band (110308)

Figure 82 represents the peak optical power transduced to a voltage for several values of APD gain. The voltage range represented here exceeds that of the TIA output limit, discussed in Section 5.10.2.

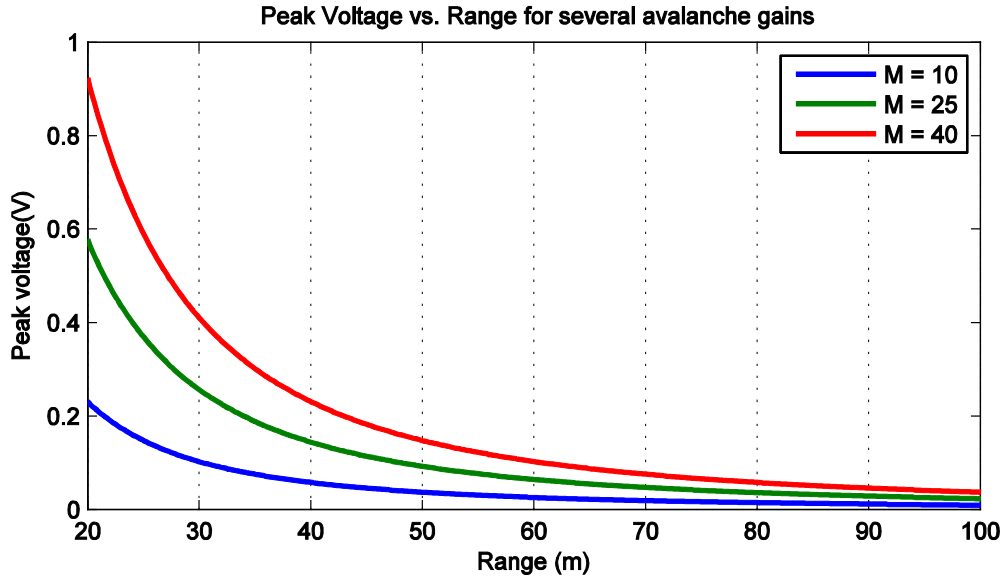

Figure 82: Estimated voltage versus range for several avalanche gains in a single band (110308)

A plot of SNR versus range and APD gain is shown in Figure 83. It is clear from this figure that the APD gain that produces the highest SNR is dependent on target range, or more exactly, received optical power that is range-dependent. The red contour in Figure 83 represents the optimal gain, which shifts from 15 at 20 m to over 40 at 100 m.

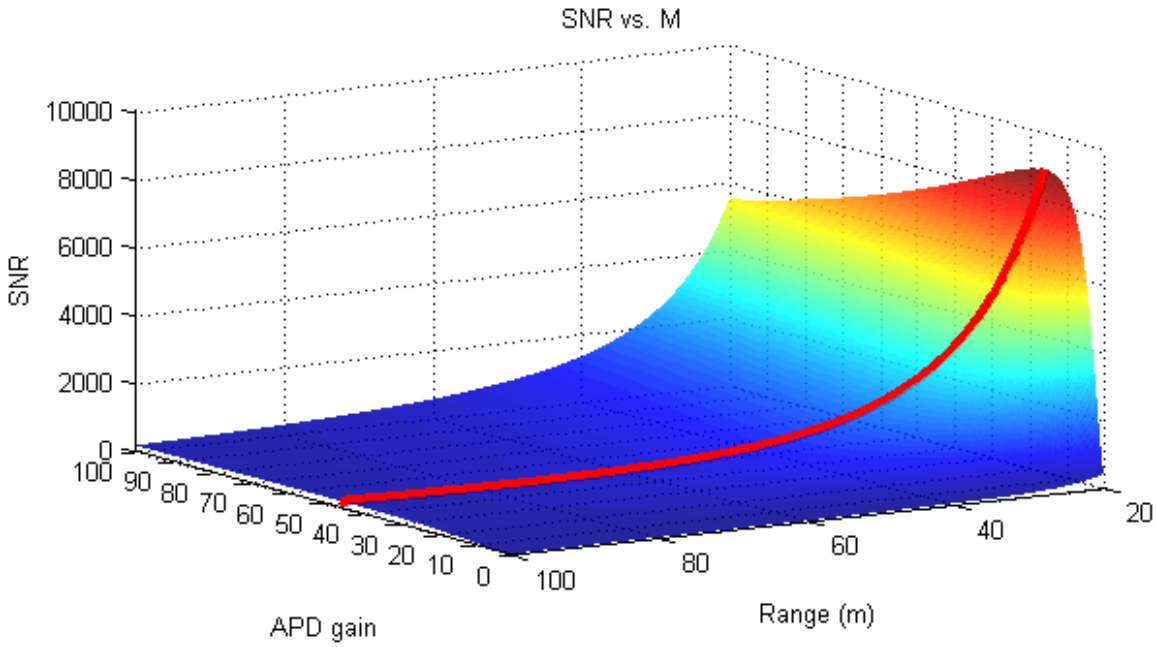

Figure 83: Estimated SNR versus range and avalanche gain for a single band

5.10.2. Photoreceiver Characterization

The photoreceiver consists of the detector module, detector board, and instruments which are necessary to operate it. These instruments include the high voltage bias supply, TIA bias supply, and temperature controller. A characterization setup was constructed to

evaluate the operation of the photoreceiver in a highly controlled configuration independent of the spectrometer and other system components.

5.10.2.1. Characterization Setup

The APD receivers are radiometrically calibrated to assess the noise equivalent power (NEP) and estimate overall sensitivity. The estimation of electrical bandwidth is implicit in these measurements.

A separate fixturing and lens system was constructed for this purpose (Figure 84). The calibration setup projects an optical pulse with a well defined spatial, temporal, and energy profile on an APD receiver. The spatial profile underfills the APD diameter to reduce the uncertainty of coupling error.

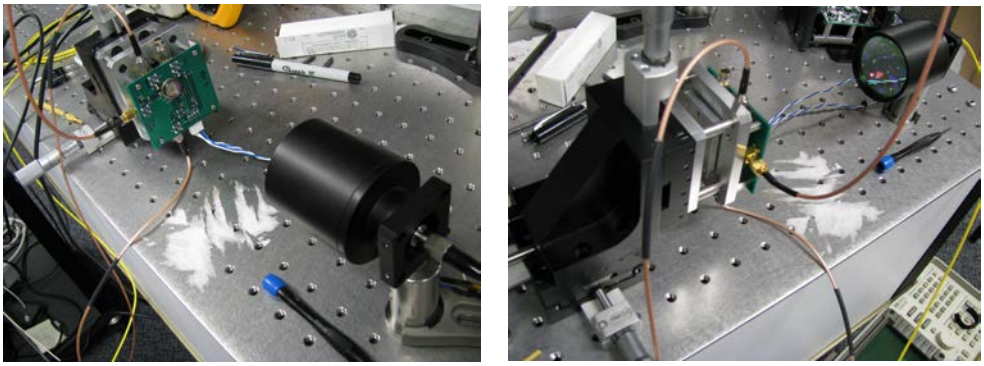

Figure 84: APD receiver calibration setup

The receiver calibration setup uses a CW tunable laser modulated by an acousto-optic modulator (AOM) to produce 5 ns to 200 ns pulses. The pulses are attenuated by a programmable optical attenuator with range from 0 to 60 dB, and delivered to the

projector lens via standard SMF-28 fiber. The projector consists of a 37 mm EFL collimator lens followed by a 150 mm EFL focusing doublet. The 1 / e^2 waist intensity diameter for the Gaussian beam projected by this system is about 40 µm. Importantly, the Rayleigh range is over 3 mm. These factors make it easy to focus the detector and ensure almost zero misalignment or focus error. The receiver board is set up in its standard configuration, connected to a temperature controller, +3.3V power supply, and high voltage bias. The differential output is connected to an oscilloscope to take peak response and RMS noise level measurements. This setup is shown schematically in Figure 85. Some receiver board support components are omitted in the figure for clarity.

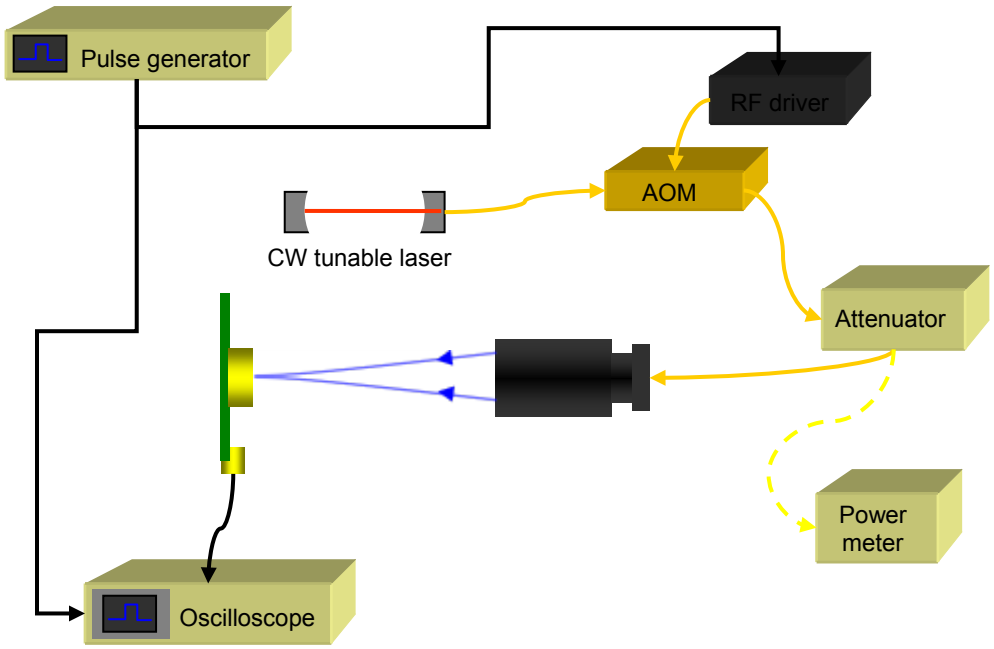

Figure 85: Calibration schematic

The tunable laser feeds a 1 mW CW signal into the AOM via a standard single mode fiber. The AOM is driven by an RF oscillator modulated by an arbitrary function

generator programmed to produce a short pulse with a kHz repetition rate. The AOM is able to chop the CW beam into pulses down to 4 ns in duration. The pulses are attenuated by a programmable, calibrated SM fiber attenuator. The attenuated signal is measured by a calibrated average power meter. Using the pulse envelope, repetition rate, and average power, the peak pulse power is computed. Following the computation of peak pulse power, the attenuated output is disconnected from the average power meter and connected to the beam projector lens. The APD is focused and aligned to the waist of the test beam.*

As the attenuator is adjusted, the peak pulse power is measured by an oscilloscope. The voltage responsivity (V / W) is calculated from the ratio of attenuated peak pulse power to peak voltage response at a fixed (feedback controlled) operating temperature and APD bias voltage. The current responsivity (A / W) can be obtained by considering an estimate of the transimpedance gain (3300 Ω, differential), and any other secondary gain in the system. Since the fundamental responsivity (M = 1) of the APD is given by the manufacturer (1.05 A / W at 1550 nm) the avalanche gain can be computed and plotted as a function of bias voltage.

* The lens may be roughly aligned by first using the output of a HeNe beam fiber coupled to the projector lens.

5.10.2.2. Characterization Test Results

Several receiver modules were tested using the method of Section 5.10.2.1. Each was identified by a unique serial number and supplied with responsivity, noise and impulse response data as measured by the manufacturer. In all tests, the APD module was stabilized to a controlled temperature of 285 K with an internal thin film TEC and was current limited by a 5.1 kΩ resistor in series with the APD. The tunable laser wavelength was fixed at 1550 nm for all tests.

Figure 86 plots a family of responsivity curves for several bias voltages. The responsivity in the linear range is obtained by linear regression to a sub-set of points. The computed slope responsivities range from 16.4 kV / W to 181 kV / W. The avalanche gain is estimated from an assumed fundamental responsivity of 1.05 A / W at 1550 nm and transimpedance gain of 3300 Ω. When examining the deviations from linearity, it is clear that the response rolls off at around 110 mV regardless of the gain of the APD. This defines the region of linear operation and establishes the TIA as the limiting factor on the upper end of the dynamic range. A TIA output of 110 mV corresponds to an input current of 33 μA. Clearly, this current limit is encountered at lower optical power when the avalanche gain is higher.

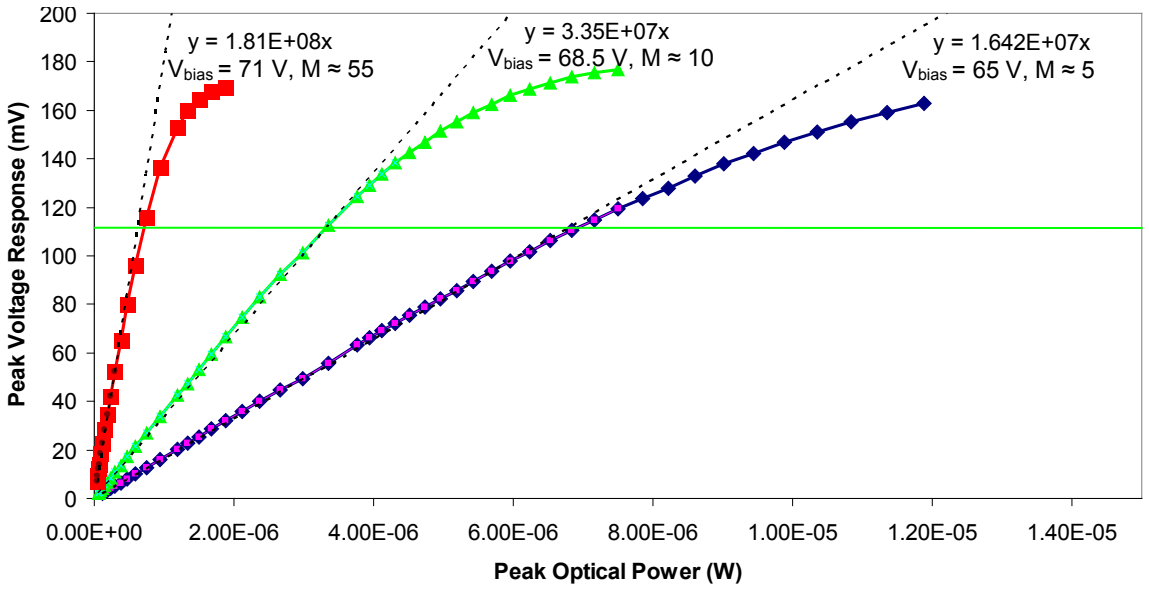

Figure 86: Voltage responsivity (3755-1 2n 100607)

To measure the avalanche gain as a function of bias voltage, as shown in Figure 87, a constant intensity optical pulse train was applied while the bias voltage was varied. Averaging of many pulses was used to increase the accuracy of the measurements. A typical exponential behavior was observed from several volts above punch through, to the threshold of breakdown where the avalanche gain was observed to be about 100.

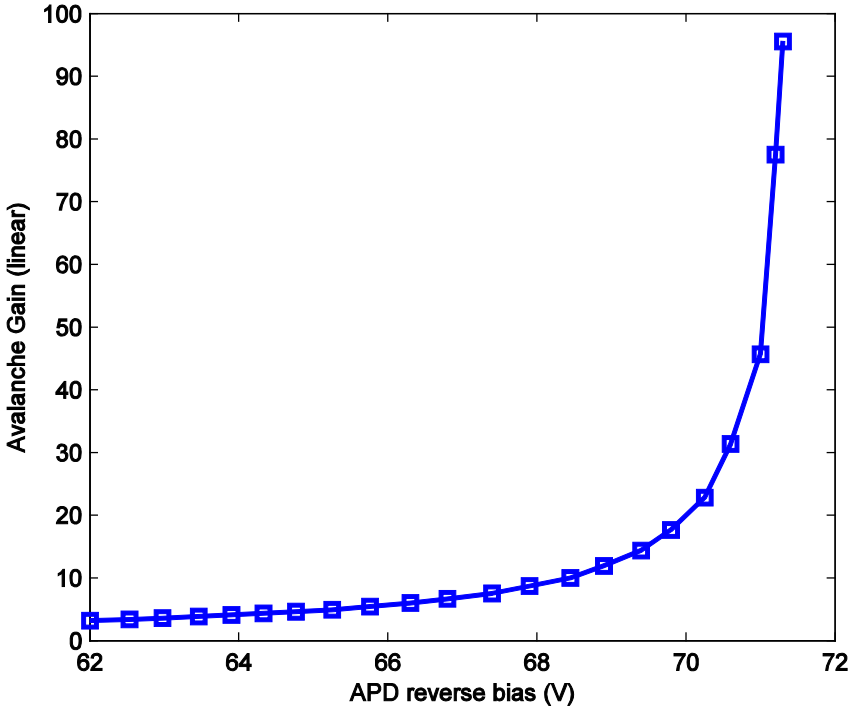

Figure 87: Avalanche gain versus bias voltage (3577-1 2n 100607)

The total voltage noise, including APD and TIA, as a function of bias voltage was measured by shielding the APD from all light and varying the bias (Figure 88). An oscilloscope digitized a trace of over 1 Mpoint and found the rms voltage value, which is plotted below. The noise represented here only includes the output-referred voltage noise of the APD and TIA. The voltage noise from the scope terminal was subtracted (in quadrature, since noise powers are additive). At very high bias levels near breakdown the noise did not appear to have a Gaussian statistical distribution and instead noise appeared in bursts. This is possibly due to partial breakdown in the APD.

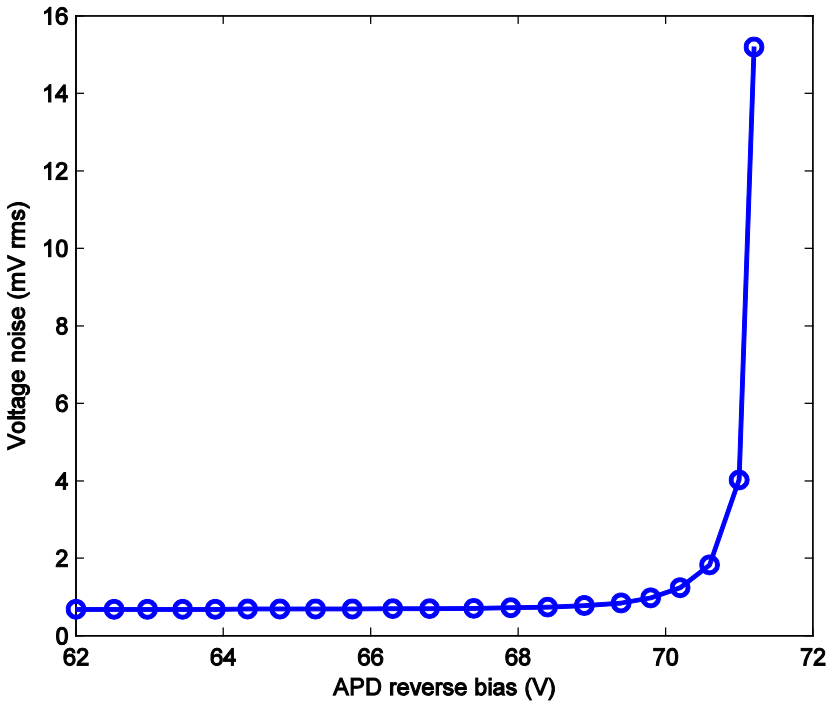

Figure 88: APD noise voltage versus bias voltage (3577-1 2n 100607)

The noise and responsivity measurements are combined in Figure 89 to produce a plot of the noise equivalent power versus bias voltage. NEP represents the optical power per square root of electrical bandwidth that produces an SNR of 1. NEP is measured in units of optical power per square root bandwidth. The square root in the denominator results from the square law property of direct detection: optical power is proportional to the square of the voltage, and electrical noise has units W / Hz. The downward sloping portion of the curve represents the region where the noise is dominated by thermal noise in the amplifier; the upward sloping portion represents the limiting case when the shot noise of the APD dominates. The optimal point lies on the boundary of these regions. Although NEP is a commonly used performance metric, it does not represent SNR in a true system since it ignores the shot noise of the signal. Noise generated at the oscilloscope input is not included in this measurement.

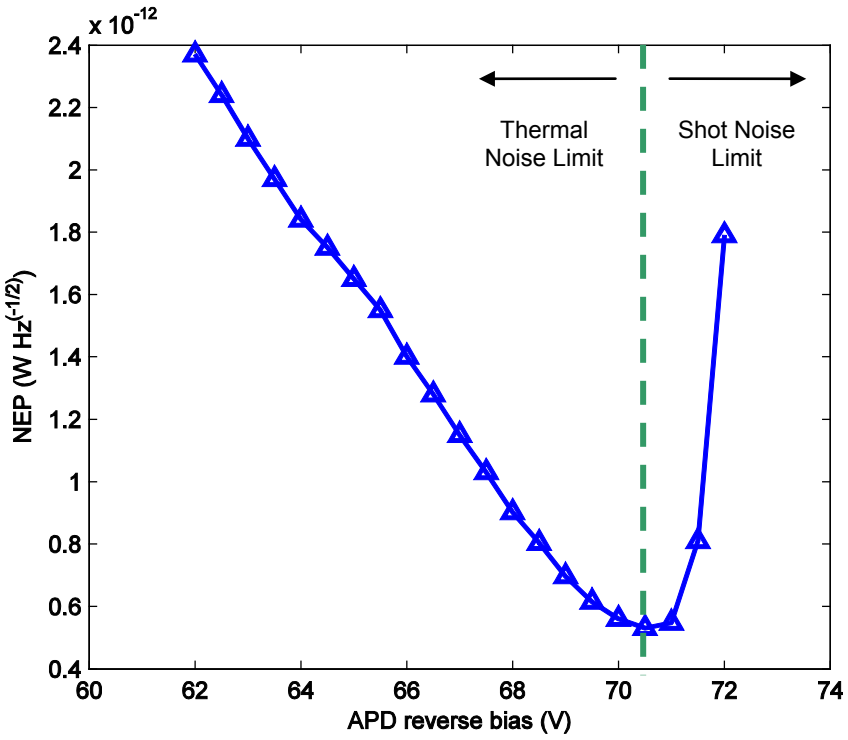

Figure 89: Receiver NEP versus bias voltage (3577-1 2n 100607)

The reach-through voltage is an important consideration in the operation and calibration of an APD. This voltage is indicated by a sharp rise in the dark current curve. When operating below this voltage, bandwidth is greatly reduced by junction capacitance / slow transit.

Linear dynamic range is the most important attribute for a Spectral LADAR receiver after NEP and bandwidth considerations. Nonlinearities in intensity response cause serious distortions in the computed spectrum of a voxel. These distortions can easily cause the misclassification of pixels and can corrupt the point cloud even (or, especially) at high SNR. In principle it is possible to correct for nonlinearities by applying a linearization transform to the data. This is difficult in practice since temporal distortions may

accompany some intensity (voltage amplitude) distortions. Also, since the noise may not have the same compression as the signal, the SNR of pulses extending into a nonlinear response region may not have proportionally increasing SNR. Nonlinear response in the receiver can come from space charge effects in the APD, but the pre-amplifier (TIA) and current limiting resistor are more likely to be limiting factors [201, 202]. The MAX3277 TIA is limited to 50 μA linear range, which produces a linear voltage response of up to 165 mV (differential). At M = 2, this limits the maximum optical power to about 24 μW. At much higher avalanche gains (M = 40) where the SNR is expected to be higher, the optical power is limited to 1.2 μW in the TIA limit.

Figure 90 plots the ratio of saturation voltage (110 mW) to NEP, converted to optical power. The linear dynamic range remains approximately constant from above the reach-through voltage to the point where APD shot noise remains insignificant. In this region, increasing bias improves the SNR without degrading the dynamic range since the dominant noise source (in terms of optical power) scales inversely with gain, balancing the reduction maximum linear optical power. As the APD noise starts to dominate, this balance is disrupted and the dynamic range is degraded.

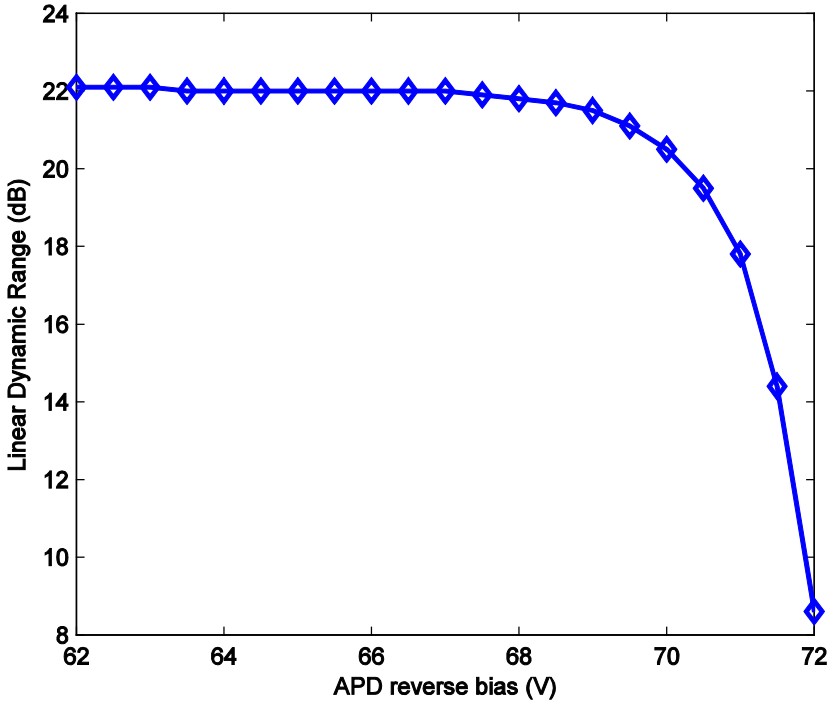

Figure 90: Linear dynamic range versus bias voltage (3577-1 2n 100607)

Inspection of Figure 89 and Figure 90 shows that the optimum bias voltage for the detector in question, which preserves dynamic range at low NEP, is about 69 V.

5.10.3. Spectrometer Calibration and Band Configuration

The focus, alignment, and calibration of the spectrometer module are among the most critical construction procedures. These procedures determine the spectral resolution, a large part of the insertion loss, and wavelength accuracy of the system. To accomplish this, the MMF connecting the receiver lens to the spectrometer's input is decoupled, and is connected to a calibration setup consisting of several instruments. This configuration

is shown in Figure 91. This setup is similar to that used for detector calibration (Section 5.10.2). A wavelength calibrated tunable laser is modulated by an AOM to produce 4 ns duration pulses with a reference signal sent to trigger a digitizer. An attenuator reduces the power of the calibration laser to be within the dynamic range of the APD.

The purpose of the calibration setup is to have the grating sweep through a very large angle, capturing multiple positive and negative diffraction orders for a particular wavelength. Repeating this for multiple wavelengths and identifying many peaks to fit Equation 43 yields an over-determined system of equations with two variables: φ_0, the grating angle for the zero-order diffraction peak, and K, the deviation angle. These parameters, plus the grating period[*], fully determine the map of grating scan angle (φ) to center wavelength.

[*] The grating period, 150 grooves / mm, is assumed to be exact.

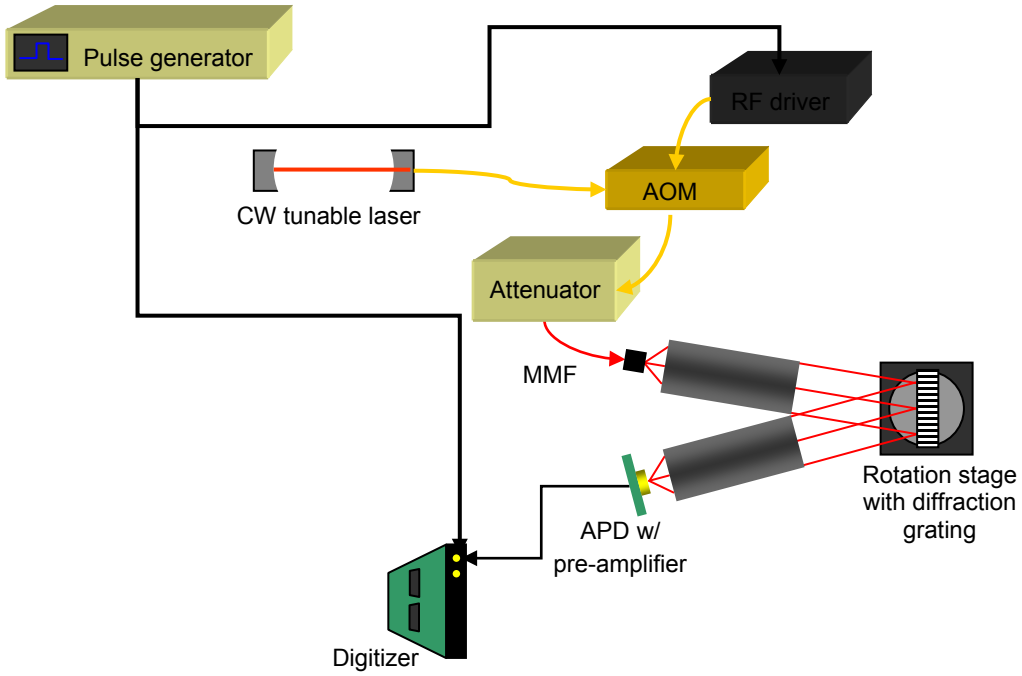

Figure 91: Spectrometer calibration mode configuration

The alignment and calibration begins by positioning the input fiber (entrance slit) very close to the axis of the collimating lens. The fiber must then be positioned axially at the focal point of the collimating lens. The distal end of the input fiber may be temporarily attached to a HeNe laser at this point to provide a visual aid for a first approximation. It is difficult to achieve exact collimation without some sort of reference. Unfortunately, a straightforward (if subjective) means of assessing collimation using a shear plate interferometer is not useful in this case due to the lack of spatial coherence in the multi-mode input. Instead, a visual assessment is made, starting with a HeNe laser. The beam from the collimator lens is adjusted until the beam appears to have a constant diameter over 4 - 5 m of propagation. Then, the focus is repeated with a NIR beam and viewed

with an IR viewer.* At this point, the beam is assumed to be collimated. Removal of the grating and grating holder is necessary to avoid obscuring the beam while testing collimation. These components are reinstalled for the next step.

The next step aligns the grating grooves normal to the incident beam in the cross-diffraction plane to eliminate conical diffraction that would cause a wavelength-dependent misalignment. A HeNe laser is used once more, and connected to the input fiber. The focusing lens is installed. A position sensitive detector, in this case a silicon lateral effect photodiode (LEP), is placed near the observed focus of the zero order beam behind the focusing lens. The LEP is to measure the focal plane height of multiple diffractive orders to make sure that the diffraction is planarized – which is indicated by zero height change in all diffracted orders. The LEP has a 4 x 4 mm active area, and an internal microcontroller that calculates and transmits position data over a USB interface if the analog output channels are not required. Alternatively, a CCD or CMOS sensor with image processing routines could be used in lieu of a LEP. The advantage of LEPs (and Quad-cell photodetectors) is a much faster response time allowing them to be used in relatively high (10 kHz) bandwidth feedback controllers. The USB interface was used in this situation since fast response time was not critical. When using position sensitive detectors, care must be taken to ensure that only one diffractive order illuminates the active area at a time, and that the stray light from very strong on-blaze orders does not interfere with the detection of weaker adjacent orders. This is frequently a problem when

* It may be desirable to use the reciprocity property of lenses to focus and align the collimating lens with the grating in the Littrow configuration. This will enforce the planarity and focus parameters, but the technique did not work well using the laboratory demonstrator hardware.

using coated refractive optics out of the anti-reflective coating band, such as in this case. Using a slit sized so that only one diffractive order may pass at a given scan angle helps by reducing stray light from scattering or adjacent diffractive orders. A control program on a PC communicates with the grating rotation stage and scans the grating, and simultaneously records the height information from the LEP. Often, the on-blaze order exceeds the adjustable dynamic range and is not useable, but many other orders are. A plot is produced, similar to those shown in Figure 92. Each point represents the height of a "spot" detected by the LEP over a particular intensity threshold. Some spurious points occur due to scattering, and each color represents a scan with a different adjustment of grating roll and pitch relative to the incident beam. The red colored points indicate excessive grating pitch by its quadratic shape, while the blue points indicate excessive grating roll by its nonzero linear slope. Combination of these two effects can appear simultaneously with a combined quadratic and sloped character. The green points are representative of relatively good alignment, showing parallelization within an assumed LEP error margin. While this alignment was done at 633 nm due to the sensitivity of the silicon LEP, the results are applicable to SWIR wavelengths within an acceptable margin of error.

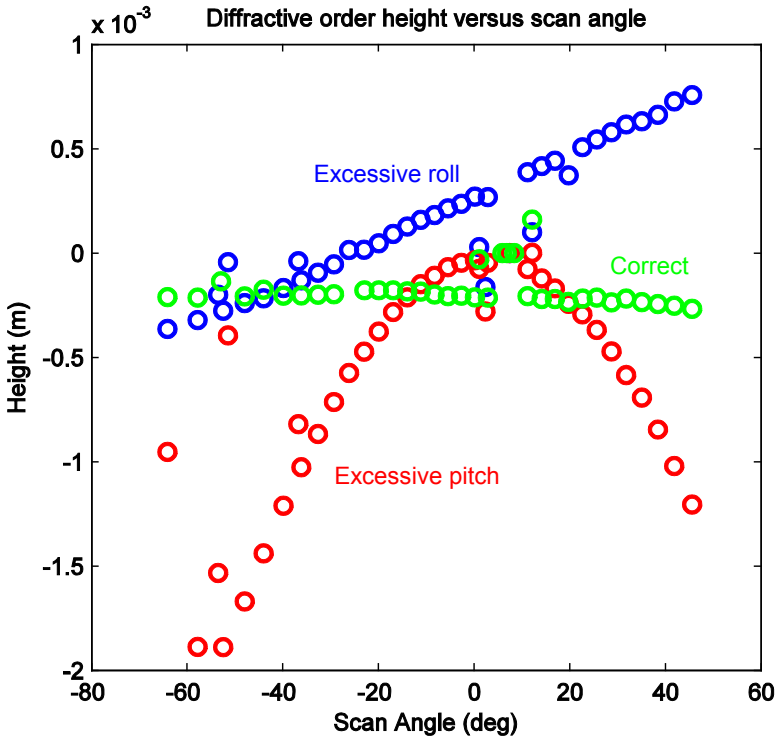

Figure 92: Height of diffracted orders on LEP (090515)

The third step is to align the APD to the focal point of the focusing lens. Prior to aligning the APD, a 100 μm or 200 μm fiber is positioned on the axis of the focusing lens using an alignment collar. A coarse grating scan is performed, identifying the peaks of a 1550 nm line. The grating is then turned to the +1 diffractive order (on-blaze) and the fiber is focus aligned. Scans over small angular ranges may be performed to assess the coupling efficiency and line spread. These scans reflect the overall image quality of the system and the degree to which the collimating lens image is at an infinite conjugate. The other purpose is to establish a wavelength and scan angle at which the +1 diffractive order is on the focusing lens axis. This is important for positioning the APD since the lateral alignment collar does not register to the detector board. To align the APD, the input fiber is connected to a HeNe laser to use as a visual pilot beam. The detector board is attached,

and aligned to the pilot beam. Then, the pulsed SWIR laser is reconnected and the APD active area is aligned at the specific wavelength and scan angle recorded earlier. Once alignment has been achieved, a wide angle scan is performed with the SWIR pulse source at a particular wavelength. This is repeated for multiple wavelengths to create the plot in Figure 93.

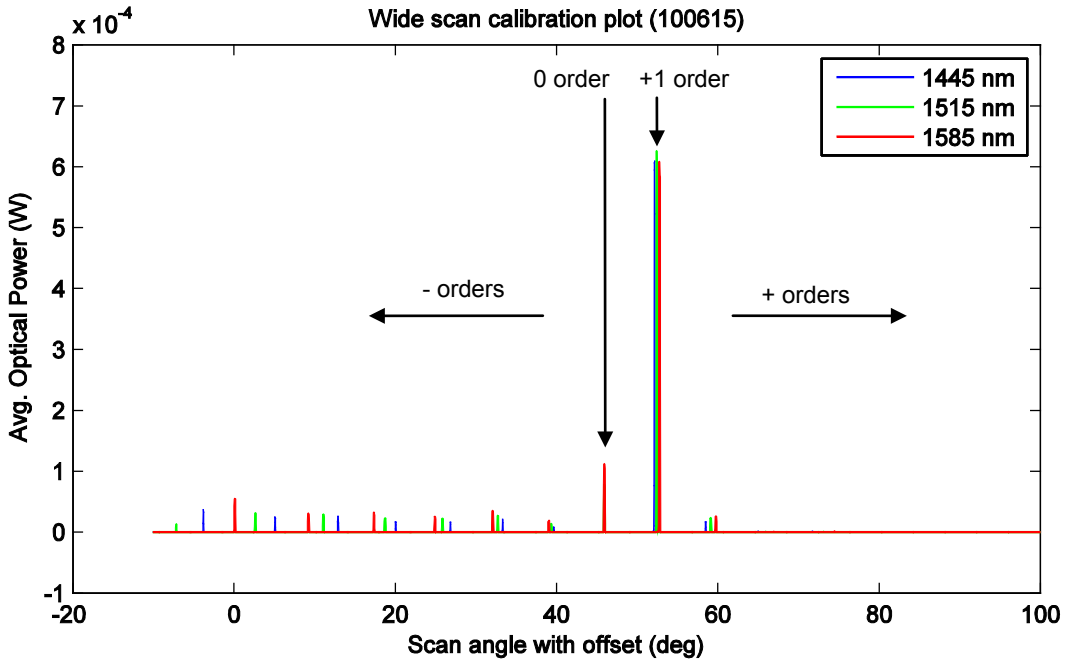

Figure 93: Wide angle calibration scan (100615)

The peaks in Figure 93 are identified by diffractive order, and the scan angles corresponding to diffractive peaks at the respective wavelengths are used in Equation 43 to fit the parameters φ and K.

The measured efficiency for random polarization in the first order of Figure 93 is approximately 69%, 68%, and 64%, for wavelengths 1445 nm, 1515 nm, and 1585 nm,

respectively. The average insertion loss of 1.7 dB, when compared to Figure 70, represents performance limited mainly by grating diffraction efficiency and not other aspects of the system such as AR coatings and optical coupling.

Optionally, a fine scan can be performed using the APD around the +1 order for several wavelengths to produce Figure 94, from which resolution and line spread performance can be evaluated. Figure 94 shows the line spread of an early APD variant, which had some significant spectral side lobes resulting from scattering from the edge of the APD die. Insertion loss is not inferred when using the APD since the uncertainty of the APD gain makes for an unreliable absolute power measurement. Insertion loss can be measured using the fiber exit slit mentioned above.

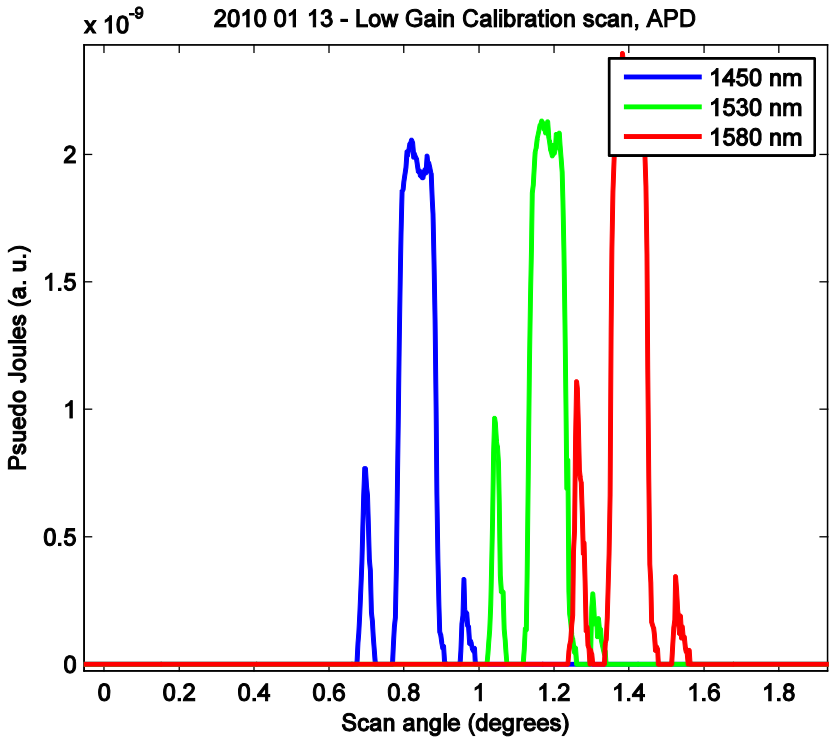

Figure 94: Line spread functions for early APD versions (100113)

The calibration procedure produces a data structure containing the variables in Table 7, along with typical values. These values are used in the data acquisition code, as shown in Figure 80.

Table 7: Typical spectrometer calibration values

Parameter	*Typical Value*
d (Groove Period)	6.67 µm
w (Exit aperture full width)	200 µm
f (Collimating focal length)	55.58 mm
m (Diffractive order)	1
φ_0 (Scan angle for zero order)	varies
K (Deviation angle)	5.65 degrees

The standard band configuration is given in Table 8. This configuration is used in all images described in Section 7, 8, and 9, unless otherwise noted.

Table 8: Standard optical band configuration

Band (#)	*Band Start (nm)*	*Band Stop (nm)*
1	1080	1104
2	1102	1126
3	1123	1147
4	1145	1169
5	1166	1190
6	1188	1212
7	1210	1234
8	1231	1255
9	1253	1277
10	1274	1298
11	1296	1320
12	1318	1342
13	1339	1363
14	1361	1385
15	1382	1406
16	1404	1428
17	1426	1450
18	1447	1471
19	1469	1493
20	1490	1514
21	1512	1536
22	1534	1558
23	1555	1579
24	1577	1601
25	1598	1622

5.10.4. Transmit / Receive Focus and Alignment

High coupling efficiency depends upon the precise alignment of the transmitter and receiver optical axes. The system is constructed so that the transmission axis is nearly coaxial with that of the receiver. This arrangement minimizes parallax error, which is the lateral separation ("walkoff") of non-coaxial beams and is range dependent. Both the

transmit and receive beams must be focused at infinity and have the same angular divergence. Under this condition, the receiver lens will image the illuminated area of the target with appropriate magnification so that the backscatter is fully captured by the receiver fiber's core diameter.

The first step is to focus the transmitted beam and the receiver lens. The fiber coupling between the receiver lens and spectrometer greatly simplifies this process since it allows the receiver lens to be operated in reverse. Reverse operation of the receiver lens relies on the reciprocal property of lenses and consists of sending an optical beam into the receiver fiber and using the receiver lens to project that beam out into object space. The beam projected in this configuration represents the instantaneous field of view of the receiver. The receiver is operated in reverse by coupling a HeNe laser into a 62.5 μm core diameter graded index fiber and then into the receiver fiber, once disconnected from the spectrometer. The receiver lens then projects a spot at a range of about 40 m. The focus of the receiver lens is adjusted so that the diameter of the projected (red) spot at range minimized. This approximates focus at infinity. Next, the transmitter is focused. For the purposes of focusing, the visible portion of the supercontinuum source is helpful, although a SWIR camera system or SWIR image intensifier could be used instead. Normally the transmitter is filtered through RG850 colored glass – this filter may be removed to perform the focus and alignment. A visible ND attenuator of 10 or 20 dB may be temporarily installed for eye safety during the alignment process. Like the receiver, the spot size of the transmitter is minimized at (at least) 40 m range to approximate collimation. The beams created by the reversed receiver and transmitter are

measured for the approximate divergence angle, 1 mrad. Once the two beams are focused, they must be angularly aligned. This straightforward process involves adjusting the small coaxial mirror so that the transmitter beam and receiver "tracer" beam are coincident at 40 m range. The receiver fiber is not laterally adjusted since it is presumed to be aligned to the receiver lens axis for best receiver lens focus. Figure 95 demonstrates the visible appearance of the beams in a misaligned (at 4 m, left) and aligned (at 40 m, right) condition. The receiver tracer is red, while the unfiltered supercontinuum appears yellow-white. The blue and red halo to either side of the transmitted beam is the result of some dispersion in the beamsplitter, which is less significant in the shortwave infrared.

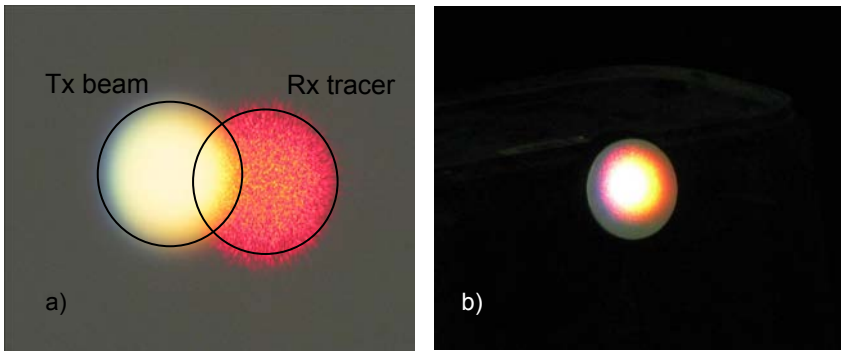

Figure 95: (a, left) Transmit and receiver tracer beam misaligned, (b, right) transmitter and receiver tracer in good alignment (100313, 100320)

Once the transmitter and receiver axes have been aligned by the reverse receiver method, the HeNe tracer beam is disconnected from the receiver fiber. The next step is to align the reference beam to the receiver lens. Since the reference beam has an excess of optical power and a large depth of field owing to its small input NA, focus is not critical. Lateral alignment is achieved by adjusting the reference beam turning mirror so that the

reference beam is aligned to the fiber. It is important to note that multiple beams diverge from the reference beam splitter, and that the proper one, the one created by Fresnel reflection, is selected. Other beams, split from AR coated surfaces, have a spectral content that is a function of AR coating reflectivity, which is not balanced (white) as is the Fresnel reflected beam. It is also important to select the right beam to align to the receiver fiber. Since the receiver lens is AR coated for SWIR wavelengths, and more reflective at visible wavelengths, several reflections bounce around in the lens to create a "starfield" pattern shown in Figure 96.

The reference beam, having low NA and launched at high angle, does not achieve equilibrium mode distribution* in about 1 m of multi-mode fiber as evidenced by Figure 65.

Figure 96: Multiple beams from reference beam at receiver lens focal plane (100125)

* At visible wavelengths, at least.

Following the alignment of the reference beam, a fine alignment is performed by using a calibrated 99% diffuse reflectivity target at 40 m. All filters are installed in the transmission path for this last step; the system is not perturbed in any way following fine alignment. First, the ND attenuators are installed and adjusted in the path of the reference beam so that the reference beam does not overload the APD. The receiver fiber is connected to the spectrometer. The control PC runs a MATLAB script that plots the intensity of the remote target at about 2 second intervals, as shown in Figure 97. The alignment of the receiver lens and reference beam steering mirror are adjusted to maximize the peak voltage amplitude subject to the linearity limit, shown by a green line. When the peak voltage of the unfiltered signal (dashed line) exceeds the linearity limit in any band, the attenuation of the transmitter or reference beam is adjusted to bring the response within the limit. Higher transmitter attenuation equates to a longer effective attenuated range, whereas the attenuation on the reference beam is relatively meaningless. The attenuation of the reference beam is adjusted so that the reference beam peak voltage amplitude is as high as possible without exceeding the linearity limit. The APD bias voltage can also be adjusted using this dynamic performance feedback technique to optimize the SNR plot for best performance.

The MATLAB script also dynamically displays the SNR, both pre-and post digital filter. A noise histogram is also displayed (Figure 97).

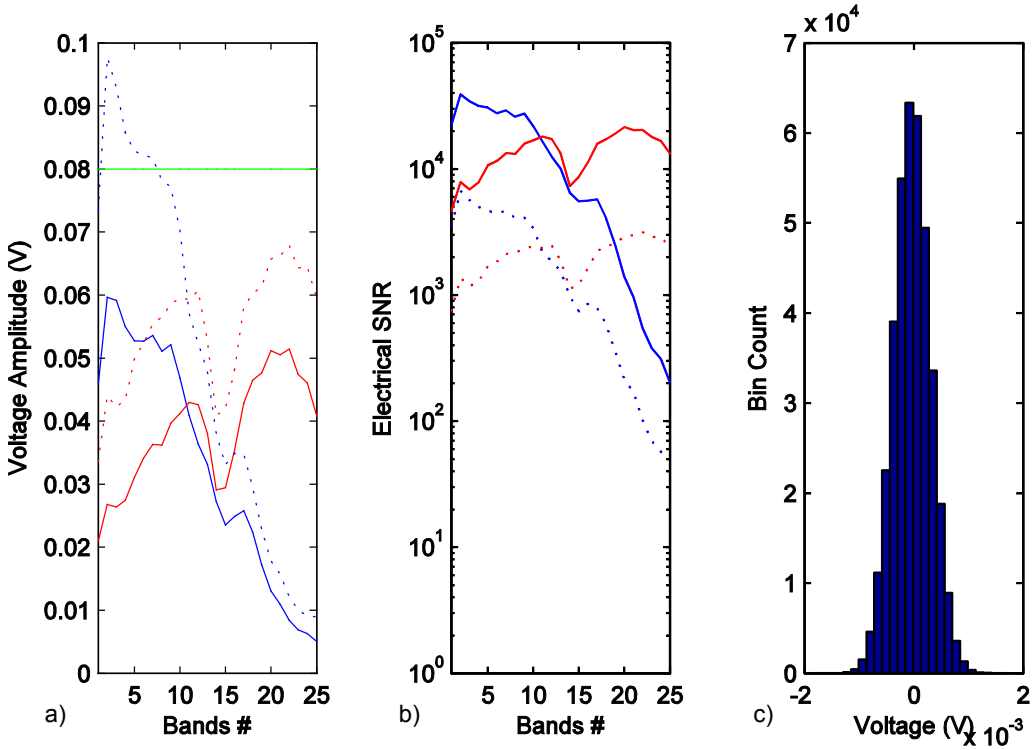

Figure 97: Fine tuning plots (l-r): Peak voltage amplitude per band (a), SNR per band (b), noise statistics (dotted line is pre-digital filter, c) (101217)

5.10.5. Operational Procedure

Following the alignment procedure, the instrument is ready to record images. Before any data collection is started, all instruments are idled for about 1 hour to come to thermal equilibrium. Because the instrument is sensitive to small thermal variations, the room air conditioning unit is turned off.

First, a canonical set of pulse profiles is obtained. This involves blocking the transmitted beam, and collecting only the reference return for a single pixel. The standard MATLAB

data acquisition script is used with a high degree of time waveform averaging to eliminate random noise. This set of reference returns determines the digital filter frequency response by the matched filter technique (Section 3.1.6.2) and also serves as the reference intensity level for source compensation.

The instrument is next configured to collect a white balance sample with a calibrated target at the approximate range of the scene. The main MATLAB script which performs the standard data acquisition is configured to acquire only a single pixel at high averaging (10,000 samples). The waveforms from this data collection are then processed to represent the white balance spectrum. Drift in the instrument over time can cause changes in the white balance, so this, along with the canonical set, are obtained prior to each measurement and are re-measured every few hours.

The scan angle range is an important parameter for a data collection. To verify the scan pattern visually, the receiver fiber may be briefly disconnected and fed in reverse with the same HeNe laser used for alignment.

The MATLAB script is configured with its operational parameters and executed. The system performs some initialization checks on the instrument, and data collection begins. A data collection session can take up to several hours to complete.

The data from the acquisition script contains the full record of all data. For each azimuth and elevation point in the scanning grid, the entire time record (trace) is captured for each

band and stored in a file. No filtering or processing occurs at this point. Since no processing occurs in the data collection stage, this affords total flexibility for modification of the signal processing routines and re-processing at a later time. This greatly enhances the ability to experiment with different processing techniques and make performance comparisons on the basis of a constant data set, and without the need to capture new data.

6. Active Polarization Imaging

This section describes a benchtop instrument constructed to measure the polarization signatures of various materials. An experimental approach was taken to evaluate the utility of this modality since the simulation of polarization scattering from random media is often inexact. Polarization sensing was not included in the laboratory demonstrator (Section 5) since the supercontinuum source was randomly polarized. Consequently, the perception information provided by comparing spectral reflectivity to spectral depolarization is not considered since only a single wavelength was used in this instrument.

6.1. Instrument

An instrument was constructed to collect reflected polarization signatures from linearly polarized laser illumination, and to capture polarization images of scenes at close range. While having the same geometry and detection scheme as an AM-CW direct detection LADAR system, the low power diode laser and low modulation frequency preclude range resolved operation since the maximum range is shorter than the range accuracy.

6.1.1. Sensor Optics

A monostatic polarimeter was constructed using an amplitude modulated laser to observe a target sample at a range of 2.5 m. The coaxial beam pattern is a geometrically similar to a long range LADAR system. This instrument implements a greatly simplified form of ellipsometry: the angle of incidence is identical to the angle of backscatter, and only orthogonal polarization is measured (DOP, Section 3.2.3). Full Mueller matrix polarimetry is eschewed since it is unlikely to be feasible for single-pulse measurements due to the required rotation of polarizers and waveplates or the need for a complicated beamsplitting receiver to determine the 16 elements of the matrix. Full polarization analysis has been shown to provide additional information that is not appreciably more useful than simple depolarization measurements [203, 204]. A schematic of the polarimeter is shown in Figure 98.

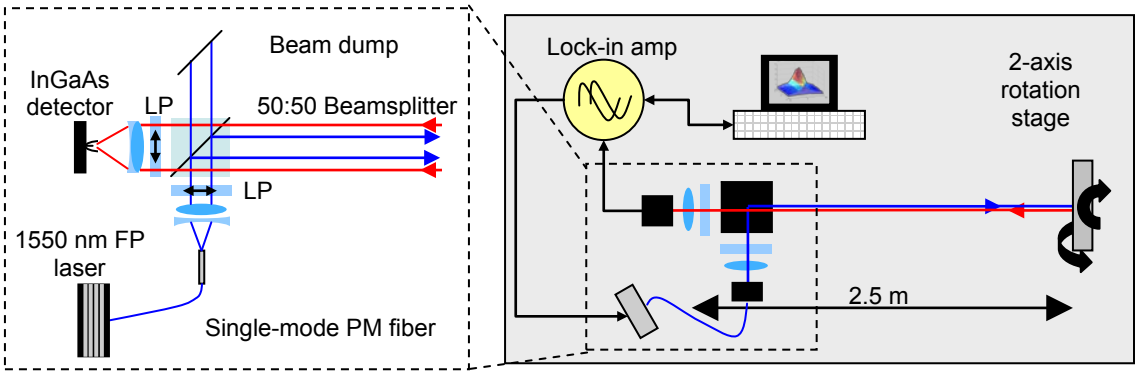

Figure 98: Polarization signatures measurement apparatus

The transmitter consists of a 1550 nm, 1 mW average power, sinusoidally modulated FP laser diode coupled into a single mode fiber. A collimator projects a 7.0 mm diameter

beam ($1 / e^2$, changed to 2.1 mm in imaging mode) which is sent through a 100,000:1 ratio linear polarizer. The transmitted light is split by a 50:50 polarization independent beamsplitter, half of which goes to the target and half of which is sent to a beam dump. The backscattered light traverses the same beamsplitter and, after passing through a rotatable linear polarizer, is focused by a 25 mm diameter lens to a 500 μm InGaAs PIN photodiode. Lock-in* amplification / detection is used at 8 kHz. A motorized two axis stage tilts the sample to obtain DOP measurements over a range of angles.

A Windows XP based PC controls the stage motors and lock-in amplifier through a LabWindows/CVI based application and ActiveX controls. Communication with the lock-in amplifier is established over a RS-232 connection. The control software scans the stage and takes magnitude readings from the lock-in amplifier with each increment of stage movement.

6.1.2. Lock-in Receiver

A lock-in amplifier is used on the receiver to achieve high SNR performance at low light levels. This device is essentially an AM homodyne system (Figure 99). A frequency mixer is the fundamental component of a lock-in. Some systems use an analog mixer however others, including the model used in this test, utilize digitizers and DSP based

* Phase-sensitive detection

techniques. This, combined with a low pass filter, allows a lock-in amplifier to make high sensitivity measurements by using very narrowband filtering. Unlike electronic bandpass filters which typically have Q-factors no greater than 100, the Q of a lock-in amplifier can be orders of magnitude higher. The primary advantage of a lock-in amplifier is the ability to extract a narrowband signal out of 60 dB or more of noise and operate at frequencies out of the range of significant $1/f$ noise.

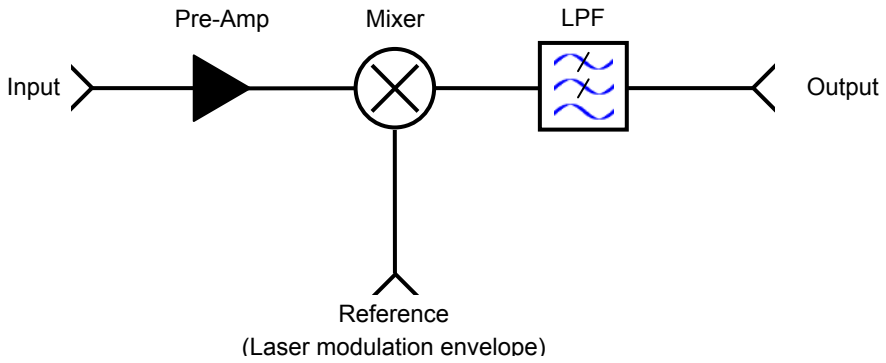

Figure 99: Lock-in amplifier

The lock-in amplifier typically generates (or receives, from an external generator) a reference signal that modulates an optical beam or other sensor. The output of a transducer is then connected to the input, and the reference and signal are mixed to demodulate the signal to a DC baseband. This technique is based on the orthogonality of sinusoids and the result of the mixing operation is apparent when product-to-sum trigonometric identities are considered, as in Equation 56. The product of cosinusoids yields the sum of two cosinusoids at the sum and difference frequencies. Note that for the case of homodyne reception, any ωt terms disappear in the difference cosine term in

the RHS. This leaves only the phase terms, which indicate the phase-sensitivity of the lock-in detection scheme.

Equation 56

$$\cos\theta\cos\varphi = \frac{1}{2}\cos(\theta-\varphi)+\frac{1}{2}\cos(\theta+\varphi)$$

For homodyne mixing, the difference frequency is DC. Mixing the reference (ω_r) with other input frequency components of the input will of course result in output components with finite frequency. When the output of the mixer is integrated (low-pass filtered) only the DC component, representing the amplitude (A) and phase (θ) of the signal, contributes to the integral when the period of integration is much longer than the period of the highest frequency input component. Components, including signal bandwidth and noise components, around DC will be included to the extent that the integration time (T) is not infinite in duration (Equation 57). The integration time corresponds to adjusting the cutoff frequency of a low pass filter.

Equation 57

$$V_{out}(t) = \frac{1}{T}\int_{t-T}^{t} A\cos(\omega_r\tau+\theta)V_{in}(\tau)d\tau$$

The advantages of this technique can also be seen from a frequency domain perspective. Since frequency domain convolution is the dual of time domain multiplication, the frequency domain convolution of narrowband spectral lines at some finite frequency will yield two spectral lines at the difference (DC for homodyne) and sum of the original

frequencies. Importantly, the low frequency noise* is frequency shifted as well, resulting in a DC baseband with the noise spectral density of higher frequencies. The form of Equation 57 has some similarity to that of the Fourier transform relations, and a lock-in amplifier also bears some similarity to a swept frequency spectrum analyzer.

6.1.3. Imaging System

A modified form of the polarimeter, using a gimbaled mirror to image a scene with a flying-spot scan, generates polarimetric images for objects at close ranges. This is primarily used with a cylindrical mounting surface, upon which materials may be affixed. Using a cylinder allows images to be created with known and continuous aspect angle variation. The geometry of this scanning configuration is shown in Figure 100.

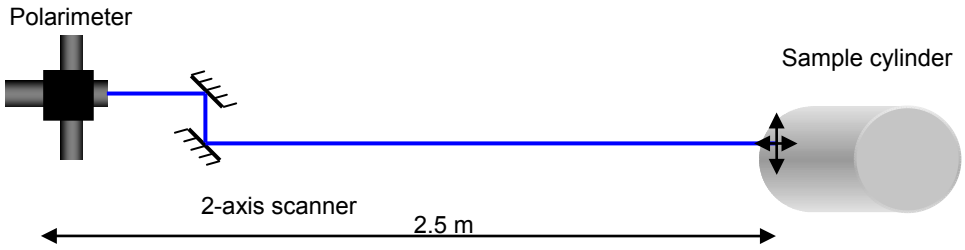

Figure 100: Imaging polarimeter geometry

* i.e., the low frequency noise that usually makes measurements close to DC a bad idea.

6.2. Procedure

The polarimeter receiver was focused and aligned with respect to the transmitter axis and beamsplitter tilt. The polarizer axes were rotationally aligned by temporarily changing the configuration to where the transmitter was aimed directly into the receiver. Also, while the beamsplitter was nominally polarization independent, calibration of the polarization splitting ratio found a slight 5% departure from the 50:50 ratio.

Before each test the instrument background was measured by effectively eliminating backscatter from the primary beam with a dark target at approximately 20 m. The background originates from any inadvertent and residual backscatter in the beam dump, beamsplitter, or mechanical mounts. This was always subtracted from the raw data.

For the polarization signature measurements, each sample was mounted as flat as possible to the two axis tilt stage. The tilt axes were adjusted to lie in the plane of the sample's front surface, adjusting for sample thickness to minimize relative beam translation resulting from tilting. The scan was performed from -50 degrees to 50 degrees in azimuth, which was the major scan axis. A smaller range of angles, -5 degrees to 5 degrees, was scanned in elevation to capture the extent of any specular peaks.

The polarimeter configuration was slightly modified to perform imaging measurements. In this case, the additional step of aligning the beam steering mirrors was added to the instrument setup.

6.3. Results

This section discusses the results obtained with the polarimeter, in the signature collection mode where a single point was observed on a sample with varied aspect angle (Section 6.3.1), and the imaging mode, where a beam was scanned over a range of angles and corresponding surfaces (Section 6.3.2).

6.3.1. Polarization Aspect Measurements

A variety of materials are measurable with the polarimeter such as painted surfaces, construction materials, and plastics. Other reports of the typical polarization differences between natural and man made materials are confirmed. Most man-made materials are less depolarizing than natural materials due to their smooth surface characteristics. One notable exception to this is foliage. Depending on the surface structure of the leaves, some foliage can be highly depolarizing while others can have highly polarized backscatter at specular angles. This is usually due to the waxy cuticle present to varying degrees on different plant leaves.

Samples which have highly similar spectral signatures are most interesting from a polarization perspective as an alternative means of differentiation and identification. One such material pair, looked at in depth, is clothing versus foliage. Since cotton clothing and foliage have cellulose as a common structural polysaccharide, the nominal spectral differences between these material classes may be less than natural and random variations within each class. A good discriminant between these materials is the presence of water, the vibrational overtones of which can be easily detected in the SWIR. Unfortunately, the ubiquity and variability of water in the environment poses a problem for signature predictability. Dry clothing and senescent foliage both contain little water, while wet clothing (a reasonably common occurrence) and live vegetation have relatively high concentrations. It is easily recognizable though, that vegetation and woven clothing have very different surface characteristics. Since these characteristics can play a large role in the polarization of the backscatter, the effort was concentrated on this particular issue.

Although leaves can vary widely in terms of their polarization characteristics, their DOP signatures have some useful and mostly general differences vis-à-vis clothing and woven materials. The results show that the DOP versus aspect angle for most leaves followed a Lambertian profile, with a specular "spike" to the degree that the leaf surface is smooth and waxy. Woven materials, on the other hand, have a DOP that is constant over a wide range of aspect angles. Dependence on grain orientation (rotation) was observed in some samples of both foliage and fabrics.

DOP plots are shown for comparison in Figure 101. Presumably, the aspect independence of fabric is due to the mezo-scale roughness of the woven fibers, which present a variety of angles to the incident beam even when the fabric is draped on a flat surface. If the surface aspect angles can be determined through the 3D spatial LADAR data and passive image processing, the DOP data can be used to discriminate natural foliage from fabric when their spectroscopic signatures are equivocal.

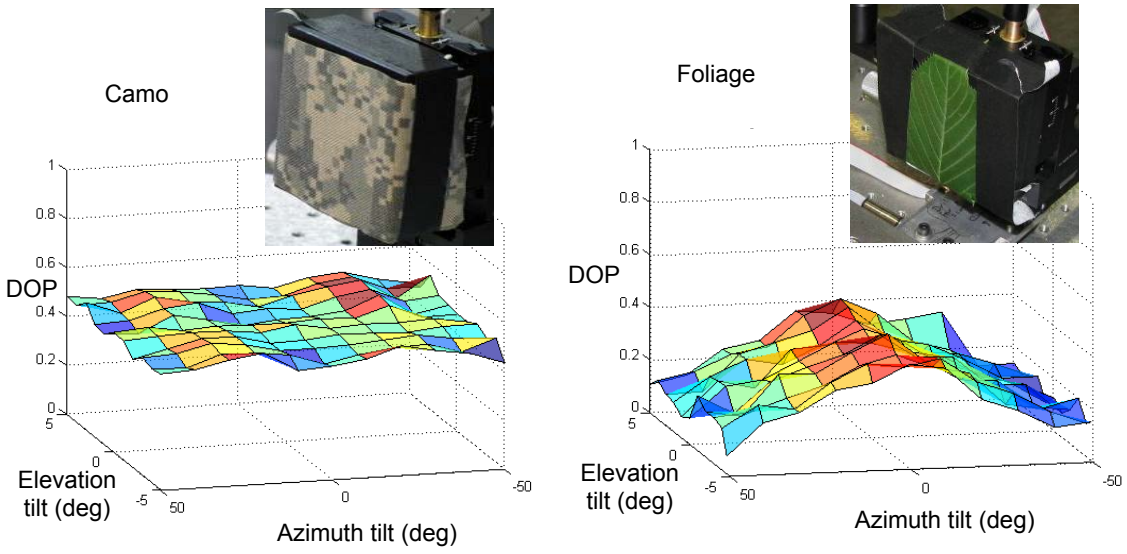

Figure 101: Backscatter DOP versus aspect angle

6.3.2. Image Based Measurements

Figure 102 is a montage of images using fabric and leaves attached to the sample cylinder. In set a, leaves are placed at various locations on the face of the camouflage

covered cylinder. In the DOP image, it is clear that the surface with camouflage fabric has a consistent degree of polarization, even as the angle increases toward glancing incidence at the edges. The leaves, however, have a polarization that depends upon placement on the cylinder, which corresponds to the incident angle. In set b, two palm leaves are wrapped around the sphere. The DOP image shows that the leaves have angular dependent depolarization while the fabric again does not. In set c, the cylinder is wrapped in a ballistic vest. The surface has highly depolarizing Velcro embellishments in a "T" shape. Two palm leaves are conformal to the surface at an approximately 45 degree angle. In the DOP image, the background fabric and Velcro depolarize the beam without respect to angle, while the leaves can be seen to have aspect dependence.

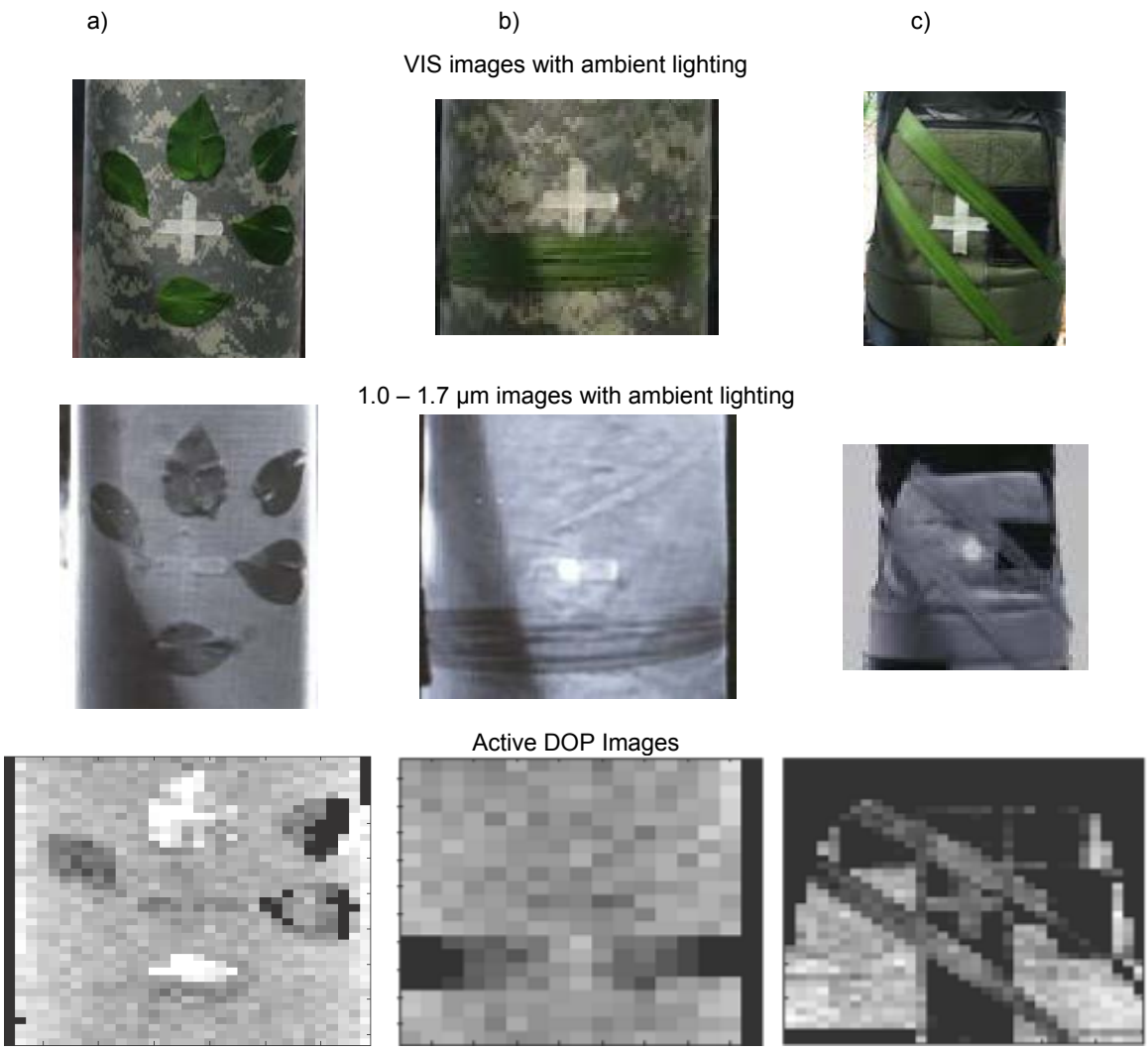

Figure 102: Polarimeter imaging geometry – sets a, b, c

The image results demonstrate that polarization and its angular dependence may be a way to classify surfaces that are otherwise ambiguous in purely spectral metrics or to segment surfaces that are spatially unresolvable. Factors yet to consider in the polarization measurements include beam size, which has a surface averaging effect.

7. Imaging Performance Measurements

The performance of the Spectral LADAR prototype system was measured and analyzed in some simple, controlled situations to predict the operational limits in complex scenes. Specifically, the spectral stability, source compensation, statistical characteristics of band energy, range accuracy, spectral linearity, and range resolution are described in this section.

7.1. Spectral Stability and Noise Analysis

Stability[*], defined as the degree to which the instrument measures the same value of a constant target at different times, is a critically important characteristic of Spectral LADAR. Long term stability is even more important in the context of the laboratory demonstrator, since the capture of one frame takes a substantial amount of time, over which low frequency fluctuations induced by environmental changes can be significant.

Stability and noise are fundamentally indistinct and degrade the fidelity to which a target's spectrum is digitally reconstructed for analysis. The term *noise* usually refers to

[*] Stability, as used here, is synonymous with repeatability.

truly random fluctuations at frequencies comparable to the front end bandwidth, i.e. above 100 kHz. Stability refers to fluctuations that can be very close to DC and may arise from deterministic processes, which by lacking complete or prior information on influential parameters are random in a practical sense, if not a theoretical sense. Applying time-domain waveform averaging is a way to reduce high frequency noise (which is uncorrelated over the averaging period) to a degree at which the low frequency effects can be studied.

Instability affects measurements in absolute and relative contexts. The Euclidean metric, an absolute spectral intensity space, is sensitive to fluctuations that affect one band, several bands, or all bands equally. In contrast, fluctuations that affect all bands equally (panchromatic) are irrelevant in the SAM context, while band-dependent fluctuations affect SAM-transformed spectra. [*]

Fluctuations may arise on the source side, to the degree that the transmitted pulse energy has an inconsistent temporal envelope, delay, magnitude, or spectrum, or on the detector side where changes in sensitivity, focus, alignment, and spectral tuning affect the measurement. Clearly, fluctuations on the transmitter and receiver side can occur contemporaneously. Optomechanical alignment of the transmitter and receiver, and changes in relative alignment between the two can cause fluctuations in measurements. Source compensation is one way to correct for some fluctuations, primarily those on the

[*] Band dependent fluctuations change the shape of the white balance vector, band independent fluctuations shift the white balance magnitude but not its spectral angle.

source side, provided that the source reference is not subject to more statistical variation than the signal.

The statistics of stability and noise are evaluated with the lab demonstrator in a so-called staring configuration. In this situation the gimbal controls are overridden such that the gimbal always points at the coordinate origin in azimuth and elevation. A target is fixed downrange at this point. The system then makes many observations of the same point on the fixed target to evaluate instrument fluctuations, whose statistics are assumed to be stationary. The dataset is analyzed to determine the statistical spread of observations. The plot shown in Figure 103 contains the key output of this analysis, showing all of the target energy observations per band. Ideally, there would be no instrument fluctuations and the variance of observations in each band would be zero. The instrumental fluctuations shown in Figure 103 combine with natural target spectral variation to degrade the accuracy of spectral perception. Each of the blue circles represents an observation of band energy, while the green line is the mean. The red lines are the +/- 2σ error bounds assuming a Gaussian distribution.

Figure 103 was generated with the instrument in staring mode, aligned to a 99% reflectivity calibration target at a range of 33 m and an effective attenuated range of approximately 75 m. This test was conducted indoors with dim ambient lighting. The calibration target has a flat spectrum in the SWIR. The spectral variations are mainly due to the spectrum of the source, atmospheric absorption, detector responsivity variation,

varied spectrometer efficiency, and wavelength dependent coupling loss. The vertical axis, labeled pseudo joules, is an arbitrarily scaled unit of energy.

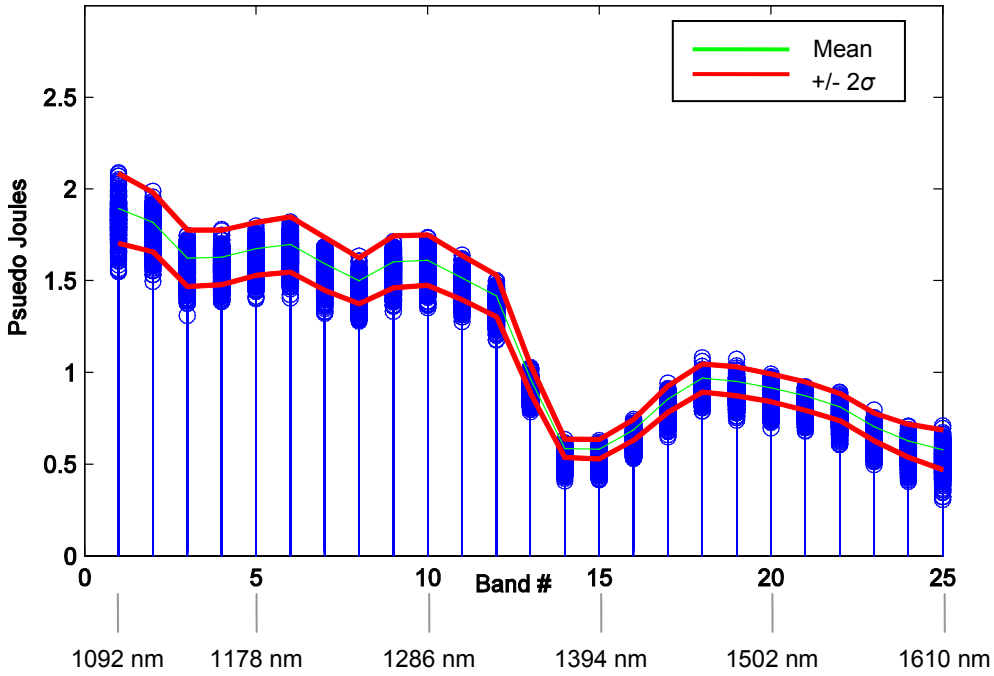

Figure 103: Per-band spectral statistics of a 99% reflective target recorded in staring configuration (100716)

7.1.1. Figure-of-Merit

The stability and noise figure-of-merit is the two-sigma fraction of the mean value (2σ / μ). This figure, expressed as a percentage, is the 95% confidence interval of band energy.

It is comparable in application to the noise-equivalent temperature difference (NETD[*]) often used as a figure-of-merit in thermal infrared imaging systems [205]. In this situation, it may be analogously referred to as the noise equivalent change in reflectivity (NEDR[†]), since the signal output in direct detection LADAR systems is linear with reflectivity. This figure-of-merit represents the system's ability to discern two targets with similar spectra on a per-band basis.

As an example, Figure 104 and Figure 105 plot the mean (plot a, respectively) and NEDR values (plot b, respectively) for the *reference* beam[‡] in the Euclidean and SAM metrics, respectively, for a run of 349 sample pixels. In the figures, the reference beam has voltage amplitude of 30 mV to 40 mV from bands 1 through 12, 20 mV to 30 mV for bands 12 through 17, after which it declines to 5 mV at band 25. Under these conditions, the electrical SNR ranges from 10^4 down to 10^2. The most important aspect of these plots is the presentation of relative independence of NEDR to mean energy (related to SNR) and the similarity of the SAM and Euclidean NEDR values. If receiver (dark or thermal) noise were to dominate, the NEDR would depend inversely on the mean signal value, since the dark noise is fixed at an absolute level. With some exceptions, the NEDR is relatively constant from bands 1 through 20, only increasing after band 20 as the signal level drops precipitously. This characteristic suggests that the SNR of the system is limited by a proportional source of noise – one that increases in proportion with

---

[*] Alternatively NEΔT, noise equivalent delta temperature

[†] The acronym for noise equivalent delta reflectivity (NEDR) was found to be more appropriate as opposed to the analogous acronym for noise equivalent reflectivity difference (NERD).

[‡] The reference beam used for source compensation

the signal strength. Source fluctuation noise has this characteristic, as does signal-limited shot noise. There is an evident NEDR floor in Figure 104 and Figure 105. The similarity of NEDR in the SAM and Euclidean metrics indicate that the fluctuations are not panchromatic, since the SAM metric is independent of panchromatic fluctuations.

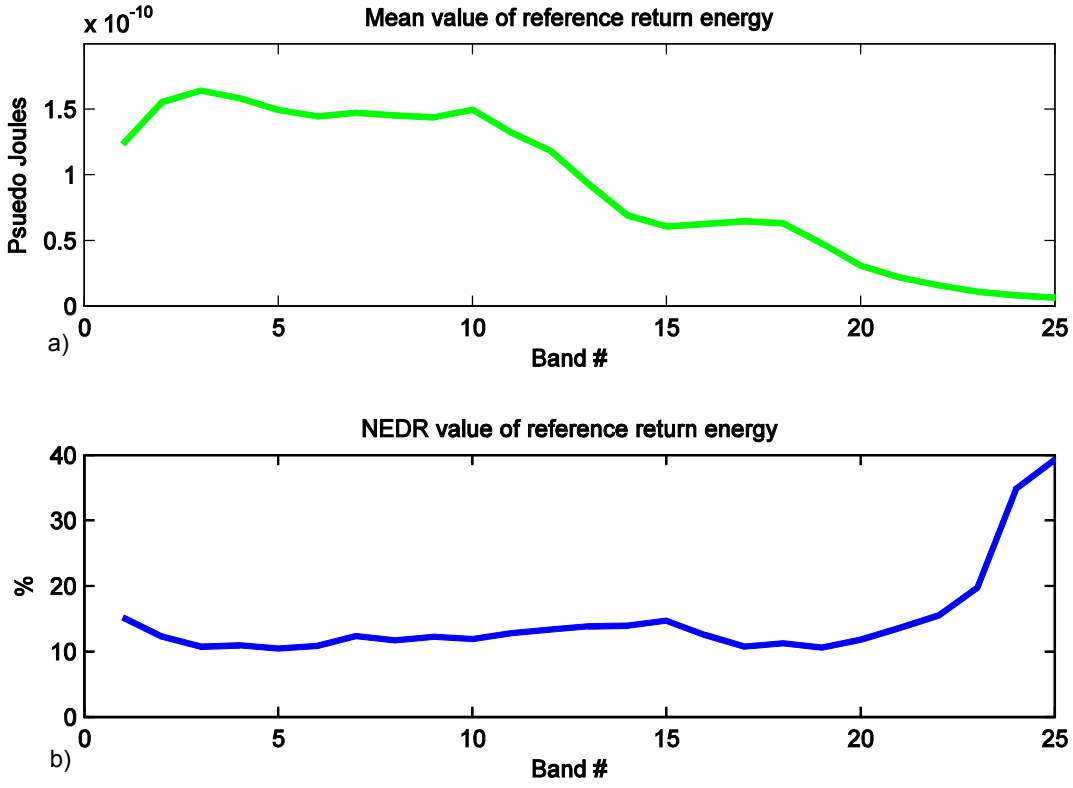

Figure 104: Fluctuation analysis of reference return, Euclidean metric (100723)

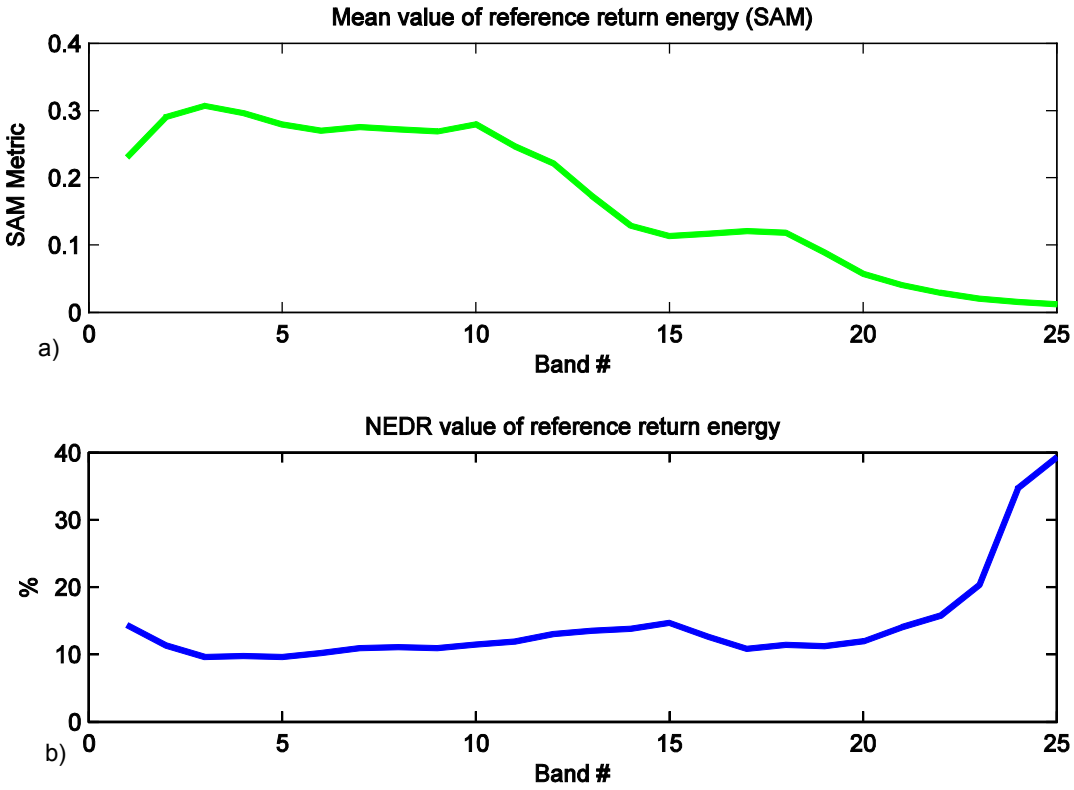

Figure 105: Fluctuation analysis of reference return, SAM metric (100723)

7.1.2. Source Compensation

One way to reduce source fluctuations and improve stability is to sample each pulse from the source and apply an adjustment (normalization) factor to match an expected pulse energy value. As shown in Figure 53 and Figure Figure 60, a pick-off beamsplitter samples each pulse and feeds it into the receiver optics.

Exact knowledge of the spectral energy of each reference pulse allows for total elimination of source fluctuations. This, however, is not possible in practice. To the

degree that the estimation of reference beam spectral energy is corrupted by noise, total elimination of source fluctuations is not possible. Clearly, it is advantageous to have the reception of the reference beam be as noise free as possible. Since a 4% beamsplitter provides an abundance of power, obtaining adequate signal intensity is not a problem. The configuration shown in Figure 53 utilizes the same receiver lens, fiber, spectrometer and detector for both the reference and signal beams. While this is advantageous in the respect that it can also compensate for detector fluctuations (e.g. temperature – gain fluctuations), it is limited in the respect that the reference beam SNR is relatively limited by the linear dynamic range of the photoreceiver. In other words, the SNR of the reference beam is limited by the linear range of the receiver, as is the signal beam. It is consequently impossible to have a reference beam SNR substantially higher than that of the maximum linear range signal.

Using the same instrument configuration and range setup used to produce Figure 103, Figure 106 compares signal return energies of several graybody calibration targets of 99%, 60%, and 40% neutral reflectivity to the reference beam collected with each respective run. In this plot, no source compensation is applied; the mean has been derived from 349 independent samples. The reference beam SNR is, at times, greater and lesser than that of the signal depending on band source energy and reflectivity level.

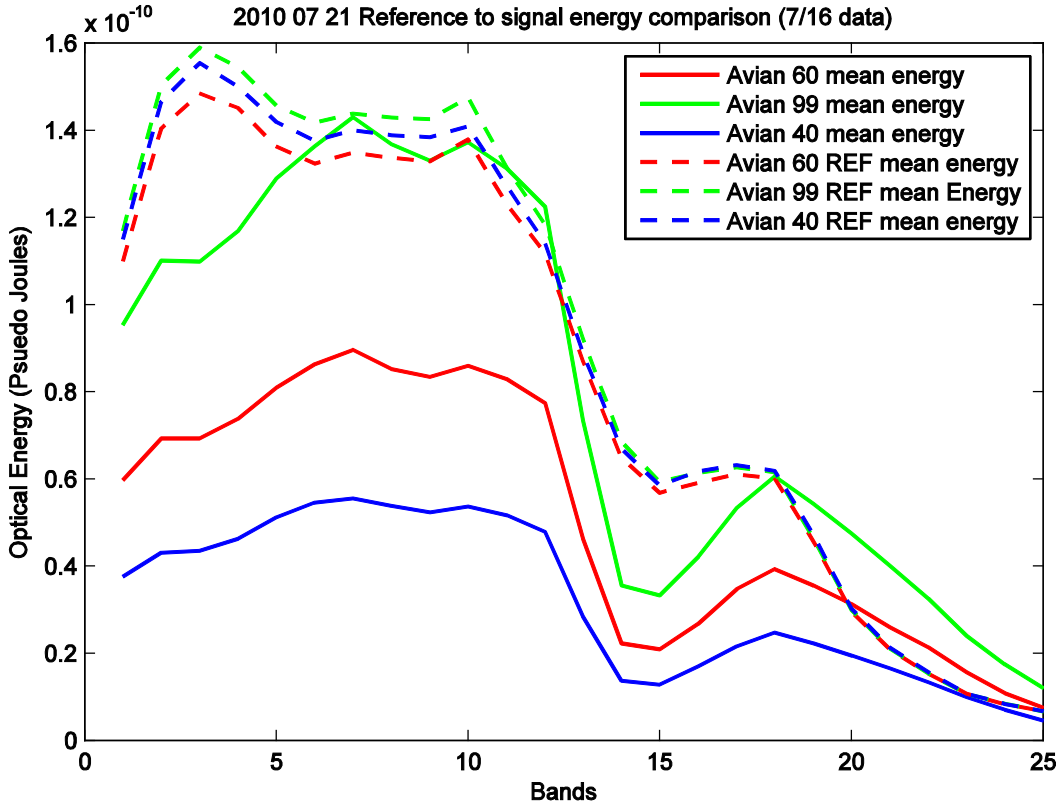

Figure 106: Reference to signal energy comparison* (100721)

Ideally, the reference beam energy should be completely correlated with the signal beam energy when making repeated observations of a fixed target. A correlation coefficient of unity would allow for complete elimination of source fluctuation. The time-series correlation between the samples used to determine the mean in Figure 106 is shown in Figure 107. The correlation is generally high and positive, and for the most part relatively higher in regions of high SNR.

* "Avian XX" refers to the target manufacturer and percent reflectivity.

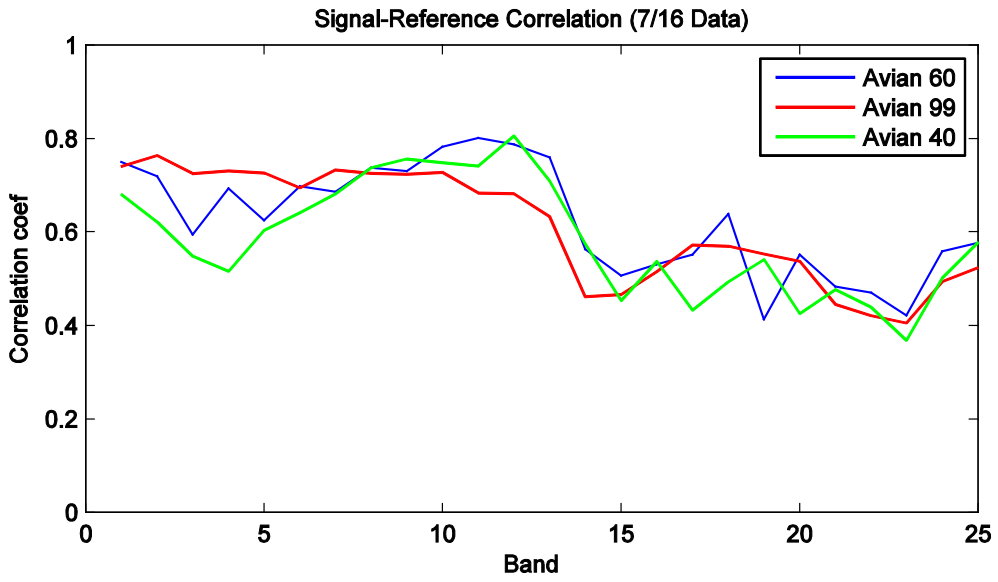

Figure 107: Reference to signal correlation (100721)

The key criterion for evaluating source compensation is the degree to which it decreases the NEDR for a given target and range. Figure 108 and Figure 109 plot the NEDR values for each band for the 99% reflectivity and 40% reflectivity targets, respectively, at an effective attenuated range of 75 m. In each figure, plot a represents the NEDR in the SAM metric while plot b represents that in the Euclidean metric. Some overall features are apparent when comparing the compensated to uncompensated NEDR. First, the observations made of the reference beam NEDR in Section 7.1.1 are also present here. There appears to be a floor value of uncompensated NEDR around 10%, where increases in SNR are not met with commensurate decreases in NEDR. The presence of source noise is a plausible explanation for this. When source compensation is applied in these cases near the apparent NEDR floor, it appears to help, but not to a large extent. Notable are the cases where the source compensation increases the NEDR value. The cases depicted in Figure 108 and Figure 109, show that points where the compensated NEDR becomes higher or equal to the uncompensated NEDR occur where the SNR of the

reference beam is lower than that of the signal beam, if the SNR of the reference beam is not exceptionally high in an absolute sense. Two practical conclusions can be drawn from this observation. First, it is important to have as high a reference beam SNR as possible, and where it is below some threshold *and* lower than that of the signal, to selectively avoid using the source compensation technique. Second, that source compensation does not entirely avoid the NEDR floor, perhaps due to the finite SNR of the reference beam, or perhaps due to other factors.

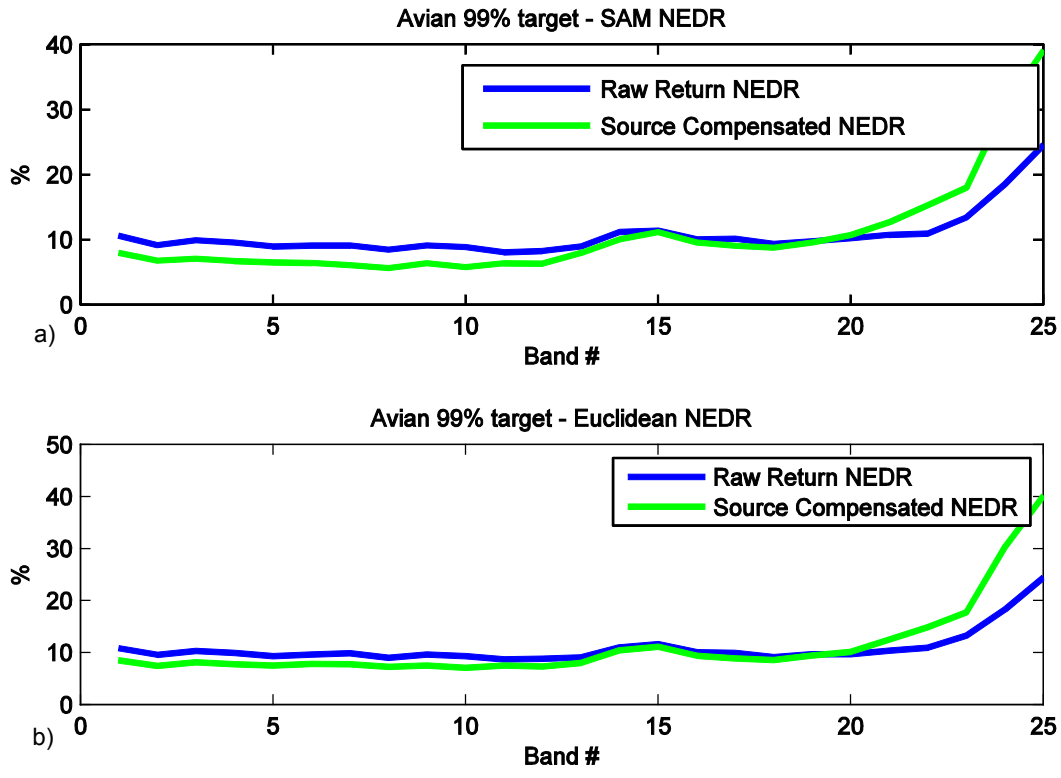

Figure 108: Source compensation efficacy with 99% target (100721)

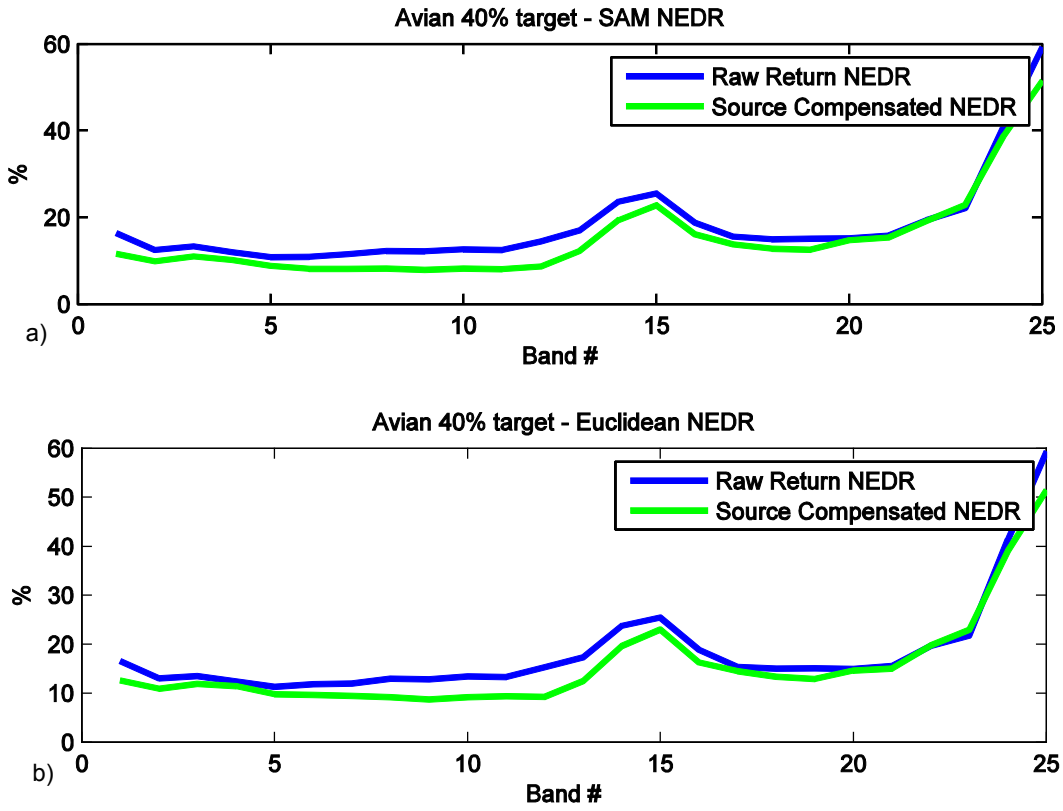

Figure 109: Source compensation efficacy with 40% target (100721)

7.1.3. Band Energy Statistics

The interpretation of NEDR assumes that the distribution of band energy observations has a Gaussian PDF. The band energy histograms for the uncompensated range statistics of the data sets shown in Figure 108 and Figure 109 are plotted in Figure 110. The best fitting Gaussian distribution is the red line in each plot. While apparently not perfect, approximating the distribution as Gaussian is useful for analysis.

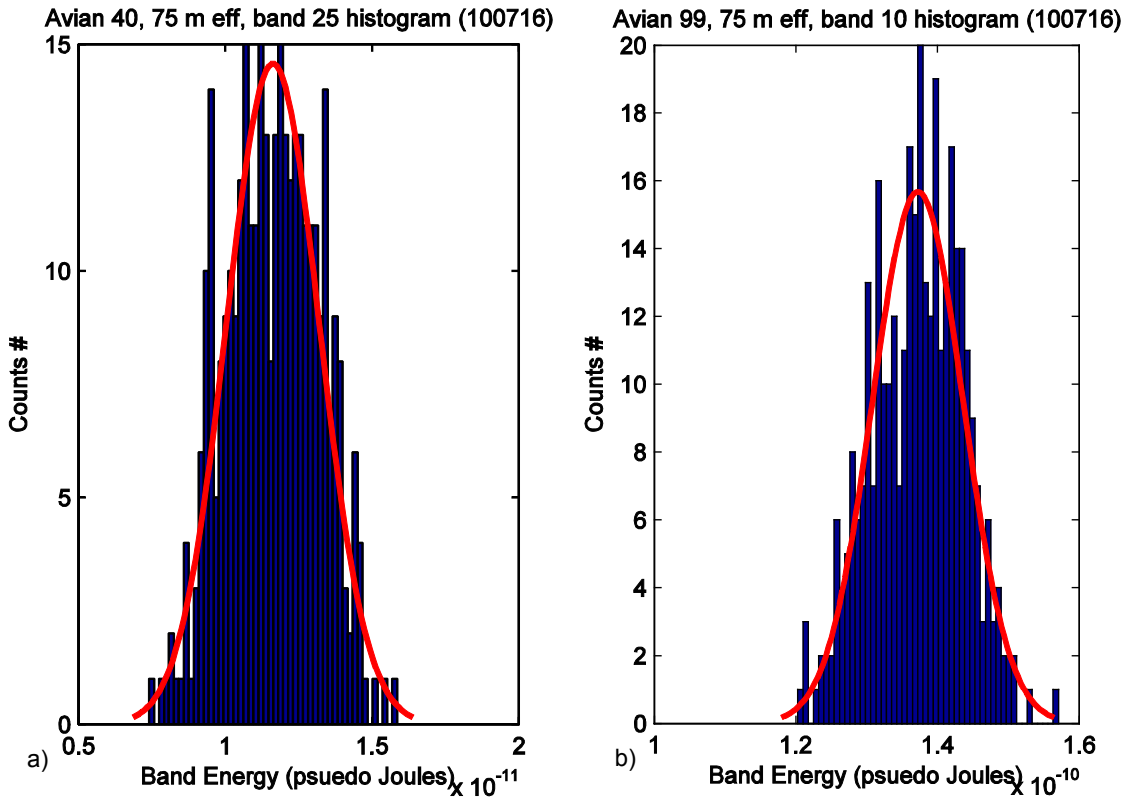

Figure 110: Spectral energy histograms (a) low SNR, (b) high SNR (100723)

7.2. Spectral Linearity Analysis

Accurate reconstruction of an object's backscatter spectrum depends upon a linear optical power to electrical current photoreceiver response, or a response curve that can be linearized through mathematical transformation. Linear response over all backscatter cross sections is difficult to achieve in LADAR systems since the dynamic range of the return signal is large (Section 5.6.2). A non-linear photoreceiver response will distort the computed spectra and lead to significant classification errors.

The transimpedance amplifier is the limiting factor of linear dynamic range in the laboratory demonstrator system, shown in Section 5.10.2 and 5.6.2. To verify linearity of spectral intensity estimation, the system was configured in the staring configuration discussed in Section 7.1. Gray scale calibration targets, consisting of a diffuse PTFE material and darkening agent, were used to measure the response. These targets have spectrally flat signatures, at 99%, 60%, and 40% diffuse reflectivity. Taking the 99% reflectivity target as the white reference, the responses of the targets are shown in Figure 111. The 60% and 40% targets had a measured reflectivity of 68% and 45%, respectively. Earlier tests demonstrated a linear detector response over this range.

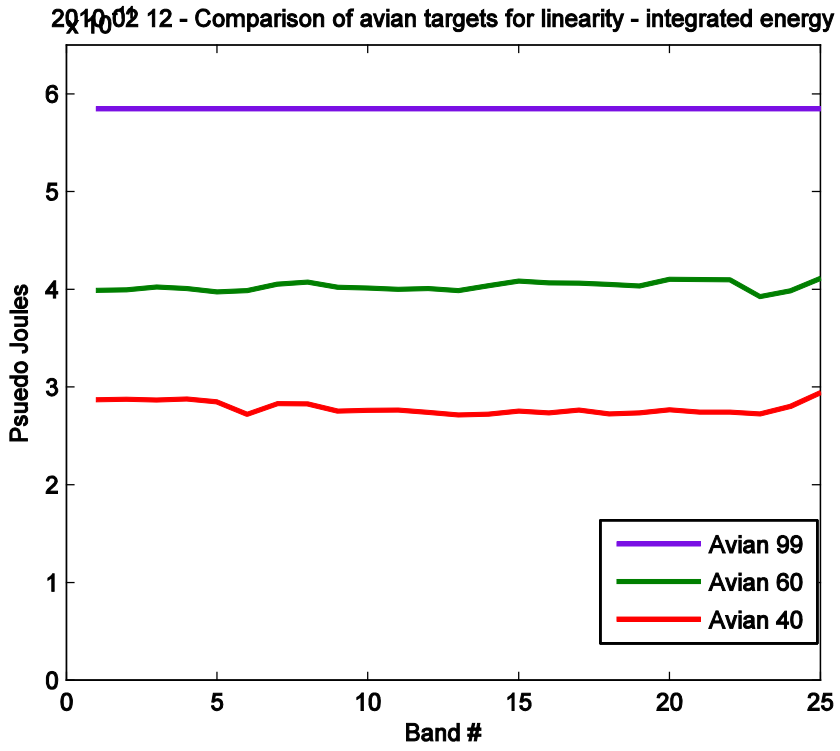

Figure 111: Spectral linearity analysis (100212)

7.3. Range Accuracy

The spatial statistics of Spectral LADAR are as important as they are for conventional LADAR systems. The accuracy of azimuth and elevation coordinate data is determined by the beam scanning system. Since the scanning mechanism of the laboratory demonstrator is a surrogate for a scanner that will be used in a practical system, the statistical performance in these axes is not evaluated.

Earlier sections (Sections 3.1.6.4) discussed the theoretical foundations for statistical range estimation. Here, range data is collected using the staring mode configuration discussed in Section 7.1. Figure 112 shows the range statistics from a 99% reflective target at an effective attenuated range of 45 m. The range distribution shown here is influenced by more factors than discussed in Section 3.1.6.4. Significantly, the jitter of the digitizer electronics plays a role.

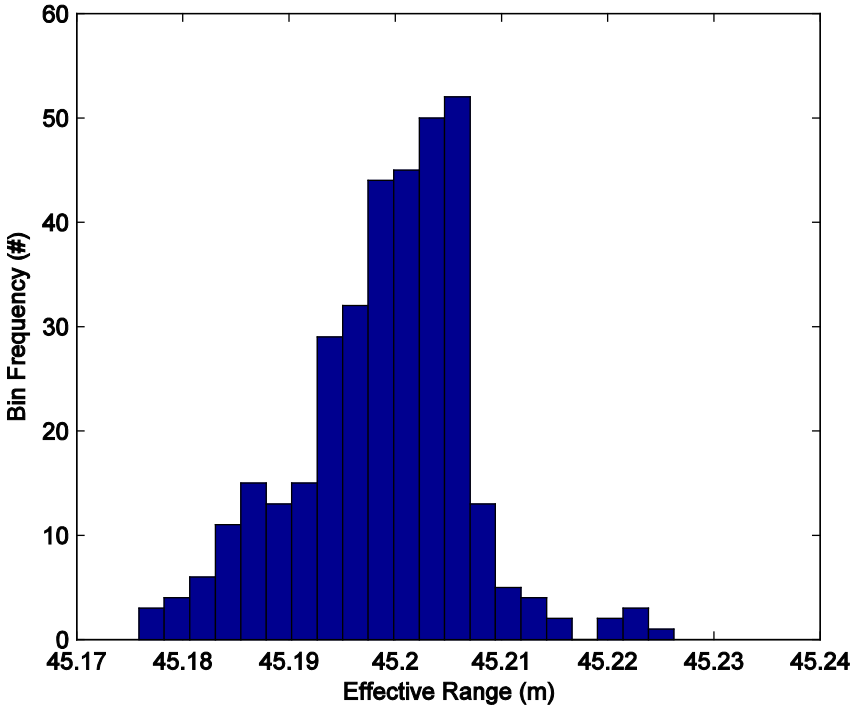

Figure 112: Range histogram (100216)

7.4. Range Resolution

The range resolution was measured using a split-pixel setup with the sensor in the staring configuration, as described in Section 7.1. Two targets were separated by a small distance, r_{res}, each occluding approximately half of the beam at their respective ranges. This is shown in Figure 113. The foreground target was ordinary Styrofoam and the background target was a combination of rare-earth oxides in a diffuse PTFE-like material. Oxides of Erbium, Dysprosium, and Holmium are mixed in this target to produce a distinct spectral signature.

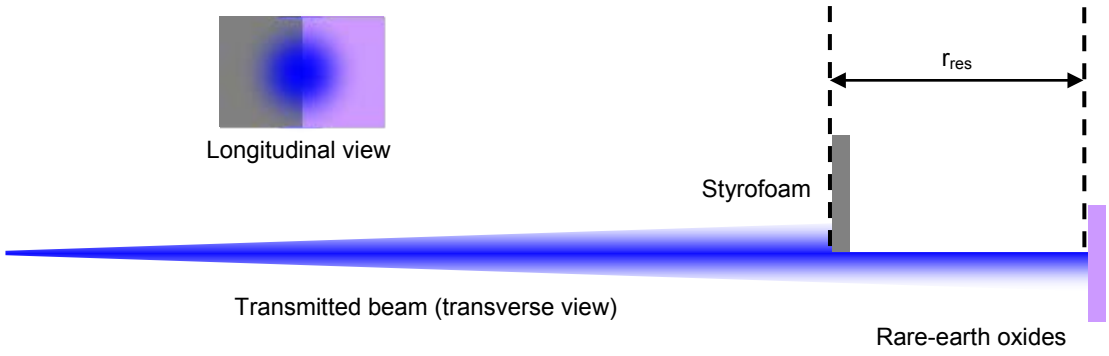

Figure 113: Split pixel test configuration

The two targets were first separated by 80 cm (r_{res} = 80 cm). A single pixel image was taken with a high degree of time-domain averaging. The raw (pre-filtered) time waveforms for each band are plotted in Figure 114. The range resolution criterion (discussed in Section 3.1.6.3) is somewhat arbitrary. Here, the strictest criterion, requiring the signal to return to zero, is used. As observed in Figure 114, this criteria results in a range resolution of approximately 80 cm, and the duration of the pulses in the shorter wavelength bands (Band 1 especially) are the limiting factor. At longer wavelengths, the pulse widths are significantly shorter, as can be seen in Figure 114.

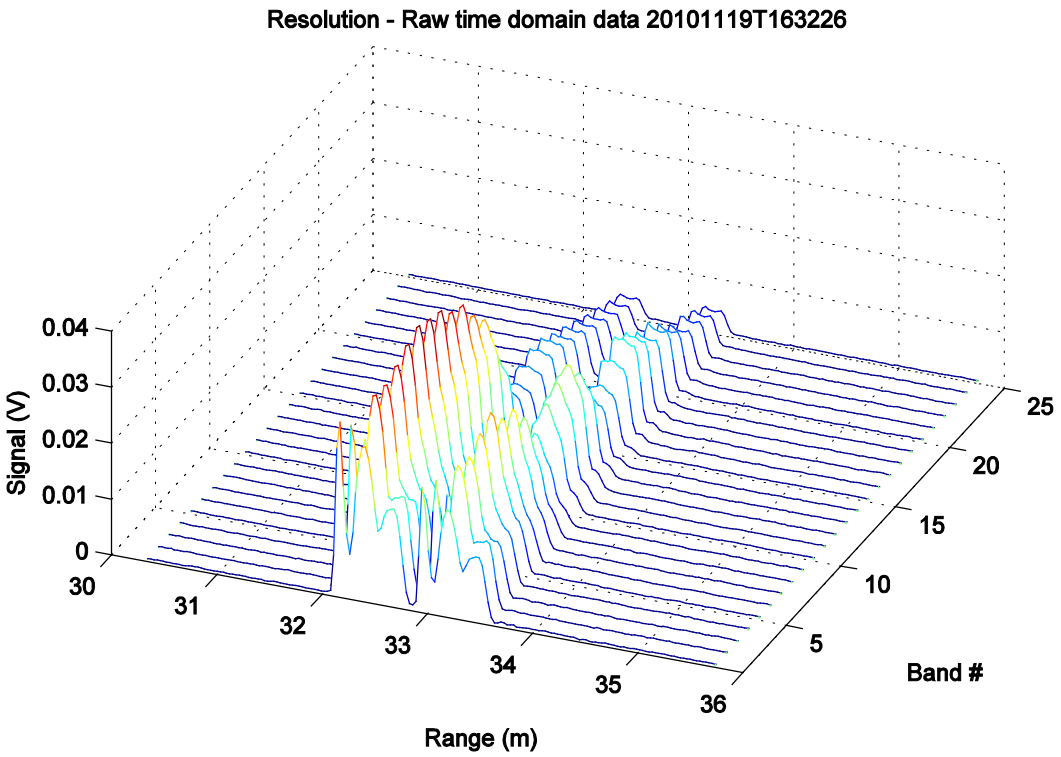

Figure 114: Time waveforms of 25 bands demonstrating range resolution (20101119T163226)

Shown in Figure 115 are the results of another resolution test scenario, with 160 cm range separation. In this case time waveform averaging was not applied. Polychromatic time waveform (range) data, as the sum of the first 20 bands, is plotted in the figure. The matched filter broadens the pulse by virtue of is autocorrelation operation, so range resolution is slightly reduced using the return to zero criteria. The inset plots of Figure 115 clearly demonstrate that an independent spectrum is unambiguously associated with each return voxel. Source compensation was not used in this case, although it could reduce the spectral uncertainty.

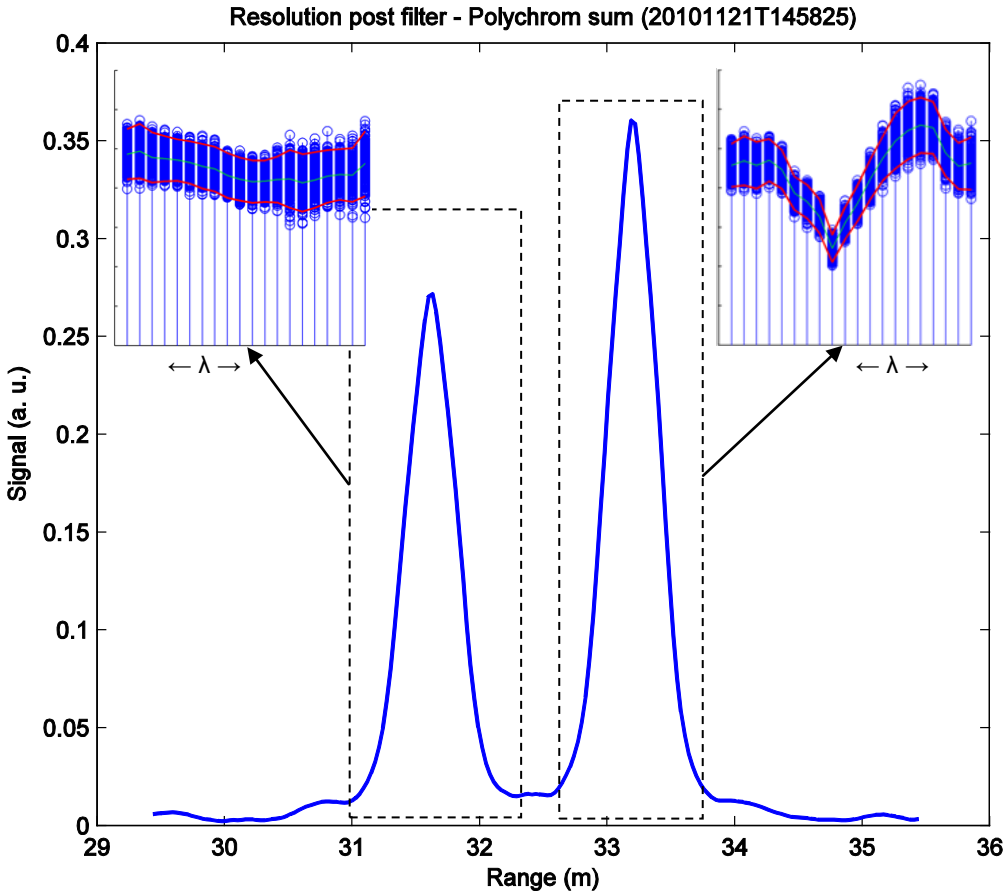

Figure 115: Multiple-return polychromatic range waveform and spectrum for a partially occluded pixel (20101121T145825)

The range resolved spectroscopic ability demonstrated in Figure 114 and Figure 115 is one clear advantage Spectral LADAR has over other sensor types. Active spectral sensors, either without range resolved ability or with inferior range resolution will mix the foreground and background spectrums. Passive sensors will also mix sub-pixel spectra. Although spectral unmixing algorithms exist, these methods are computationally intensive, imperfect, and ambiguous. Even if spectral unmixing can be performed with high certainty, the assignment of foreground and background spectrums will be entirely arbitrary. Additionally, passive ranging techniques require the surfaces to be "textured"

to compute a range value by stereo correspondence. Spectral LADAR requires no surface texture or second sensor to unambiguously find two partially occluding targets and definitively assign an observed spectrum to each.

7.5. Sub-Voxel Spectral Uniformity

The white balance calibration transform, used to normalize the spectral response of the system to a known white target, is described in Section 5.10.5. The white balance transform is obtained by imaging the known white target, an extended target,[*] at range. An implicit assumption in this process is that any arbitrary sub-region of the illuminated portion of the target will have the same spectral white balance, i.e., the spectral space transform computed from the integration of the entire voxel area will also white balance the spectrum of any smaller portion of the illuminated area. In a practical situation, this means that split-pixel targets (Section 7.4, Figure 113) will have a consistent white balance regardless of the sub-region of the beam occluded by the target.

Unfortunately, chromatic aberrations in the transmitter and receiver lenses result in a spatial–spectral coupling that, to the extent aberrations are present, can distort split-pixel spectra with respect to the spectrum of the full, integrated illuminated area. Axial and lateral color aberrations, along with the failure to correct for spectrally-dependent

[*] A target larger than the lateral extent of the beam

Gaussian beam parameters can result in different white balance corrections for different sub-regions of the illuminated area as well as range-dependent white balance correction if spectral coupling varies with target range. This is diagramed in Figure 116.

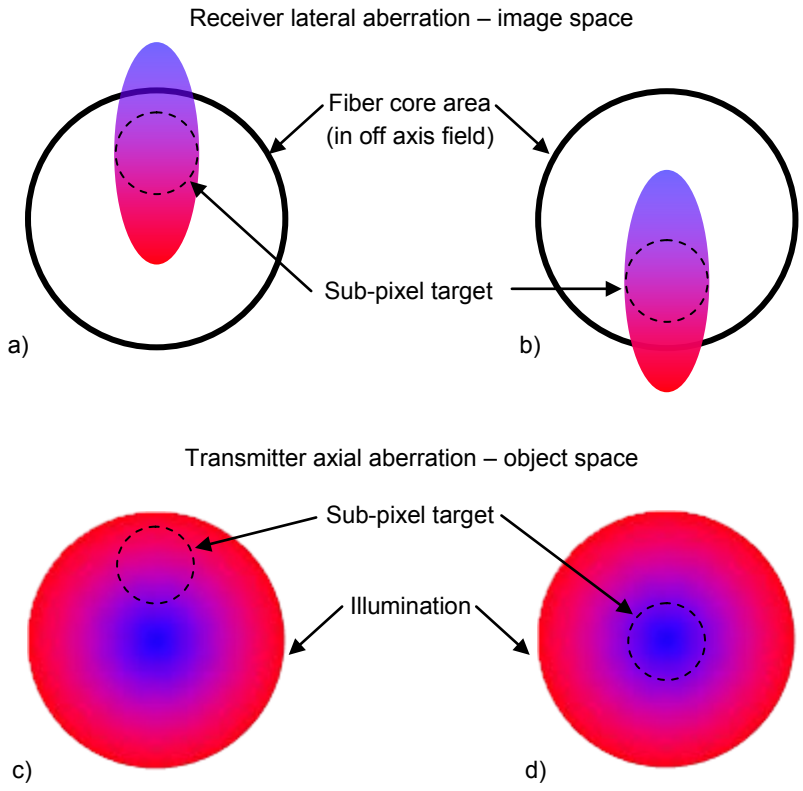

Figure 116: Spectrum distorting aberrations

Figure 116 presents two cases of aberrations that can distort split target spectra. In addition, receiver axial color and transmitter lateral color can have the same effects. Figure 116a and b depict how lateral chromatic aberration on the receiver side can effect the split-target spectral uniformity. In a, the target sub-region, indicated by a dashed line, is red enhanced since part of the blue lies outside of the fiber core area. Figure 116b is the opposite, where the sub-region is blue enhanced. An extended target would fill the

entire fiber core area, and would have some degree of wavelength dependent loss due to the lateral color, but this wavelength dependent loss is the same for all extended targets. Figure 116c and d show a similar situation when the axial color (or beam divergence mismatch) of the transmitter cause a radial spectral imbalance of the beam imaged at the target where the center is blue enhanced and the edges are red enhanced. The spectral uniformity of sub-regions is dependent upon the location within the illuminated zone. Correction by calibration is not possible in any of these cases since the sub-region location is unknown and spatially irresolvable.

Analysis of aberrations with ZEMAX show that the receiver lens chromatic aberrations are small. Lateral color is an off-axis aberration, and since the receiver is nominally used on-axis and is well compensated, this is an insignificant effect. The transmitter lens, on the other hand, was not custom designed for this application and shows considerable chromatic aberration. Axial color is significant, and lateral color can be up to 40% of the beam divergence angle when the fiber core is just a few hundred microns off-axis. Lateral color on the transmitter side may also result from the prismatic effect in the beamsplitter, however analysis reveals this to be quite small.

Tests on sub-voxel spectra show how serious this effect can be. Figure 117 shows the results of one such test for a given system alignment. These measurements use a standard white calibration target and a dark mask with a cut-out to define the beam sub-region to be analyzed. The mask, placed on the surface of the white target, is moved to expose

various sub-regions of the beam to the highly reflective white target. Time-domain averaging is applied to remove the effects of detector and laser intensity noise.

The full beam illumination region, shown as the gray circle on the left in Figure 117, was used to find the white balance transform that normalizes the spectrum. After SAM transformation, this is plotted as line 1 on the right. Five other sub regions are transformed to the white balance of the full beam and transformed to the SAM spectral space. The five lines corresponding to the five sub-regions demonstrate that the spectral variation across the beam is significant, and exceeds the spectral variation of many target signatures. Consequently, split-voxel target identification is compromised since the white balance spectrum of a particular sub-region occlusion is unknown at the time of measurement. Voxels on the edges of objects are subject to these distortions, later referred to as "edge errors." This can be especially serious when camouflage or foliage partially obscures an object.

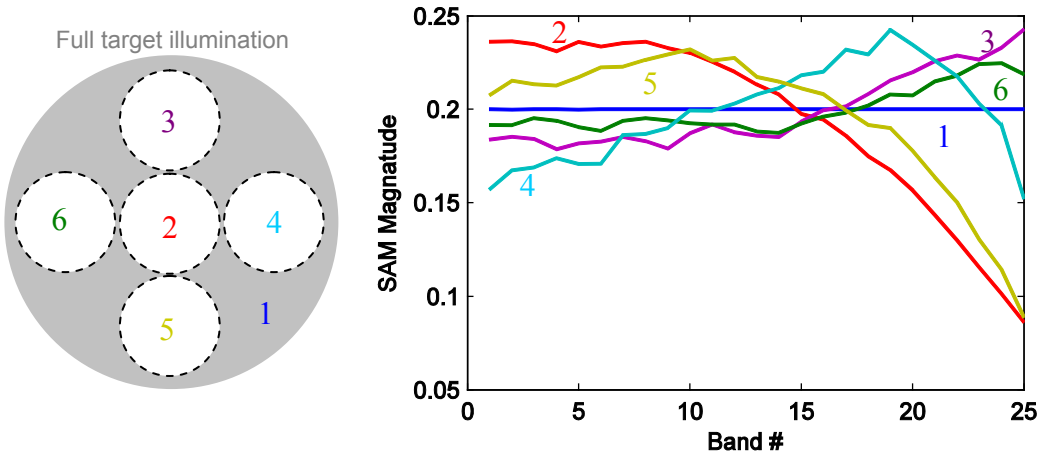

Figure 117: Test of sub-region spectral uniformity (101129)

Although Figure 117 does not conclusively establish the cause of the spectral imbalance, calculations show that much more chromatic aberration is inherent in the transmitter lens than other lens components. Chromatic aberration in the spectrometer lenses is irrelevant to this issue because propagation through the multi-mode fiber effectively scrambles any spectral-spatial coupling.

Figure 118 is the result of an effort to reduce chromatic aberration with improved focus and alignment. In this case, the transmitter was filtered by a 25 nm bandpass filter around 1550 nm, and imaged with an InGaAs based camera. Specific focus at long wavelengths was shown to reduce aberrations, as predicted by ZEMAX calculations. The improved spectral uniformity reduces spectral-spatial coupling, but not to the extent that it can be assumed negligible relative to the SAM signature variations in the training data. Focusing the transmitter lens using this technique also proved to enhance coupling at longer wavelengths and flatten the white balance, which is desirable to maintain high dynamic range in all bands.

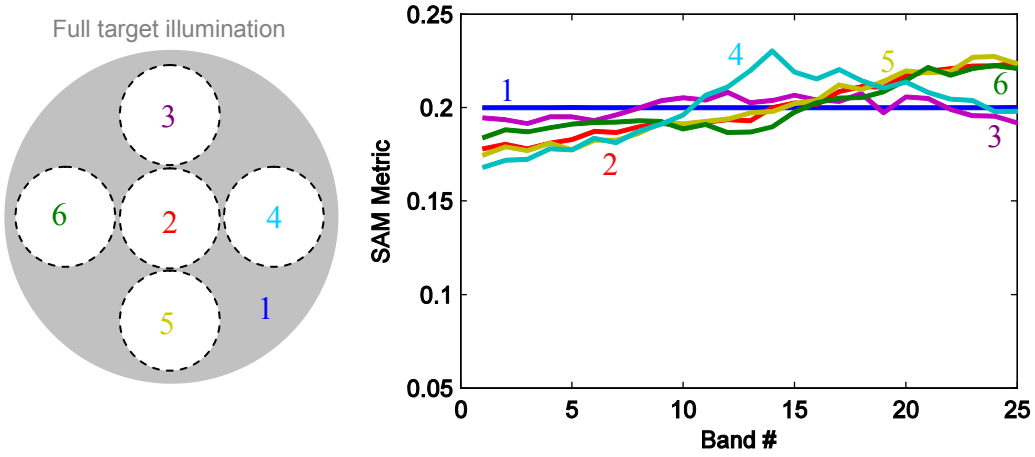

Figure 118: Test of sub-region spectral uniformity (101217)

8. Training Data Collection

Sample data for Spectral LADAR may be collected by the procedure outlined in Section 8.1 as needed to observe spectral variation and provide supervised classification algorithms (KNN, maximum likelihood) with adequate training data. The samples discussed in Section 8.2 are representative of what a UGV might encounter during outdoor operation. Training data for supervised algorithms is most effective when it represents the entire range of statistical variation for a particular class, e.g., all types of clothing and not just cotton fabric clothing, or all types of foliage and not merely deciduous varieties. As shown in Figure 28, the detail to which material classes are divided is somewhat arbitrary. These choices depend on the importance of differentiation to navigational or mission objectives, subject to the limits of the NEDR of the imager. Additionally, the spectral resolution of the system limits differentiation capability. All signatures were obtained with approximately 24 nm resolution, as shown in Figure 72. The Monte-Carlo simulations presented in Section 8.3 predict classification accuracy by the collected training data and the KNN and MLC algorithm.

8.1. Procedure

Training sample data is obtained by positioning a broad area sample at an actual range of about 33 m. Target samples which extend over a large scanning area are preferred, as this will result in 300 – 500 area samples across the surface of the material and characterize surface variations. Time waveform averaging (usually 200 waveforms) is applied when obtaining data for training samples to remove short-term noise fluctuations from the data since it is intended to characterize only variations in material signatures.

Like all image data, the training data spectra are normalized via the standard white-balance function of the signal processing software to a calibrated white, PTFE-like target with uniform 99% reflectivity. White balance calibration is performed at approximately the same distance as the samples.

In all other respects, training data acquisition follows the same procedure as image acquisition. Instrument configuration (aside from time-domain averaging) and signal processing follow the same routines. A special routine is used in post-processing to extract the training samples and aggregate multiple target signatures into a single data structure to be used as input to supervised classification algorithms. Source compensation is not used in the generation of training data.

8.2. Object Classes

In the signature plots below, the individual samples across the surface of the material are represented with thin multi-colored lines. The mean is the thick green line and the +/- 2σ bounds under the assumed Gaussian distribution are shown by the thick red lines.

The backdrop signature class (Figure 119) represents a black synthetic cloth background draped over painted metal cabinets at the far end of the test range. The signature is close to a graybody. All graybodies, regardless of absolute reflectivity, are represented by a flat spectrum in the SAM domain with per-band SAM metrics equal to the inverse square root of the number of bands, or 0.2 for 25 bands. The spectrum in Figure 119 is collected from 357 samples across the surface of the target at about 36 m. The beam diameter at this range is about 3.6 cm. A 3 dB attenuator was applied to the transmitter beam to reduce the intensity at the receiver to within the linear range of the detector.

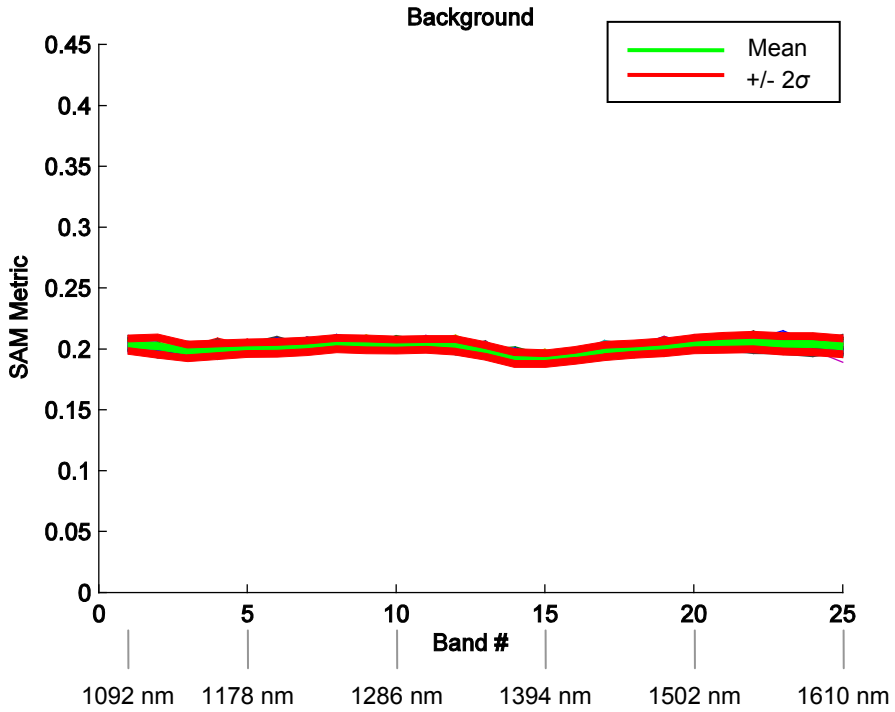

Figure 119: Backdrop class training data (101230)

Figure 120 is the signature obtained from samples collected on a standard uniform, at an actual range of 33 m and using an attenuation of 3 dB. A small dip around band 5 may be seen with a broad and shallow depression from band 12 and reaching a minimum around band 21. The samples were collected from a uniform jacket spread out on a supporting structure. Small embellishments on the uniform, including zippers and Velcro were sampled along with the bulk fabric.

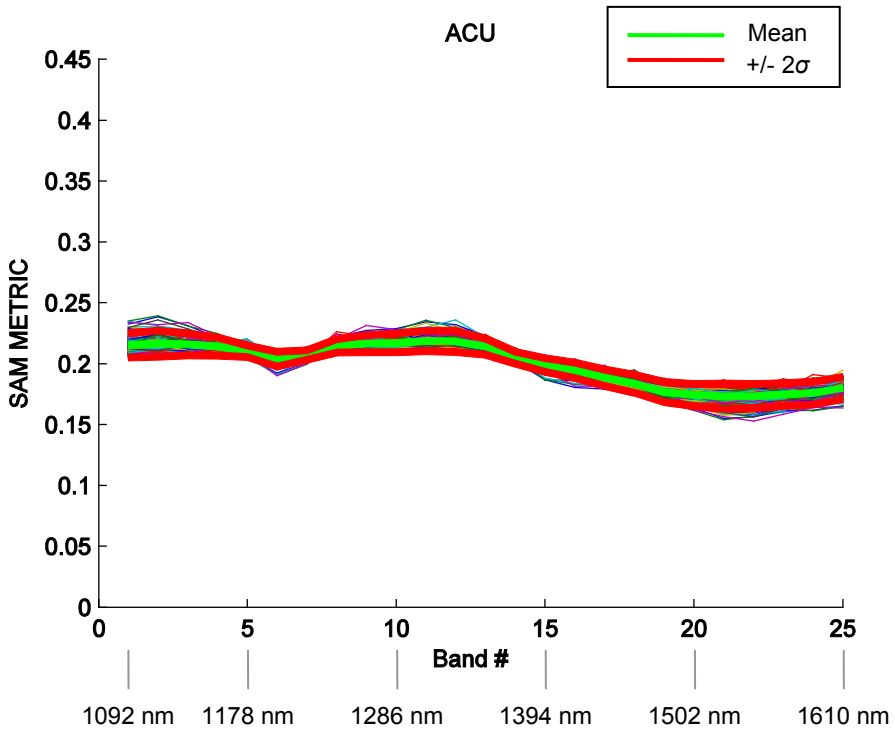

Figure 120: Uniform (ACU) class training data (101230)

Foliage was one of the more difficult signatures to obtain since a very broad section (1 m x 1 m) of plant material is seldom present in nature. Since chromatic aberrations of the transmitter can cause spectral distortions on the edges of surfaces, some errors in signature collection are expected (Section 7.5). Three indoor office type plants were used, two palm-like species and one elephant ear type plant. These were staggered in front of a backdrop such that the scanned beam would be occluded by leaves of the three plants to the maximum extent possible. After collecting the data using 3 dB attenuation, range gating was used to remove pixels at the backdrop range. The result is shown in the 494 spectral samples of Figure 121. The variation of this plot is clearly greater than all other material types analyzed. This may be partially due to natural variations in plant

spectral signatures across different parts of the plant structure (e.g., leaves and stems), variations among the three individual plants tested, or to some extent the undesirable spectral-spatial coupling discussed in Section 7.5. The most prominent feature is a broad, deep absorption line centered at band 18 with increasing proportional reflectivity at longer wavelengths. A small increase at the first band is also noticeable.

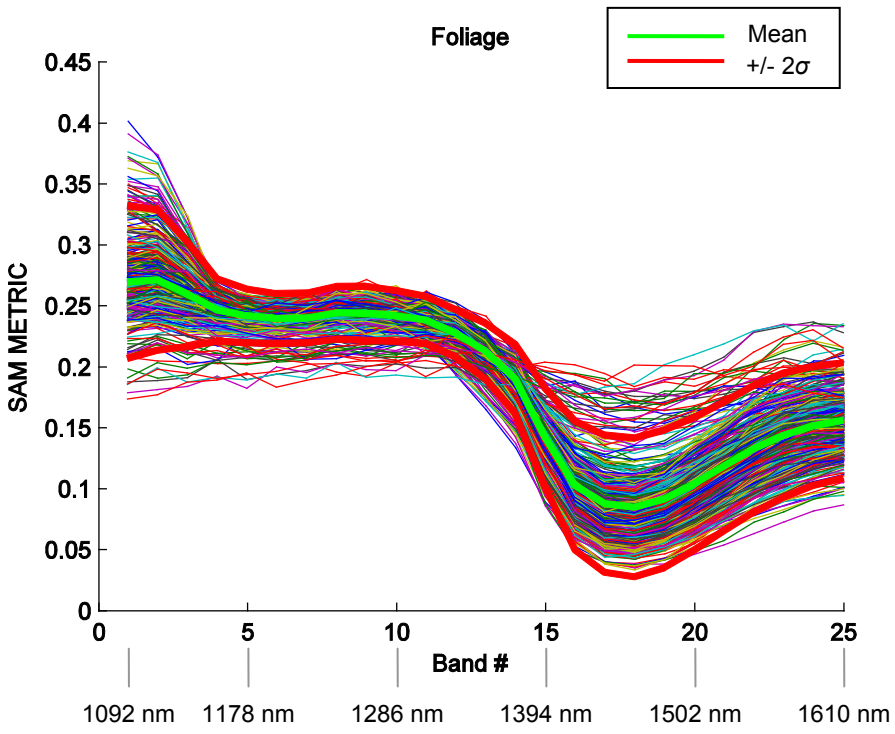

Figure 121: Foliage class training data (101230)

The vehicle spectral signature was obtained from an Army standard HMMWV vehicle. The front door of a vehicle was removed and placed upright in the test range, at near normal incidence to the transmitter beam. The door was painted a standard tan color, although it was apparent from some overspray on the edges that it was originally painted in the standard green color. The surface of the door had little dirt and showed normal signs of wear, such as scratches, dings, and other small defects. The 357 samples

(obtained with 3 dB attenuation at a range of 33 m) across the surface of the door show a relatively consistent and featureless spectral profile that slopes gradually downward towards long wavelengths (Figure 122).

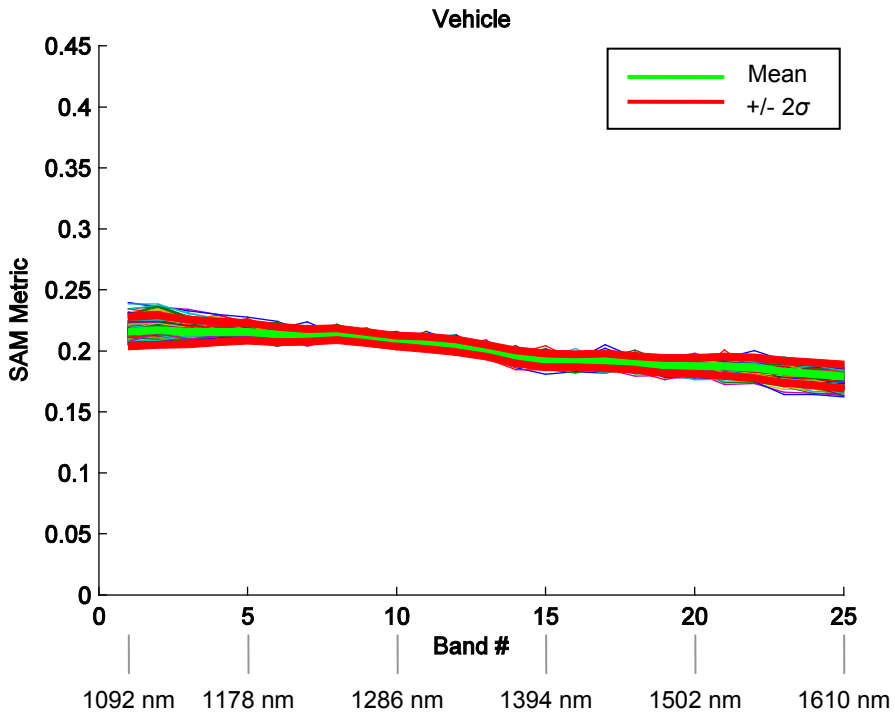

Figure 122: HMMWV class training data (101230)

The training spectrum for wood (Figure 123) was measured from a sheet of plywood, estimated to be "B" grade with some knots and visual color variation. The sheet was placed at a range of 33 m, approximately normal to the transmitted beam. The 357 samples across the surface obtained with 3 dB attenuation show two features, a shallow and broad line at band 6, and a very broad absorption, peaking around band 17 to 18 and, unlike the spectral signature of foliage, not quickly recovering at longer wavelengths.

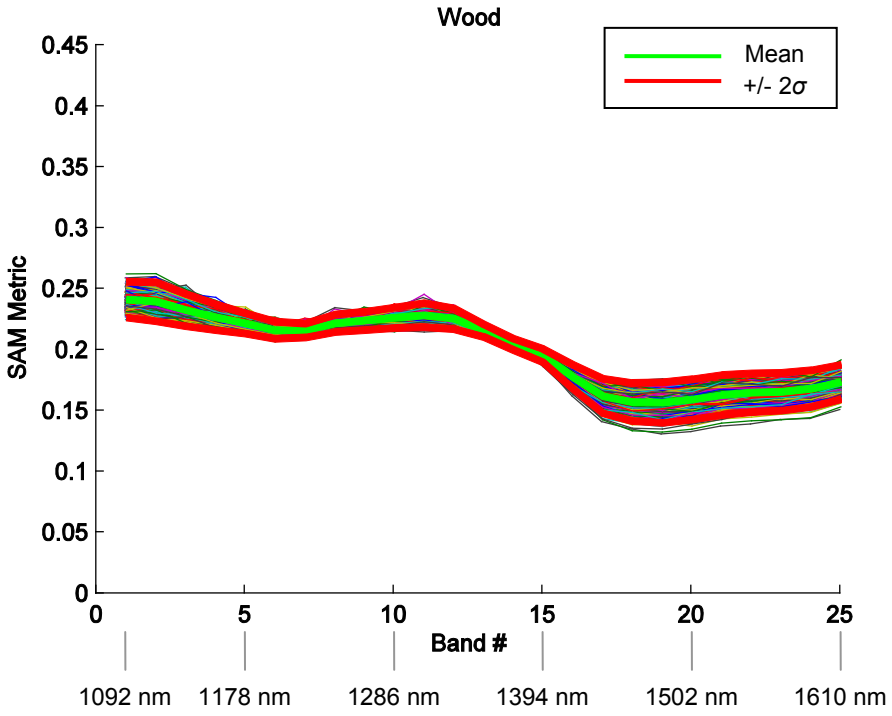

Figure 123: Wood class training data (101230)

The signature of a type of plastic was taken from large white sheets approximately 1 – 2 mm thick. Like other samples, the plastic sheets were secured to a structure, approximately normal to the transmitter beam, and at 33 m range with 3 dB attenuation. The SWIR backscatter spectrum of the plastic is highly distinct, having two very prominent absorption features at band 7 and 16. The spectral variation over the surface of the plastic sheets, as observed with most manufactured materials, is small (Figure 124).

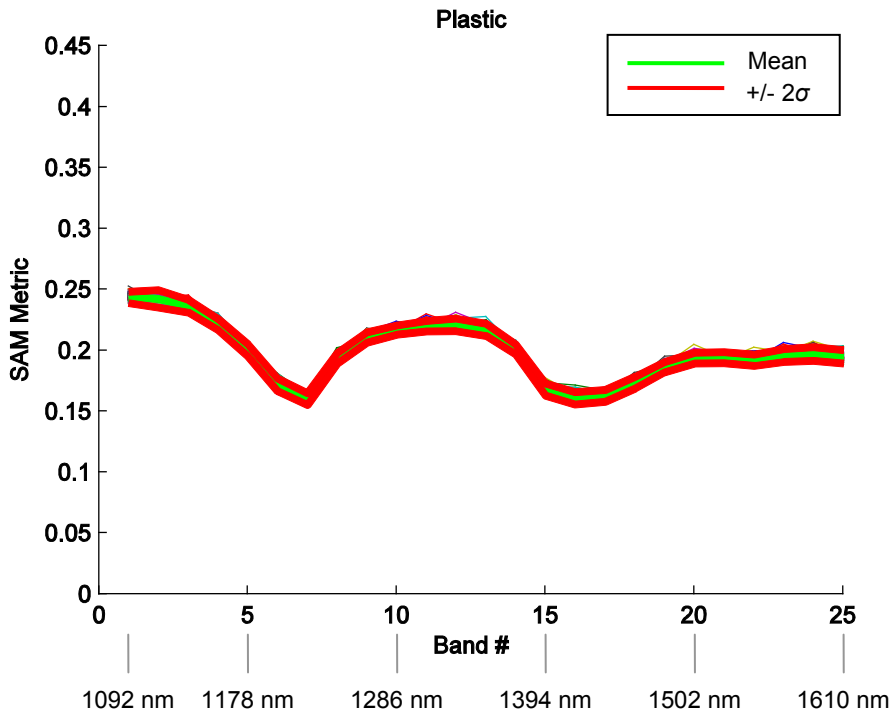

Figure 124: Plastic class training data (101230)

Single point observations were made of small samples of various types of thermoplastics (Figure 125). The range, attenuation, and instrument configuration for making these observations was the same as in the large sample of plastic with spectra of Figure 124, except more time domain waveforms were averaged. The transparent samples (acetate, PVC, acrylic (PMMA), and polycarbonate) were fixed in front of the 99% reflectivity calibration target in order to obtain the transmission spectrum, which would be representative of the material as a coating or if it were formulated as a diffusely scattering type. The other samples (polystyrene, UHMW polyethylene, nylon, polyester, delrin, ABS, and Teflon, were opaque or translucent to some degree and were placed in front of a dark (~2% reflectivity) target so that any transmitted light would contribute negligibly to the observed spectra. In practice, the thickness and scattering characteristics affect the

propagation depth and therefore the effective absorbance of the sample. From observing Figure 125 one may conclude that the training sample in Figure 124 is a reasonable representation of a variety of plastics and that plastic types in general have features around band 5, 15, and 25. Likely contributors to the signature of thermoplastics include hydrocarbon, amine, and hydroxide overtones that are consistent with the discussion of overtone spectroscopy in Section 3.2.1.1. Notably, the spectrum of Teflon (PTFE) lacks pronounced features as it includes none of these chemical groups.

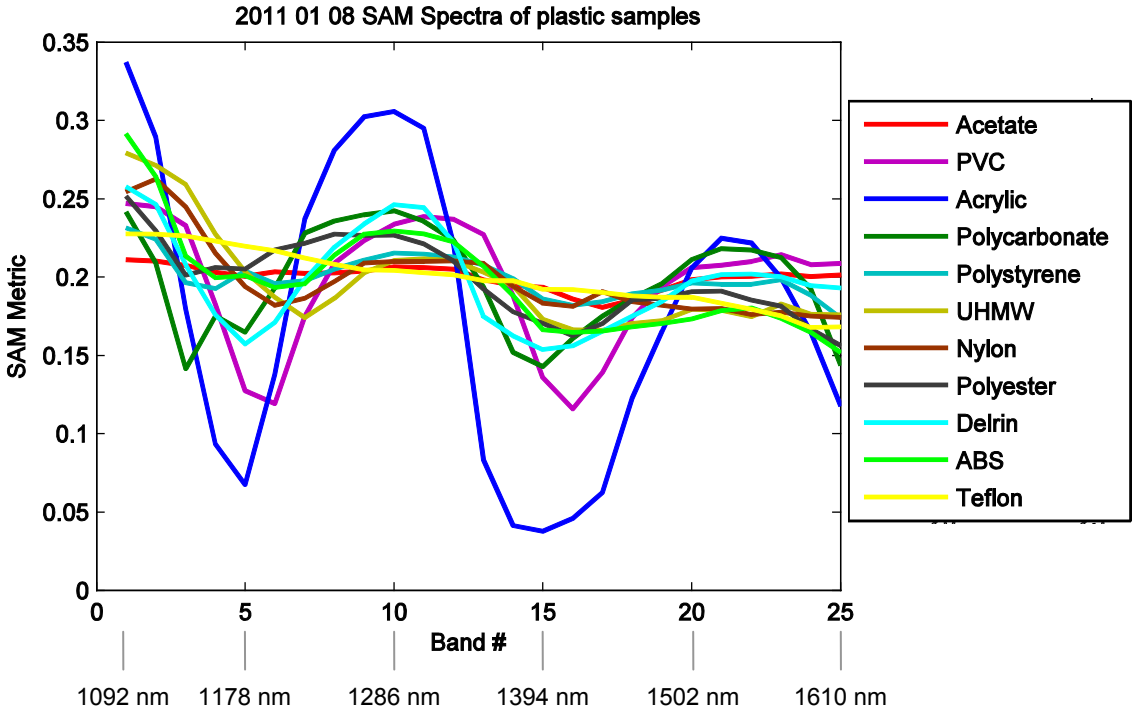

Figure 125: SAM spectra obtained from single point observations of plastic samples (110111)

The taggant training data acquisition procedure is different from the other samples. The taggant material, a mixture of rare earth oxides in a diffuse PTFE-like host, is a small 5 cm diameter disk and thus the variation over surface area is not obtainable from the small

sample. Instead, the spectrum (Figure 126) was obtained using a slightly modified white-balance spectrum procedure. Gaussian noise, having a standard deviation of 2.5% of the mean, was added numerically to the single-point observation to account for estimated manufacturing tolerances. The observed spectrum of this sample depends significantly on the spectral resolution of the system. The actual spectrum contains many fine spectral lines that are only apparent in a merged and broadened representation in Figure 126 due to the significant linespread (Figure 72) with respect to the spectral linewidth of the absorption features.

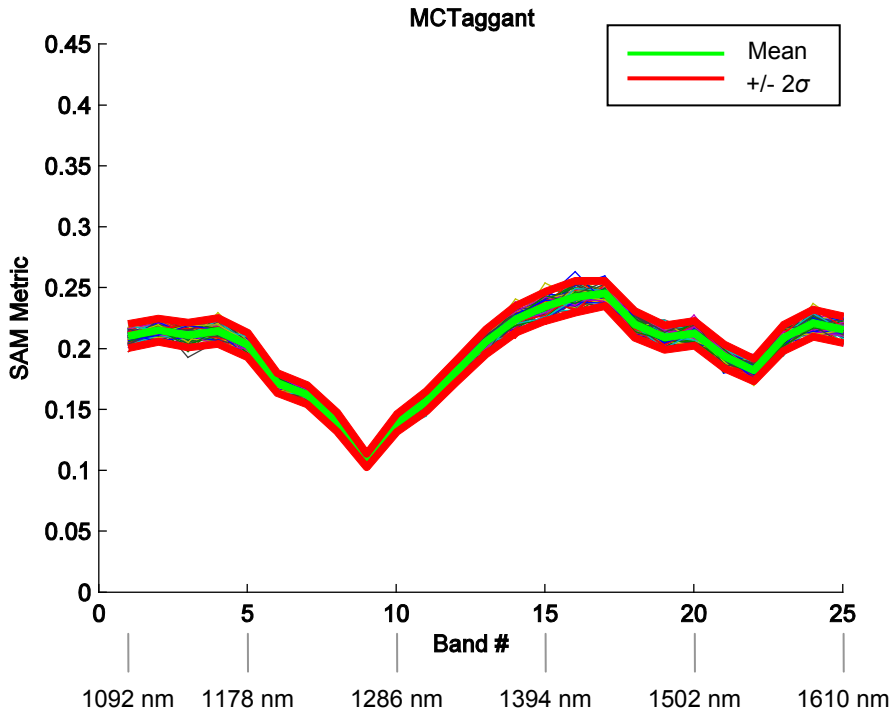

Figure 126: Taggant class training data (101230)

Figure 127 is a high resolution spectrum of the taggant measured by NIST-traceable calibrated equipment. In comparing Figure 126 to Figure 127, it is clear that the

laboratory demonstrator obtains wavelength-accurate spectra, albeit at lower spectral resolution.

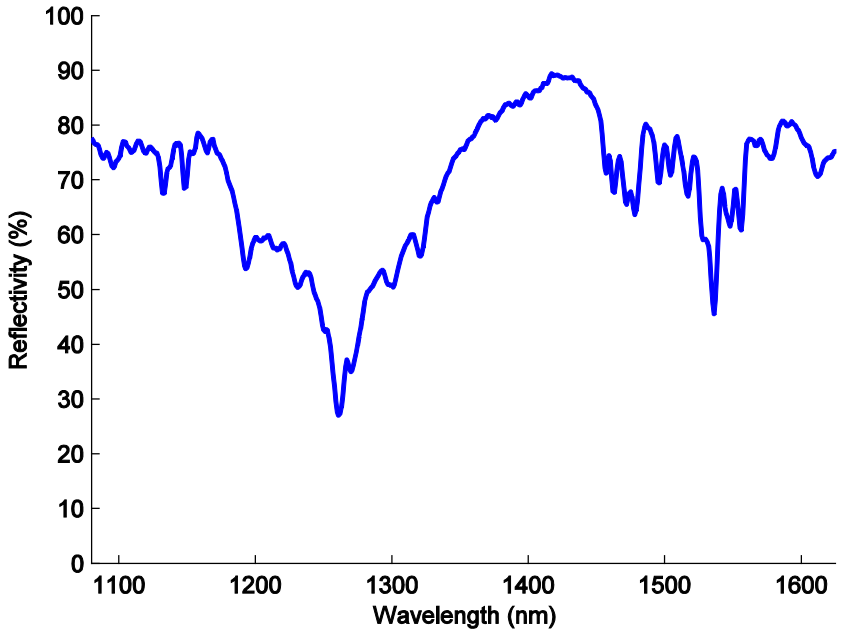

Figure 127: High resolution taggant spectrum (vendor supplied data)

The SWIR signature of human epidermis is shown in Figure 128. Thirty seven samples were obtained by imaging the lower back of a person at a range of 33 m. The SAM signature is highly distinct from other classes and corresponds well to observations published in the literature [206].

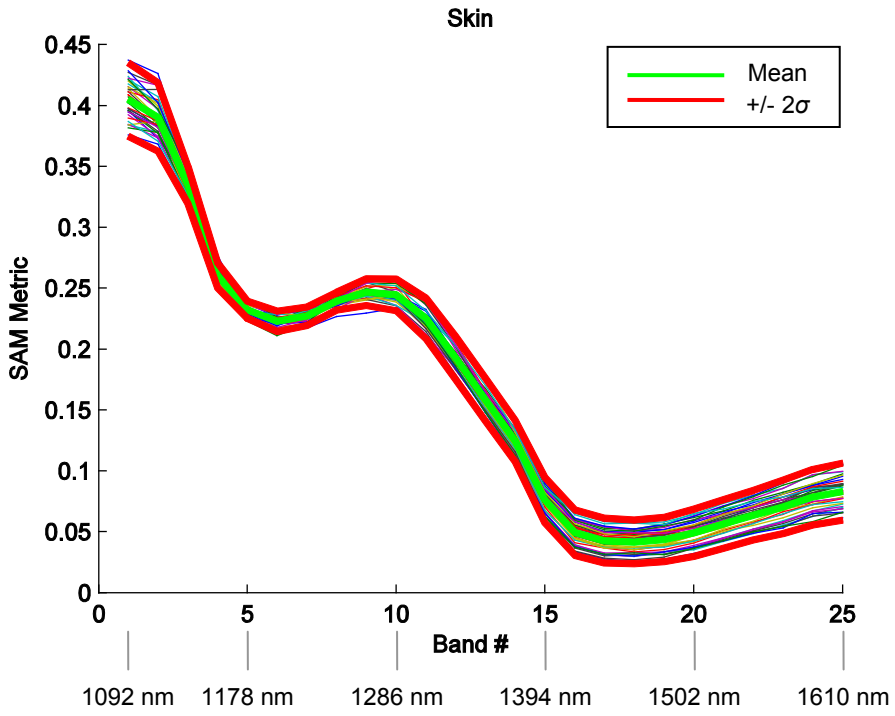

Figure 128: Skin class training data

The spectral signature for dirt, mud, and sand are shown in Figure 129, Figure 130, and Figure 131, respectively. Approximately 200 samples were obtained for each class at a range of 25 m, using 2 dB attenuation. The sample material was topsoil purchased from a local home and garden retailer and paving sand. The sample materials were loaded into a tray, and inclined to maintain a 68 degree angle of incidence, which is typical of terrain observations from UGVs. Mud was formulated by adding water to the topsoil until achieving near saturation and allowing it to settle for about 20 minutes.

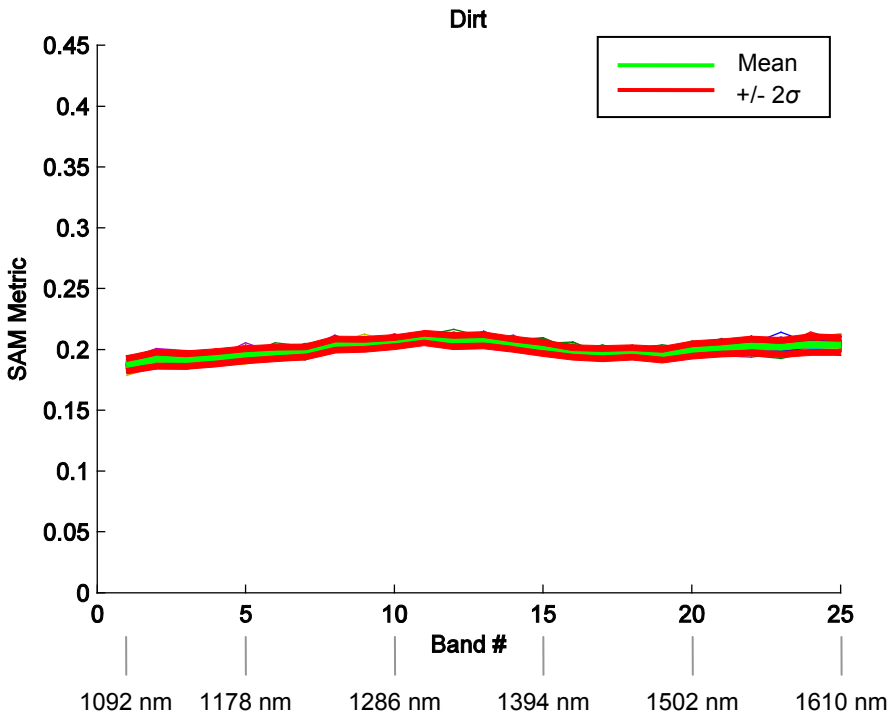

Figure 129: Dirt class training data (110109)

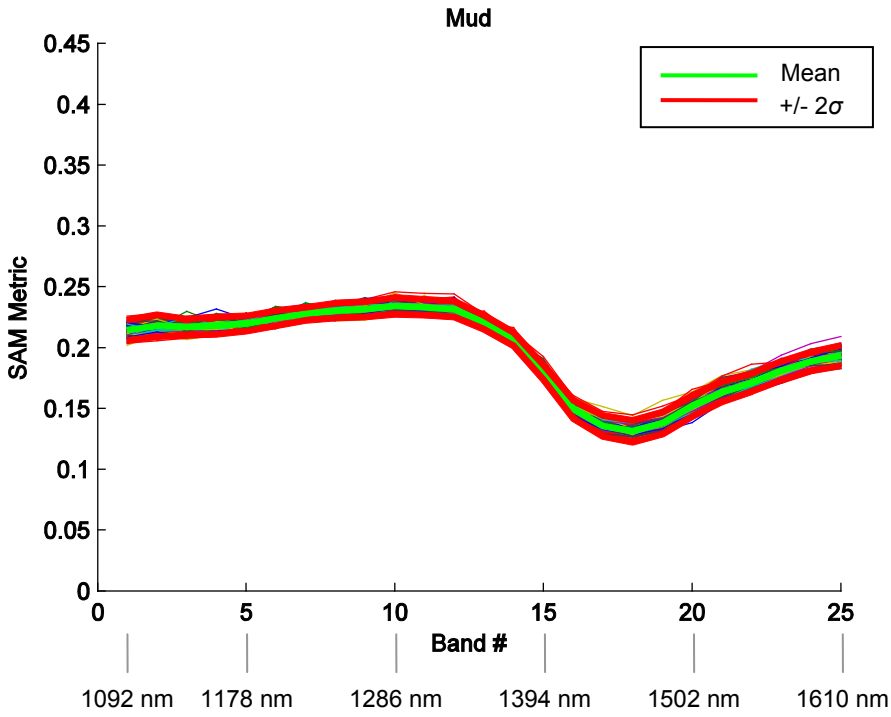

Figure 130: Mud class training data (110109)

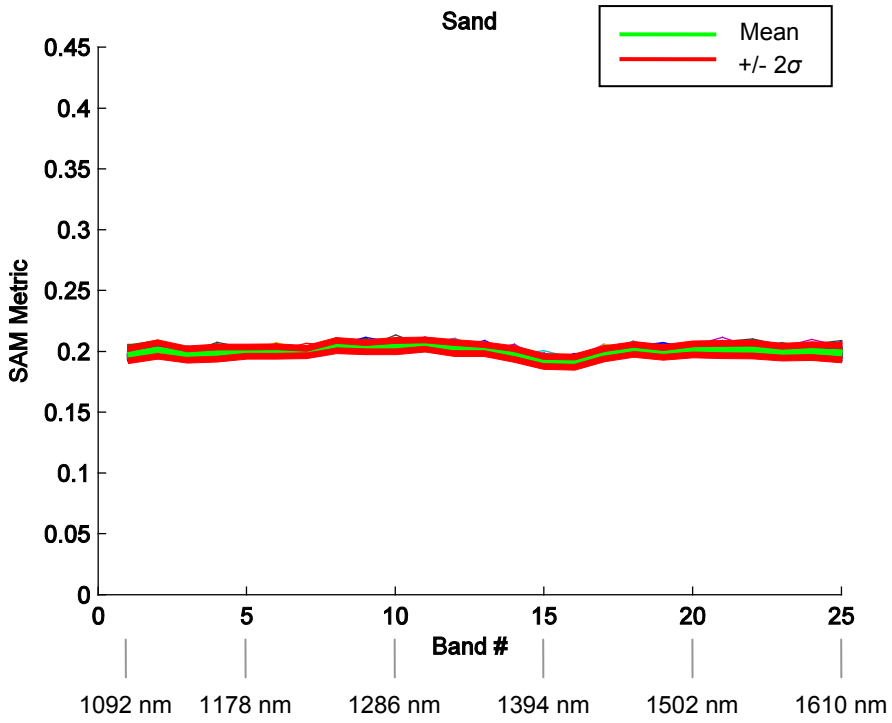

Figure 131: Sand class training data (110109)

A zoomed in view of the mean terrain signatures is shown in Figure 132. Dirt and sand have some apparent absorption bands, but are difficult to distinguish, especially when instrumental noise is considered. Mud is easily distinguished by its hydroxide resonances of water.

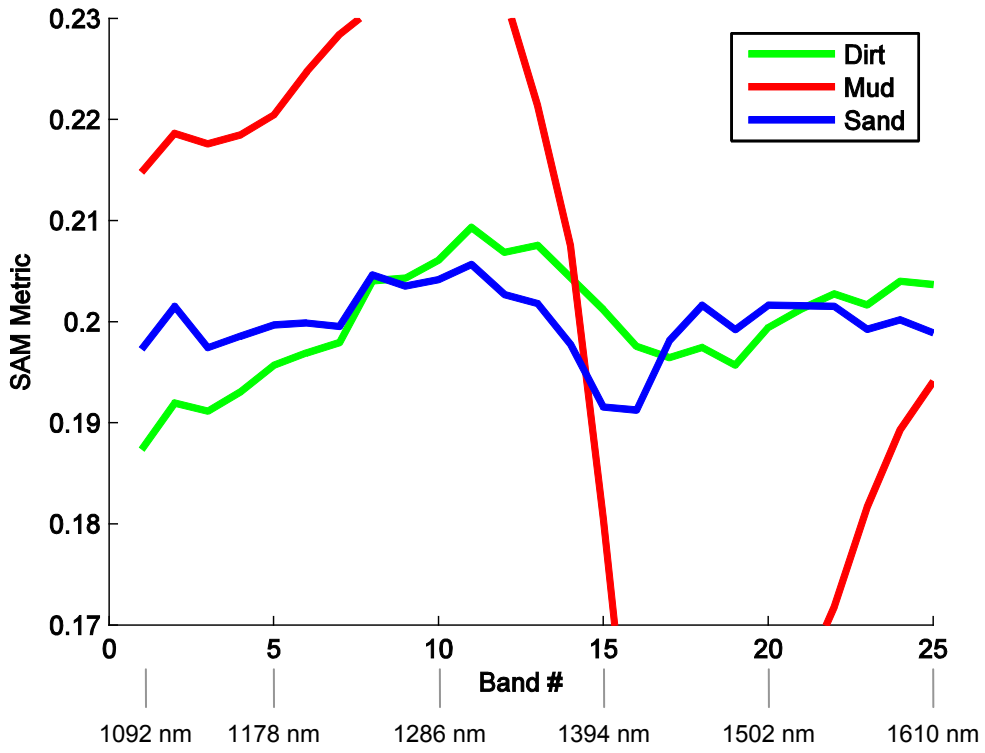

Figure 132: Comparison of terrain classes (110111)

It is worthwhile to analyze the training data set using the principal components technique to appreciate the characteristics of training data spectral differentiation. Using training data, rather than real images, is more suitable for this purpose since the averaging applied when acquiring the training data sets eliminates the random receiver noise and source fluctuations which contribute to the variance of the set of spectral vectors but add no information.

Figure 133 is the results of such analysis, using the axes associated with the three largest eigenvalues to plot all training data points reduced to three dimensional space. The resultant diagonalized covariance matrix indicates that the first three eigenvalues express 95% of the total variance in the training dataset. This shows that (for the classes

considered) there is a substantial amount of redundancy (correlation) among the 25 bands in the system.

Although a high degree of correlation is seen in the training data, correlated bands are not necessarily useless when computing pixel classification in actual images. The PCA analysis is performed using the training data alone, without the addition of instrumental noise (NEDR). Source fluctuation and receiver noise is assumed to be independent per-band with zero mean. To the degree which instrumental noise contributes to the statistical variance of actual observations, the correlated bands become uncorrelated and an inherent averaging process improves classification accuracy.

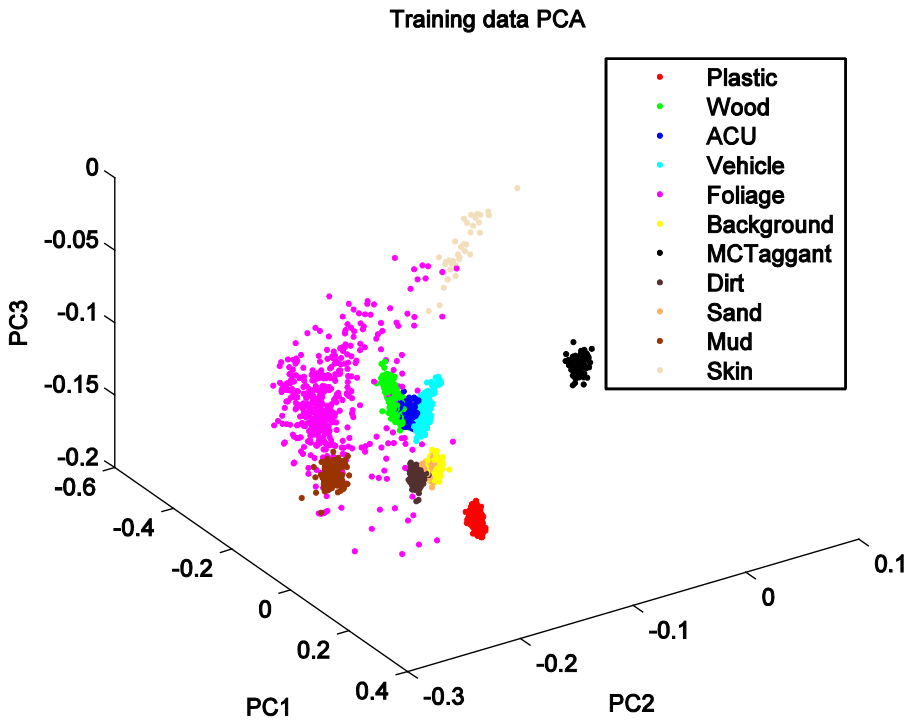

Figure 133: Principal component analysis of training data in three dimensions (101230)

8.3. Estimated Classification Accuracy

To assess the accuracy and robustness of the classifiers and spectral separation of training data, Monte Carlo-based simulation is performed. The image data to be presented in Section 9 is an important assessment of performance, however, the number of pixels and difficulty in establishing a "ground-truth" classification for each pixel suggests that numerical analysis will be most helpful in estimating the ideal and noise-corrupted error probabilities class by class.

Although an exact solution for classification accuracy is possible using parametric classifiers such as maximum likelihood, a Monte Carlo based method is applicable to non-parametric algorithms as well. Ideal classification accuracy may be calculated in parametric algorithms by multi-variate integration* of the statistical distributions of each class subject to the limits of the classifier decision surfaces.

Monte Carlo simulation generates a large number of random spectral vectors based on the covariance matrix of each class. Upon generation, the class association of each random vector is known. The set of random vectors is passed to the classification algorithm, which returns the assigned classification as estimated. The known classification is compared to the classifier estimated data and the probability of detection and probability

* Monte-Carlo integration is often used to approximate integrals of multi-variate functions when analytic techniques are unsuitable and numeric integration by grid sampling is computationally infeasible.

of false alarm vis-à-vis each class is tabulated in a matrix. The diagonal of the matrix represents correct classification while off-diagonal values are misclassifications. The Monte-Carlo results are based on the noise-perturbed training data samples, according to a specified NEDR.

The Monte Carlo method may be performed using only the statistics of the training data to estimate fundamental class overlap. This estimates the ideal classification performance given a noiseless imager. It should be noted that these predictions are general to the extent the training data is general, i.e., unrepresented variations will not be considered in class overlap analysis. For a more practical assessment of classifier performance, a second random vector is added to the class statistics generated random vector to account for instrumental noise and fluctuations. The statistics of this vector may be derived from an actual measurement such as that represented in Figure 109.

Table 9 is the numeric class assignment that represent material types in all other tables in this section. The 11 classes are represented by the signature data presented in Section 8.2.

Table 9: Class assignments

Class number	*Material type*
1	Plastic
2	Wood
3	Uniform
4	Vehicle
5	Foliage
6	Background
7	IFF taggant
8	Dirt
9	Sand
10	Mud
11	Skin

The simulation runs are tabulated for three NEDR values: 0.00, 0.05, and 0.15. [*] A NEDR of 0.00 is an ideal situation where measurement noise is zero. The classification probabilities in this case are the overlap of training data distributions. In each of the classification probability tables, the rows represent the class trials where $1x10^6$ random vectors generated with the row class covariance matrix and additive NEDR noise were classified according to column. Diagonal elements are correct classifications while off-diagonal elements are errors. The probability matrices are not necessarily symmetric, but approach symmetric for equal class probability distributions in the case of MLC.

Table 10 (MLC) and Table 11 (KNN) are computed assuming zero additive instrument noise. It is clear from these tables that the class signatures including only natural variance in the training data are well separated. Using the MLC classifier, all classes but skin (11) have practically zero overlap after rounding to the nearest percent. Correct identification of the skin class is observed to improve when noise is added.

[*] Although a constant NEDR is assumed per-band in the Monte Carlo simulations, an actual NEDR may vary with spectral band, target signature, and range.

Table 10: MLC classification probabilities for NEDR = 0.00

	1	2	3	4	5	6	7	8	9	10	11
1	1.00	0.00	0.00	0.00	0.00	0.00	0.00	0.00	0.00	0.00	0.00
2	0.00	1.00	0.00	0.00	0.00	0.00	0.00	0.00	0.00	0.00	0.00
3	0.00	0.00	1.00	0.00	0.00	0.00	0.00	0.00	0.00	0.00	0.00
4	0.00	0.00	0.00	1.00	0.00	0.00	0.00	0.00	0.00	0.00	0.00
5	0.00	0.00	0.00	0.00	1.00	0.00	0.00	0.00	0.00	0.00	0.00
6	0.00	0.00	0.00	0.00	0.00	1.00	0.00	0.00	0.00	0.00	0.00
7	0.00	0.00	0.00	0.00	0.00	0.00	1.00	0.00	0.00	0.00	0.00
8	0.00	0.00	0.00	0.00	0.00	0.00	0.00	1.00	0.00	0.00	0.00
9	0.00	0.00	0.00	0.00	0.00	0.00	0.00	0.00	1.00	0.00	0.00
10	0.00	0.00	0.00	0.00	0.00	0.00	0.00	0.00	0.00	1.00	0.00
11	0.00	0.00	0.00	0.00	0.02	0.00	0.00	0.00	0.00	0.00	0.98

Table 11: KNN classification probabilities for NEDR = 0.00

	1	2	3	4	5	6	7	8	9	10	11
1	1.00	0.00	0.00	0.00	0.00	0.00	0.00	0.00	0.00	0.00	0.00
2	0.00	0.99	0.00	0.00	0.00	0.00	0.00	0.00	0.00	0.00	0.00
3	0.00	0.00	0.99	0.00	0.00	0.00	0.00	0.00	0.00	0.00	0.00
4	0.00	0.00	0.00	1.00	0.00	0.00	0.00	0.00	0.00	0.00	0.00
5	0.00	0.00	0.00	0.00	0.95	0.00	0.00	0.00	0.00	0.05	0.00
6	0.00	0.00	0.00	0.00	0.00	0.98	0.00	0.00	0.02	0.00	0.00
7	0.00	0.00	0.00	0.00	0.00	0.00	1.00	0.00	0.00	0.00	0.00
8	0.00	0.00	0.00	0.00	0.00	0.00	0.00	1.00	0.00	0.00	0.00
9	0.00	0.00	0.00	0.00	0.00	0.01	0.00	0.00	0.99	0.00	0.00
10	0.00	0.00	0.00	0.00	0.00	0.00	0.00	0.00	0.00	1.00	0.00
11	0.00	0.00	0.00	0.00	0.01	0.00	0.00	0.00	0.00	0.00	.98

Table 12 and Table 13 are the MLC and KNN classifier probabilities when the NEDR is 0.05.[*] A NEDR of this value is expected to be the practical limit to spectral fidelity for single pulse measurements at stand-off ranges assuming the use of source compensation and improved signal processing. The results show near perfect identification for all but

[*] A diagonal variance matrix equivalent to the NEDR is added to the covariance matrix of the MLC routine for each class.

two classes, background cloth (6) and sand (9) which are identified correctly with probability of about 0.86. The KNN classifier demonstrates close to the same results.

Table 12: MLC classification probabilities for NEDR = 0.05

	1	2	3	4	5	6	7	8	9	10	11
1	1.00	0.00	0.00	0.00	0.00	0.00	0.00	0.00	0.00	0.00	0.00
2	0.00	1.00	0.00	0.00	0.00	0.00	0.00	0.00	0.00	0.00	0.00
3	0.00	0.00	1.00	0.00	0.00	0.00	0.00	0.00	0.00	0.00	0.00
4	0.00	0.00	0.00	1.00	0.00	0.00	0.00	0.00	0.00	0.00	0.00
5	0.00	0.00	0.00	0.00	0.99	0.00	0.00	0.00	0.00	0.01	0.00
6	0.00	0.00	0.00	0.00	0.00	0.87	0.00	0.00	0.13	0.00	0.00
7	0.00	0.00	0.00	0.00	0.00	0.00	1.00	0.00	0.00	0.00	0.00
8	0.00	0.00	0.00	0.00	0.00	0.00	0.00	0.98	0.02	0.00	0.00
9	0.00	0.00	0.00	0.00	0.00	0.12	0.00	0.02	0.86	0.00	0.00
10	0.00	0.00	0.00	0.00	0.00	0.00	0.00	0.00	0.00	1.00	0.00
11	0.00	0.00	0.00	0.00	0.00	0.00	0.00	0.00	0.00	0.00	1.0

Table 13: KNN classification probabilities for NEDR = 0.05

	1	2	3	4	5	6	7	8	9	10	11
1	1.00	0.00	0.00	0.00	0.00	0.00	0.00	0.00	0.00	0.00	0.00
2	0.00	0.99	0.00	0.00	0.01	0.00	0.00	0.00	0.00	0.00	0.00
3	0.00	0.00	0.99	0.01	0.00	0.00	0.00	0.00	0.00	0.00	0.00
4	0.00	0.00	0.00	1.00	0.00	0.00	0.00	0.00	0.00	0.00	0.00
5	0.00	0.00	0.00	0.00	0.95	0.00	0.00	0.00	0.00	0.05	0.00
6	0.00	0.00	0.00	0.00	0.00	0.90	0.00	0.00	0.10	0.00	0.00
7	0.00	0.00	0.00	0.00	0.00	0.00	1.00	0.00	0.00	0.00	0.00
8	0.00	0.00	0.00	0.00	0.00	0.00	0.00	0.97	0.02	0.00	0.00
9	0.00	0.00	0.00	0.00	0.00	0.23	0.00	0.03	0.75	0.00	0.00
10	0.00	0.00	0.00	0.00	0.00	0.00	0.00	0.00	0.00	1.00	0.00
11	0.00	0.00	0.00	0.00	0.02	0.00	0.00	0.00	0.00	0.00	.98

Table 14 and Table 15 are the classification results when the NEDR is assumed to be 0.15. This is close to the performance of the lab demonstrator system used to obtain the results described in Section 9, as indicated by the plots in Section 7. Discrimination

among classes 6, 8, and 9 (background, dirt, and sand) and classes 3 and 4 (uniform and vehicle) is done with less than 90% accuracy using the MLC routine. Notably, the identification probability of skin, plastic, and the IFF tag remains at unity, when rounded to the nearest percent. In particular, the IFF tag signature (7) had no false alarms.

Table 14: MLC classification probabilities for NEDR = 0.15

	1	2	3	4	5	6	7	8	9	10	11
1	1.00	0.00	0.00	0.00	0.00	0.00	0.00	0.00	0.00	0.00	0.00
2	0.00	0.93	0.05	0.01	0.00	0.00	0.00	0.00	0.00	0.00	0.00
3	0.00	0.04	0.85	0.10	0.00	0.00	0.00	0.00	0.00	0.00	0.00
4	0.00	0.00	0.09	0.86	0.00	0.01	0.00	0.00	0.03	0.00	0.00
5	0.00	0.01	0.00	0.00	0.95	0.00	0.00	0.00	0.00	0.04	0.00
6	0.00	0.00	0.00	0.02	0.00	0.61	0.00	0.11	0.25	0.00	0.00
7	0.00	0.00	0.00	0.00	0.00	0.00	1.00	0.00	0.00	0.00	0.00
8	0.00	0.00	0.00	0.01	0.00	0.09	0.00	0.76	0.14	0.00	0.00
9	0.00	0.00	0.00	0.03	0.00	0.30	0.00	0.19	0.47	0.00	0.00
10	0.00	0.00	0.00	0.00	0.01	0.00	0.00	0.00	0.00	0.99	0.00
11	0.00	0.00	0.00	0.00	0.00	0.00	0.00	0.00	0.00	0.00	1.0

Table 15: KNN classification probabilities for NEDR = 0.15

	1	2	3	4	5	6	7	8	9	10	11
1	1.00	0.00	0.00	0.00	0.00	0.00	0.00	0.00	0.00	0.00	0.00
2	0.00	0.86	0.05	0.01	0.07	0.00	0.00	0.00	0.00	0.01	0.00
3	0.00	0.05	0.79	0.10	0.04	0.00	0.00	0.00	0.00	0.00	0.00
4	0.00	0.01	0.09	0.83	0.03	0.02	0.00	0.01	0.01	0.00	0.00
5	0.00	0.00	0.00	0.00	0.94	0.00	0.00	0.00	0.00	0.05	0.00
6	0.00	0.00	0.00	0.03	0.02	0.71	0.00	0.10	0.14	0.00	0.00
7	0.00	0.00	0.00	0.00	0.00	0.00	1.00	0.00	0.00	0.00	0.00
8	0.00	0.00	0.00	0.01	0.05	0.14	0.00	0.70	0.10	0.00	0.00
9	0.00	0.00	0.00	0.04	0.02	0.45	0.00	0.19	0.30	0.00	0.00
10	0.00	0.00	0.00	0.00	0.05	0.00	0.00	0.00	0.00	0.94	0.00
11	0.00	0.00	0.00	0.00	0.08	0.00	0.00	0.00	0.00	0.00	0.92

9. 3D Spectral Imaging Results

This section presents image data collected with the laboratory demonstrator prototype. Section 9.1 presents spectral point-cloud results obtained from scenes containing multiple objects in varied layouts. False color images are presented to make the spectral differentiation visually evident. The point clouds are spectrally classified using K-Means, KNN, or Maximum-Likelihood algorithms. Section 9.2 presents results from situations where multiple returns are common or necessary to recognize objects hidden in foliage or camouflage and highlights the unique range-resolved spectroscopic ability of the system. Terrain sensing results are discussed in Section 9.3. The parameters tested here should not be considered to be the present or ultimate limits of the system, i.e., it should not be inferred that demonstrations at 40 m maximum range indicates poor results are obtained at longer ranges. Importantly, the supercontinuum power spectral density was not constant for all tests. Repairs to the source unit decreased the power output in later tests.

9.1. Many-Object Scenes

Four scenes were constructed using objects that would typically be found in UGV operations, or similar applications. The first scene, scene 1 in the numbered sequence,

involves a mannequin dressed in a combat uniform behind a HMMWV door and office plant in a wood wicker basket (Figure 134). The office plant has broad leaves, larger than the beam at its distance. Although the scanned field of view is small, portions of each object will be visible, including part of the backdrop cloth. The backdrop is at a range of 36 m. For the scene 1 measurement the APD is reversed biased at 64.7 V, and 2 dB attenuation is used to reduce the beam within the linear range of the receiver. The attenuation reduces the backscatter intensity as if the backdrop were at a range of approximately 46 m, its effective attenuated range.

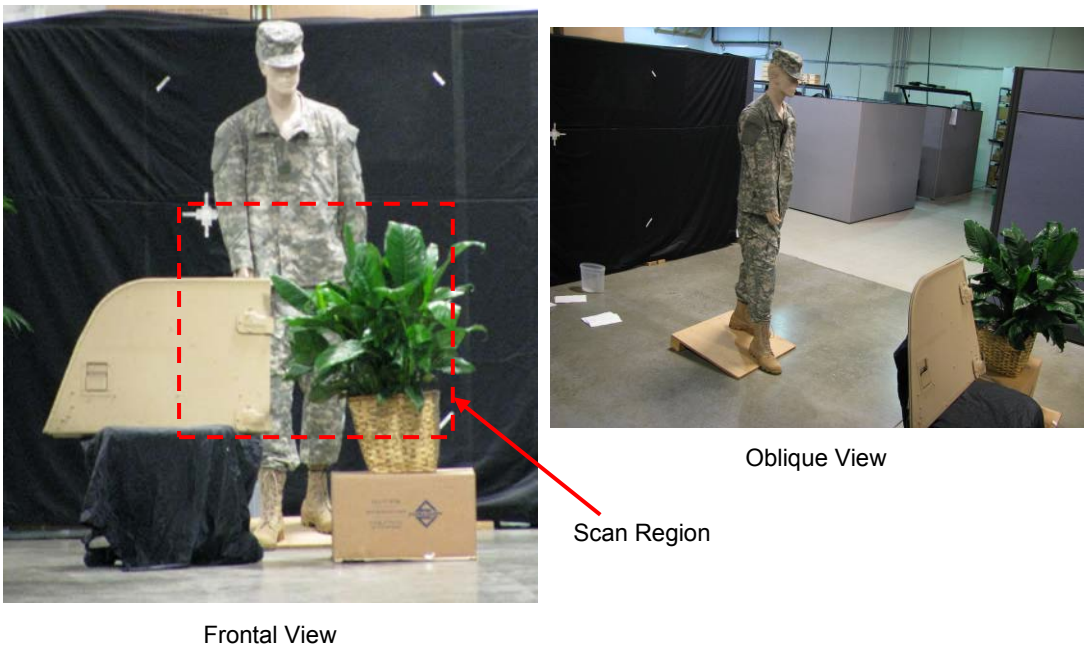

Figure 134: Scene 1 at 46 m maximum effective attenuated range (100328)

Scene 2 is very similar to scene 1 with a few exceptions (Figure 135). The mannequin is moved to the left, and the HMMWV door is moved forward by a small distance. A large

palm-type plant is added close to the cloth backdrop on the right side of the image. Scene 2 utilizes the same range, APD bias, and attenuator parameters as scene 1.

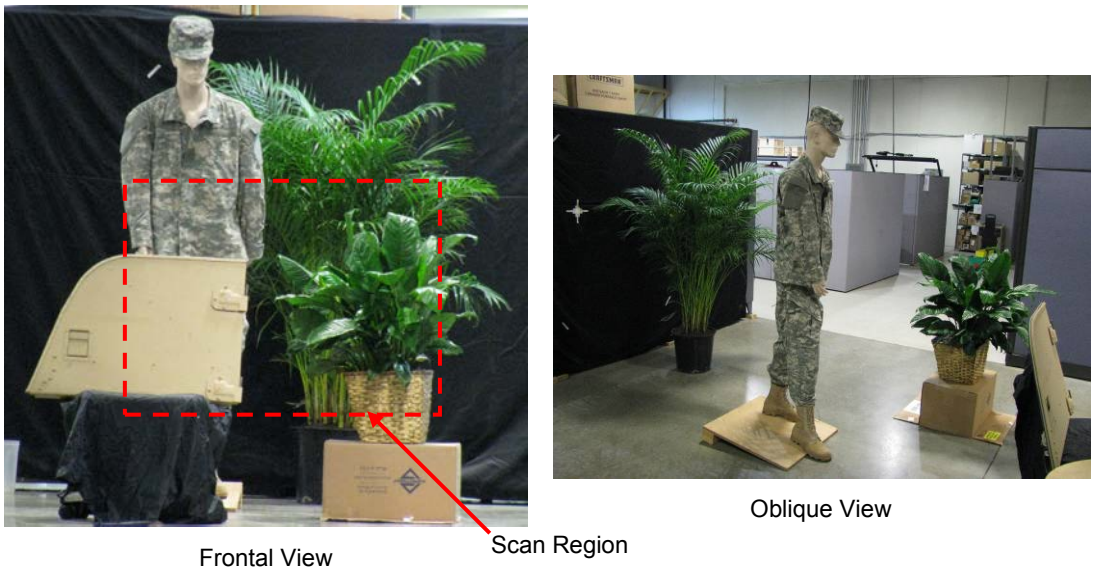

Figure 135: Scene 2 at 46 m maximum effective attenuated range (100328)

Scene 3 involves a sheet of plywood, plastic, and a different broad-leaf plant (Figure 136). The sheet of plastic is notable for its lack of optical texture, i.e., lack of image features from which stereo correspondence and therefore range may be computed. The plastic has a spectral signature that, as the training data shows, is very distinct from other scene elements. Like scenes 1 and 2, the backdrop is at 36 m actual range and 2 dB attenuation yields an effective attenuated range of 46 m. The APD is biased at 68.9 V for higher gain.

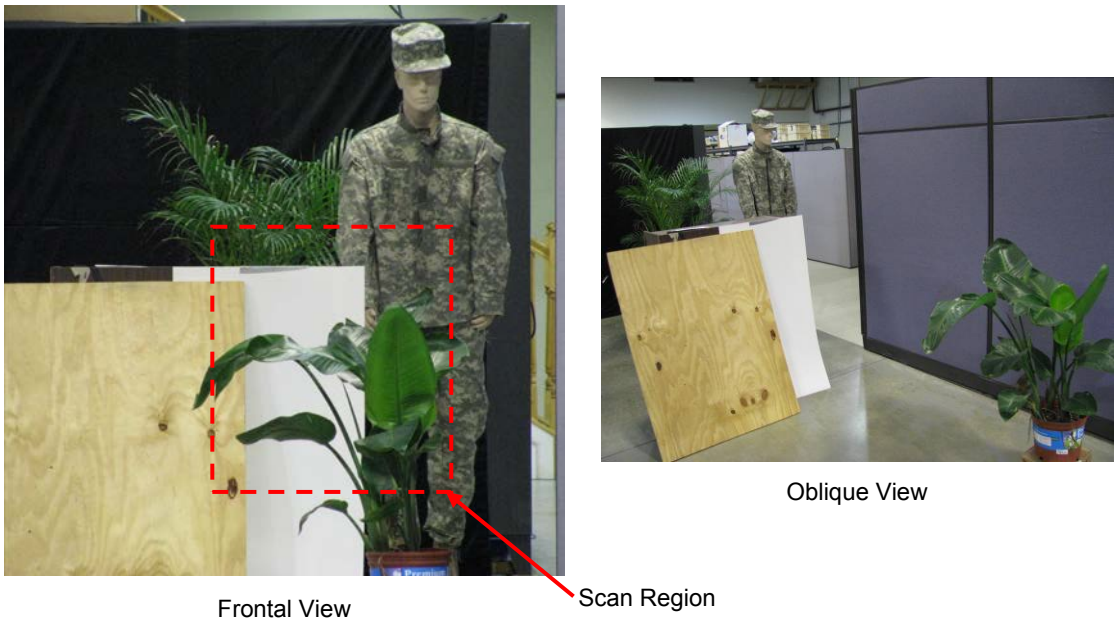

Figure 136: Scene 3 at 46 m maximum effective attenuated range (101230)

Scene 4 represents vehicle and dismount operations in a foliated environment (Figure 137). The vehicle (HMMWV) is marked with a passive spectral IFF taggant having a specific SWIR signature that indicates the vehicle is friendly. The taggant has an unremarkable light pink appearance in the visible spectrum. The range, attenuation, and APD bias settings for scene 4 are identical to those used to image scene 3.

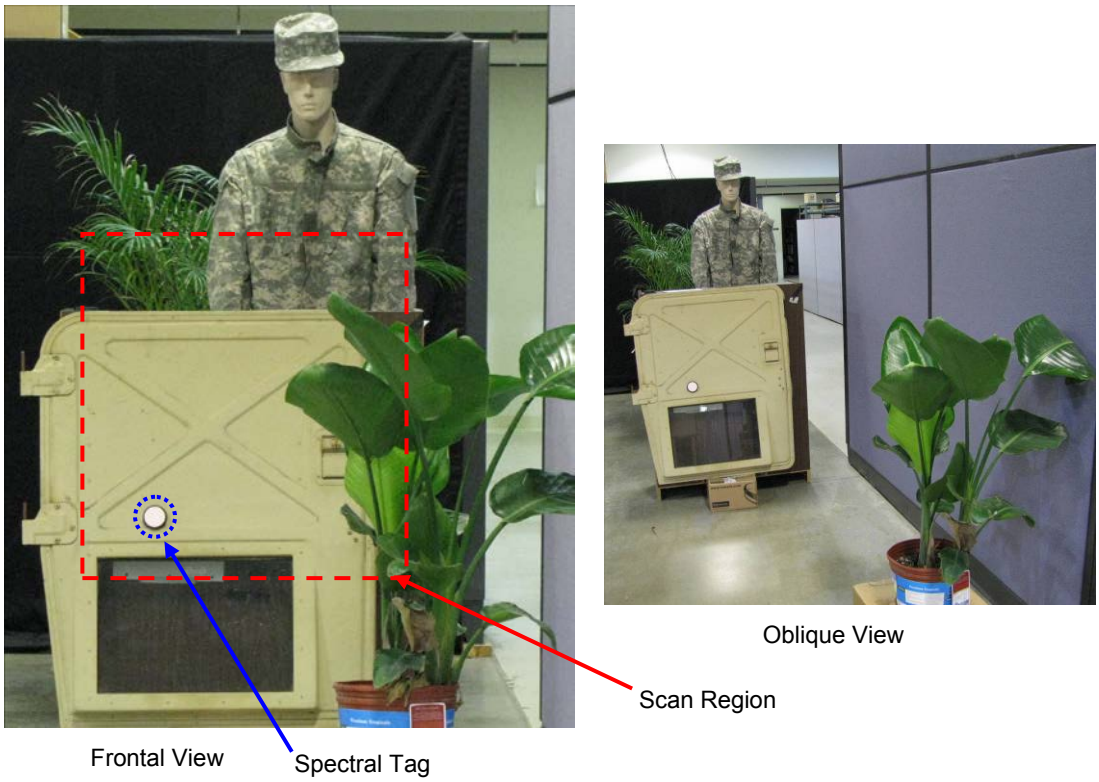

Figure 137: Scene 4 at 46 m maximum effective attenuated range (101230)

9.1.1. False Color Images

Two dimensional false color images were created from the spectral point cloud to visualize the spectral contrast of the images using the Euclidean metric, which is responsive to absolute reflectivity, and the SAM metric, which is sensitive only to relative spectral features. These images are not used to classify the pixels and make use of 3 selected bands, or linear combinations of 3 bands, from the 25 available. Unlike

point clouds which may display multiple voxels for a single pixel, the false color images display the spectral response of only the first return pulse (after the reference return).

Figure 138 and Figure 139 are created from scene 1. Both false color images represent bands 17, 12, and 2 in RGB color space, respectively. Contrast stretching is performed on the images, and allows the brightest 2% and dimmest 2% of the pixels to saturate. These images were obtained without using averaging or source compensation of any kind. In Figure 138 which maps to RGB color space from the high dimensional Euclidean space, foliage is clearly distinct from all other objects owing to its strong contrast in band 17. The vehicle door also stands out. The uniform and backdrop, both consisting of cloth material, are somewhat distinct but more so when an image extracted from time domain averaged waveforms is examined (not shown). It is clear that the brightest object in the scene, in an absolute sense, is the wicker basket which appears in the bottom right of the image.

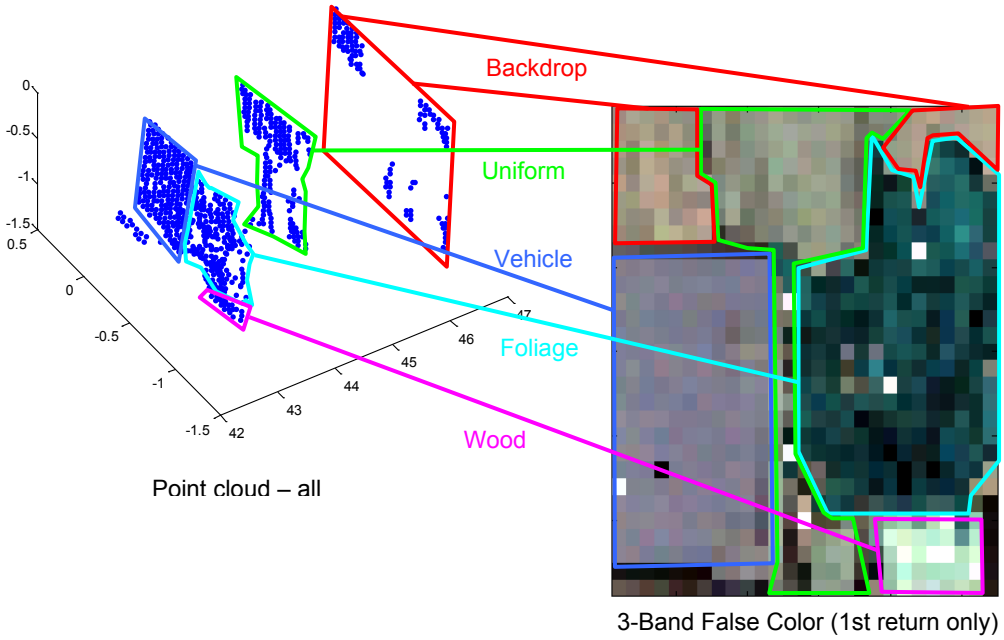

Figure 138: Scene 1 - 3-band Euclidean false color image of first return (20100328T155908)

Figure 139 is created from the same source data used for Figure 138, but using the SAM projection. Each distinct object in Figure 138 is also distinct in Figure 139, however noise is more apparent in the SAM image since the intensity of each vector in 25-band space is normalized. Several white and black pixels in Figure 138 and Figure 139 represent glitches in the acquisition process that may be the result of EMI.

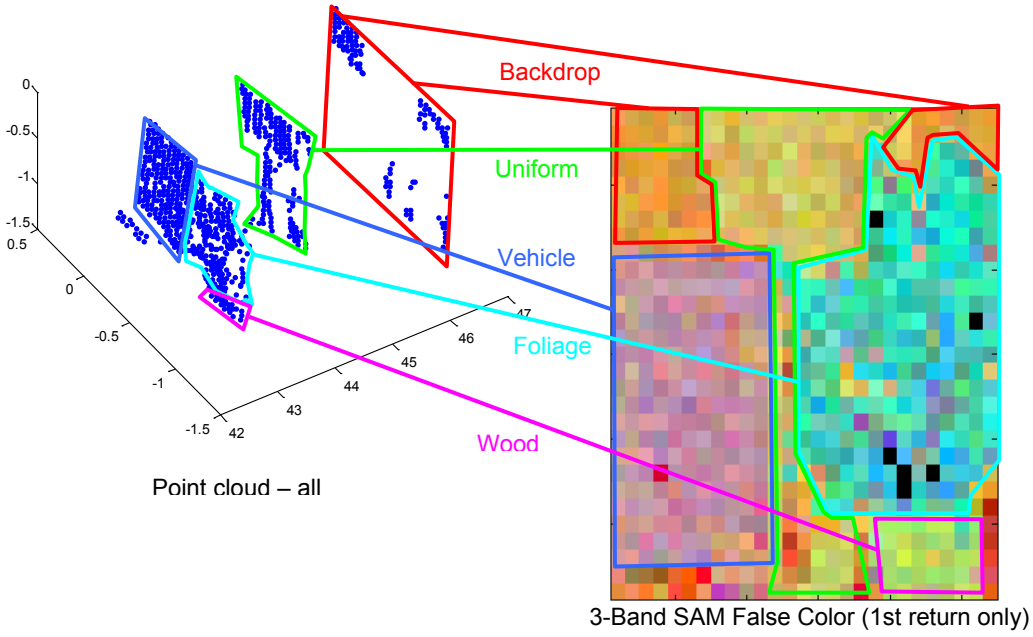

Figure 139: Scene 1 - 3-band SAM false color image of first return (20100328T155908)

Figure 140a through e are false color images from scene 3. The top row, a through c, are obtained using time waveform averaging of 200 waveforms while d and e are obtained without averaging. Figure 140a is a Euclidean metric image while Figure 140b is its SAM projection, each using bands 18, 7, and 25 mapped to RGB color space, respectively. In both a and b, the wood, plastic, foliage, and uniform are clearly distinct. They remain distinct in d and e, the images taken without averaging, but increased noise is apparent. Figure 140c is an image generated from the SAM spectral vectors, but instead of selecting three bands, PCA was used to transform the data. PCA factored the covariance matrix and yielded linear combinations of bands that correspond to uncorrelated variance values. The three vectors having the highest variance are selected as the RGB color space of Figure 140c and account for 97% of the total image variance.

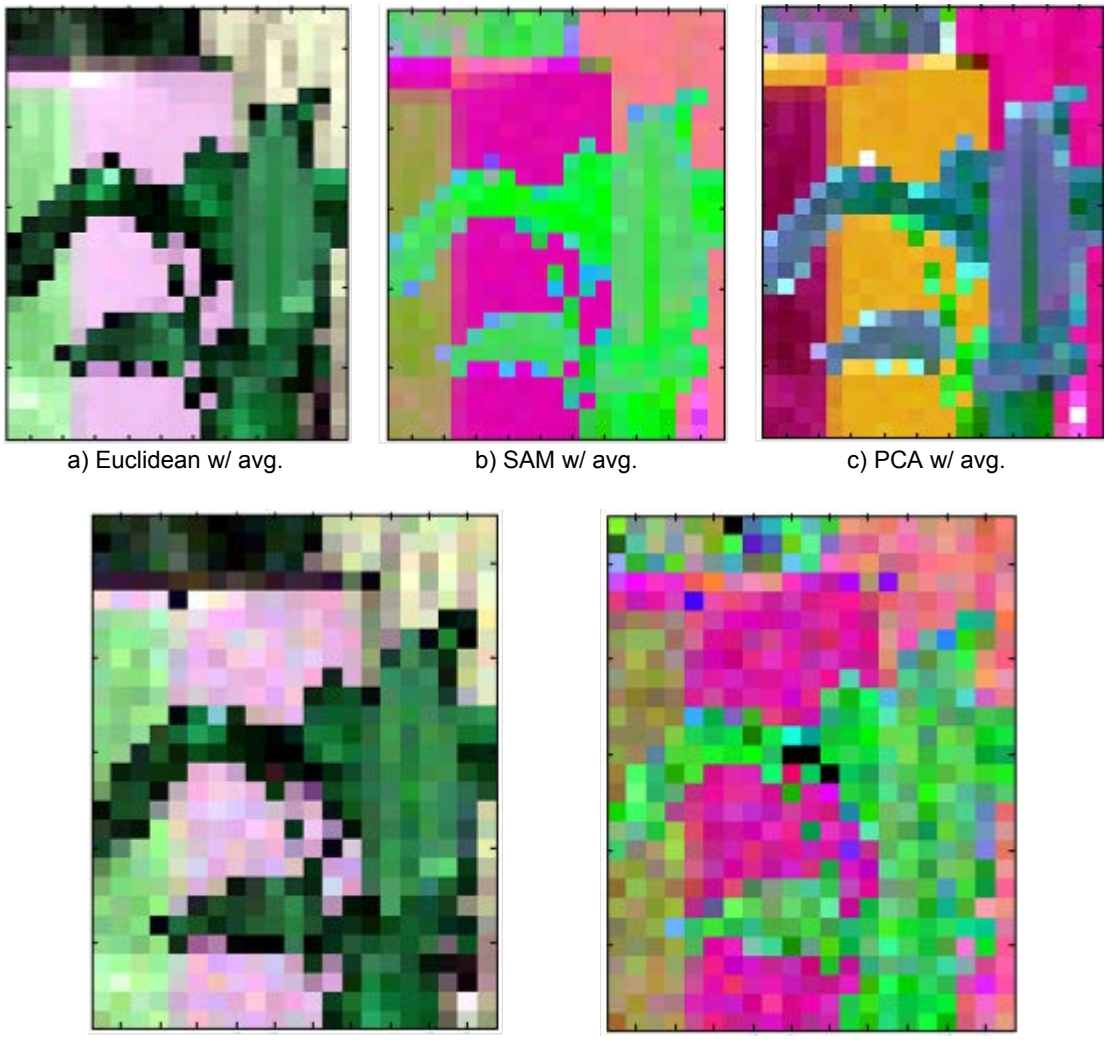

Figure 140: Scene 3 false color images
(20101230T133528 pp 20110101T170644, 20101230T142201 pp 20110101T160115)

Figure 141 follows the same explanation as Figure 140, but produced using data from scene 4. Objects in the scene are clearly distinct in bands 18, 7, and 25 (mapped to R, G, B) as shown in Figure 141a and b. Unique to scene 4 is the spectral taggant, applicable as a passive IFF device, in the images as indicated by the blue dashed circle. The limitations of reducing spectral space to three dimensions are apparent as the spectral taggant is not uniquely identifiable. The pixel representing the IFF spectral taggant

saturates the RGB color space in the red and blue band in the Euclidean and SAM images, and saturates the blue band in the PCA image. The principal components image, Figure 141c, accounts for 98% of the total image variance.

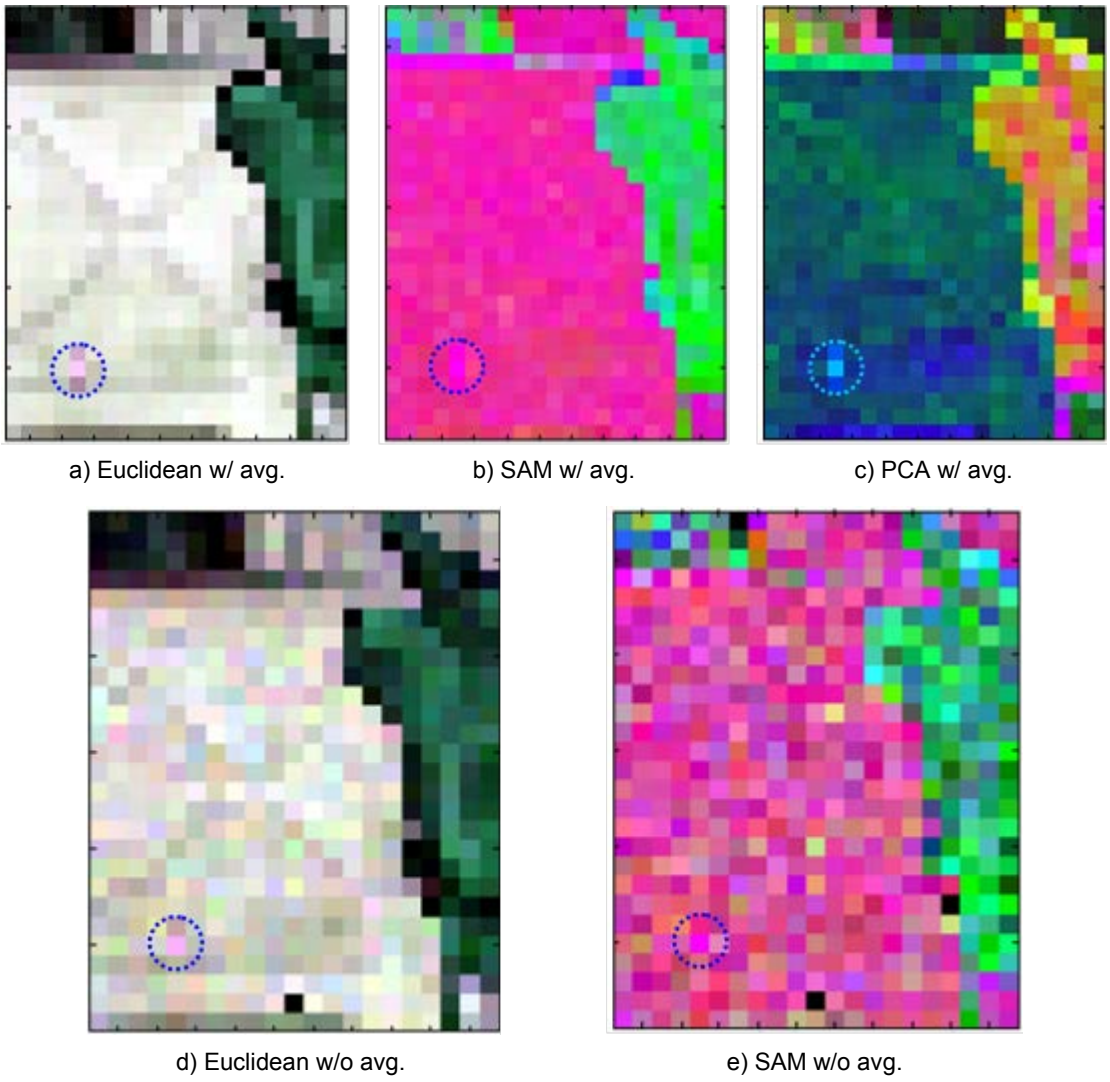

a) Euclidean w/ avg. b) SAM w/ avg. c) PCA w/ avg.

d) Euclidean w/o avg. e) SAM w/o avg.

Figure 141: Scene 4 false color images
(20101230T164558 pp 20110102T153136, 20101230T154245 pp 20110102T150833)

9.1.2. K-Means Classified

The K-Means classifier, fully discussed in Section 3.4.1, is a non-parametric, unsupervised algorithm that seeks to group similar spectral vectors into a number of classes represented by class centroid vectors (or class means). Since this technique does not require training data, it adapts to observations of new signatures. All of the point clouds presented in this section were obtained without using time-domain averaging or source compensation. The spectral vectors following transformation to SAM space are used exclusively.

Figure 142 is the point cloud obtained from scene 1, with points color coded according to K-Means classification. Four classes were used, with no division or fusion of classes performed in the clustering process. Vehicle surfaces are represented in green, foliage in dark blue, uniform fabric and wood in red, and background fabric in light blue. Overall the results correspond to a high degree of classification accuracy, with some exceptions. First, when 4 classes are specified, the wood class is indistinct from the uniform class. Second, errors are visible on the vehicle door in specific places- along the top edge, and on the two hinge plates located along the right edge. Errors on the top edge are explained by the spatial-spectral coupling effect (Section 7.5). Errors on the hinge plate are likely the result from scratches and exposed metal on the surface. Various other edge effect errors can be seen along the edges of the mannequin and backdrop, which is expected given the discussion in Section 7.5.

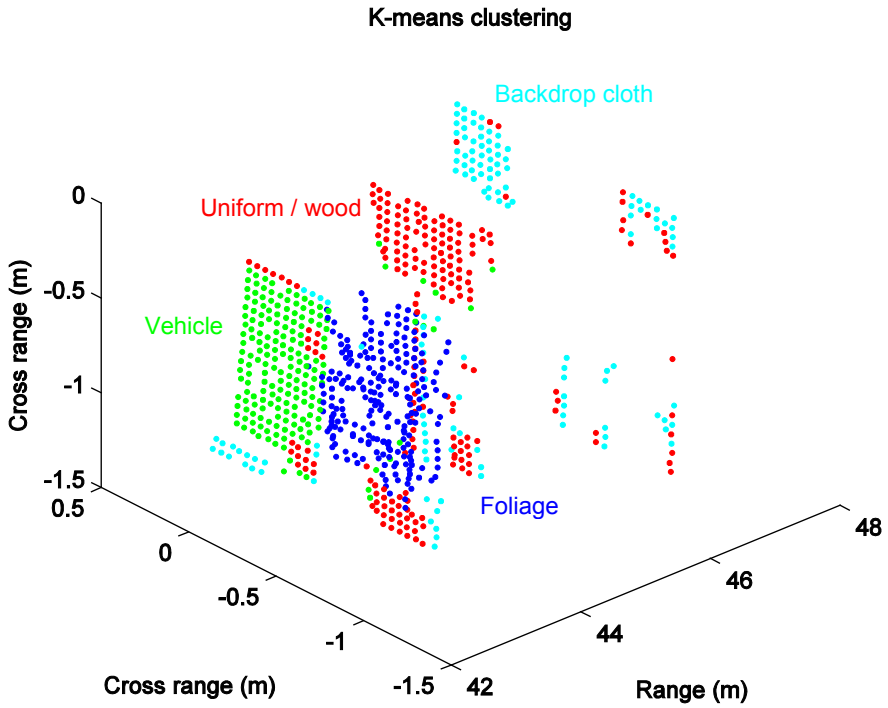

Figure 142: Scene 1 - spectrally-coded point cloud from K-Means classification (20100328T155908; 100421)

Figure 143 is the K-Means classified point cloud of scene 2. Five clusters were used for this scene. The vehicle door is represented in magenta, uniform in red, foliage in green and cyan, and the background in blue. Notably, foliage is represented by two clusters. This is not particularly surprising given the broad variation seen in the foliage class, as depicted in Figure 121. Again, wood is grouped with the uniform material. Edge errors are seen, similar to Figure 142, as are errors on the hinge plates of the vehicle door.

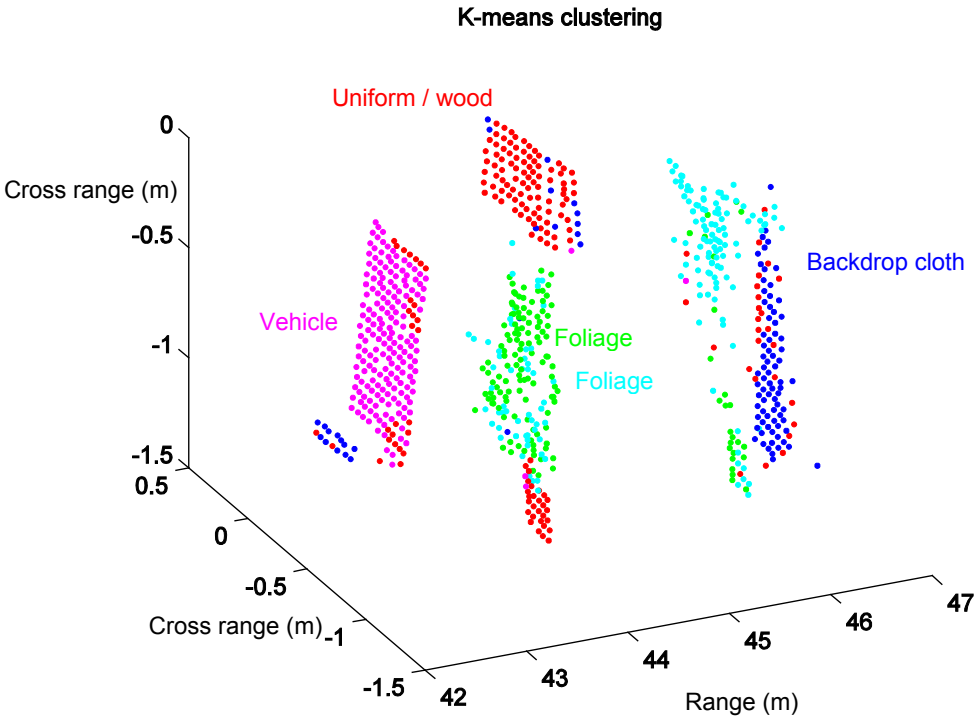

Figure 143: Scene 2 - spectrally-coded point cloud from K-Means classification (20100328T174349; 100421)

The cluster centroids that represent the classes coded in Figure 143 are shown in Figure 144. The two clusters representing foliage are unmistakable. The other cluster centroids are easily traceable to the mean values in the training data of Section 8.2, with the exception of uniform / wood, which is slightly distorted, likely due to specular reflections from the wicker basket.

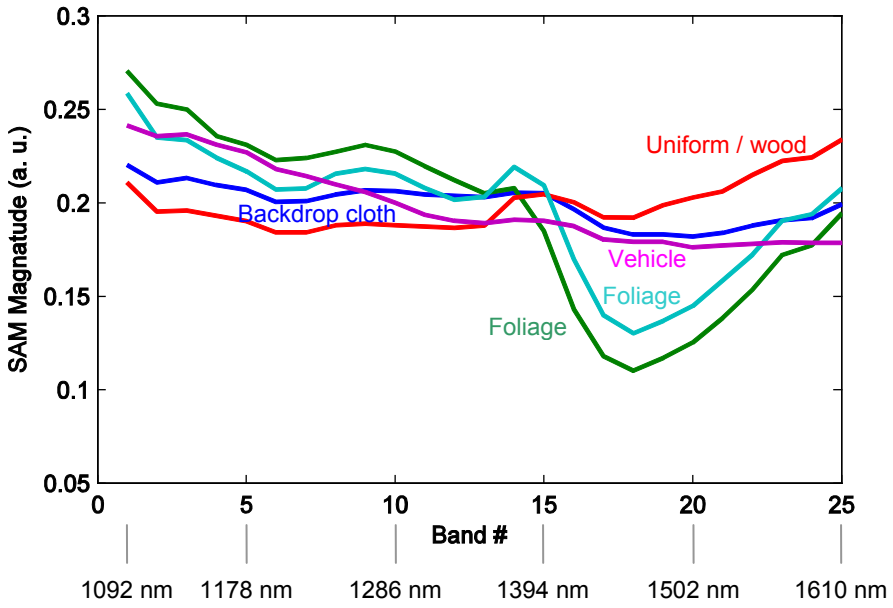

Figure 144: Scene 2 – 4 cluster K-Means cluster centroids (100421)

The 5-cluster K-Means classified point cloud for scene 3 is shown in Figure 145 and the cluster centroids in Figure 146. Similarly, two clusters represent foliage, shown in the cyan and magenta colors. Wood is represented by red, and plastic by blue. Green represents the uniform class. Some edge errors appear on the edge of the plastic sheet and on the mannequin.

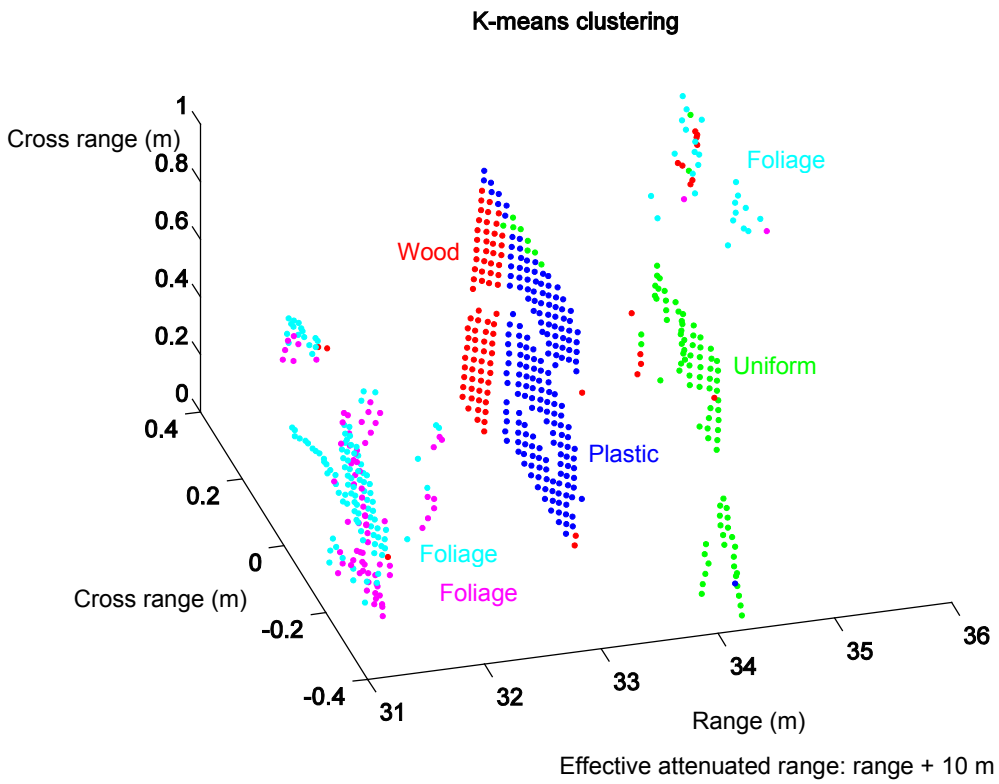

Figure 145: Scene 3 - spectrally-coded 5 cluster K-Means point cloud (20101230T142201 pp 20110101T160115)

The cluster centroids in Figure 146 closely match the training data in Section 8.2. Especially notable is the variation in the two foliage classes, something also observed in Figure 121. Since two different plants were used in Scene 3, the two foliage classes may be attributable to variation among plant species, or various plant internal structures.

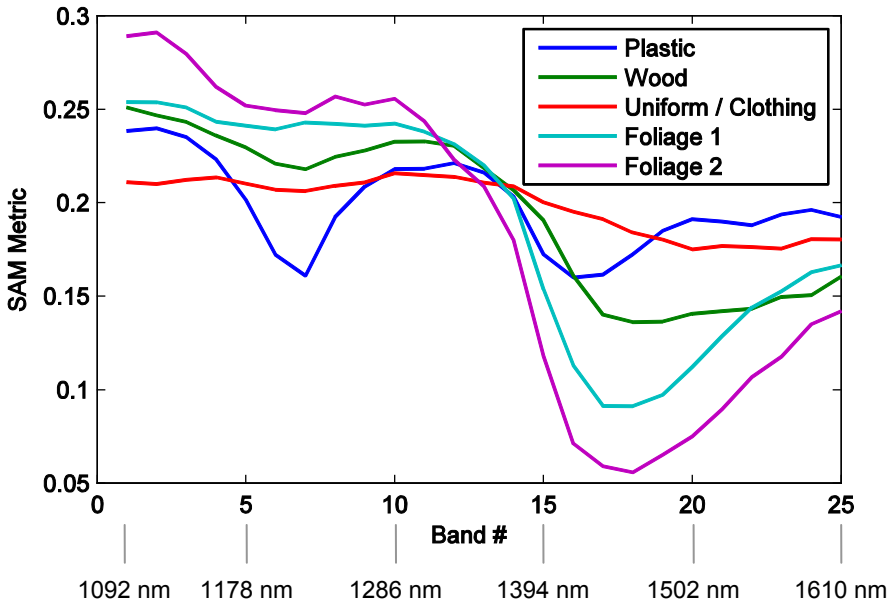

Figure 146: Scene 3 - 5 cluster K-Means centroids (20101230T142201 pp 20110101T160115)

9.1.3. KNN Classified

This section presents the K-Nearest-Neighbor (KNN) classification results for all 4 scenes. Section 3.4.2 describes the KNN algorithm in detail. As a supervised classifier, the algorithm is supplied with training data for each class. The output of the KNN routine provides, unlike K-Means, a specific semantic label for each class without the need for further interpretation (e.g., interpreting the cluster centroids from K-Means). Using the first nearest neighbor was found to be a reliable method, however extending this to determine classification from a quorum or weighted quorum of the next nearest neighbors is straightforward. The classification time of KNN was notably slower than the MLC routine since a distance must be computed for every observed vector to every

training vector.* One advantage of KNN is that it is non-parametric, and does not make any assumptions about the statistical distribution of target signatures. Bimodal or multimodal distributions may be handled without special consideration. Neither averaging nor source compensation was used in any of the point clouds in this section.

Figure 147 is the scene 1 point cloud classified by the KNN algorithm. Good results were obtained in this case. All scene objects were identified distinctly, with infrequent classification error. Foliage was occasionally confused with wood, and edge errors appeared in some places. Because the training data used for the KNN classifications of scene 1 and scene 2 contained edge errors, edge effects were handled better than they may be by training data not containing edge voxels. Similar results were obtained for the KNN classification of scene 2, depicted in Figure 148. The multi-class region located in front of the bottom edge of the vehicle door in Figure 147 and Figure 148 is blackout cloth material which was not represented in the training data. Although this region was classified correctly using K-Means, which is adaptive, it is improperly classified in KNN due to the absence of training vectors.

* A more advanced implementation may limit this calculation to a smaller neighborhood of training data elements.

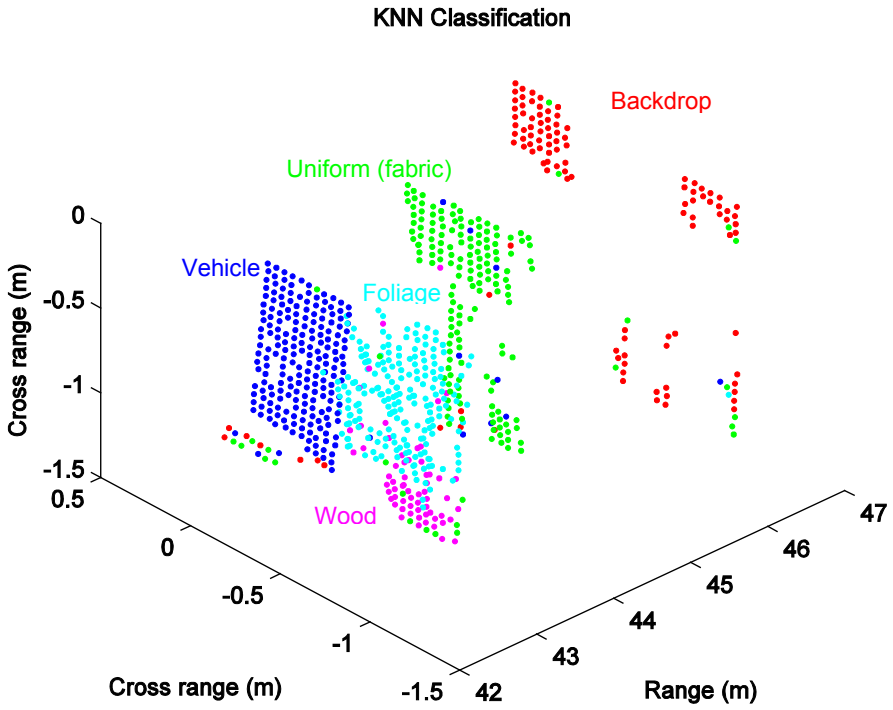

Figure 147: Scene 1 - spectrally-coded point cloud from KNN classification (20100328T155908; 100421)

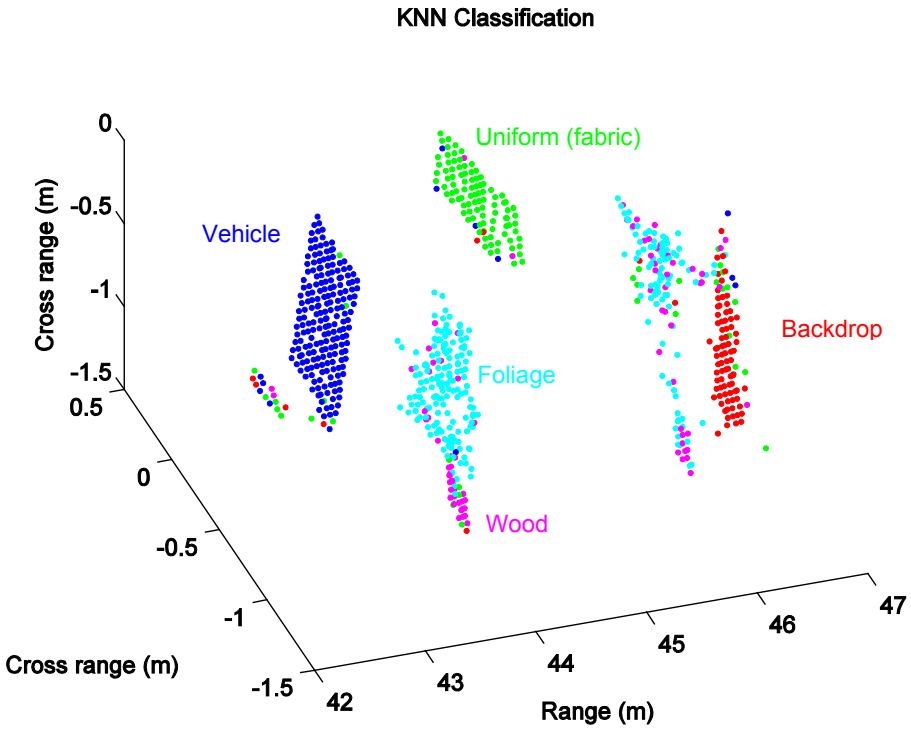

Figure 148: Scene 2 - spectrally-coded point cloud from KNN classification (20100328T174349; 100421)

The KNN results for scene 3 are shown in Figure 149. A total of 681 voxels were obtained in processing the scene 3 point cloud. Of these, 563 were first returns from a target surface, while 118 were from second, third, and in a few cases higher order returns. Obtaining 17% more pixels by allowing secondary and tertiary returns in a complex, multi-object scene makes Spectral LADAR especially capable in situations involving targets in cluttered environments. Similar to scenes 1 and 2, good results were obtained. Edge errors remained a problem, and the backdrop was highly misclassified since nearly all voxels suffered from the edge effect by being partially occluded by other scene objects.

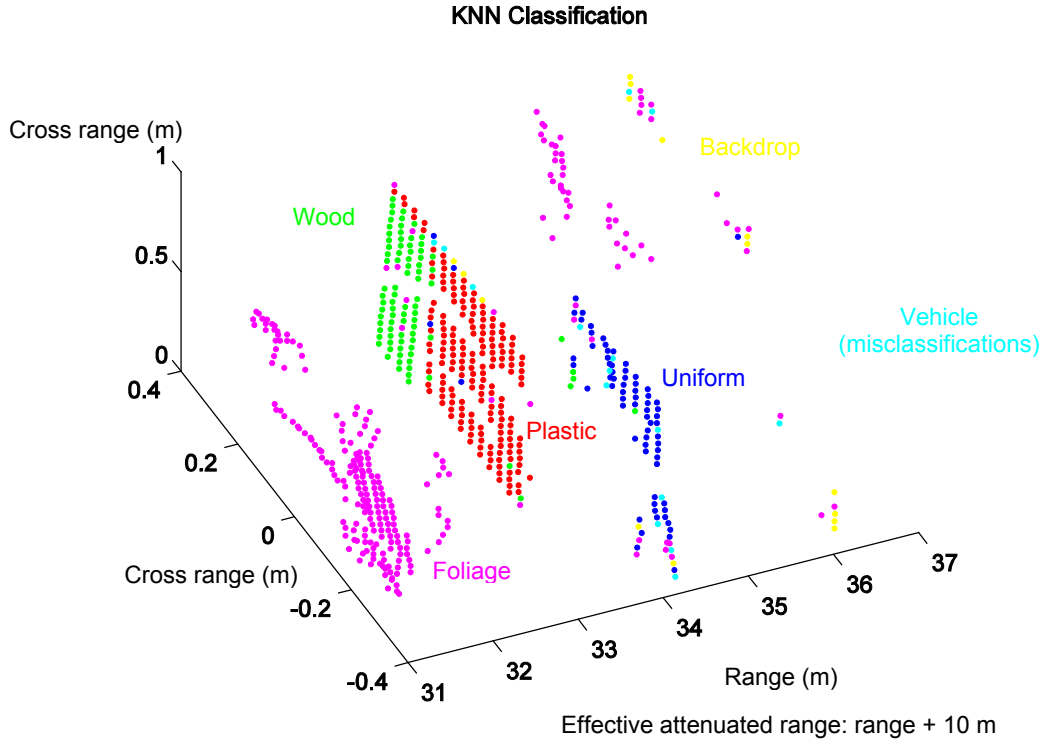

Figure 149: Scene 3 - spectrally-coded point cloud from KNN classification (20101230T142201 pp 20110101T160115)

Scene 4 is intended to demonstrate the use of spectral taggants to identify friendly forces or indicate other labels of interest. As shown in Figure 137, the spectral tag has an inconspicuous visible signature, but Figure 126 reveals a highly featured and unique SWIR spectrum. Identification of rare and highly important signatures is difficult using K-Means since infrequent observations have little influence over class centroids. In a supervised algorithm, like KNN, this situation is handled in a straightforward manner. The KNN classified point cloud of scene 4 is shown in Figure 150. A single black voxel, indicating the classification of the voxel as the spectral taggant is observed in the proper location. The inset figure plots the actual observed spectrum. Aside from the sole and correct identification of the spectral taggant, edge errors are visible in many of the

expected locations. An unexpectedly large number of classification areas appeared on the door surface. This may be from imperfections or contamination on the surface. Using a higher order KNN algorithm where more than the first nearest neighbor determines the classification may help this, or by using spatial averaging among neighboring voxels.

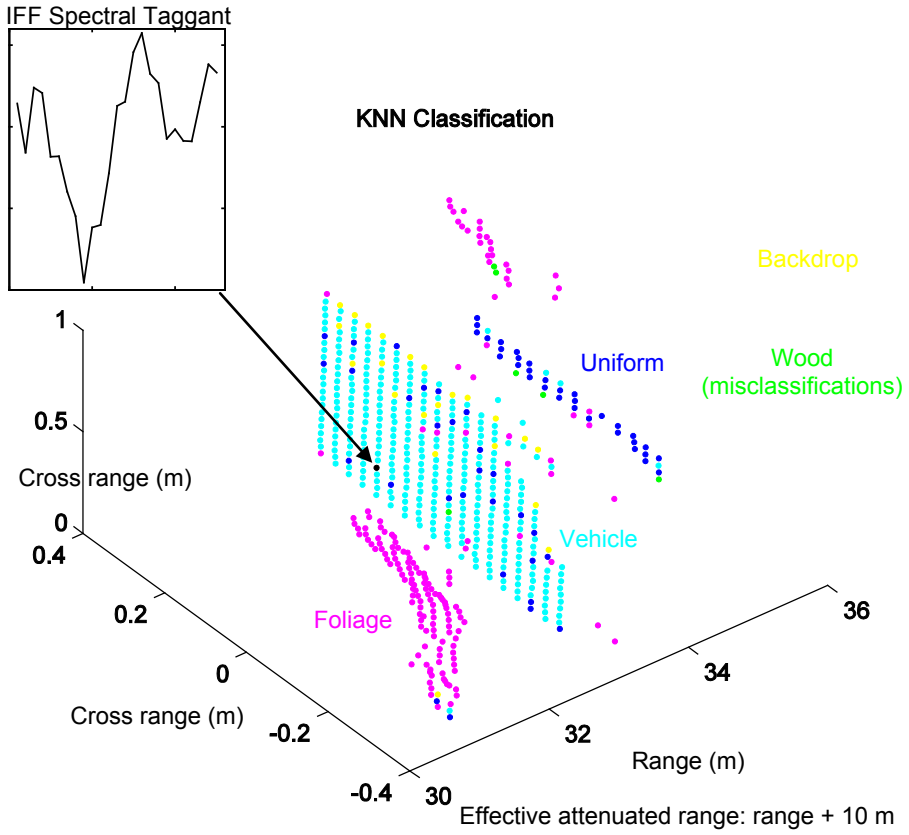

Figure 150: Scene 4 - spectrally-coded point cloud from KNN classification (20101230T154245 pp 20110102T150833)

9.1.4. Maximum Likelihood Classified

Scenes 3 and 4 were classified using the maximum-likelihood classifier (MLC), which is elaborated upon in Section 3.4.3. Like the KNN classifier, the MLC is based on the analysis of training data and is accurate and comprehensive to the extent that the training data is accurate and comprehensive. Unlike the KNN classifier, however, the MLC is a parametric method which characterizes the training data classes by a covariance matrix under the assumption that Gaussian statistics adequately describes the natural variation of signatures. One key advantage the MLC has over KNN is speed, since the classification may be made on the result of a calculation of observation vector to class mean vector distances. In addition to class covariance matrices, the MLC requires some reasonable estimate of instrument noise, NEDR in the case of Spectral LADAR. The instrument noise, assumed to be band independent, adjusts the diagonal (variance) terms of the covariance matrix to adapt to the expectation of broader multivariate PDFs on the account of random instrument fluctuations. Lacking this adjustment misclassifies observations of classes with naturally low variance into classes with naturally high variance. For the analysis in this section a NEDR of 0.15 is assumed, following the observations of Figure 108 and Figure 109. No averaging or source compensation was used to classify the point clouds in this section.

Figure 151 is the MLC point cloud of scene 3. The accuracy of the MLC is observed to be similar to that of KNN. Edge errors were observed, however the background was classified more accurately than the KNN point cloud shown in Figure 149. A notable

cluster of errors occurs in Figure 151 along the top edge of the plastic sheet. As shown in Figure 136, duct tape used to secure the plastic sheet to the supporting structure is visible, but not represented in the training data. The duct tape is classified as its nearest spectral match in this case, variously the backdrop or vehicle classes.

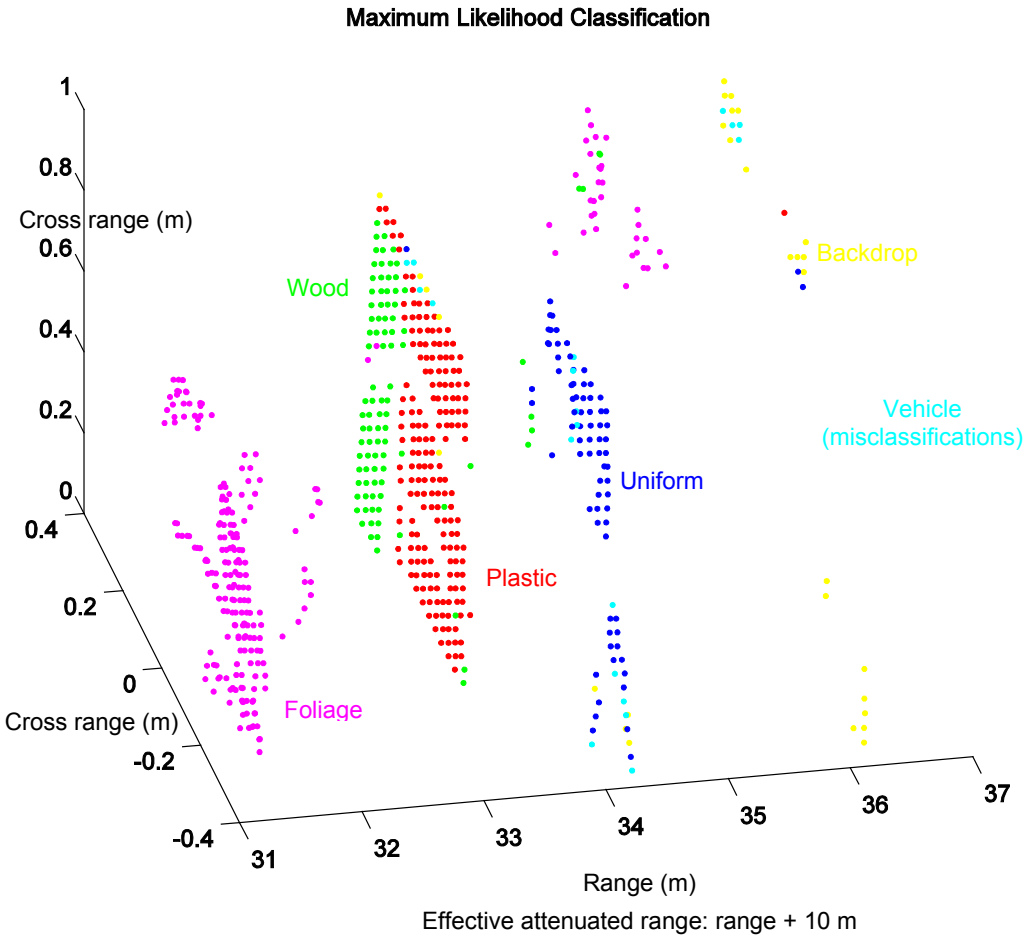

Figure 151: Scene 3 – spectrally-coded point cloud from MLC (20101230T142201 pp 20110101T160115, 110104)

The MLC point cloud of scene 4 is shown in Figure 152. Again, as in Figure 150, the spectral taggant was uniquely identified in the single voxel that it occupies with no false alarms elsewhere in the image. This successful result demonstrates a unique capability of

Spectral LADAR as an IFF interrogator, discussed further in the conclusion (Section 10.4).

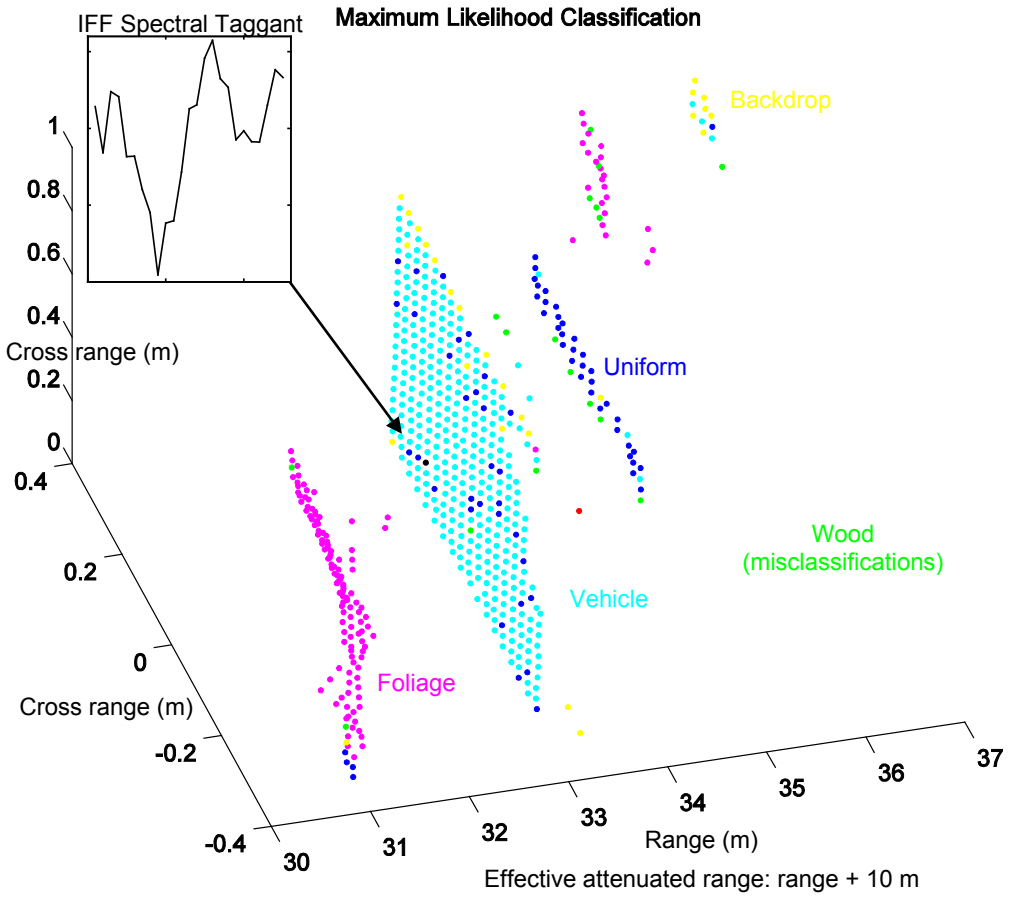

Figure 152: Scene 4 – spectrally-coded point cloud from MLC (20101230T154245 pp 20110102T150833, 110104)

9.2. Multiple Returns

Scenes with foliage and camouflage are among those which benefit from the range resolved ability of LADAR. In the case of foliage, leaves often partially occlude pixels but allow some regions of transmission. This is also true of most camouflage used in

practical situations. In this way, LADAR can penetrate obscurants to identify objects behind partial occlusions.

9.2.1. Clothing Behind Foliage

This scene demonstrates a situation involving personnel (mannequins for demonstration purposes) partially obscured by foliage. This scene (photographed in Figure 153) was scanned by 21 pixels in azimuth and 17 pixels in elevation, for a total of 357 pixels. As usual, source compensation and time waveform averaging were not used. The point cloud of the scene, with K-Means classification, is shown in Figure 154. Of the 357 pixels, 66 contained multiple voxels per pixel with the threshold settings used (1 mV). There were 239 voxels that indicated the presence of the combat uniform or foliage.[*] K-Means clustering misclassified 7 pixels yielding an error rate of 3%. Bands 21 through 25 were ignored due to transmitter focusing problems.

[*] Other voxels were incident on the backdrop

Figure 153: Foliage and fabric test scene photo (101119)

The centroids of the clusters are plotted in Figure 155, with the characteristic absorption of foliage clearly visible. The spectral vectors were analyzed following transformation to the SAM mapping (as usual for data analyzed in this work), since inversion of the LADAR equation to find reflectivity is very difficult due to unknown target cross sections.

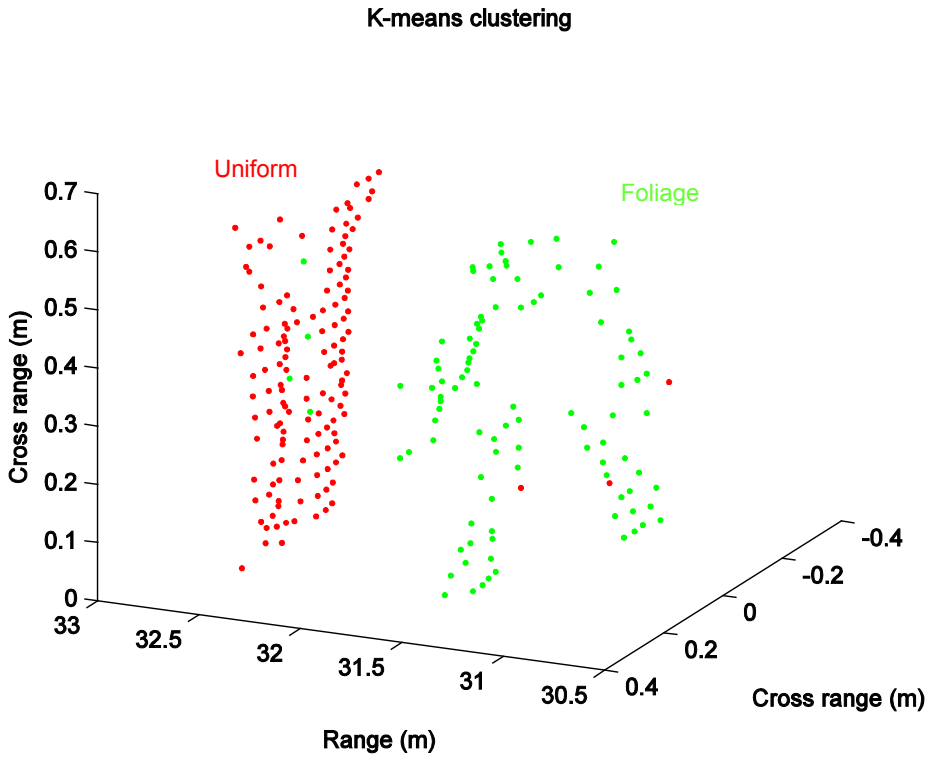

Figure 154: Foliage and fabric - K-Means classified point cloud (20101119T174229, 101122)

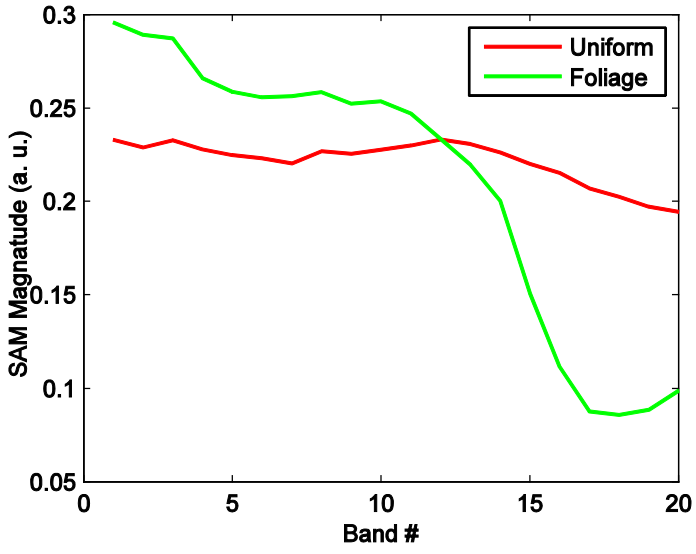

Figure 155: Foliage and fabric - K-Means cluster centroid spectrum (20101119T174229, 101122)

9.2.2. Objects Behind Camouflage

A second test involving scenes in which multiple returns and range resolution are significant features involves a camouflaged vehicle (Figure 156). In this case, the openings in the camouflage netting are smaller than the beam size at the range of the scene so every pixel contains multiple returns, whether above threshold or not.

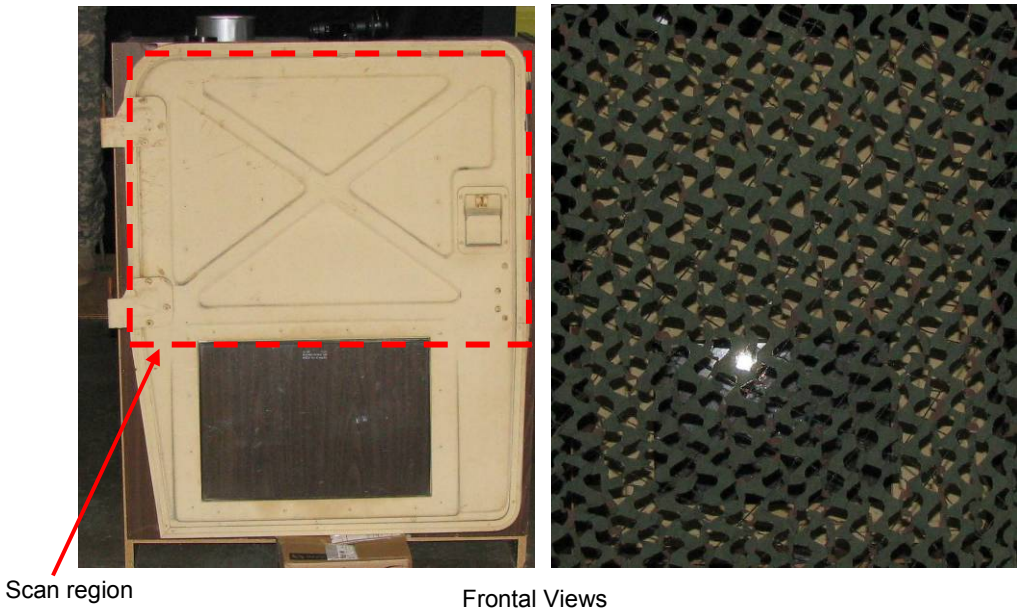

Figure 156: Camouflage and vehicle test scene photo (101121)

The point cloud results from imaging this scene are shown in Figure 157. The range resolved and camouflage penetrating abilities are readily apparent. The two-class K-Means clustering is not able to discriminate between the vehicle surface in the background and the camouflage netting in the foreground to a useful degree. This is true even when time-domain averaging is applied to the waveforms to greatly reduce detector

noise and pulse-to-pulse source fluctuations, as is done in producing Figure 157. One can conclude that camouflage and vehicle surfaces are spectrally indistinct in the SWIR bands used or that something other than random noise is perturbing the reconstructed spectra.

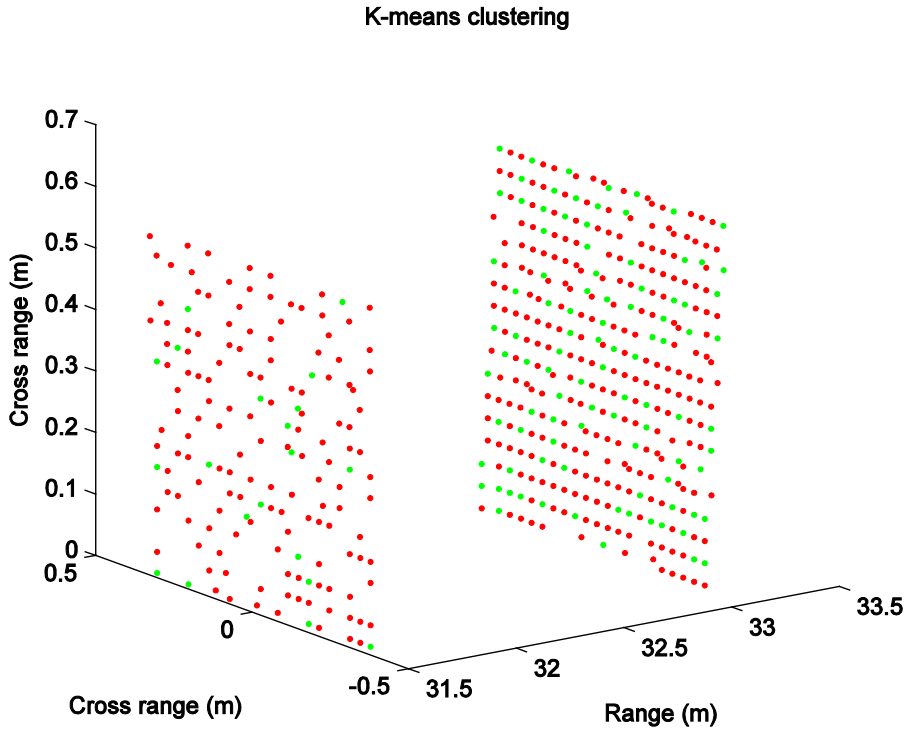

Figure 157: Camouflage and vehicle – K-Means classified point cloud (20101121T171504 pp 20101129T133109, 101212)

The lack of distinct clustering is evident when the spread of spectral signatures is examined. Figure 158 plots the observed spectra of all image points relating to the vehicle (a) and camouflage (b) surfaces separately. This data is time-domain averaged, so apparent fluctuations are not the result of receiver noise or pulse to pulse transmitter fluctuations. The spectral spread in Figure 158a, which should be highly similar to Figure 122, instead bears resemblance to the split pixel spectral analysis of Figure 117.

In fact, since the mesh size of the camouflage is less than that of the beam diameter, all voxels are subject to the distortions discussed in Section 7.5. It is observed in Figure 158 that the mean spectra, indicated by the bold green line, are relatively similar. Unlike the previous situation of Figure 153, the spectral differences among camouflage and vehicle surface are not greater than the sub-region spectral fluctuations of the beam.

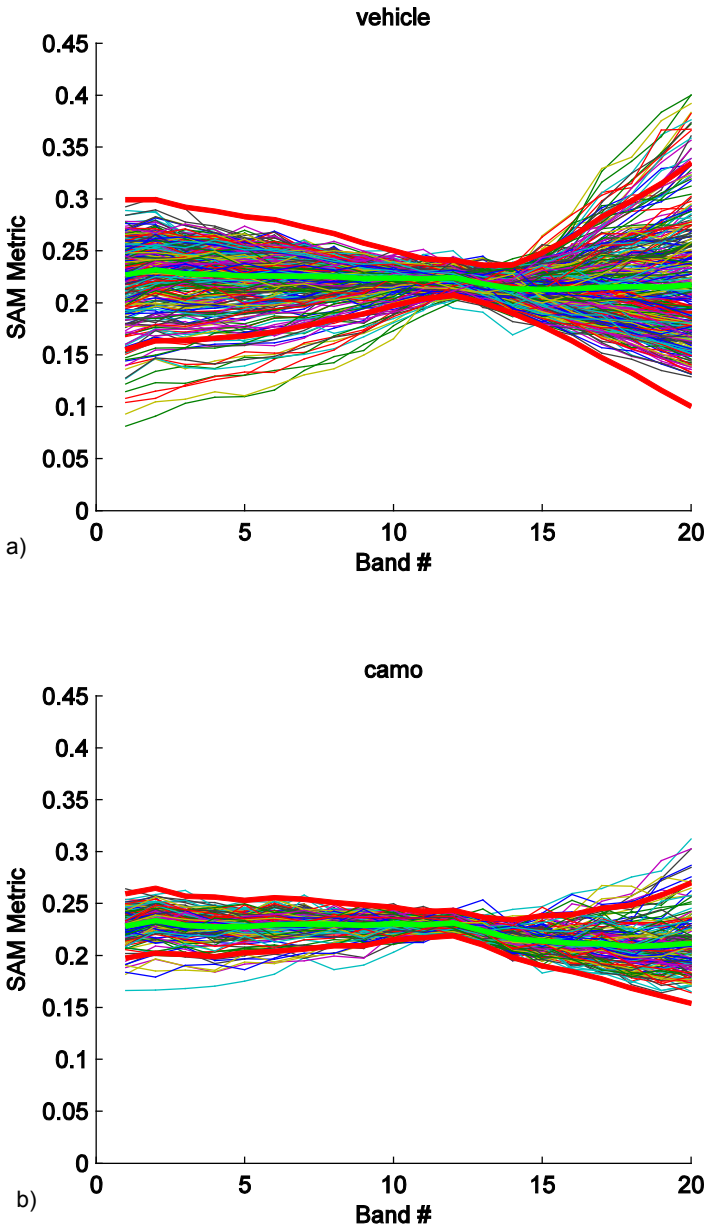

Figure 158: Spectral variation of camouflage and vehicle observed behind camouflage (20101121T171504 pp 20101129T133109, 101212)

Obtaining good clustering results from this scenario requires reduced chromatic aberrations and matched spectral beam parameters, in recognition of results in Section 7.5.

This test was repeated with improved focus, substituting the vehicle door for a more spectrally distinct plastic sheet. The focus of the transmitter was improved prior to conducting this test run to try to reduce the edge error (spectral-spatial coupling) to the extent possible without using an improved lens system (Figure 118).

A plain plastic sheet behind camouflage netting presents serious difficulties to ranging with passive stereo vision. The plastic sheet has no optical image texture from which stereo correspondence, and therefore range, may be calculated. The camouflage netting, on the other hand, has optical image texture but is quasi-periodic. This, combined with the background seen through the gaps of the netting may result in ambiguous stereo correspondence and unreliable or absent range data.

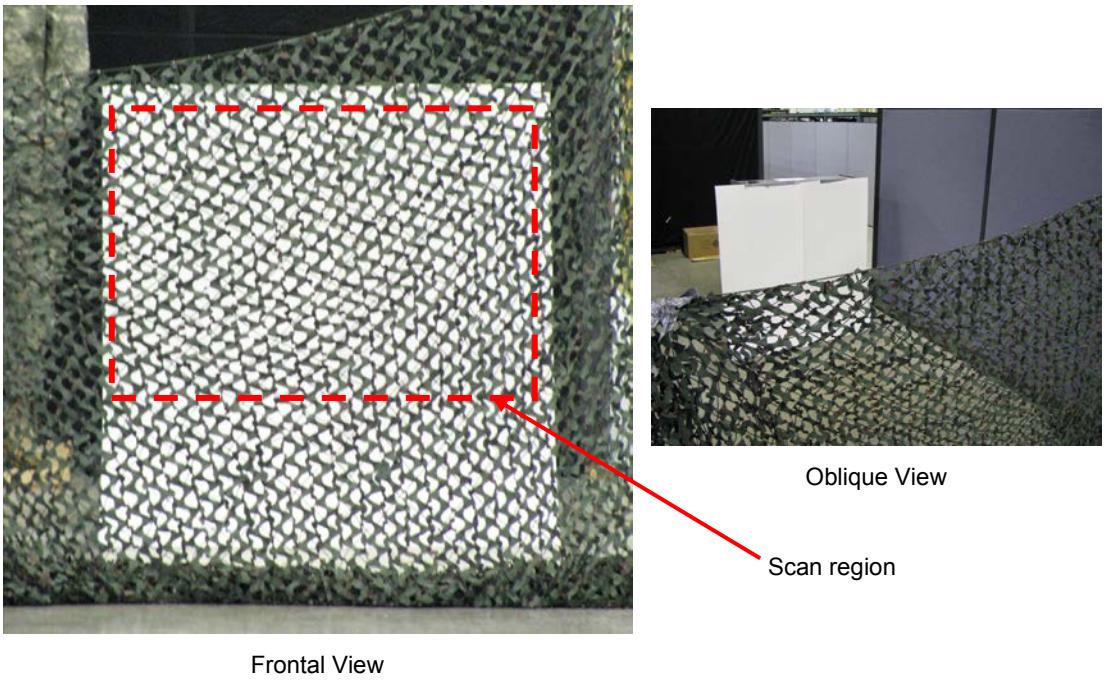

Figure 159: Plastic sheet obscured by foliage (101231)

The point clouds obtained from this scene are shown in Figure 160a when time waveform averaging is applied, and Figure 160b without averaging. Source compensation was used in neither case. Importantly, nearly every pixel in the image has two associated voxels for two return pulses for each transmitted pulse. Obtaining two range values per pixel is not possible using stereo imaging in this case. The point cloud is dense, which also would not be obtained from stereo imaging for the reasons just described. The spectral signatures of camouflage and plastic are clearly separated by K-Means without the need for a spectral unmixing algorithm since the spectral observations are inherently unmixed and range resolved. This situation demonstrates a case where Spectral LADAR offers capabilities that are not obtainable with passive techniques, and situations such as this occur with considerable frequency in military environments.

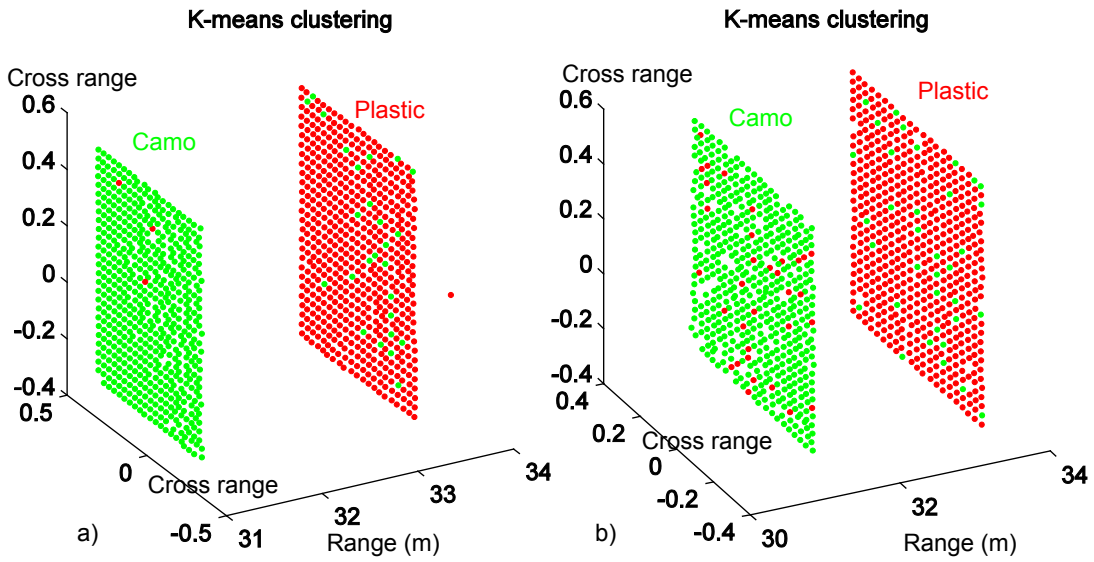

Figure 160: Point cloud images of plastic obscured by camouflage (K-means classified) (a) with time waveform averaging applied and (b) without averaging (20101231T130802 pp 20110102T192248, 20101231T134017 pp 20110102T193521)

In the averaged data set, the 563 voxels on the camouflage netting were correctly identified in 99.5% of cases, and the 568 voxels on the plastic surface were correctly identified in 95.4% of cases. Good statistical results were also obtained for the dataset with quasi-single-pulse measurements, with 535 voxels on the camouflage netting identified correctly in 93.8% of cases and the 562 voxels on the plastic surface identified correctly in 93.6% of cases.

The spectral vectors associated with the clusters in Figure 160 are in Figure 161, where a and c are from the image taken with time waveform averaging and b and d are obtained without averaging. Comparing Figure 161c with Figure 124 (which should be nearly identical) clearly shows how the edge error (spectral-spatial coupling) distorts spectral signatures when partially obscured objects are involved and the Spectral LADAR system

has chromatic aberrations of Figure 118. It is evident in Figure 161b and d that the low signal level allows for random fluctuations to corrupt the data to some extent as well.

The good results obtained from the second camouflage test show how Spectral LADAR enables significantly enhanced identification effectiveness, especially versus passive sensing, in cluttered environments and with partially obscured targets. With improved transmitter optics, further reduction in classification errors is expected.

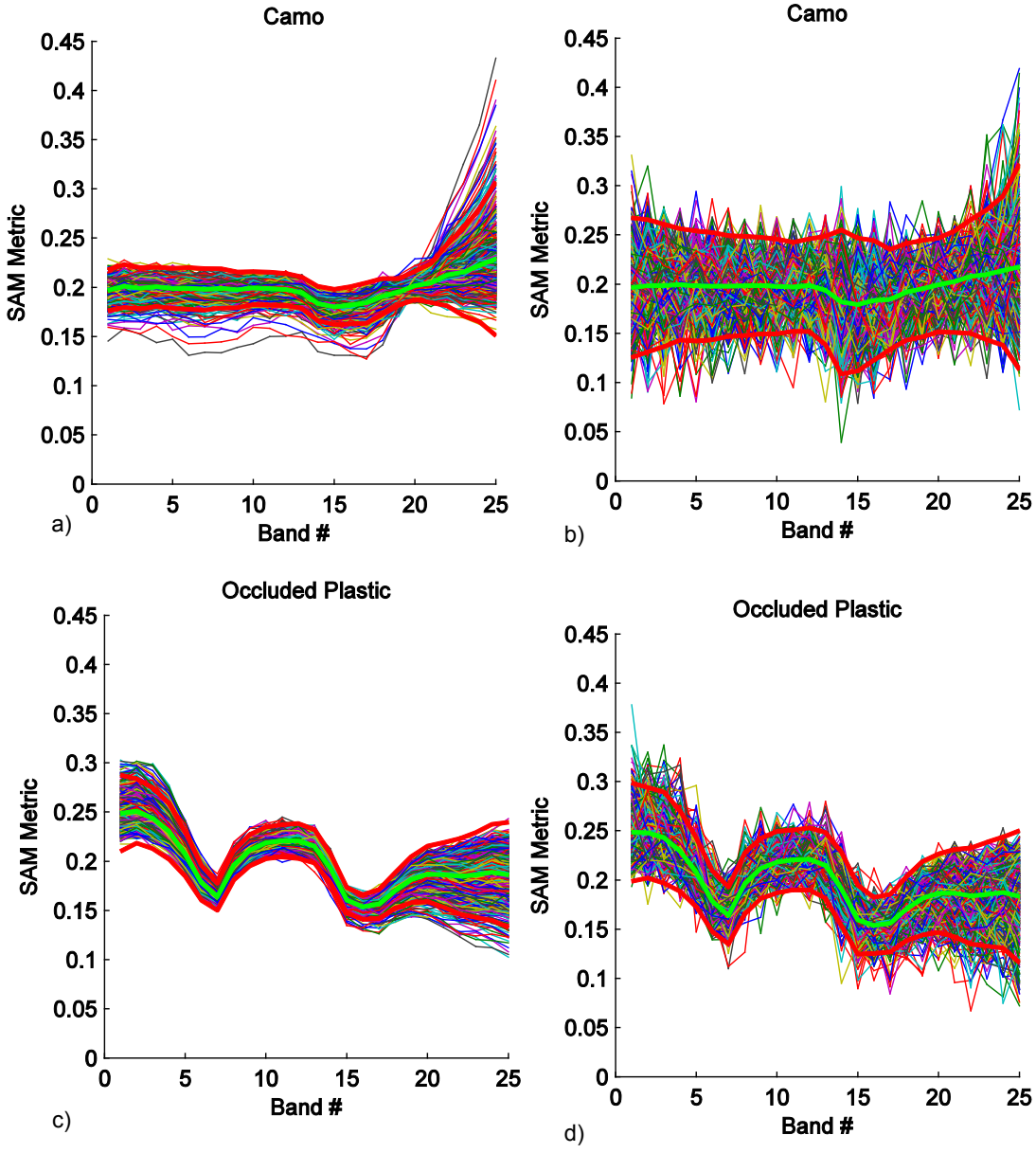

Figure 161: Spectral signatures obtained from camouflage obscured scenes, with time waveform averaging (left column, a and c) and without averaging (right column, b and d) (20101231T130802 pp 20110102T192248, 20101231T134017 pp 20110102T193521)

9.3. Terrain Images

Distinguishing terrain types is an essential part of safe navigation. When UGVs get stuck in hazards like mud and sand, the means to extract them is far more limited compared to manned vehicles.

Terrain hazards often do not have spatial signatures that are distinct from safe terrain. Dry dirt and mud, for example, have similar surface profiles with statistically insignificant differences. Thus, these terrain types can not be distinguished with conventional LADAR or passive sensors using shape recognition.

To test the ability of Spectral LADAR to discern mud from dry dirt, a 40 lb bag of inexpensive topsoil was obtained from a local home and garden retailer. The dirt was placed in a tray 25 m from the sensor aperture in ground distance, with an elevation difference of 1.05 m. An attenuation of 3 dB was applied to the transmitted beam. The tray was inclined toward the sensor at a 20 degree angle, for a sensor-to-surface normal angle of 68 degrees. Water was added to the left half of the tray to the point of saturation and mixed thoroughly. Dirt on the right side of the tray was completely dry, and had a hard consistency.

The tray was scanned by 42 pixels in azimuth, and 3 pixels in elevation. The profile of the beam on the surface of the sample was highly elongated due to the large aspect angle.

The results obtained from this, using normal post-processing, are shown in Figure 162 and Figure 163.

Figure 162a is a photograph taken from the perspective of the sensor. Figure 162b through d are classified point clouds projected in a similar perspective. The K-Means algorithm was used to classify the points into one of two clusters, representing dirt in green colored voxels and mud in red colored voxels. Figure 162b demonstrates that this clustering technique was highly effective in discerning mud from dirt despite lack of discriminating spatial features. The results of KNN and MLC classifiers, shown in Figure 162c and d, respectively, reported results close to ground truth. There were a number of occasions where the terrain was misclassified as several other material types.

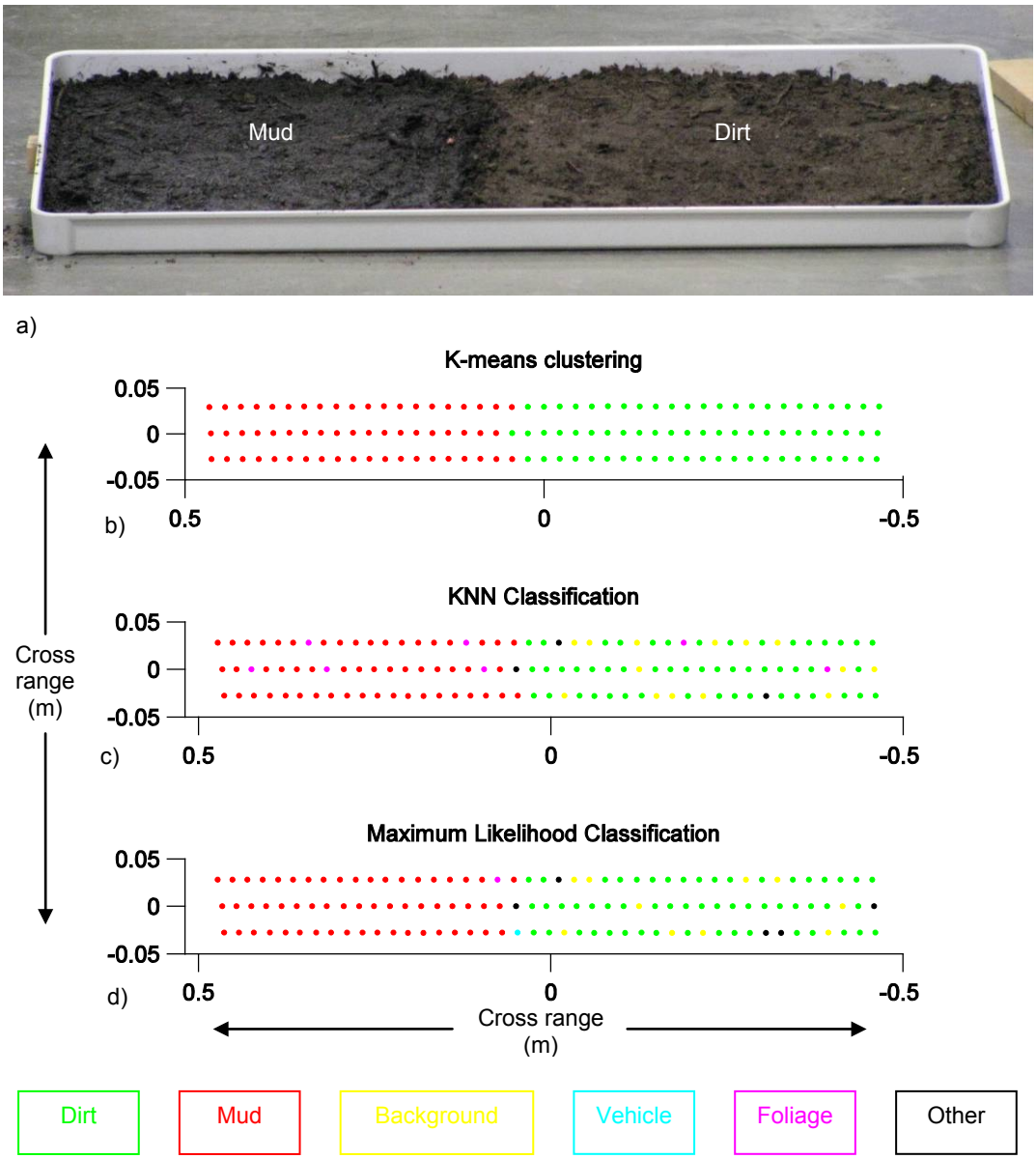

Figure 162: Photo and classifications of a point cloud distinguishing mud from dry dirt (20110109T153505, 110112)

Figure 163 contains images from the same data set, where the top photograph is taken from a perspective much closer to the surface normal of the sample tray. The image at the bottom is a false color image using band 7 for the red channel and band 18 for the

green with zero blue channel. Pixels with red color are associated with the mud region of the sample tray.

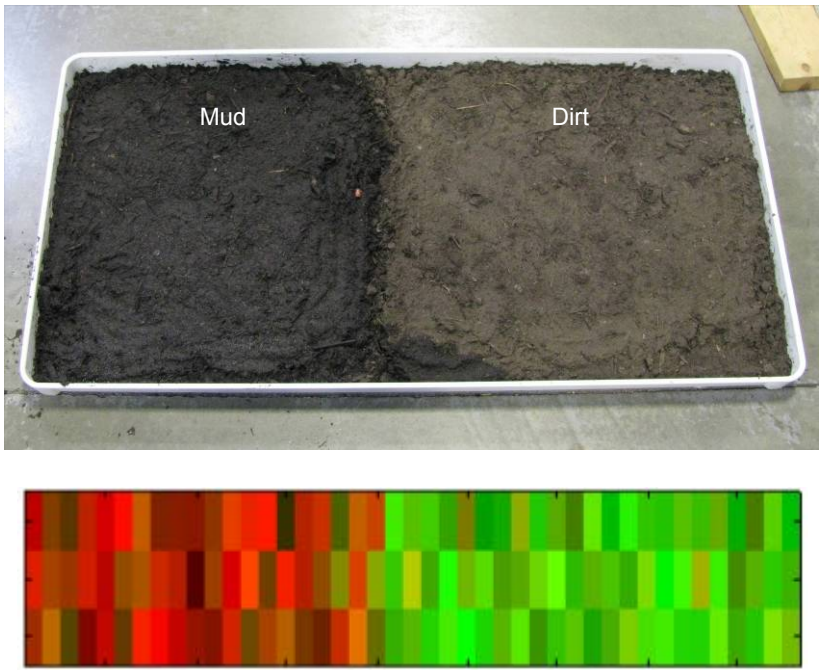

Figure 163: Photo and two band false color image contrasting dirt from mud (20110109T153505)

Combining this with the results of Section 9.2, it is plausible that Spectral LADAR can detect mud obscured by other objects, something that may confuse passive sensors.

This procedure was repeated for a tray containing dirt on the left side and sand on the right. The paver sand used in the test is easily obtained from a home and garden retailer. Figure 164a is the top-down image of the tray, which was arranged in the same geometry and parameters as the previous example. Figure 164b and c clearly show that dirt and sand may be distinguished when time waveform averaging is applied. However, consistent with the predictions of Section 8.3, dirt and sand are very difficult to

distinguish at relatively high NEDR, assumed to be at least 0.15 (Figure 164d and e). Enhancements to the optics by increasing the optical bandwidth and signal processing by implementing source compensation may be able to improve this capability.

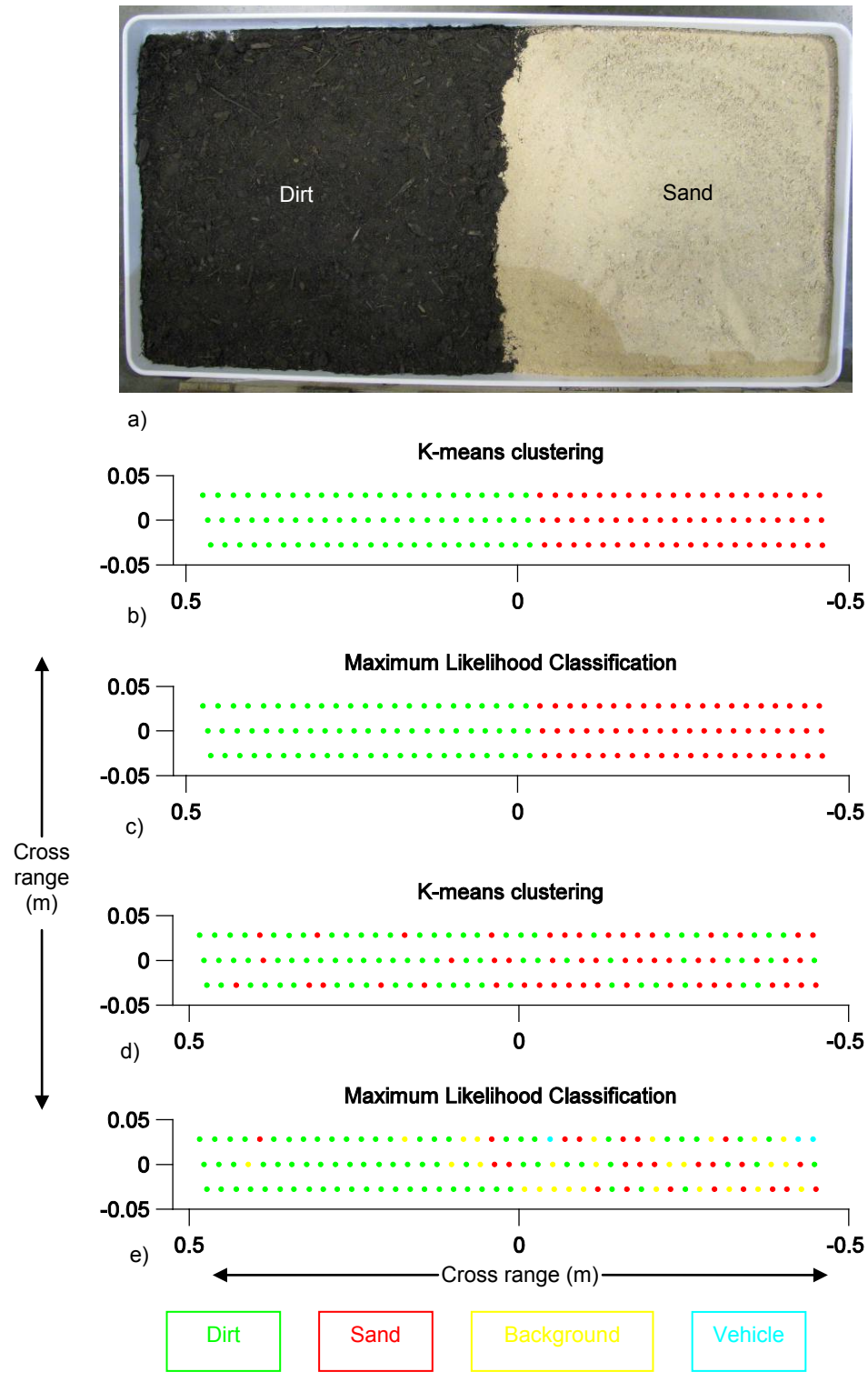

Figure 164: Dirt and sand point cloud classification, averaged (b-c) and quasi-single-pulse (d-e) (20110109T123708, 20110109T133113, 110112)

10. Conclusion

In this section, the results are summarized with a discussion of benefits to UGV applications. Other applications in which Spectral LADAR may be useful are considered. Finally, plans for future work are outlined.

10.1. Summary of Results

This study and experimental demonstration of the Spectral LADAR concept presents a unique imaging method with several advantages over conventional LADAR and spectral imaging. Spectral LADAR combines these techniques at a physical level, and by implementing each spectral band as an independent LADAR channel provides capabilities that are not obtainable from data-level fusion of conventional sensors.

This work has detailed a method of range-unmixed spectral imaging, not previously demonstrated by similar work discussed in Section 2. Not only are range separated

targets unambiguously assigned spectral vectors, the ranging operation does not rely on the texture of objects* to compute unambiguous stereo correspondence.

Section 3 presents the fundamental theory of direct detection LADAR in general, and an approach to Spectral LADAR. This discussion is a foundation for future developmental work, at the system level (e.g., another Spectral LADAR suited to a specific purpose) or the component level (e.g., rapidly tunable APD-based spectrometers).

Beyond the development of a new sensor architecture, some of the most significant technical challenges (Sections 4 and 5) overcome in this work included the development of highly achromatized / high NA lenses for the receiver and spectrometer modules, high modulation bandwidth / high étendue spectrometer with circular apertures, sensor calibration and maximization of sensitivity, and the signal processing of Spectral LADAR data.

The overarching experimental research result, detailed in Sections 7, 8, and 9, is the demonstration of material type classification by spectral signatures in 3D point clouds. This is the first known demonstration of a LADAR imager based on a pulsed-modulated shortwave infrared supercontinuum source. Common classification algorithms were used with the 3D spectral image to partition point clouds into clusters or classes corresponding to training data and assigned a specific label.

---

* Texture, in an imaging sense, implies features in an image to which correspondence is found in a camera with different perspective.

One of the central problems in spectral imaging is the selection of optical bands that are both specific and sensitive identifiers of materials, and that the materials identified are in turn specific markers of items of interests (e.g., skin signatures found only on humans and never on tanks). The signatures analyzed as training data and observed in K-Means clustering achieve this to some extent. Absorption from water, which peaks near bands 17 and 18, is the most prominently observed feature specifically associated with a chemical constituent. Other significant spectral features are assumed to be that of hydrocarbon, amine, and possibly peptide bonds, in keeping with the discussion of overtone spectroscopy in Section 3.2.1.1. Rare-earth electronic absorption features are also evident in the materials used as taggants. The use of SWIR wavelengths, combined with the long standoff range and small absorption path lengths of diffuse backscatter, make highly specific chemical identification a persistent challenge.

One may speculate, on the account of the signature and K-Means clustering results, that a two-wavelength Spectral LADAR may be useful for the detection of anomalies in natural environments. This reduced system may be inadequate for materials identification, but may be very useful as far as 3D object segmentation is concerned. This scheme is highly similar to differential absorption (DIAL) LIDAR often used in atmospheric sensing.

10.2. Benefit to UGV Applications

Spectral LADAR research was motivated by UGV navigational sensing applications, which involve vehicles operating in forested, urban, or battlefield environments, among others. Current challenges include the identification of objects when their shape is obstructed or distorted by surroundings (clutter) or when shape is an unreliable method for identification. In these cases, spectral sensing can provide valuable clues by obtaining chemical / material signatures.

Spectral LADAR addresses these needs by generating 3D images with spectral vectors uniquely associated with each voxel. Difficult perception situations such as the differentiation of mud from dirt, sensing behind foliage and camouflage, and materials identification of partially obscured objects are demonstrated. In relatively easy situations that are handled by existing monochromatic LADAR and image processing, Spectral LADAR will provide an additional level of confidence.

From the start, the physical parameters of the laboratory demonstrator were limited to the confines of a practical sensor for a UGV. The sensor aperture of 75 mm is reasonable for vehicles of this type. A full prototype is expected to have size, weight, and power characteristics that are within acceptable bounds since components that may violate practical envelope restrictions were avoided (e.g., no cryogenic cooling, no bulky laser cavities).

In UGV systems, existing 3D spatial perception algorithms may be used with Spectral LADAR, and in doing so implement augmented identification algorithms with spectral classification. With this data, higher level system software may create a world model with a higher level of fidelity and semantic understanding of the vehicle's surroundings. This world model is the input to path planning and mission control software that direct the operation of the vehicle in real-time.

The ranges at which the experiments were conducted, 25 to 75 m, are adequate forward look distances for vehicles moving at moderate speed. This enables the control software to "see" far enough ahead to have time to react to unexpected obstacles. This long standoff range enables situational awareness for vehicles either at low speeds or when stationary.

In addition to UGV sensing, general military sensing applications (e.g., RSTA, geospatial mapping) will benefit from the capabilities of Spectral LADAR.

10.3. Other Applications

The Spectral LADAR technique may be useful in other applications that benefit from the foliage penetrating and time resolved spectroscopic capability. Agricultural monitoring and assessment is one such area. It is clear that the optical bands used by the prototype have a high sensitivity for detecting water content in foliage. This type of information

can be of use to agricultural analysts who can, by producing 3D images of crops, assess health and hydration. By utilizing better information on crop health and hydration one may be able to increase yield and improve the allocation of scarce irrigation resources. The range resolution and multiple return ability of Spectral LADAR can unmix the spectral signature of outer leaves from the inner structure of a plant to improve image results and accuracy. Note that in Figure 140c and Figure 141c, the principal components transform highlighted the vascular structures of the plant.

Biomedical imaging may also benefit from the techniques described in this work. Spectral LADAR implements range-resolved sensing, but this is indistinct from time-resolved sensing, which is common in fluorescence applications. Techniques used with Spectral LADAR may benefit fluorescent lifetime imaging (FLIM) equipment, which may be used in conjunction with fluorescent tags which specifically identify biological structures on the skin surface or in surgical settings. Unlike gating techniques using image intensifiers, Spectral LADAR captures the full time waveform of the photoluminescent response in a single pulse.

Advanced FLIM protocols using many fluorophores may improve the diagnosis of dermatological conditions or to specifically identify tissues and surgical margins to improve medical outcomes. A large part of this adaptation will require developing suitable marker chemistries that are highly photoluminescent, have highly specific chemical affinity, and are also non-toxic.

10.4. Future Work

In addition to seeking new applications, improvements may be made to address some weaknesses inherent in the design and performance of the laboratory demonstrator. The next steps may involve the correction of particular problems in this prototype, including:

- Reduction of chromatic aberration in transmitter lens

  Custom design to improve sub-pixel white balance uniformity

- Better utilization of source compensation techniques

  Improve reference beam coupling over spectral bandwidth

- Increased dynamic range

  Design and implement custom TIA, likely with discrete components

- Increased digitizer resolution

  Utilize latest 10 and 12 bit ADCs, true differential pair input, DC level correction

- Improved signal processing

  Implement better parameter estimation techniques, improved spectral classification algorithms

- Implementation of polarization sensitivity

  Augment spectral signatures with polarization information

- Extended long wavelength operation to 2500 nm

  Implement extended wavelength InGaAs APDs, or alternative material APDs

Later, the pixel rate performance must be improved in order to attain adequate frame rates to image scenes with motion or when the sensor is mounted on a moving platform. As noted in Section 5.2, the slow band-to-band tuning time and scanning speed results in most of the transmitted pulses, occurring at regular intervals with a repetition frequency of 20 kHz – 25 kHz, being ignored by the receiver while waiting for the mechanical servo motors to move into position. The final pixel rate of about 0.5 pixels / s means that a mere 0.002% of pulses are monitored for backscatter returns while the rest are discarded. This low fraction of pulse utilization is the consequence of the bottlenecks currently constraining the laboratory demonstrator system in its present form. The two main bottlenecks, the mechanically scanned spectral receiver and slow beam scanner, are the result of an economic trade-off enabling proof-of-concept operation at slow pixel rates with easily justified development costs. Significant improvements in pixel rate are unlikely with the present mechanical scanning techniques, as very high performance motors are already implemented and well-tuned for near-optimal step times. Eliminating these bottlenecks to monitor all transmitted pulses and achieve a 50,000x speed-up in pixel rate requires the substitution of mechanical scanning by an APD array with parallel read-out and fixed grating position. Custom APD arrays and ROICs are substantial investments. Also necessary in obtaining higher pixel rates is the design of a high speed scanning system to replace the large gimbaled mirror. Development and implementation of higher PRF supercontinuum sources may increase pixel rates even further, if mechanical elements are no longer limiting factors.

While the results of Section 9 are encouraging, there is clearly a long way to go towards practical deployment and wide end-user acceptance, including factors that transcend the performance and features of the instrument itself. First, the classification algorithms used in this demonstration are relatively basic compared to new, groundbreaking methods. Implementing classifier thresholds to label some outlier spectral vectors as "unclassifiable," and combining spatial and spectral recognition is expected to yield much better performance. Sub-pixel spectral classifiers will prove necessary when the range separation of multiple signatures is below the resolution limit.

Second, obtaining large amounts of training data will be a priority for a high pixel rate system. The classification results presented here demonstrate good statistical performance, but within the confines of the materials tested. It is premature to conclude that the training data gathered in this work approaches completeness and universality, and that the same level of classification performance will be upheld in real-world environments which may exhibit unexpected spectral signature variance. Further, all testing has been performed indoors and in a controlled climate. Simulation and experimentation is needed to determine the impact of varied atmospheric conditions. To address these concerns, a significantly improved prototype with objective level performance is needed, especially in terms of pixel rate. While such an advanced prototype need not have all attributes necessary for a final deployable system, it must have a SWaP envelope and durability suitable for limited use on board a vehicle platform. This highly mobile advanced prototype may be used to collect copious

amounts of data from realistic environments for training sample and performance estimation purposes.

It will also prove important to validate the eye-safety of the laboratory demonstrator and initial prototypes. Current ANSI standards do not directly address the maximum permissible exposure to supercontinuum radiation (Section 3.5).

As an additional benefit in the robotics / UGV application domain, the Spectral LADAR prototype may be used to demonstrate a new capability, the use of passive spectral taggants to improve checkpoint and urban security operations with autonomous technology. Such tags may indicate that a vehicle or individual is considered "safe" or "friendly." Taggant materials may consist of combinations of rare-earth oxides, fluorescent molecules, or quantum dots. These taggants will have unique spectral signatures, and possibly time domain properties (i.e., fluorescent lifetime) [207, 208].

Finally, in looking at the spectral signatures used in this study, it is clear that object spectra contain broad undulations with few sharp and well separated peaks. This is often the nature of overtone spectroscopy in the SWIR using diffuse backscatter. One would instead prefer to obtain signatures containing sharp and distinct spectral lines, the kind often observed in Raman scattering or LWIR absorption spectra obtained from FTIR spectroscopy. The LWIR is often favored for its spectral specificity, and is referred to as the fingerprint region since chemical signatures are often distinct. Future work may explore the possibility of a LWIR Spectral LADAR.

REFERENCES

[1] E. V. Miseo, N. A. Wright, "Developing a Chemical-Imaging Camera," The Industrial Physicist, October/November 2003, pp. 29.

[2] G. W. Flint, "Analysis and Optimization of Laser Ranging Techniques," IEEE Transactions on Military Electronics **8**, 22–48 (1964).

[3] R. M. Measures, *Laser Remote Sensing* (Wiley-Interscience, 1984).

[4] G. R. Osche, D. S. Young, "Imaging Laser Radar in the Near and Far Infrared," Proceedings of the IEEE **84**, 103 (1996).

[5] D. C. Carmer, L. M. Peterson, "Laser Radar in Robotics", Proceedings of the IEEE **84**, 299 (1996).

[6] Team CajunBot, University of Louisiana, www.cajunbot.com, Accessed November 2007.

[7] "DARPA Grand Challenge (2007)", http://en.wikipedia.org/wiki/DARPA_Grand_Challenge_%282007%29, Accessed November 2007.

[8] IndyRobotics, LLC: www.indyrobotics.com, Accessed November 2007.

[9] A. L. Rankin and L. H. Matthies, "Passive Sensor Evaluation for Unmanned Ground Vehicle Mud Detection," Journal of Field Robotics **27**, 473 (2010).

[10] M. Hebert, "Active and Passive Range Sensing for Robotics," in *Proc. of the 2000 IEEE Int'l Conf on Robotics and Automation* (IEEE, 2000), pp. 102–110.

[11] A. L. Rankin, A. Huertas, L. H. Matthies, "Stereo vision based terrain mapping for off-road autonomous navigation," Proc. SPIE **7332**, 732210 (2009).

[12] B. W. Schilling, D. N. Barr, G. C. Templeton, L. J. Mizerka, C. W. Trussell, "Multiple-return laser radar for three-dimensional imaging through obscurations," Applied Optics **41**, 2791 (2002).

[13] M. L. Nischan, R. M. Joseph, J. C. Libby, J. P. Kerekes, "Active Spectral Imaging," *Lincoln Laboratory Journal*, **14**, 131, (2003).

[14] D. C. Carmer, L. M. Peterson, "Laser Radar in Robotics", Proceedings of the IEEE **84**, 299 (1996).

[15] E. Friedman, J. L. Miller, Photonics Rules of Thumb: Optics, Electro-Optics, Fiber Optics, and Lasers, 2nd ed. (SPIE Press and McGraw-Hill, 2003), pp. 4.

[16] D. A. Cremers and L. J. Radziemski, *Handbook of Laser-Induced Breakdown Spectroscopy* (Wiley, 2006).

[17] A. W. Miziolek, V. Palleschi, I. Schechter, *Laser-Induced Breakdown Spectroscopy: Fundamentals and Applications* (Cambridge University Press, 2006).

[18] C.-S.-C. Yang, E. Brown, U. Hommerich, S. B. Trivedi, A. P. Snyder, A. C. Samuels, "Laser-Induced Breakdown Spectroscopy Infrared Emission from Inorganic and Organic Substances," in *Conference on Lasers and Electro-Optics/Quantum Electronics and Laser Science Conference and*

Photonic Applications Systems Technologies, OSA Technical Digest (CD) (Optical Society of America, 2007), paper PWC3.

[19] Y. Dikmelik, C. McEnnis, J. B. Spicer, P. Dagdigian, "Femtosecond Laser-Induced Breakdown Spectroscopy of Trinitrotoluene," in *Conference on Lasers and Electro-Optics/Quantum Electronics and Laser Science Conference and Photonic Applications Systems Technologies*, OSA Technical Digest (CD) (Optical Society of America, 2007), paper CThY4.

[20] R. B. Miles, Z. Zhang, M. N. Scheider, S. H. Zaidi, "RADAR REMPI: A New Approach to Detection, Spectroscopy, and the Dynamics of Gases for Combustion, Fluid Dynamics, and Homeland Defense," in *Conference on Lasers and Electro-Optics/Quantum Electronics and Laser Science Conference and Photonic Applications Systems Technologies*, OSA Technical Digest (CD) (Optical Society of America, 2007), paper CThY2.

[21] S. K. Sharma, P. G. Lucey, M. Ghosh, H. W. Hubble, K. A. Horton, "Stand-off Raman spectroscopic detection of minerals on planetary surfaces," Spectrochimica Acta **59,** 2391 (2003).

[22] W.M. Tolles, R. D. Turner, "A Comparative Analysis of the Analytical Capabilities of Coherent Anti-Stokes Raman Spectroscopy (CARS) Relative to Raman Scattering and Absorption Spectroscopy," Applied Spectroscopy **31**, 96 (1977).

[23] W. M. Tolles, J. W. Nibler, J. R. McDonald, A. B. Harvey, "A Review of the Theory and Application of Coherent Anti-Stokes Raman Spectroscopy (CARS)," Applied Spectroscopy **31**, 253 (1977).

[24] D. A. Harris, J. C. Shane, V. V. Lozovoy, M. Dantus, "Remote Chemical Detection Using SUPER-CARS," in Conference on Lasers and Electro-Optics/Quantum Electronics and Laser Science Conference and Photonic Applications Systems Technologies, OSA Technical Digest (CD) (Optical Society of America, 2007), paper CTuA6.

[25] J.-F. Daigle et al., "Long Range Trace Detection in Aqueous Aerosol using Remote Filament-Induced Breakdown Spectroscopy," *CLEO Conference, Paper CThY5*. Baltimore, MD 2007.

[26] C. Bauer, J. Burgmeier, G. Holl, W. Schade, "A fiber-coupled eye safe spectrometer for the stand-off detection of explosives," in *Conference on Lasers and Electro-Optics/Quantum Electronics and Laser Science Conference and Photonic Applications Systems Technologies*, OSA Technical Digest (CD) (Optical Society of America, 2007), paper PWA3.

[27] R. J. Fogler, Multi- and Hyper-Spectral Sensing for Autonomous Ground Vehicle Navigation (Sandia Report SAND2003-1980, 2003).

[28] G. A. Shaw, H. K. Burke, "Spectral Imaging for Remote Sensing," Lincoln Laboratory Journal **14**, 3 (2003).

[29] NASA Jet Propulsion Laboratory / CalTech - http://aviris.jpl.nasa.gov/html/aviris.cube.html. Accessed Oct 2007.

[30] US Patent Application 11/649,793, M. Campbell, SPARTA, inc. 2007

[31] M. L. Nischan, R. M. Joseph, J. C. Libby, J. P. Kerekes, "Active Spectral Imaging," Lincoln Laboratory Journal **14**, 13 (2003).

[32] B. Johnson, R. Joseph, M. Nischan, A. Newbury, J. Kerekes, H. Barclay, B. Willard, J. J. Zayhowski, "A compact, active hyperspectral imaging system for the detection of concealed targets," Proceedings of SPIE **3710**, 144 (1999).

[33] R. C. Hardie, M. Vaidyanathan, P. F. McManamon, "Spectral band selection and classifier design for a multispectral imaging laser radar," Optical Engineering **37**, 752 (1998).

[34] M. Vaidyanathan, T. P. Grayson, R. C. Hardie, L. E. Myers, P. F. McManamon, "Multispectral Laser Radar Development and Target Characterization," Proceedings of SPIE **3065**, 255 (1997).

[35] B. R. Foy, B. D. McVey, R. R. Petrin, J. J. Tiee, C. W. Wilson, "Remote mapping of vegetation and geological features by lidar in the 9-11 um region," Applied Optics **40**, 4344 (2001).

[36] B. R. Foy, R. R. Petrin, C. R. Quick, T. Shimada, J. J. Tiee, *Comparisons Between Hyperspectral Passive and Multispectral Active Sensor Measurements* (Los Alamos National Laboratory Report LA-UR-02-1633, 2002).

[37] K. Nassau, *The Physics and Chemistry of Color 2nd ed.,* (Wiley-Interscience, 2001).

[38] A. D. Gleckler, A. Gelbart, J. M. Bowden, "Multispectral and hyperspectral 3D imaging lidar based upon the multiple slit streak tube imaging lidar," Proc. SPIE **4377**, 328 (2001).

[39] A. Bénière, M. Alouini, F. Goudail, A. Grisard, J. Bourderionnet, D. Dolfi, I. Baarstad, T. Løke, P. Kaspersen, X. Normandin, G. Berginc, "Snapshot active polarimetric and multispectral laboratory demonstrator," Proc. SPIE **7323**, 732310-1 (2009).

[40] S. Kaasalainen, T. Lindroos, J. Hyyppä, "Toward Hyperspectral Lidar: Measurement of Spectral Backscatter Intensity With a Supercontinuum Laser Source," IEEE Geoscience and Remote Sensing Letters **4**, 211 (2007).

[41] J. F. Andersen, J. Busck, H. Heiselberg, "Pulsed Raman fiber laser and multispectral imaging in three dimensions," Applied Optics **45**, 6198 (2006).

[42] A. M. Wallace, G. S. Buller, R. C. W. Sung, R. D. Harkins, A. McCarthy, S. Hernandez-Marin, G. J. Gibson, R. Lamb, "Multi-spectral laser detection and ranging for range profiling and surface characterization," Journal of Optics A: Pure and Applied Optics **7**, S438 (2005).

[43] G. S. Buller, R. D. Harkins, A. McCarthy, P. A. Hiskett, G. R. MacKinnon, G. R. Smith, R. Sung, A. M. Wallace, R. A. Lamb, K. D. Ridley, J. G. Rarity, "Multiple wavelength time-of-flight sensor based on time-correlated single-photon counting," Review of Scientific Instruments **76**, 083112 (2005).

[44] B. A. Kinder, J. P. Garcia, R. D. Habbit, E. L. Dereniak, "Ranging-Imaging Spectrometer," Proceedings of SPIE **5159**, 73 (2003).

[45] Y. Wang, Y. Wang, H. Q. Le, "Multi-spectral mid-infrared laser stand-off imaging," Optics Express **13**, 6572 (2005).

[46] J. R. Miller, *A 3D Color Terrain Modeling System for Small Autonomous Helicopters* (Ph.D. Thesis, Carnegie Mellon University, 2002).

[47] A. Ben-David, S. L. Emery, S. W. Gotoff, F. M. D'Amico, "High pulse repetition frequency, multiple wavelength, pulsed CO_2 lidar system for atmospheric transmission and target reflectance measurements," Applied Optics **31**, 4224 (1992).

[48] R. M. Narayanan, "Field Measurements of Natural and Artificial Targets Using a Mid-Infrared Laser Reflectance Sensor," IEEE Photonics Technology Letters **6**, 1023 (1994).

[49] C. S. Fox (ed.), *The IR/EO Handbook, Vol. 6* (SPIE Press, 1993).

[50] J. M. Cathcart, J. T. Harrell, T. West, "Electro-optical signature analysis for personnel detection in urban environments," Proceedings of SPIE **6538**, 65381N (2007).

[51] B. Mauro, J. M. Cathcart, "Analysis of visible band sensor for personnel detection," Proceedings of SPIE **6231,** 62310D (2006).

[52] E. Angelopoulou, "Understanding the color of human skin," Proceedings of SPIE **4299**, 243 (2001).

[53] J. L. Miller, "Multispectral infrared BRDF measurements of potential surfaces of interest (skin, oil, water, sand, etc.)," Proceedings of SPIE **5811**, 75 (2005).

[54] R. L. Byer, M. Garbuny, "Pollutant Detection by Absorption Using Mie Scattering and Topographic Targets as Retroreflectors," Applied Optics **12**, 1496 (1973).

[55] M. S. Shumate, S. Lundqvist, U. Persson, S. T. Eng, "Differential reflectance of natural and man-made materials at CO_2 laser wavelengths," Applied Optics **21**, 2386 (1982).

[56] P. V. Cvijin, D. Ignjatijevic, I. Mendas, M. Sreckovic, L. Patani, and I. Pippi, "Reflectance spectra of terrestrial surface materials at CO_2 laser wavelengths: effects on DIAL and geological remote sensing," Applied Optics **26**, 4323 (1987).

[57] W. B. Grant, "Effect of differential spectral reflectance on DIAL measurements using topographic targets," Applied Optics **21**, 2390 (1982).

[58] S. Breugnot, P. Clemenceau, "Modeling and performances of a polarization active imager at $\lambda = 806$ nm," Optical Engineering **39**, 2681 (2000).

[59] C. S. L. Chun, F. A. Sadjadi, "Polarimetric laser radar target classification," Optics Letters **30**, 1806 (2005).

[60] C. S. L. Chun, F. A. Sadjadi, "Target Recognition Study Using Polarimetric Laser Radar," Proceedings of SPIE **5426**, 274 (2004).

[61] J. Savage, C. Coker, B. Thai, O. Aboutalib, N. Yamaoka, C. Kim, "Irma 5.1 Multi-Sensor Signature Prediction Model," Proceedings of the SPIE **5811**, 199 (2005).

[62] F. Goudail, P. Réfrégier, "Improving target detection in active polarimetric images," Proceedings of SPIE **4387**, 140 (2001).

[63] J. M. Cathcart, R. D. Bock, "Analysis of Infrared Polarization Signatures for Backgrounds and Objects," in *Proceedings of IEEE IGARSS* (IEEE, 2004), pp. 1593.

[64] S. Tan, R. M. Narayanan, "Design and performance of a multiwavelength airborne polarimetric lidar for vegetation remote sensing," Applied Optics **43**, 2360 (2004).

[65] R.D. Richmond, B.J. Evans, “Polarimetric Imaging Laser Radar (PILAR) Program,” in *Advanced Sensory Payloads for UAV* (Meeting Proceedings RTO-MP-SET-092, Neuilly-sur-Seine, France: RTO., 2005) UNCLASSIFIED / DISTRIBUTION UNLIMITED pp. 19-1 – 19-14.

[66] M. I. Skolnik, *Introduction to RADAR Systems, 3rd ed.* (McGraw-Hill, 2002), pp. 77, 318.

[67] F. L. Pedrotti, L. S. Pedrotti, *Introduction to Optics 2nd ed.* (Prentice Hall, 1993), pp. 334.

[68] C. C. Davis, *Lasers and Electro-Optics: Fundamentals and Engineering* (Cambridge University Press, 1995), pp. 327.

[69] W. Ruff, K. Aliberti, J. Dammann, M. Giza, P. Shen, and B. Stann, "Performance of an FM/cw prototype ladar using a 32-element linear self-mixing detector array," Proc. SPIE **5086**, 58 (2003).

[70] C. C. Davis, *Lasers and Electro-Optics: Fundamentals and Engineering* (Cambridge University Press, 1995), pp. 599.

[71] C. C. Davis, *Lasers and Electro-Optics: Fundamentals and Engineering* (Cambridge University Press, 1995), pp. 600, 607–608.

[72] G. W. Kamerman, “Laser Radar,” in The Infrared and Electro-Optical Systems Handbook, Active Electro-Optical Systems (Vol 6), C. S. Fox, ed. (SPIE Press, 1993), pp. 9.

[73] C. G. Bachman, *Laser Radar Systems and Techniques* (Artech House, 1979).

[74] A. V. Jelalian, *Laser Radar Systems* (Artech House, 1992).

[75] C. M. Johnson, “Laser Radars,” in *Radar Handbook,* M. I. Skolnik, ed. (Mc-Graw Hill, 1970), ch. 37.

[76] R. M. Measures, *Laser Remote Sensing: Fundamentals and Applications* (Wiley-Interscience, 1984).

[77] P. C. D. Hobbs, *Building Electro-Optic Systems: Making it all work* (Wiley-Interscience, 2000), pp. 117.

[78] C. C. Davis, *Lasers and Electro-Optics: Fundamentals and Engineering* (Cambridge University Press, 1995), pp. 561.

[79] G. P. Agrawal, *Fiber-Optic Communication Systems, 3rd ed.* (Wiley-Interscience, 2002).

[80] H. Nyquist, “Thermal Agitation of Electric Charge in Conductors,” Physical Review **32,** 110 (1928).

[81] J. Johnson, “Thermal Agitation of Electricity in Conductors,” Physical Review **32**, 97 (1928).

[82] M. A. Powers, “Measurement of Thermal Noise Voltage in Electric Conductors,” Physics Graduate Laboratory (PHYS 621), Unpublished report, 2007.

[83] C. C. Davis, *Lasers and Electro-Optics: Fundamentals and Engineering* (Cambridge University Press, 1995), pp. 564 – 567.

[84] ASTM G173-03 Reference Spectra Derived from SMARTS v. 2.9.2, http://rredc.nrel.gov/solar/spectra/am1.5/

[85] P. N. Slater, *Remote Sensing: Optics and Optical Systems* (Addison-Wesley, 1980), pp. 115.

[86] M. I. Skolnik, *Introduction to RADAR Systems, 3rd ed.* (McGraw-Hill, 2002).

[87] G. R. Osche, *Optical Detection Theory for Laser Applications* (Wiley-Interscience, 2002), pp. 49.

[88] R. N. McDonough, A. D. Whalen, *Detection of Signals in Noise, 2nd ed.* (Academic Press, 1995), pp. 159.

[89] J. Minkoff, Signals, Noise and Active Sensors: radar, sonar, laser radar (Wiley-Interscience, 1991), pp. 90-96.

[90] G. R. Osche, *Optical Detection Theory for Laser Applications* (Wiley-Interscience, 2002), pp. 59.

[91] J. Minkoff, Signals, Noise and Active Sensors: radar, sonar, laser radar (Wiley-Interscience, 1991), pp. 92.

[92] R. N. McDonough, A. D. Whalen, *Detection of Signals in Noise, 2nd ed.* (Academic Press, 1995), pp 158.

[93] M. I. Skolnik, *Introduction to RADAR Systems, 3rd ed.* (McGraw-Hill, 2002), pp. 41.

[94] J. Minkoff, Signals, Noise and Active Sensors: radar, sonar, laser radar (Wiley-Interscience, 1991), pp. 92.

[95] M. I. Skolnik, *Introduction to RADAR Systems, 3rd ed.* (McGraw-Hill, 2002), pp. 281.

[96] J. J. Minkoff, Signals, Noise and Active Sensors: radar, sonar, laser radar (Wiley-Interscience, 1991), pp. 100.

[97] M. I. Skolnik, *Introduction to RADAR Systems, 3rd ed.* (McGraw-Hill, 2002), pp. 276-278.

[98] R. N. McDonough, A. D. Whalen, *Detection of Signals in Noise, 2nd ed.* (Academic Press, 1995), pp 215.

[99] G. R. Osche, *Optical Detection Theory for Laser Applications* (Wiley-Interscience, 2002), pp. 46

[100] M. I. Skolnik, *Introduction to RADAR Systems, 3rd ed.* (McGraw-Hill, 2002).

[101] M. I. Skolnik, *Introduction to RADAR Systems, 3rd ed.*, (McGraw-Hill, 2002) pp. 318.

[102] M. I. Skolnik, *Introduction to RADAR Systems, 3rd ed.* (McGraw-Hill, 2002), pp. 320.

[103] H. Tian, *Noise Analysis in CMOS Image Sensors* (Ph.D. Dissertation, Stanford University, 2000).

[104] J. H. Taylor, H. W. Yates, "Atmospheric Transmission in the Infrared," Journal of the Optical Society of America **47**, 223 (1957).

[105] J. D. Rigden, E. I. Gordon, "The Granularity of Scattered Optical Maser Light," Proceedings of the IRE **50**, 2367 (1962).

[106] J. W. Goodman, "Some fundamental properties of speckle," J. Opt. Soc. Am. **66**, 1145 (1976).

[107] J. W. Goodman, "Statistical Properties of Laser Speckle Patterns," in *Topics of Applied Physics: Laser Speckle and Related Phenomena,* J. C. Dainty, ed. (Springer-Verlag, 1975), pp. 19.

[108] J. D. Rigden, E. I. Gordon, "The Granularity of Scattered Optical Maser Light," Proceedings of the IRE **50**, 2367 (1962).

[109] R. C. Hardie, M. Vaidyanathan, P. F. McManamon, "Spectral band selection and classifier design for a multispectral imaging laser radar," Optical Engineering **37**, 752 (1998).

[110] J. W. Goodman, "Statistical Properties of Laser Speckle Patterns," in *Topics of Applied Physics: Laser Speckle and Related Phenomena,* J. C. Dainty, ed. (Springer-Verlag, 1975), pp. 46 – 51.

[111] J. W. Goodman, "Some fundamental properties of speckle," J. Opt. Soc. Am. **66**, 1145 (1976).

[112] N. George, A. Jain, "Speckle Reduction Using Multiple Tones of Illumination," Applied Optics **12**, 1202 (1973).

[113] M. Elbaum, M. Greenebaum, M. King, "A wavelength diversity technique for reduction of speckle size," Optics Communications **5**, 171 (1972).

[114] E. V. Miseo, N. A. Wright, "Developing a Chemical-Imaging Camera," The Industrial Physicist, October/November 2003, pp. 29.

[115] J. M. Cathcart, R. Campbell, S. Greenwood, R. D. Bock, B. Mauro, "Impact of soil and environmental processes on hyperspectral infrared signatures," Proceedings of the SPIE **5415**, 638 (2004).

[116] C. C. Davis, *Lasers and Electro-Optics: Fundamentals and Engineering* (Cambridge University Press, 1995), pp. 207 – 217.

[117] S. T. Thornton, A. Rex, *Modern Physics for Scientists and Engineers, 2nd ed.* (Saunders College Publishing, 2000), pp. 313.

[118] L. Bokobza, "Origin of Near-Infrared Absorption Bands," in *Near Infrared Spectroscopy: Principles, Instruments, Applications*, H. W. Seisler, ed. (Wiley-VCH, 2002), pp. 12-16.

[119] G. R. Fowles, *Introduction to Modern Optics 2nd ed.* (Dover Publications, 1989, reprint of Holt, Reinhart and Winston, 1975), pp. 256 – 257.

[120] H.W. Seisler, "Introduction, Ch. 1," in in *Near Infrared Spectroscopy: Principles, Instruments, Applications*, H. W. Seisler, ed. (Wiley-VCH, 2002), pp. 6.

[121] R. Anderson, W. Malila, R. Maxwell, and L. Reed, *Military Utility of Multispectral and Hyperspectral Sensors* (Environmental Research Institute of Michigan (ERIM), 1994), Appendix A, pp. A-1 to A-9.

[122] E. Hecht, *Optics, 3rd ed.* (Addison Wesley, 1998), pp. 111.

[123] F. Nicodemus, "Directional Reflectance and Emissivity of an Opaque Surface," Applied Optics **4**, 767 (1965).

[124] F. L. Pedrotti, L. S. Pedrotti, *Introduction to Optics 2nd ed.* (Prentice Hall, 1993), pp. 11 – 12.

[125] G. W. Kamerman, "Laser Radar," in The Infrared and Electro-Optical Systems Handbook, Active Electro-Optical Systems (Vol 6), C. S. Fox, ed. (SPIE Press, 1993), pp. 30.

[126] B. Hapke, *Theory of Reflectance and Emittance Spectroscopy* (Cambridge University Press, 1993).

[127] J. M. Cathcart, R. V. Worrall, D. P. Cash, "Hyperspectral signature modeling for terrain backgrounds," Proceedings of SPIE **6239**, 62390A (2006).

[128] L. Le Hors, P. Hartemann, D. Dolfi, S. Breugnot, "A phenomenological model of paints for multispectral polarimetric imaging," Proceedings of SPIE **4370**, 94 (2001).

[129] J. Jafolla, W. Reynolds, "Bidirectional reflectance measurements for high resolution signature modeling," Proceedings of SPIE **5431**, 184 (2004).

[130] T. L. Troy, S. N. Thennadil, "Optical properties of human skin in the near infrared wavelength range of 100 to 2200 nm," Journal of Biomedical Optics **6**, 167 (2001).

[131] A. N. Bashkatov, E. A. Genina, V. I. Kochubey, V. V. Tuchin, "Optical properties of human skin, subcutaneous and mucous tissue in the wavelength range from 400 to 2000 nm," Journal of Physics D: Applied Physics **38**, 2543 (2005).

[132] J. A. Viator, B. Choi, G. M. Peavy, S. Kimel, J. S. Nelson, "Spectra from 2.5-15 um of tissue phantom materials, optical clearing agents and ex vivo human skin: implications for depth profiling of human skin," Physics in Medicine and Biology **48**, N15 (2003).

[133] L. Debelle, A. J. P. Alix, S. M. Wei, M-P Jacob, J-P Huvenne, M Berjot, P. Legrand, "The secondary nature and architecture of human elastin," European Journal of Biochemistry **258**, 533 (1998).

[134] B. B. Doyle, E. G. Bendit, E. R. Blout, "Infrared spectroscopy of collagen and collagen-like polypeptides," Biopolymers **14**, 937 (1975).

[135] C. M. Canal, A. Saleem, R. J. Green, and D. A. Hutchins, "Remote identification of chemicals concealed behind clothing using near infrared spectroscopy," Analytical Methods **3**, 84 (2011).

[136] D. M. Gates, H. J. Keegan, J. C. Schleter, V. R. Weidner, "Spectral Properties of Plants," Applied Optics **4**, 11 (1965).

[137] S. Jacquemoud, F. Baret, "PROSPECT: A model of leaf optical properties spectra," Remote Sensing of Environment **34**, 75 (1990).

[138] J. E. Solomon, "Polarization Imaging," Applied Optics **20**, 1537 (1981).

[139] J. L. Pezzaniti, R. A. Chipman, "Mueller matrix imaging polarimetry," Optical Engineering **34**, 1558 (1995).

[140] G. Horváth, D. Varjú, *Polarized Light in Animal Vision: Polarization Patterns in Nature* (Springer-Verlag, 2004).

[141] E. Hecht, *Optics, 3rd ed.* (Addison Wesley, 1998), pp. 366 – 371.

[142] W. G. Egan, "Enhancement of Optical Detectability with Polarization," Proc. SPIE **3699**, 38 (1999).

[143] D. Manolakis, D. Marden, G. A. Shaw, "Hyperspectral Image Processing for Automatic Target Detection Applications," Lincoln Laboratory Journal **14**, 79 (2003).

[144] J. A. Richards, X. Jia, *Remote Sensing Digital Image Analysis 4th ed.* (Springer, 2006), pp. 137-156.

[145] R. A. Schowengerdt, *Remote Sensing: Models and Methods for Image Processing 3rd ed.* (Academic Press, 2007), pp. 193-202.

[146] B. R. Foy, B. D. McVey, R. R. Petrin, J. J. Tiee, C. W. Wilson, "Remote mapping of vegetation and geological features by lidar in the 9-11 um region," Applied Optics **40**, 4344 (2001).

[147] Y. Wang, Y. Wang, H. Q. Le, "Multi-spectral mid-infrared laser stand-off imaging," Optics Express **13**, 6572 (2005).

[148] R. A. Schowengerdt, *Remote Sensing: Models and Methods for Image Processing 3rd ed.* (Academic Press, 2007), pp. 407.

[149] R. A. Schowengerdt, *Remote Sensing: Models and Methods for Image Processing 3rd ed.* (Academic Press, 2007), pp. 419.

[150] J. A. Richards, X. Jia, *Remote Sensing Digital Image Analysis 4th ed.* (Springer, 2006), pp. 195.

[151] Laser Institute of America, *American National Standard for Safe Use of Lasers* ANSI Z136.1-2007.

[152] R. Haring, R. Paschotta, R. Fluck, H. Gini, H. Melchior, U. Keller, "Passively Q-switched microchip laser at 1.5 μm," Journal of the Optical Society of America B **18**, 1805 (2001).

[153] J. J. Zayhowski, "Microchip Lasers," Optical Materials **11**, 255 (1999).

[154] M. Eichhorn, S. D. Jackson, "High-pulse-energy actively Q-switched TM^{3+}-doped silica 2 μm fiber laser pumped at 792 nm," Optics Letters **32**, 2780 (2007).

[155] F. Di Teodoro, C. D. Brooks, "1.1 MW peak-power, 7 W average-power, high-spectral-brightness, diffraction-limited pulses from a photonic crystal fiber amplifier," Optics Letters **30**, 2694 (2005).

[156] P. C. Becker, N. A. Olsson, J. R. Simpson, *Erbium-Doped Fiber Amplifiers: Fundamentals and Technology* (Academic Press, 1999).

[157] M. J. F. Digonnet ed., *Rare-Earth-Doped Fiber Lasers and Amplifiers, 2nd ed.* (CRC Press, 2001).

[158] M. Jiang, P. Tayebati, "Stable 10ns Peak-Power Pulse Generation from Gain-Switched Thulium-Doped Fiber Laser," *Spectrode, LLC Corporate Publication*.

[159] S. D. Jackson, T. A. King, "CW Operation of a 1.064-um Pumped Tm-Ho-Doped Silica Fiber Laser," IEEE Journal of Quantum Electronics **34**, 1578 (1998).

[160] S. D. Jackson, "Midinfrared Holmium Fiber Lasers," IEEE Journal of Quantum Electronics **42**, 187 (2006).

[161] M. Yamada, M. Shimizu, "Ultra-wideband Amplification Technologies for Optical Fiber Amplifiers," NTT Technical Review **1**, 80 (2003).

[162] S. A. E. Lewis, “Triple wavelength pumped silica-fibre Raman amplifiers with 114nm bandwidth,” Electronics Letters **35**, 1761 (1999).

[163] J. M. Dudley, G. Genty, S. Coen, “Supercontinuum generation in photonic crystal fiber,” Reviews of Modern Physics **78**, 1135 (2006).

[164] W. J. Wadsworth, N. Joly, J. C. Knight, T. A. Birks, F. Biancalana, P. St. J. Russell, “Supercontinuum and four-wave mixing with Q-switched pulses in endlessly single-mode photonic crystal fibers,” Optics Express **12**, 299 (2004).

[165] L. Provino, J. M. Dudley, H. Maillotte, N. Grossard, R. S. Windleler, B. J. Eggleton, “Compact broadband continuum source based on microchip laser pumped microsctructure fiber,” Electronics Letters **37**, 558 (2001).

[166] J. M. Dudley, G. Genty, S. Coen, “Supercontinuum generation in photonic crystal fiber,” Reviews of Modern Physics **78**, 1135 (2006).

[167] D. Mogilevtsev, T. A. Birks, P. St. J. Russell, “Group-velocity dispersion in photonic crystal fibers,” Optics Letters **23**, 1662 (1998).

[168] F. Träger, ed., *Springer Handbook of Lasers and Optics* (Springer, 2007), pp. 533.

[169] G. Keiser, *Optical Fiber Communications 3rd ed.* (McGraw-Hill, 2000), pp. 259.

[170] B. E. A. Saleh, M. C. Teich, *Fundamentals of Photonics, 2nd ed.* (Wiley-Interscience, 2007), pp. 773.

[171] P. P. Webb, R. J. McIntyre, J. Conradi, “Properties of Avalanche Photodiodes,” RCA Review **35**, 234 (1974).

[172] F. Capasso, W. T. Tsang, G. F. Williams, “Staircase Solid-State Photomultipliers and Avalanche Photodiodes with Enhanced Ionization Rates Ratio,” IEEE Transactions on Electron Devices **30**, 381 (1983).

[173] R. Chin, N. Holonyak Jr., G. E. Stillman, J. T. Tang, K. Hess, “Impact ionization in multilayered heterojunction structures,” Electronics Letters **16**, 467 (1980).

[174] P. Yuan, S. Wang, X. Sun, X. G. Zheng, A. L. Holmes Jr., J. C. Campbell, “Avalanche Photodiodes with an Impact-Ionization-Engineered Multiplication Region,” IEEE Photonics Technology Letters **12**, 1370 (2000).

[175] S. Wang, J. B. Hurst, F. Ma, R. Sidhu, X. Sun, X. G. Zheng, A. L. Holmes Jr., A. Huntington, L. A. Coldren, J. C. Campbell, “Low-Noise Impact-Ionization-Engineered Avalanche Photodiodes Grown on InP Substrates,” IEEE Photonics Technology Letters **14**, 1722 (2002).

[176] G. Keiser, *Optical Fiber Communications 3rd ed.* (McGraw-Hill, 2000), pp. 259.

[177] P. C. D. Hobbs, *Building Electro-Optic Systems: Making it all work* (Wiley-Interscience, 2000), pp. 625.

[178] CRi, inc., www.cri-inc.com. Accessed 22 September 2010.

[179] P. V. Kelkar, F. Coppinger, A. S. Bhushan, B. Jalali, “Time-domain optical sensing,” Electronics Letters **35**, 1661 (1999).

[180] R. J. Bell, *Introductory Fourier Transform Spectroscopy* (Academic Press, 1972).

[181] P. Griffiths, J. de Haseth, *Fourier Transform Infrared Spectroscopy* (Wiley-Interscience, 1986).

[182] D. G. Winters, P. Schlup, R. A. Bartels, "Highly achromatic Fourier-transform spectrometer," Optics Express **15**, 1361 (2007).

[183] E. LeCoarer, S. Blaize, P. Benech, I. Stefanon, A. Morand, G. Lerondel, G. Leblond, P. Kern, J. M. Fedeli, P. Royer, "Wavelength-scale stationary wave integrated Fourier-transform spectrometry," Nature Photonics **1**, 473 (2007).

[184] P. J. Winzer, W. R. Leeb, "Fiber coupling efficiency for random light and its applications to lidar," Optics Letters **23**, 986 (1998).

[185] C. D. Brewer, B. D. Duncan, K. J. Barnard, E. A. Watson, "Coupling efficiencies for general-target-illumination ladar systems incorporating single-mode optical fiber receivers," J. Opt. Soc. Am. A **15**, 736 (1998).

[186] J. H. Moore, C. C. Davis, and M. A. Coplan, *Building Scientific Apparatus 4th ed.* (Cambridge University Press, 2009).

[187] C. Palmer, E. Loewen, *Diffraction Grating Handbook, 6th ed.* (Newport Corporation, 2005), pp. 125.

[188] E. Hecht, *Optics, 3rd ed.* (Addison Wesley, 1998), pp. 435 – 436, 501 – 505.

[189] F. L. Pedrotti, L. S. Pedrotti, *Introduction to Optics 2nd Ed.* (Prentice Hall, 1993), pp. 533.

[190] C. Palmer, E. Loewen, *Diffraction Grating Handbook, 6th ed.* (Newport Corporation, 2005), pp. 119.

[191] J. F. James, R. S. Sternberg, *Design of Optical Spectrometers* (Chapman and Hall, 1969), pp. 2.

[192] P. C. D. Hobbs, *Building Electro-Optic Systems: Making it all work* (Wiley-Interscience, 2000), pp. 220.

[193] J. F. James, R. S. Sternberg, *Design of Optical Spectrometers* (Chapman and Hall, 1969), pp. 69.

[194] J. H. Moore, C. C. Davis, and M. A. Coplan, *Building Scientific Apparatus 4th ed.* (Cambridge University Press, 2009), pp. 293.

[195] C. Lin, R. H. Stolen, "New nanosecond continuum for excited-state spectroscopy," Applied Physics Letters **28**, 216 (1976).

[196] C. C. Davis, *Lasers and Electro-Optics: Fundamentals and Engineering* (Cambridge University Press, 1995), pp. 363.

[197] B. E. A. Saleh, M. C. Teich, *Fundamentals of Photonics, 2nd ed.* (Wiley-Interscience, 2007), pp. 94.

[198] W. J. Smith, *Modern Optical Engineering, 3rd ed.* (McGraw-Hill, 2000), pp. 61 – 89.

[199] F. L. Pedrotti, L. S. Pedrotti, *Introduction to Optics 2nd Ed.* (Prentice Hall, 1993), pp. 533-535.

[200] P. C. D. Hobbs, *Building Electro-Optic Systems: Making it all work* (Wiley-Interscience, 2000), pp. 447-448, 494, 612.

[201] K. J. Williams, R. D. Esman, “Design Considerations for High-Current Photodetectors,” Journal of Lightwave Technology **17**, 1443 (1999).

[202] Y-L Huang, C-K Sun, “Nonlinear Saturation Behaviors of High-Speed p-i-n Photodetectors,” Journal of Lightwave Technology **18**, 203 (2000).

[203] S. Breugnot, P. Clémenceau, “Modeling and performances of a polarization active imager at λ=806nm,” Optical Engineering **39**, 2681-2688 (2000).

[204] C. S. L. Chun, F. A. Sadjadi, "Polarimetric laser radar target classification," Optics Letters **30**, 1806-1808 (2005).

[205] R. Anderson, W. Malila, R. Maxwell, L. Reed, *Military Utility of Multispectral and Hyperspectral Sensors* (Environmental Research Institute of Michigan, 1994), Section 5.4.3.

[206] J. M. Cathcart, J. T. Harrell, T. West, “Electro-optic signature analysis for personnel detection in urban environments,” Proc. SPIE **6538**, 65381N-1 (2007).

[207] E. H. Sargent, “Infrared Quantum Dots,” Advanced Materials **17**, 515 (2005).

[208] G. M Williams, et al., “Optically coded nanocrystal taggants and optical frequency IDs,” Proc. SPIE **7673**, 76730M (2010).